Electrochemical Reduction of Oxygen

Author:
Qian LI

Supervisor:
Prof. Richard G. Compton

Submitted to the University of Oxford for the degree of
Doctor of Philosophy

Physical and Theoretical Chemistry Laboratory
and St John's College

January 2014

Abstract

The main aim of the work reported is the design of proof-of-concept of at point-of-use hydrogen peroxide electrogeneration from air. The experimental work discussed within this thesis explores five major areas: the kinetics of electrocatalysis, ion-pairing, change of solvent media, the electrode surface modification by a redox mediator, and the electrochemical reduction of oxygen within enhanced mass transport systems.

The electrocatalytic rates and mass transport of two oxygen reduction redox meditors, viz. anthraquinone and methyl viologen, are studied in aqueous solutions. The investigation is facilitated through the use of a boron-doped diamond electrode, allowing the catalytic response to be clearly delineated from that of the direct oxygen reduction process. The use of simulation software is highlighted in combination with experimental voltammograms to extract kinetic data. Specifically, the voltammetric features, such as the 'reverse' peak and the 'split waves', are given particular attention. Consequently, it is possible to deconvolute the electrocatalytic reaction mechanisms. The reactivity of the viologen radical cation is comparable to the semiquinone radical anion in aqueous solution ($(4.8 \sim 6) \times 10^9$ M^{-1} s^{-1}), but over a far wider pH range (pH 2.5 – pH 8.5). The change of local proton concentration, and sequential electron transfers play key roles here. Moreover, the reduced reactivity of semiquinone is observed upon formation of ion-pairs with tetrabutylammonium cations in alkaline solutions.

The electro-reduction of oxygen and its mediated pathways are also investigated in non-aqueous media; in particular the thermodynamics, the kinetics, and mass transport involved in these processes. Through a variable temperature study in electrolytic acetonitrile solution, the oxygen dissolution is quantitatively shown to be an endothermic process. Moreover, the diffusion coefficients and concentration of oxygen upon change of acetonitrile mole fraction is also explored in water-acetonitrile mixtures. The rates of bimolecular reactions are extracted from simulation programs, involving semiquinone in anhydrous acetonitrile and viologen radical cation in ethanol, and show a 3 – 4 orders of magnitude reduction compared to that in aqueous solution. Although the solubility of oxygen is *ca.* 6 – 8 times larger in non-aqueous solvents, the much reduced homogeneous rates limit the electrogeneration of hydrogen peroxide in pure organic media.

Novel surface modification methodologies for graphitic surfaces with covalently attached anthraquinonyl groups are studied and characterised. The anthraquinonyl-modified carbon surfaces show much reduced overpotentials required for oxygen reduction. In the final chapter, utilising the new surface modification methodology and novel designs, two gravity-feed flow cells for electrochemical reduction of oxygen in aqueous solutions are proposed and characterised, one based upon the tubular electrode geometry. The other exhibits much enhanced current conversion by using a porous reticulated vitreous carbon electrode. The latter may provide a prototype hydrodynamic system to produce dilute hydrogen peroxide solution at point-of-use.

Contents

The research presented in this thesis comprises work published in the following articles, listed in order of appearance within the text:

- Li, Q., Batchelor-McAuley, C., Lawrence, N. S., Hartshorne,R. S. and Compton, R. G. *ChemPhysChem* 2011, 12, 1255-1257
- Lin, Q., Li, Q., Batchelor-McAuley, C., Compton, R. G. *Physical Chemistry Chemical Physics* 2013, 15, 7760-7767
- Li, Q., Batchelor-McAuley, C., Lawrence, N. S., Hartshorne,R. S. and Compton, R. G. *Chemical Communications* 2011, 47, 11426-11428
- Li, Q., Batchelor-McAuley, C., Lawrence, N. S., Hartshorne,R. S. and Compton, R. G. *Journal of Electroanalytical Chemistry* 2013, 688, 328-335
- Nissim, R., Batchelor-McAuley, C., Li, Q., Compton, R. G. *Journal of Electroanalytical Chemistry* 2012, 681, 44-48
- Lin, Q., Li, Q., Batchelor-McAuley, C., Compton, R. G. *Journal of Electrochemical Science and Technology* 2013, 4, 71-80
- Li, Q., Batchelor-McAuley, C., Lawrence, N. S., Hartshorne,R. S. and Compton, R. G. *New Journal of Chemistry* 2011, 35, 2462-2470
- Li, Q., Batchelor-McAuley, C., Lawrence, N. S., Hartshorne,R. S. and Compton, R. G. *Physical Chemistry Chemical Physics* 2013, 15, 7854-7865
- Li, Q., Batchelor-McAuley, C., Lawrence, N. S., Hartshorne,R. S. and Compton, R. G. *Journal of Solid-State Electrochemistry* 2013, DOI: 10.1007/s10008-013-2250-9

Symbols

A	area	cm^2
a_i	activity of species i	mol cm^{-3}
C_i	concentration of bulk species i	mol cm^{-3}
		or mol dm^{-3} (M)
C_{DL}	double layer capacitance	μF cm^{-2}
C_{sp}	specific capacitance	μF cm^{-2}
D_i	diffusion coefficient of bulk species i	cm^2 s^{-1}
E	electrode potential	V
ΔE	difference in sequential formal potentials	V
$E^{\ominus}$	electrode potential under standard conditions	V
$E_f^{\ominus}$	formal electrode potential	V
E_p	peak potential	V
$E_{a,i}$	diffusional activation energy of species i	J mol^{-1}
F	Faraday constant = 96485.3 C mol^{-1}	
f	fractional current conversion	dimensionless
$\Delta G_{solv}^{\ominus}$	change in Gibbs energy under standard conditions	J mol^{-1}
$\Delta H_{solv}^{\ominus}$	standard enthalpy change of solvation	J mol^{-1}
$\mathbf{I}$	ionic strength	mol cm^{-3}
I_p	peak current	A
I_{ss}	steady-state current	A
j_o	flux	mol s^{-1} cm^{-2}
K_a	acid dissociation constant	dimensionless
k_b	Boltzmann constant = 1.38×10^{-23} J K^{-1}	
K_{eq}	equilibrium constant	dimensionless
k_f	homogeneous rate constant	dm^3 mol^{-1} s^{-1}
k_s	heterogeneous rate constant	cm s^{-1}
m_T	rate of mass transport	cm s^{-1}

n	number of electrons transferred	dimensionless
n'	number of electrons transferred prior to the RDS	dimensionless
N	number of experimental data points	dimensionless
r_e	electrode radius	cm
R	universal gas constant = 8.31447 J K^{-1} mol^{-1}	
Re	Reynolds number	dimensionless
R_s	solution resistance	Ω
R_u	uncompensated solution resistance	Ω
$\Delta S^{\ominus}_{solv}$	standard entropy change of solvation	J mol^{-1} K^{-1}
q or Q	charge passed	C
t	time	s
T	temperature	K
V_f	volume flow rate	cm^3 s^{-1}
v_o	solution velocity through the centre of electrode	cm s^{-1}
v_x	solution axial velocity	cm s^{-1}
x_e	electrode length	cm
x_l	tubular electrode length	cm
z_i	charge number of species i	dimensionless

α, β	Butler-Volmer transfer coefficients	dimensionless
γ_i	activity coefficient of species i	dimensionless
ε_i	dielectric constant of species i	dimensionless
η	overpotential	V
μ	micro-	
τ	dimensionless time parameter	
ν	scan rate	V s^{-1}
	or kinematic viscosity of reaction solution	cm^2 s^{-1}
ϕ_m, ϕ_s	local electrostatic potential at metal and solution phases	V
$\Delta\phi_{OD}$	ohmic drop	V
χ_i	mole fraction of species i solubility	dimensionless
Γ	surface coverage	mol cm^{-2}
Λ	the Matsuda-Ayabe parameter	
Σ	sum of	

Acknowledgements

Firstly, I would like to thank my supervisor, Professor Richard Compton, for having me in the group. Without his guidance, motivation, and endless willingness to help I would not have made it through. I would also like to thank Dr. Christopher Batchelor-McAuley. Chris has been extremely supportive since my Part II. He's never tired of sharing his scientific enthusiasm, intellectual curiosity, and mind-blowing insights with me. More importantly, I learned 'attitude' from these two persons. Whether they are attitudes towards the production of rigorous and solid scientific work; or ones beyond, humour or sarcasm, diligence or relaxation, ... I will truly treasure them for life.

I am fortunate to be funded by Schlumberger during my DPhil. Thanks to Nathan and Seth, who are wonderful company reps to drive the project forward, and cherish us with plenty of beers! Also, Ivana (Qianqi Lin) merits a special mention due to her efforts to output excellent work during the past year. Thanks to Charlie Jones for his valuable help towards the flow cell final design and fabrication.

It has been a great pleasure to be part of such an international and dynamic group during the past three years. The epic '**Lin**' sign is a masterpiece created by Lin and Min, symbolising a PhD's attitude, mastering of lab technique, and a true reflection of current social life. Emma, Ying, Xiaojun, Kristina, Petty and Her-Shuang are always amazing lunch buddies with intriguing stories to burst at any time. Sven and John have always been very helpful, even it's just about how to drive pass a roundabout. A big thank you goes to Barbara Kozub, who left the lab two years ago, for introducing me the beauty of LaTeX; and Martin and Edmund who helped to demystify it later on. I remember with gratitude those (doctors) who have already left the group: Eduardo Laborda, Neil Rees, and Leigh Aldous for fixing me up with lots of fresh ideas, sometimes even free alcohols (of course, Chris too); the bubbly Kass Toghill for positive energies at all time; Denis Menshykan, Juan Limón-Peterson, and Stephen Belding for jokes at teas and group drinks; the naughty Yige Zhou with her versatile personality; and Jane Panchompoo for her sweetness.

I would also like to thank Daian for accompanying me throughout the undergrad and postgrad years at low and high times. Also, lots of gratitude go to ones that are really special: Ms Anne de Graeve, who's always there for me; my fiancé, Mr Cheng Ge, who shared happiness and dismay with me throughout the past three and a half years; and Cheng's parents – Mr Ning Ge and Ms Xiaohua Lian, who have offered ceaseless care all the way through. Last but not the least, I cannot express how grateful and lucky I am to have such supportive and caring parents. Much love and many thanks go to – mom and dad.

Chapter 1

Fundamentals of electrochemistry

This chapter introduces the fundamental principles necessary to understand the research presented in this thesis. Electrochemical processes engage with the study of chemical changes caused by the passage of an electric current or overpotential with the production or storage of electric energy by chemical reactions. In order to scrutinize these chemical systems, an understanding of the inter-relation of electrical and chemical effects which take place at an electrode/solution interface is required.

1.1 Electrochemical equilibrium

Consider the following electrochemical equilibrium established at an electrode/solution interface,

$$\mathrm{A}_{(aq)} + e^-_{(metal)} \rightleftharpoons \mathrm{B}_{(aq)} \tag{1.1}$$

where $\mathrm{A}_{(aq)}$ and $\mathrm{B}_{(aq)}$ are a solution phase (aq) redox couple with arbitrary concentrations. A metal wire, for example, acts as a source or sink of electrons and thus as an electrode. An electron might leave the metal and join $\mathrm{A}_{(aq)}$ in the solution to form $\mathrm{B}_{(aq)}$. Alternatively, $\mathrm{B}_{(aq)}$ might give up its electron to the metal so turning

itself into $A_{(aq)}$. Such a process takes place very shortly after the wire is placed in the solution. The equilibrium seeks to minimise the total Gibbs energy of the system. Figure 1.1 shows the energy of electrons in the metal and in the aqueous species. The electronic structure of a metal is commonly described by the 'electron sea' model, in which the conduction electrons form a band of continuum energy levels and are free to move. These are filled up to an energy maximum known as the Fermi level. In contrast, electrons in the two solution phase ions are localised and restricted to certain discrete energy levels. As shown in Figure 1.1, the lowest unfilled molecular orbital (LUMO) of $A_{(aq)}$ can gain an electron from the metal. The LUMO of $A_{(aq)}$ is close in energy to the highest occupied molecular orbital (HOMO) of $B_{(aq)}$. It is a thermodynamically favourable process as the energy difference forms a 'driving force' for the electron transfers. Ultimately, the Fermi level seeks to lie in between the energy levels of the solution phase species, so that the rate at which electrons leave the metal to reduce $A_{(aq)}$ is exactly matched by the rate at which electrons join the metal from $B_{(aq)}$ which become oxidised.

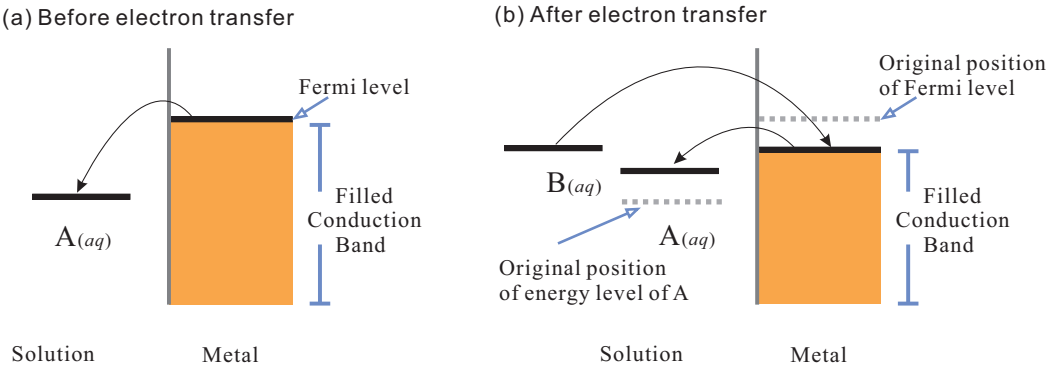

FIGURE 1.1: An energy diagram of electrons in the electrode/solution interface (a)before and (b)after electron transfers.

Once the system reaches dynamic equilibrium, no further net charge is possible. However, the charge separation will remain, and this is the origin of the electrode

potential established at the electrode/solution interface. It is not possible to measure the absolute value of the potential difference, but it may be measured relative to a second (reference) electrode, as will be discussed in the next section (Section 1.2).

This relationship between potential and the concentration of $A_{(aq)}$ and $B_{(aq)}$ is quantitatively described by the Nernst equation [1]:

$$E = E_f^{\ominus} + \frac{RT}{F} \ln \left(\frac{C_{A,o}}{C_{B,o}} \right) \tag{1.2}$$

where E (V) is the potential difference between the electrode of interest and the reference electrode, $E_f^{\ominus}$ is the formal electrode potential (relative to the same reference electrode) when solution species are present at equal concentration, R is the gas constant (8.314 J K^{-1} mol^{-1}), T (K) is the absolute temperature, F is the Faraday constant (96485 C mol^{-1}), $C_{A,o}$ and $C_{B,o}$ (mol cm^{-3}) are the concentration of species in the bulk solution.

An assumption of an 'ideal' solution is made here as the activity coefficient, γ_i, is unity. However, in reality this is *not* the case in electrolytic solutions. The activity, a_i (mol cm^{-3}), is used to describe the *effective* concentration of a species i in a non-ideal solution, where $a_i = \gamma_i C_i$. Debye-Hückel limiting law is used to interpret this deviation from ideality [2]:

$$\log_{10} \gamma_i = -C z_i^2 \sqrt{\mathbf{I}} \tag{1.3}$$

where C is a temperature and solvent dependent parameter, z_i (unitless) is the charge number on the ion, and the ionic strength, $\mathbf{I}$ (mol cm^{-3}), is defined as

$$\mathbf{I} = \frac{1}{2}\sum_i C_i z_i^2 \tag{1.4}$$

where the sum is over all the ions in solution. The theory works well in dilute solutions of concentration $\lesssim 10^{-2}$ M. More advanced theories, such as the Extended Debye-Hückel limiting law which takes account of the finite ionic radius rather than assuming ions are point charges, have also been developed. However, the fact of ignoring ion-solvent interactions still limits the application at dilute solutions. Only empirical formulae such as the Robinson and Stokes equation, or Pitzer equations are able to address this issue. Further discussion of these theories are outside the scope of this thesis.

The adopted form of the Nernst equation (Eqn. 1.2) is possible because high 'background electrolyte' concentrations are used in most experiments, which ensures the non-ideality being uniform across the solution. Consequently, the formal potential of the reactant is maintained relatively constant. Note that standard electrode potentials ($E^{\ominus}$) provide approximate values for formal potentials, for which the former are measured (relative to a standard hydrogen electrode) at different ionic strengths and extrapolating to zero ionic strength, where the activity coefficients approach unity. In working solutions at a pH different from the 'standard' condition of pH 0, the formal potentials need to be corrected according to 59 mV per proton per pH unit at 25 °C (Chapter 3).

Electrode potentials are only established when an electrochemical equilibrium is truly reached at the electrode and this requires fast electrode kinetics. In Secction 1.3, an electrode kinetics model interprets and sets out to rationalise why some electrode processes are fast and some slow.

1.2 Electrochemical cells

Rather than measuring a potential difference resulting from the solution composition as in potentiometry as introduced in the previous section, a typical 'dynamic' electrochemical experiment involves applying a potential difference at an electrode in order to drive a redox reaction, *i.e.* so-called Faradaic processes are induced to occur. Information about the reaction may then be extracted by measuring the resulting current as a function of the applied potential.

In order to measure the current at the electrode of interest (working) a reference electrode is required, such that a closed circuit can be established. Common examples of a reference electrode in aqueous set-ups are the saturated calomel electrode and the silver/silver chloride electrode. The potential difference between these two electrodes can be expressed as follows:

$$\text{potential difference} = (\phi_m - \phi_s)_{reference} - (\phi_m - \phi_s)_{working} + \Delta\phi_{OD} \tag{1.5}$$

where ϕ_m and ϕ_s (V) are the local electrical potentials of the metal and solution phases respectively. The first and second terms are the potential difference at each electrode interface. The third term is the solution ohmic drop ($\Delta\phi_{OD}$, V), and is defined by Ohm's law:

$$\Delta\phi_{OD} = IR_s \tag{1.6}$$

where I (A) is the driven current, and R_s (Ω) is the solution resistance. Experimentally, IR_s can be reduced to a certain extent if the working and reference electrodes are place closed to each other. A two-electrode system, however, cannot fulfil experimental conditions when a large current is passed. An uncertainty

against the reference point occurs for two reasons. The composition within the reference electrode can no longer be held constant once a current of opposite charge passes through. Second, the ohmic drop through solution is also a variable as a function of current. Therefore, a third electrode is required, known as the counter (or auxiliary) electrode. Figure 1.2 shows a schematic demonstration of such a system. The electrodes, from left to right, are the working, reference and counter electrodes.

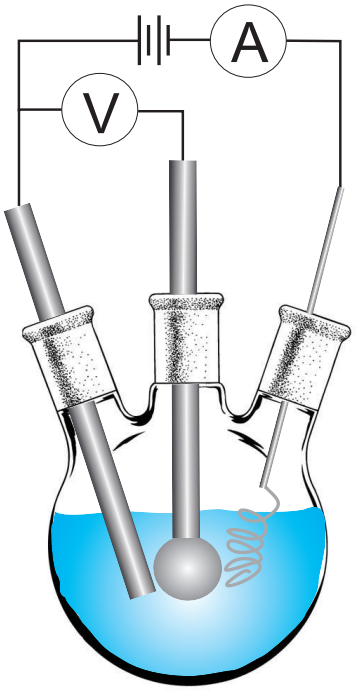

FIGURE 1.2: An experimental set-up for a three-electrode system within a three-necked round bottom flask.

With a three-electrode system, no current is passed between working and reference electrodes. As a result, a potential applied to the electrode of interest can be measured accurately, and solution ohmic drop is minimised. Meanwhile, a current is passed between the working and counter electrodes, but not the reference electrode. Usually, a candidate counter electrode should be inert and sufficiently large enough to support the current passed, a choice of which can be a platinum wire

or a graphite rod. Such a system is controlled through the use of a potentiostat so that measurement of the current at the working electrode as a function of the potential can be achieved.

1.3 Dynamic electrochemistry

For a one-electron reaction as outlined in Eqn. 1.1, the current (I) may be described by:

$$I = FAj_o \tag{1.7}$$

where A (cm^2) is the area of the electrode and j_o (mol s^{-1} cm^{-2}) is the Faradaic flux at the electrode interface:

$$j_o = -k_{\text{red}}c_{\text{A}} + k_{\text{ox}}c_{\text{B}} \tag{1.8}$$

where k_{red} and k_{ox} (cm s^{-1}) are the rate constants for reduction and oxidation respectively and c_{A} and c_{B} are the concentrations of species $A_{(aq)}$ and $B_{(aq)}$ (mol cm^{-3}) at the electrode surface. The rate constants depend on potential as described in Section 1.3.1.

In practice the current is a function of the rate of consumption of $A_{(aq)}$ at the electrode (electrode kinetics) and the supply of $A_{(aq)}$ to the electrode. For a redox couple dissolved in solution the latter is determined by the rate at which $A_{(aq)}$ is replenished from bulk solution (mass transport). Section 1.3.2 discusses such a mass transport process. If the redox couple is bound to the electrode surface it is simply a function of how much unreacted reactant remains.

1.3.1 Electrode kinetics

The Butler-Volmer model is a phenomenological and molecular model for electron transfer reactions, and in particular describes dependence on the electrode potential [3–5], for which the rate constants are given by:

$$k_{\text{red}} = k_o \exp\left[-\frac{\alpha F}{RT}(E - E_f^{\ominus})\right] \tag{1.9}$$

$$k_{\text{ox}} = k_o \exp\left[+\frac{\beta F}{RT}(E - E_f^{\ominus})\right] \tag{1.10}$$

where k_o is the standard heterogeneous rate constant, α and β (unitless) are known as transfer coefficients which indicate the 'position' of the transition state. Typically these take values around 0.5 for a one-electron reaction, $\alpha + \beta = 1$ [6]. The term $(E - E_f^{\ominus})$ represents the overpotential (η). Consequently, the full Butler-Volmer equation, which describes the relationship between electrode kinetics and potential difference at the electrode/solution interface, is:

$$I = FAk_o\left(\exp\left[\frac{+\beta F\eta}{RT}\right]c_{\text{B}} - \exp\left[\frac{-\alpha F\eta}{RT}\right]c_{\text{A}}\right) \tag{1.11}$$

It is interesting to note that at fast electrode kinetics, the ratio of $I/k_o \rightarrow 0$, the above equation collapses to the Nernst equation (Eqn. 1.2). Furthermore, at high overpotentials the Butler-Volmer equation reduces to only one exponential term, *i.e.* the Tafel equation. Under these conditions, a Tafel plot of $\ln \mid I \mid$ *vs.* η should yield a straight line of gradient $\alpha F/RT$. Voltammetrically, the Tafel region is at the beginning of the Faradaic process; data nearer the voltammetric peak reflects both electrode kinetics and diffusional depletion. Graphical analysis *via* Tafel plots allows the determination of the position of the transition state for an irreversible electron transfer.

The Butler-Volmer expression is only a simple model. It has some limitations. From Eqn. 1.11, as the overpotential tends to infinity so does the rate of electron transfer, which is physically unrealistic. That is to say, this model does not predict a maximum rate of electron transfer. On the other hand, other theories, such as the Marcus-Hush model, are able to predict the decrease of rate of electron transfer at highly thermodynamically driven reactions, known as the 'inverted region'. All the simulation programs involved in this thesis are based on Butler-Volmer model, which has been shown to be a good approximation to the Marcus-Hush model for solution phase reactants [7].

1.3.2 Mass transport

For a redox couple dissolved in solution, once the electrode surface is depleted of species i the current is limited by the rate of mass transport. Three main processes contribute to mass transport: diffusion, migration and convection, which can be quantified by the one-dimensional form of the *Nernst-Planck* equation [6]:

$$J_i(x) = -D_i\frac{\partial C_i(x)}{\partial x} - \frac{z_i F}{RT}D_i C_i\frac{\partial \phi(x)}{\partial x} + C_i\upsilon(x) \tag{1.12}$$

where $J_i(x)$ is the flux (mol cm^{-2} s^{-1}), D_i is the diffusion coefficient (cm^2 s^{-1}), C_i is the concentration of i (mol cm^{-3}), z_i is the species charge, $\frac{\partial\phi(x)}{\partial x}$ (V cm^{-1}) is the gradient of potential, and $\upsilon(x)$ is the solution velocity in the x direction (cm s^{-1}).

Of the three modes of mass transport, diffusion is most generally of interest to

electrochemists. Diffusion is the spontaneous movement of a species down a concentration gradient in order to maximise system entropy. Mathematically, diffusion is aptly described *via* Fick's laws. Fick's first law states that at a given point the flux is proportional to the product of diffusion coefficient and concentration gradient (derivation see Appendix A) [6], represented by the first term in Eqn. 1.12. Note that the negative sign implies the flux is down the concentration gradient from high to low level. Under so-called 'diffusion-only' conditions the rate of change of concentration in solution is described by Fick's second law [6]:

$$\frac{\partial C_i(x)}{\partial t} = D_i \frac{\partial^2 C_i(x)}{\partial x^2} \tag{1.13}$$

which can be derived based upon Fick's first law (see Appendix A). The value of D_i gives a measure of how far a molecule can travel during a period of time. The statistical view of diffusion is a random walk process, which suggests that the root-mean-square displacement in one direction (x) diffused by a species in time t is

$$\sqrt{\langle x^2 \rangle} = \sqrt{2 D_i t} \tag{1.14}$$

Generally, values of D_i for solution phase species are in the range of $(1-10)\times10^{-6}$ cm^2 s^{-1} (25 °C) [8]. Take an example of a species i with a diffusion coefficient of 1×10^{-5} cm^2 s^{-1}, the root-mean-square displacement after one second will only be 50 μm. The implication is that with a typical voltammetric experiment lasting a few seconds, the electrolysis is only confined to a spatial layer of solution adjacent to the electrode of the order of tens of microns in size. Thus, if bulk electrolysis is attempted, stirring or other forms of convection will be needed to ensure rapid and efficient conversion of the analyte material. The application of this concept is found in Chapter 7. Furthermore, it should be noted that the diffusion coefficient

is highly temperature dependent; it commonly exhibits Arrhenius type behaviour. A more detailed discussion is in Section 5.1.

In any electrochemical reaction, migration (second term in Eqn. 1.12) gives rise to a complex physical transport process upon electrolysis, and is usually undesirable. This problem can be overcome by adding a high concentration of inert background electrolyte, usually in excess of 0.1 M potassium chloride (in water) or tetraalkyl ammonium perchlorate salts (in non-aqueous solutions). The addition of salt elevates the solution conductivity and compresses the electrochemical double layer (see next section). Consequently, the potential difference at electrode/solution interface occurs over a distance of $10 - 20$ Å, which is comparable with electron quantum tunnelling distance. As a result, the potential gradient throughout the bulk solution is approximately zero, and hence the movement of charged species within such an electric field is minimised. However, exceptions may occur in a reduction of a positively charged intermediate species under conditions of low ionic strength, as will be discussed in Section 5.3. Moreover, the high electrolyte concentration also ensures minimised solution 'ohmic drop' (Section 1.2). In Chapter 7, it can be seen that in some cases large ohmic drop causes distortion of voltammetric features even at large excess of salt.

Mass transport due to convection is described by the third term in Eqn. 1.12. There are two forms of convection. Natural convection, arises from thermal or density gradient, may be neglected if experimental timescales are kept short [9]. For instance, $\lesssim 20$ seconds for macroelectrodes and $\lesssim 5$ seconds for microelectrodes in aqueous and organic solvents [1]. Another class is forced convection, which forms a field of *hydrodynamic* studies. It deliberately introduces controllable mechanical forces, such as insonation, electrode rotation, solution flow rates, or impinging jets. The corresponding experiments are sonoelectrochemistry, rotating disc electrodes,

flow cells (channel and tubular), wall-jet or wall-tube electrodes [1, 10, 11]. Part of this thesis (Chapter 7) will be concerned exclusively with tubular flow cell systems, where solution will be flowed through a tubular glassy carbon and a reticulated vitreous carbon mounted in a tubular wall.

1.4 Non-faradaic processes

Electrolysis takes place under sufficient applied electrode potentials; consequently a d.c. (or 'Faradaic') current will pass. However, a fluctuating a.c. voltage will induce ion redistribution and/or dipoles reorientation in close proximity to the electrode. Under this condition, an a.c. current is induced to pass through the interface although *no* electrons will actually cross the electrode/solution interface. This is termed a non-Faradaic (or 'charging') current [6].

An 'electrical double layer' model was developed to describe the electrode/solution interface. It was first proposed by Helmholtz in 1853 and later developed by Stern and Grahame in the 1940s. A potential difference at the electrode/solution interface can be built up resulting from different energy levels of electrode and solution species or applied potentials. In order for the interface as a whole to maintain electrical charge neutrality, oppositely charged ions or dipoles can form a 'compact' layer at the electrode surface, beyond which a 'diffuse' layer exists containing species under thermal (Brownian) motion and electrostatic forces. Such redistribution of ions and/or the reorientation of dipoles in solvent molecules are driven by electrostatics. Consequently, a potential gradient across this charge separation layer is created. Figure 1.3 shows the Stern model of the electrical double layer. The attracted ion is able to approach the electrode to a minimum distance corresponding to the radius of the solvated ions, depicted as the OHP (Outer Helmholtz

Plane). Grahame's model includes an additional Inner Helmholtz Plane (IHP), which represents a layer of some 'specifically adsorbed' ionic or uncharged species to reduce the charge density in solution and compensate the charge on electrode. It consists part of the compact layer. The potential drop within this compact layer is shown to be linear, whilst that in the diffuse layer drops approximately exponentially with distance away from the phase boundary.

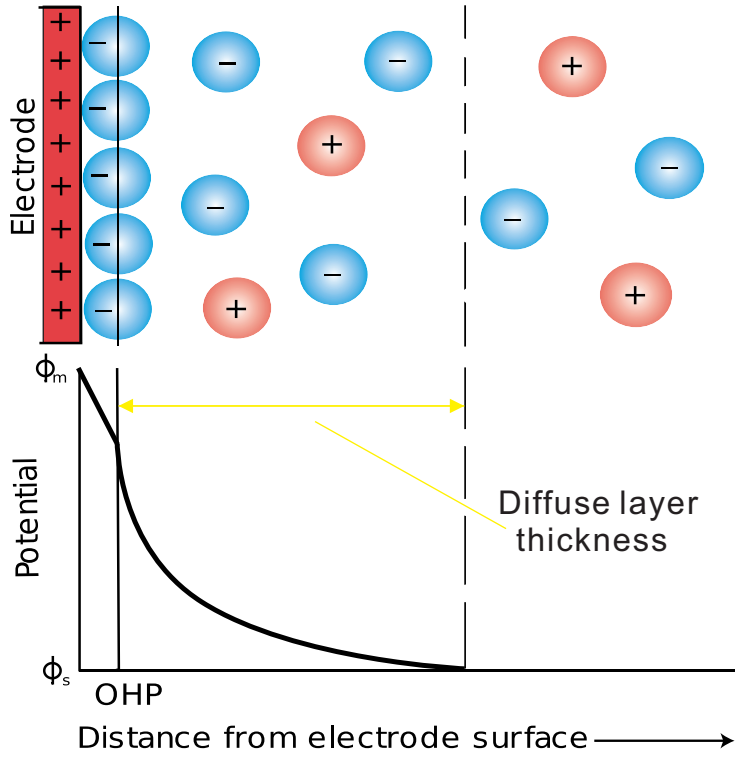

FIGURE 1.3: The Stern model of the electrical double layer.

The electrical double layer model acts like a capacitor, where the interface is capable of 'storing' charge (charged electrolyte ions) that is accumulated or depleted in comparison with their bulk values. For a simple parallel plate electrical capacitor, an equal and opposite charge (q, C) stored on the plates is directly proportional to the applied potential [12]:

$$q = CAE \tag{1.15}$$

where A (cm^2) is the electrode area, and the capacitance (C, μF cm^{-2}) is constant, independent of potential, as the separation of the plates is fixed. However, the electrical double layer represents a slightly more complicated problem as the capacitance is dependent upon the applied potential. This rises due to a change of double layer thickness, being analogous to the separation of the plates, when potential is applied. The charge held upon the interface may be described by:

$$q = C_{DL}A(E - E_{pzc}) \tag{1.16}$$

where C_{DL} is the double layer capacitance, which typically have values of $10 - 40$ μF cm^{-2} in aqueous solutions. The E_{pzc} term is the 'potential of zero charge' of the electrode, which is when the potential difference between the working electrode and bulk solution is zero, *i.e.* the working electrode is uncharged.

The further away the potential E from the E_{pzc} the greater attraction or repulsion for the electrolyte ions and the more compressed the dimensions of the double layer. Consequently the larger C_{DL} is. Therefore, C_{DL} varies with potential as the double layer changes. Moreover, it can also vary with the composition of the electrolyte. At low concentrations of electrolyte ($\lesssim 0.001$ M) and potentials close to E_{pzc}, the thickness of the diffuse layer is large as only a weak attraction from the electrode exists. As a result, the smaller C_{DL} is. This idea is implemented in Chapter 5, where the E_{pzc} may be found at the minimum of the 'average' capacitance of the double layer. On the other hand, high concentrations of electrolyte compress the thickness of the double layer, and help to mitigate the migration effect in solution.

In electrochemical measurements, the charging current can be useful to determine either the solution resistance (R_s), the C_{DL} or the surface area of an electrode. The related experiments are discussed in Chapter 7. The system is similar to a

resistor-capacitor (RC) circuit. The derivation of the following equations based on such a system can be seen in Appendix B.

A potential step experiment, or chronoamperometry, can be used to determine the R_s. The charging current, when applying a potential step of ΔE, is:

$$I = \frac{\Delta E}{R_s} e^{-t/AR_sC_{DL}} \tag{1.17}$$

Since C_{DL} is a function of potential, this RC circuit model is strictly accurate only when the change of overall cell potential is small. Otherwise, approximate results can be obtained using an 'average' capacitance (C_d) over the potential range. Usually, it takes *ca.* 0.1 ms to complete the double layer charging, if $R_s = 1\ \Omega$ and $C_{DL} = 20\ \mu$F. Experimentally, during the Shoup and Szobo analysis on a chronoamperomogram from a micro-disc the charging current is discarded for the sake of analytical accuracy (Section 2.3).

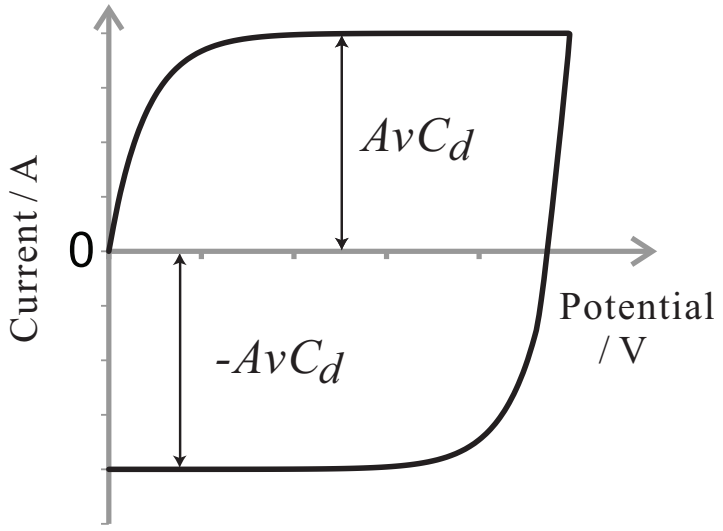

FIGURE 1.4: Current-potential plot resulting from a cyclic voltammetry applied to an RC circuit.

A linear potential sweep or a cyclic voltammetry technique (as will be discussed

in the following section) can be used to determine the C_d or surface area of an electrode. Usually, the reaction solution only contains supporting electrolyte, *i.e.* there is no Faradaic current. The charging current is:

$$I = \nu A C_d [1 - e^{-t/AR_s C_d}] \tag{1.18}$$

As the $t \geqslant AR_sC_d$, the charging current becomes a constant size of νAC_d. Figure 1.4 shows a current-potential plot resulting from a cyclic voltammetry applied to an RC circuit. From Figure 1.4, the current rises from zero as the potential increases. It then reaches a steady-state current with a value of νAC_d or $-\nu AC_d$. In the rest of this thesis, this charging current is also referred to the background current.

1.5 Experimental techniques

There are two common methodologies used in kinetic electrochemistry: voltammetry and chronoamperometry. In voltammetry, the current is recorded as a function of potential; whilst amperometry refers to a set potential with the current measured as a function of time.

1.5.1 Cyclic voltammetry

In order to study the kinetics of a redox couple, a technique known as voltammetry is utilised. In cyclic voltammetry (CV), the potential is scanned linearly at a constant scan rate (ν, V s^{-1}), from a starting potential E_1 to a second potential E_2, and then reverses back to E_1, as shown in Figure 1.5(a). Usually, linear sweep

voltammetry (LSV) consists only the first half of the potential-time profile. The voltammetric responses for macroelectrodes (electrode radius, $r_e \gtrsim 1$ mm) and microelectrodes (at least one dimension in the micro range) differ significantly, and are discussed in turn.

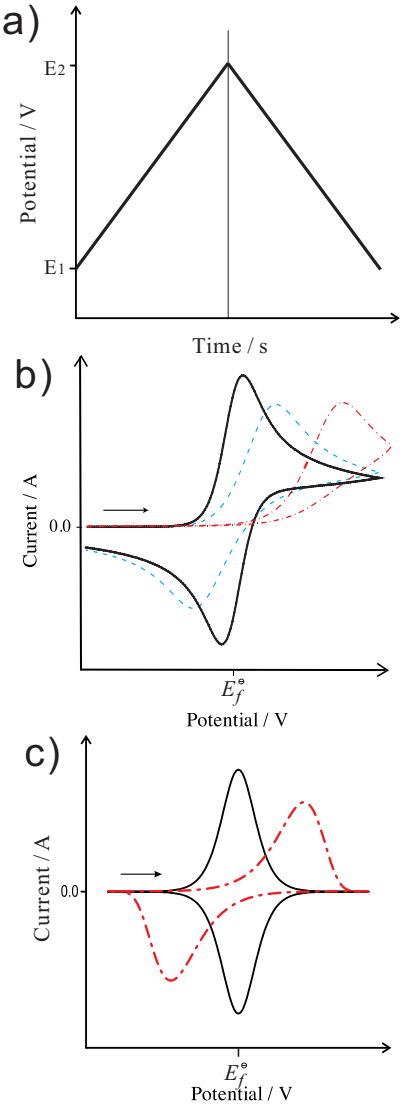

FIGURE 1.5: (a)The potential-time profile in cyclic voltammetry. Different wave-shaped cyclic voltammograms on a macroelectrode exhibit reversible (solid line), quasi-reversible (dash line), and irreversible (dash-dotted line) kinetics for (b)diffusional and (c)surface-bound systems.

Recall the electrochemical equilibrium for a one-electron system (Eqn. 1.1), $A_{(aq)}$ can be considered to reach the electrode by diffusion. Figure 1.5(b) depicts three

different voltammetric responses for a diffusional process at a macroelectrode. At $E \ll E_f^{\ominus}$, no faradaic current is passed. As E increases, a near exponential increase in the current is shown, representing conversion of $A_{(aq)}$ to $B_{(aq)}$. This corresponds to a situation at which $A_{(aq)}$ is under the 'electrode kinetic' control and the current flowing is sensistive to the electrode potential. Under such a process, Nernstian formation (Eqn. 1.2) of $B_{(aq)}$ describes a reversible electron transfer; Butler-Volmer kinetics (Eqn. 1.11) describes an irreversible electron transfer. At $E \gg E_f^{\ominus}$, the rate of consumption of $A_{(aq)}$ becomes dominated by the rate at which it is replenished *via* mass transport. Consequently, a peak appears. On the reverse scan, a back peak is observed as $B_{(aq)}$ is converted to $A_{(aq)}$. Given an electron transfer being fully reversible, the mid-point potential will be equal to the $E_f^{\ominus}$ (assuming that both diffusion coefficients of $A_{(aq)}$ and $B_{(aq)}$ are equal). This mid-point potential is defined as the half of summation of the forward and backward peak potentials, *i.e.* $E_f^{\ominus} = (E_{p,forward} + E_{p,backward})/2$.

Analytically, the interpretation of a voltammogram is usually based on the peak current for the forward scan and the peak-to-peak separation of the forward and reverse scans. The Randles-Ševčík equations describes the voltammetric forward peak current on a macroelectrode. Mathematically, this can be derived from Fick's second law (Eqn. 1.13) by the approximation of one-dimensional planar diffusion to the electrode surface. It contains two forms, for a reversible n electron redox species:

$$I_p = (2.69 \times 10^5) n^{1.5} A D_i^{0.5} C_i \nu^{0.5} \tag{1.19}$$

and for an irreversible n electron redox species:

$$I_p = (2.99 \times 10^5) n (n' + \alpha_{n'})^{0.5} A D_i^{0.5} C_i \nu^{0.5} \tag{1.20}$$

where n' is the number of electrons transferred before the rate determining electron transfer and $\alpha_{n'}$ is the transfer coefficient of this slow step. The use of the Randles-Ševčík equations will be discussed further in Chapter 3 – 5, in particular for measuring diffusion coefficients. It is interesting to note that there is a non-zero (*ca.* 59 mV at 25 °C) peak-to-peak separation even at the fast kinetics. This reflects the influence of the mass transport upon the system. On the other hand, the peak-to-peak separation increases towards the irreversible limit, depicted in Figure 1.5(b). A relatively large overpotential is required to drive the electron transfer. Consequently, there is a delay in depletion of the electroactive species at the surface; hence it leads to the large peak-to-peak separation. Moreover, at even slower kinetics, it can also result in the disappearance of the back peak.

For a diffusional species the boundary of an electrochemical process as being 'reversible' or 'irreversible' is rather blurred since 'fast' and 'slow' are relative terms; in particular relative to the mass transport. The Matsuda-Ayabe parameter, Λ, quantifies this kinetic reversibility for an electrochemical process at macroelectrodes [13]:

$$\Lambda = \frac{k_o}{\left(\frac{FD_i\nu}{RT}\right)^{1/2}} \tag{1.21}$$

where k_o is the standard heterogeneous rate constant, ν is the scan rate, and the denominator is termed as the rate of mass transport (m_T). At the reversible limit:

$$\Lambda \geq 15 \qquad k_o \geq 0.3\upsilon^{1/2} \tag{1.22}$$

quasi-reversible regime:

$$15 > \Lambda > 10^{-3} \qquad 0.3\upsilon^{1/2} > k_o > 2 \times 10^{-5}\upsilon^{1/2} \tag{1.23}$$

and irreversible limit:

$$\Lambda \leq 10^{-3} \qquad k_o \leq 2 \times 10^{-5} \upsilon^{1/2} \tag{1.24}$$

where the numerical values relate to 298 K and α is assumed to be 0.5. Take an example at the transition between reversible to quasi-reversible, $\Lambda \simeq 15$, at scan rate of 0.05 V s^{-1}, the k_o can be approximated to be 0.07 cm s^{-1}. More detailed studies are required to determine the k_o precisely. In particular, numerical simulation might be employed (refer to Section 2.4).

Chapter 6 and Chapter 7 discuss some surface-bound redox systems. Such surface-bound species exhibit distinct features different from solution phase species in cyclic voltammograms, as shown in Figure 1.5(c). Of interest is that the forward and backward peaks can be symmetrical and *no* peak-to-peak separation is observed (reversible). In the irreversible regime, the peak-to-peak separation becomes non-zero and the peak shape is no longer symmetrical. Moreover, at high overpotentials the current drops to zero. These features arise because a limited quantity of the electroactive species exists on the surface and hence the wave shape is controlled only by the electron transfer kinetics, *i.e.* there is no diffusion involved.

At the reversible electron transfer limit, assuming no interactions between the adsorbed species, the surface coverage of the electroactive species (Γ_{tot}) are at equilibrium. Note that the surface coverage is the sum of both reactant and product. Under this system, the current becomes limited by the availability of reactant species, which can be eventually annihilated. The forward peak current can be described by the following equation through the use of Nernst equation

(see derivation in Appendix C [14]):

$$I_p = \frac{n^2 F^2 \nu}{4RT} A\Gamma_{tot} \tag{1.25}$$

The peak current of a surface-bound species is proportional to the scan rate, ν. In comparison with the Randles-Ševčík equations (Eqn. 1.19 and Eqn. 1.20), the peak current of a diffusional species is a function of $\sqrt{\nu}$. Hence, through the I_p–ν analysis it can be readily ascertained whether the electroactive species of interest is surface-bound or diffusional. This concept will be implemented throughout the entire thesis.

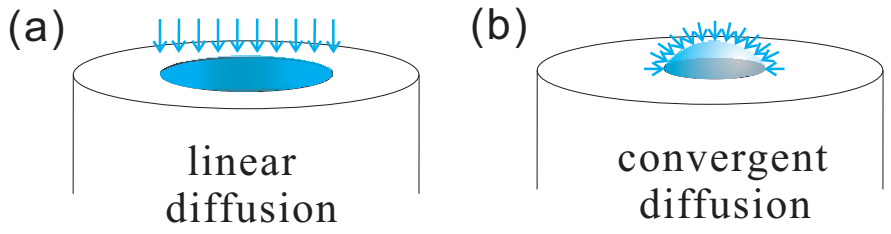

FIGURE 1.6: Schematic diagram of (a)linear and (b)convergent diffusion regimes.

So far, the above discussion has focused on macroelectrodes. As the electrode size decreases, the diffusional regime may change from 'linear' to 'convergent' at a microelectrode [15], as shown in Figure 1.6. Within the experimental timescale, a hemispherical diffusion layer on a microdisc is well developed at slow scan rate, due to electroactive materials not only drawn from above the disc but also rapidly from the sides. Such 'efficient' diffusion results in a transport-limited steady-state current, I_{ss}, defined as [16]:

$$I_{ss} = 4nFr_e D_i C_i \tag{1.26}$$

However, the diffusional regime may change relative to the change of mass transport on microelectrodes. The rate of mass transport (m_T) can be outrun by the electrode kinetics if the scan rate is very fast, *i.e.* the diffusion changes from 'convergent' to 'linear' regime. Figure 1.7(a) depicts the simulated cyclic voltammograms at increasing scan rates from 0.02, 1 to 7 V s^{-1}. Such behaviour at high scan rates is strongly dependent upon the diffusion coefficient of the redox species and the electrode size.

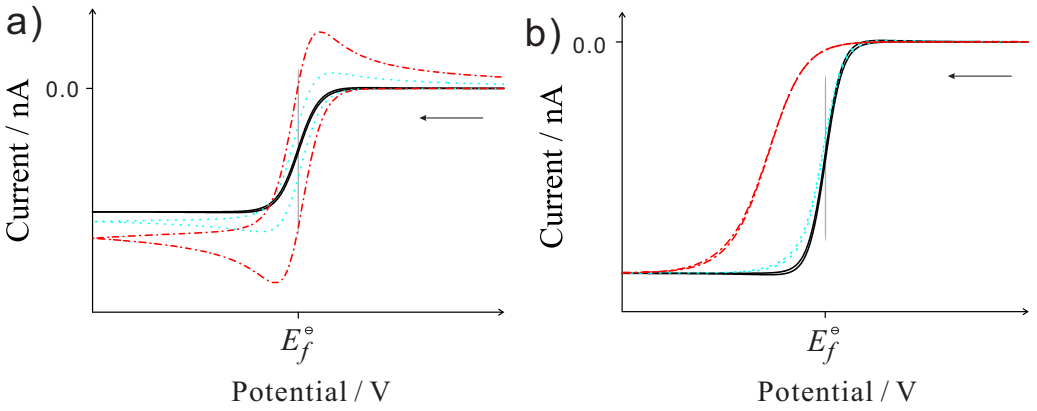

FIGURE 1.7: Cyclic voltammograms on a microelectrode exhibit changes of (a) diffusion from 'convergent' to 'linear' regime when ν increases from 0.002 (solid line), 1 (dotted line) to 7 V s^{-1} (dash-dotted line) and (b) reversible to irreversible limit when k_o decreases from 1×10^5 (solid line), 0.1 (dotted line) to 0.001 cm s^{-1} (dash-dotted line) for a species with $D_i = 1 \times 10^{-5}$ cm^2 s^{-1}, $C_i = 1 \times 10^{-6}$ mol cm^{-3}, $r_e = 5 \times 10^{-4}$ cm, and $\alpha = 0.5$; $k_o = 1$ cm s^{-1} and $\nu = 0.002$ V s^{-1} unless otherwise specified.

Furthermore, the electrochemical irreversibility or quasi-reversibility can take place when the rate of mass transport is much greater than the standard heterogeneous rate constant. Voltammetrically, the change from reversible to irreversible limit is demonstrated in Figure 1.7(b), where k_o decreases from 1×10^5, 0.1 to 0.001 cm s^{-1}. Given the electron transfer being fully reversible, the half-wave potential, $E_{1/2}$, will be equal to the $E_f^{\ominus}$, which is defined as the potential at half I_{ss}. In contrast for a redox species which possesses slow electrode kinetics, $E_{1/2} \gg E_f^{\ominus}$. The kinetic data can be extracted by fitting an experimentally obtained cyclic

voltammogram with a simulation program to match the wave shape and I_{ss}, as described in Section 2.4. This point is exemplified further within Chapter 5.

1.5.2 Chronoamperometry

The preceding section identifies the voltage scan rate as the key parameter in cyclic or linear sweep voltammetry. A limiting situation of the latter experiment occurs at which the potential of the working electrode is instantaneously stepped from an initial potential E_1, at which little or no current flows, to a second potential E_2, at which the electrode reaction is typically transport controlled, as shown in Figure 1.8(a).

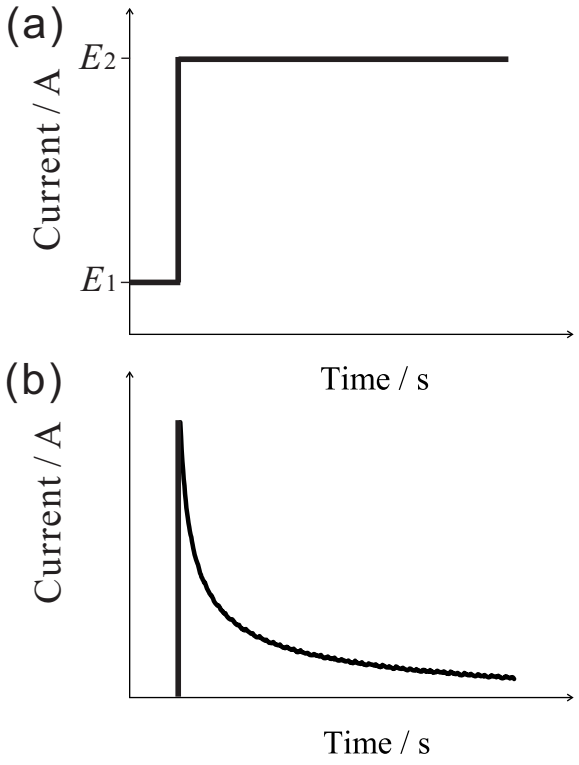

FIGURE 1.8: (a) The potential-time profile for a single step chronoamperometric experiment. (b) The current response in the potential step experiment. Note that at long t, the current approaches to zero for macroelectrodes and I_{ss} for microelectrodes.

Immediately following the potential step, a large current flows. This arises since the concentration gradients shortly after the step are extremely large. Gradually, the current drops steadily and is controlled by the rate of diffusion of $A_{(aq)}$ to the electrode surface. As time increases, the concentration gradient decreases and hence current decreases, shown in Figure 1.8(b).

It is insightful to consider the long-time and short-time limits here. When time is long, a hemispherical diffusional layer can be developed. For an electrode of smaller or comparable size as the diffusional layer, usually a microelectrode, a convergent diffusion is resulted, and leads to efficient mass transport. Under such a condition, the current at the microelectrode during chronoamperometry may be described empirically by the Shoup and Szabo eqution [17]:

$$I = 4nFD_iC_ir_ef(\tau) \tag{1.27}$$

$$f(\tau) = 0.7854 + 0.8863\tau^{-\frac{1}{2}} + 0.2146\exp(-0.7823\tau^{-\frac{1}{2}}) \tag{1.28}$$

where the dimensionless time parameter, τ is given by:

$$\tau = \frac{4D_it}{r_e^2} \tag{1.29}$$

As time becomes longer, the above equation collapses to the steady-state current (Eqn. 1.26).

In the case of short-time limit, or equivalent of a situation in which the electrode dimensions are significantly larger than the diffusional layer, the diffusional regime switches to the linear diffusion. Under this condition, the current may be described

by the Cottrell equation [18]:

$$I = \frac{nFA\sqrt{D_i}C_i}{\sqrt{\pi t}} \tag{1.30}$$

It is of particular importance to note that this expression tends to zero as time goes to infinity.

The chronoamperometric experiment provides a pathway to measure diffusion coefficients. This technique is further discussed in Section 2.3, and used throughout the rest of this thesis.

This chapter has provided a brief introduction of the fundamental basis underpinning this thesis. The next chapter will outline the experimental set-ups and simulation programs. In the main body of the thesis, the discussion will be focused on coupled homogeneous kinetics, effect of ion paring, change of solvent media, and redox mediator modified graphite surfaces of electrochemical reduction of oxygen. Finally, all the knowledge obtained from the early chapters is collected and used in the development of a prototype hydrodynamic system for electrochemical reduction of oxygen to produce hydrogen peroxide.

Chapter 2

Experimental methods

This chapter outlines all chemical reagents used, and the general electrochemical cell set-ups together with their configurations under both static and hydrodynamic systems. General microdisc electrode radius calibration methods are also introduced. Finally, there is a brief overview of the simulation programs used throughout this thesis.

2.1 Chemical reagents

All chemicals were of analytical grade and were purchased from Sigma-Aldrich, unless otherwise specified. They were used without any further purification. These are acetonitrile (MeCN, density of 0.786 g mL^{-1} at 25 °C, for HPLC, $\geqslant$ 99.9%), 1-aminoanthraquinone (1AAQ), 2-aminoanthraquinone (2AAQ), anthraquinone (AQ), anthraquinone-2-sulfonic acid sodium salt monohydrate (or anthraquinone

monosulfonate, AQMS, >97%), dichloromethane (DCM, Fisher Scientific), 6,7-dichloro-1,4-dihydroxyanthraquinone (6,7-DC-1,4-DH-AQ), 1,4-dihydroxyanthraquinone (1,4-DH-AQ), 1,5-dihydroxyanthraquinone (1,5-DH-AQ), 1,8-dihydroxyanthraquinone (1,8-DH-AQ), 1-chloro-an-thraquinone (1CAQ), ferrocene (Fc), hydrochloric acid (HCl), hydrogen peroxide (H_2O_2, 30% solution), 2-hydroxymethylanthraquinone (2-HM-AQ), methyl viologen dichloride hydrate (MV^{2+}), nitrosonium tetrafluoroborate ($[NO^+][BF_4^-]$), potassium chloride (KCl), potassium hydroxide (KOH), potassium phosphate dibasic (K_2HPO_4), potassium phosphate monobasic (KH_2PO_4), sodium hydroxide (NaOH), tetra-n-butylammonium chloride (TBACl), tetra-n-butylammonium perchlorate (TBAP), tetra-n-butylammonium hydroxide (TBAOH), tetra-n-ethylammonium hydroxide (TEAOH), tetra-n-methylammonium hydroxide (TMAOH), rubidium hydroxide (RbOH).

The anthraquinone-2-diazonium tetrafluoroborate ($[AQ\text{-}N_2^+][BF_4^-]$), used for the surface modification of carbon electrodes, was synthesized according to a method developed by Milner [19]. 1.00 g of 2-aminoanthraquinone was added to a slurry of *ca.* 50% molar excess of nitrosonium tetrafluoroborate in 100 mL of dichloromethane. The reaction mixture was placed in an ice-bath while stirring for one hour before the solvent was removed under vacuum in an ice-bath. The resulting anthraquinone-2-diazonium tetrafluoroborate product was then stored at -5 °C. Due to the thermal instability and light sensitivity, all diazonium stock solutions were kept in an ice-bath, well wrapped up with foil paper and prepared on a daily basis to prevent decomposition.

All aqueous solutions were prepared with deionised water of resistivity not less than 18.2 MΩ cm at 298 K (Millipore UHQ, Vivendi, U.K.). The phosphate buffer solution (PBS) was composed of 50 mM monobasic potassium phosphate, 50 mM dibasic potassium phosphate, supported with either 0.1 M or 3 M potassium

chloride electrolyte. The PBS of pH 6.74 can be adjusted to pH 3.13 by using concentrated hydrochloric acid.

2.2 Electrochemical cell set-up

An Autolab PGSTAT20 computer controlled potentiostat (EcoChemie, Utrecht, The Netherlands) was used to perform electrochemical measurements. A standard three-electrode configuration was used for electrochemical cell with static aqueous solution. The working electrode was one of the following: a glassy carbon (GC, 0.15 cm radius, BASi, Bioanalytical Systems, Inc., MF-2012); a boron-doped diamond (BDD, 0.15 cm radius, Windsor Scientific, Slough); an edge-plane pyrolytic graphite (EPPG, 0.25 cm radius); a basal-plane pyrolytic graphite (BPPG, 0.25 cm geometric radius); a highly ordered pyrolytic graphite (HOPG, 0.27 cm radius); a platinum (Pt, 0.08 cm radius, BASi, MF-2013); a gold (Au, 0.09 cm radius, BASi); a micro-carbon fiber (μ-C, BASi, MF-2007); a micro-platinum (μ-Pt, calibrated radius of 8.80 μm) electrode. The μ-Pt electrode was fabricated in-house by thermally sealing a 18μm diameter Pt wire (Goodfellow Ltd., Cambridge, UK) into a borosilicate glass capillary. The cell assembly was completed by using a platinum wire (99.99%, 0.05 cm diameter, GoodFellow, Cambridge, UK) acting as the counter electrode, and a reference electrode being a 0.05 cm diameter silver wire, or a leakless Ag/AgCl (1 M KCl aqueous solution) electrode (eDAQ, ET072, Dublin, Ireland), or a standard calomel electrode (SCE, Radiometer, Copenhagen, Denmark).

The BDD, EPPG, Au, Pt and μ-Pt electrodes were polished by using alumina with decreasing particle sizes (Buehler Ltd., $0.3 - 0.05$ μm, USA). The GC and μ-C electrodes were polished by diamond spray of decreasing sizes (Kemet Ltd.,

$0.3 - 0.01$ μm, U.K.). The electrode refreshing procedure was accomplished after 1 minute sonication (D/78224 Singen/Htw sonicator, 50/60 Hz, 80 W, U.K.) in corresponding experimental solvents and nitrogen blown dry afterwards. Both BPPG and HOPG electrodes were prepared by renewing the surfaces with adhesive tape.

With the hydrodynamic systems (refer to Chapter 7), either a tubular glassy carbon electrode (TGCE) or a reticulated vitreous carbon electrode (RVCE) was housed within a flow cell, which is part of a gravity-feed system of glass and Teflon tubes (Figure 7.1 and Figure 7.16). The flow cell has a three-electrode configuration. The working electrode (WE) can be (a) commercially available TGCEs (Goodfellow, Cambridge, U.K., internal radius 0.148 cm, outer radius 0.5 cm) of variable lengths being 0.515 cm, 1.024 cm, and 10.039 cm; (b) house-fabricated RVCEs (Goodfellow, Cambridge, U.K., thickness of 0.32 cm, bulk density of 0.05 g cm^{-3}, porosity of 96.5% and pore sizes of 24 cm^{-1}). A leakless Ag/AgCl (1.0 M KCl aqueous solution) reference electrode (RE, eDAQ, ET072, Dublin, Ireland) was fitted into a compartment at downstream close to the working electrode. The RE was placed and sealed from outside with parafilm. Its potential was frequently monitored against a SCE reference electrode by using a high impedance digital voltmeter (Fluke 845AB). The flow cell set-up assembly was completed by mounting a platinum gauze downstream of the RE as the counter electrode (CE). The cross-section of such a flow cell is given in Figure 7.1 or Figure 7.16. The order of alignment of these three electrodes is essential. Due to the substantial length of TGCEs or the large current responses on RVCEs, a significant amount of uncompensated solution resistance (R_u), some fraction of solution resistance (R_s), can be developed between the WE and RE. Modern potentiostats are designed to recognise and partially compensate the voltage drop of IR_u only when the RE is

positioned in between WE and CE in the potential profile or IR_u is small [20–22]. Altered alignment was observed to cause measurement of large current oscillations, relating to the loss of potentiostatic control.

Both TGCE and RVCE working electrodes were fabricated as follows. Due to the brittle nature of glassy carbon, TGCE was purchased with mechanically cut finishing for all variable lengths (x_e). The smooth mechanical finishing at the electrode edges, especially the inner wall, ensures minimum local turbulence. In the TGC flow cell, the electrical contact was achieved by a copper ring fitted on a TGCE outer wall. Each end of TGCE connects to a piece of chemically inert PEEK (polyether ether ketone) tube of exact internal radius, acting as inlet and outlet (Section 7.1). Two plastic O-rings sitting in a trench at each joint with PEEK tubes to form a leak-free system. Another outer PEEK ring was tailor-made to fit variable lengths of TGCE, and acts as a seal-secure screw in order to keep all three pieces attached together. The minimum required lead-in length (x_l) for full laminar flow condition to develop was estimated from:

$$x_l \approx 0.1 \times r_e \times Re \tag{2.1}$$

where r_e is the tubular electrode internal radius, and R_e is Reynolds number. The x_l was calculated to be 2.2 cm [11]. The actual fabricated x_l was approximately 5 cm, which was in excess of the minimum requirement.

The fabrication of the RVCE working electrode was accomplished as follows. Chemically inert PEEK material was used as the casing. PEEK is colourless organic polymer, semicrystalline thermoplastic that exhibits a high chemical resistance retained at high temperatures, far beyond those of electrochemical experiments. Two pieces of RVC foam, radius of 0.3 cm, were stacked within the PEEK

tube (Section 7.2) to make a length (x_e) of 0.64 cm circular cylinder. Electrical contact was achieved by inserting a thin graphite rod (0.05 cm radius) into the PEEK body. Inside the insulating PEEK tube, the graphite rod was covered with an in-house produced conducting araldite based graphite powder glue, and a physical contact was made to the RVC foam. The electrode design was accomplished by capping both ends with PEEK so that solution was able to flow through a hole of radius 0.15 cm. Outside, a copper ring was attached to the PEEK body touching the graphite rod. The maximum electrical contact resistance of this in-house fabricated RVCE was below 50 Ω for all experimental measurements. Two plastic O-rings sat in a trench at each end of the PEEK tube to provide a leak-free system.

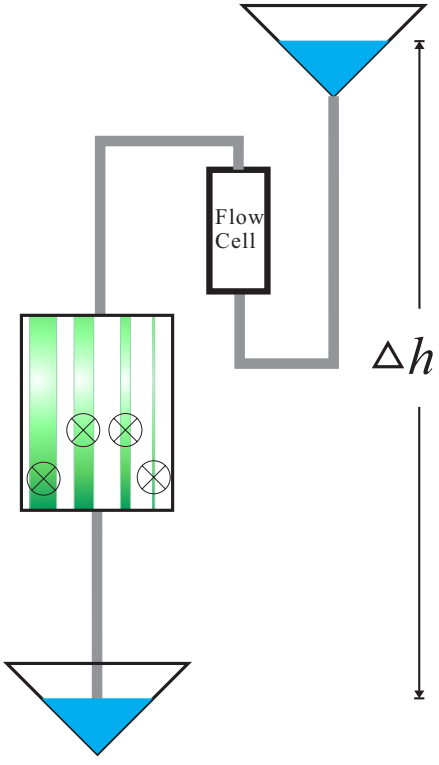

FIGURE 2.1: Schematic demonstration of a continuous flow system. Glass capillaries are highlighted in green, with a control switch on each of them.

Under the flow cell system, the reaction solution was equilibrated under atmospheric pressure for one hour under room temperature so that the analyte oxygen from air can fully dissolve into the aqueous solution. A scheme of such a gravity-feed continuous flow system is shown in Figure 2.1. The reaction solution then flowed vertically upwards through the cell in order to avoid trapped air bubbles. An upper reservoir was fixed in position and constantly supplying solution *via* Teflon tubing to the cell. The flow rates were regulated by both glass capillaries and variation in height differences (Δh) of the upper and lower reservoirs. The glass capillaries situated at downstream with different inner bore sizes, through which the waste solution flowed. The volume flow rate (V_f) of a solution was obtained by measuring the volume of waste solution collected in the lower reservoir over the recorded time. This procedure was repeated for a combination of glass capillaries at a range of Δh for variable values of V_f. For oxygen-free conditions, nitrogen gas was bubbled into the upper reservoir for at least 30 minutes. In order to prevent oxygen dissolution during the solution transport process, a small pre-nitrogen bubble can be deliberately set into the transportation Teflon tubing. All experiments were conducted immediately after the N_2 bubble passes the flow cell. The TGCE surfaces were polished between experiments by using NMR tube cleaners sprayed with variable diamond sizes (3, 1 and 0.1 micron, Kemet International Ltd., U.K.).

All electrochemical experiments were conducted in a water bath at (298 ± 0.5) K under atmospheric pressure, unless otherwise specified, within a Faraday cage to minimise background noise. Errors were evaluated from repeated experimental procedures for at least five times.

2.3 Microdisc calibration

The radius (r_e) of the working micro-electrode can be calibrated by analyzing either the steady-state current or the single potential step chronoamperogram, in a 2 mM ferrocene anhydrous acetonitrile supported with 0.1 M tetra-n-butylammonium perchlorate at 298 K.

For the steady-state current measurement, the electrode was scanned at 10 mV s^{-1} in the electrolytic acetonitrile solution. A literature diffusion coefficient, of 2.43×10^{-5} cm^2 s^{-1} for ferrocene in the corresponding electrolytic solution at 298 K [23], was adopted to determine the radius by using the following equation [1]:

$$I_{ss} = 4nFr_eD_iC_i \tag{1.26}$$

where I_{ss} is the steady-state current, n is the number of electrons transferred ($n = 1$), F is the Faraday constant, D_i is the diffusion coefficient of ferrocene, and C_i is the bulk concentration of ferrocene.

The electrode radius can also be accurately determined by fitting the obtained chronoamperogram with Shoup and Szobo analysis [17], the result of which should agree with that obtained from the steady-state current analysis. Single potential step chronoamperometry, due to the varying influence of both spherical and planar diffusion at a microdisc electrode over the experimental timescale, may be exploited to allow independent deconvolution of one or two parameters out from r_e, D_i, and nC_i within one single transient [24–26]. The analysis is based only on the knowledge of one or more of these parameters. In the case of radius calibration, both D_i and nC_i are known. The experiments were undertaken using a sample time of 0.001 s. Prior to the potential step the system was pretreated by

holding at a potential for 2 s where no faradic current was passed. Immediately after the current transient was obtained by stepping to a potential corresponding to the transport limited oxidation of ferrocene and held for 0.5 s. Note that data collected at the first 3 ms were discarded due to extensive double layer charging (Section 1.4). The time-dependent current response obtained was then analysed by using a nonlinear fitting function in OriginPro 8.5.1 (Microcal Software Inc.) based on the following equations, as first proposed by Shoup and Szabo [17], which sufficiently describe the current response, I, over an entire time domain, with a maximum error of less than 0.6%:

$$I = 4nFD_iC_ir_ef(\tau) \tag{1.27}$$

$$f(\tau) = 0.7854 + 0.8863\tau^{-\frac{1}{2}} + 0.2146\exp(-0.7823\tau^{-\frac{1}{2}}) \tag{1.28}$$

where the dimensionless time parameter, τ is given by:

$$\tau = \frac{4D_it}{r_e^2} \tag{1.29}$$

Consequently, the r_e can be experimentally measured from the best-fit data to a potential step transient. Furthermore, the chronoamperometric technique can also be used to obtain unknown D_i and nC_i of analyte by using a calibrated microdisc electrode. Such a procedure is applied in Chapter 3, Chapter 4, and Chapter 5, where both D_i and nC_i can be measured independently and simultaneously.

2.4 Simulation programs

Cyclic voltammetric and chronoamperometric techniques can readily provide qualitative information about a redox system. Yet the extraction of quantitative data, such as kinetic rates, diffusion cofficients of both reactant and product, still manifests difficulties if approximate analytical theory is used. Hence, the use of modelling software is often required to simulate voltammetric responses. All the simulation programs involved in this thesis are based on Butler-Volmer kinetics.

All macro-electrode voltammetric simulations were carried out by using a commercial software package DIGISIM® (version 3.0, BASi Technicol, West Lafayette, IN). DIGISIM® is based on a fully implicit finite difference (IFD) method suggested by Rudolph [27, 28]. Rudolph's work developed ideas originally proposed by Newman [29]. Subsequent modifications by Feldberg and Rudolph [30, 31] led to the current computationally efficient algorithm. DIGISIM® can be used to simulate any electrochemical mechanism in terms of single or multiple electron transfer reactions, and first- or second-order homogeneous reactions. Moreover, DIGISIM® can generate dynamic concentration profiles. Such operation enables qualitative evidence for the existence of predicted intermediate species at any potential along the scan range. The DIGISIM® simulated data can be used to fit with imported experimental data. However, DIGISIM® can only simulate diffusion to those electrode geometries where diffusion can be described by a single dimensional variable *e.g.* linear diffusion at a macroelectrode.

For microelectrode voltammetries, simulations were achieved by using four different in-house developed computer programs by Klymenko [26, 32], Henstridge [24], and Ward [33].

Double potential step chronoamperometry allows the determination of the diffusion coefficients for both reactant and product of an electrochemical reaction. The first step of the process is identical to a single potential step chronoamperometry (see previous section). The second part of the current transient can be obtained by immediately stepping back to the potential corresponding to the transport limited conversion of product to reactant. The first part of the time-dependent current response can be analysed to result the information of reactant, by using a nonliner fitting function in OriginPro 8.5.1 (Microcal Software Inc.) based on Shoup and Szabo analysis [17]. The product information can be extracted from simultaneous fitting of the entire double potential step chronoamperogram *via* a computational program described by Klymenko *et al.* [26]. The spatial grid of size $N\Theta \times N\Gamma = 70 \times 70$ (where Θ and Γ are the transformed grid coordinates), and the time grid expansion parameter, ϖ, being 0.001 are sufficient to achieve convergence error of less than 1%.

The simulation to derive the heterogeneous electron transfer kinetic parameters was developed by Klymenko *et al.* [32] based on two dimensional mass transport equations. Both wave shape and steady-state current were fitted with experimental data. The simulated voltammograms were performed at a grid size of $N\Theta \times N\Gamma = 200 \times 200$ (where Θ and Γ are the transformed grid coordinates), and the time grid expansion parameter, Nt, of 3000. These parameters are sufficient to achieve convergence error of less than 1%.

In order to quantify the accuracy of fitting and hence the accuracy of the obtained values of diffusion coefficient (D_i) and concentration (C_i) from a chronoamperogram, a simulation program was developed by Henstridge *et al.* [24] through measurement of the difference in current between experimental and simulated

responses. This difference in current was expressed as a *mean scaled absolute deviation* (MSAD), based on Shoup and Szabo analysis [17]. The MSAD defines as the average error per point over the entire chronoamperometric transients.

$$\text{MSAD}\% = \frac{1}{N}\sum_{N}\left|\frac{I_{sim} - I_{exp}}{I_{exp}}\right| \times 100 \tag{2.2}$$

where N is the number of experimental data points, I_{exp} is the experimental current and I_{sim} is the simulated current from Shoup and Szabo equation (Equation (1.27)). This procedure was computed and repeated by narrowing down the value ranges for nC_i (n is the number of electron transferred) and D_i in the same chronoamperomogram, until the minimum MSAD can be obtained.

The simulation program to determine the homogeneous reaction kinetic parameters was developed by Ward *et al.* [33], which simulates a simple electrocatalytic EC' mechanism at a microelectrode by coupling with mass transport equations. After inputting the micro-disc radius (r_e), heterogeneous rate constant (k_s), diffusion coefficients (D_i) and concentrations (C_i) of the reactants, reductive current responses can be generated by adjusting the input homogeneous reaction rate constant (k_f), in order to fit the experimental voltammograms in terms of wave shape and magnitude.

Chapter 3

Kinetic studies of the electrocatalysis of oxygen reduction in aqueous media

This chapter investigates the electrocatalytic rates, thermodynamics, and mass transport of two redox mediators, viz. anthraquinone-2-monosulfonic acid sodium salt (or anthraquinone monosulfonate, abbreviated as AQMS) and methyl viologen dichloride (abbreviated as MV^{2+} by using its cationic form), in aqueous media. The author highlights the use of simulation software in combination with experimental results to extract kinetic data. Specifically, the voltammetric features, such as the 'reverse' peak on the backward scan and the 'split waves', have drawn particular attention. Through the use of simulation software the electrocatalytic oxygen reduction mechanism has been fully modelled. The work presented herein was published in two articles '*ChemPhysChem 2011, 12, 1255-1257*' and '*Phys.Chem.Chem.Phys. 2013, 15, 7760-7767*'. The assistance of Ms Q. Lin in collection of the experimental data is acknowledged.

3.1 Exceptionally high reactivity of semiquinone intermediates

3.1.1 Introduction

The quinone mediated reduction of oxygen is of great importance, both industrially and biologically. One of the quinone derivatives, 2-alkyl anthraquinone, acts as a crucial catalyst to chemically reduce oxygen to hydrogen peroxide (H_2O_2) in industry. There was approximately 2.2 million metric tonnes of H_2O_2 being produced worldwide *via* this chemical method in 2006 [34]. Beyond industry, a prime example of quinones for medicinal use lies within the anthracycline antibiotics. Anthracycline antibiotics are powerful chemotherapeutic drugs and are employed against a variety of cancers. Although highly successful their use is in part limited due to their high cardiotoxicity [35]. Over the last decade it has been proposed that this toxicity is directly related to, and is a result of, the biological redox cycling of the quinone moiety within the anthracycline molecule, leading to the production of reactive oxygen species [36, 37]. The structure of daunorubicin, the first discovered anthracycline drug, is shown in Figure 3.1. Understanding the mechanism for such a mediated oxygen reduction pathway is therefore imperative not only for the optimisation of industrial processes but also to aid development of more suitable chemotheraputic drugs.

The direct electrochemical investigation of organic molecules and their interaction with oxygen is often hindered by the direct reduction of oxygen at the electrode. Hence the voltammetric response of interest has to be carefully resolved from that of the background. In this section, it is demonstrated that this issue is circumvented through the use of a boron-doped diamond electrode (BDD). This

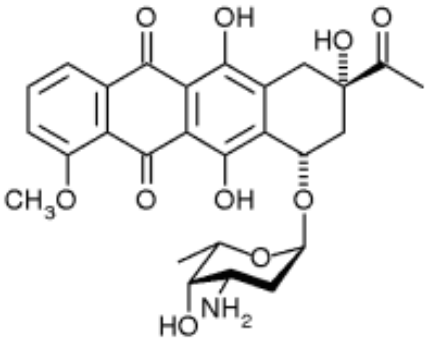

FIGURE 3.1: Molecular structure of daunorubicin.

is achievable due to the very large overpotential required for oxygen reduction at a BDD interface. Another important factor is the experimentally low capacitance values measured at the BDD surface. The outcome may arise either due to the fact that BDD is a semiconductor (albeit highly doped $\sim 0.1\%$) or it may also be related to its near atomically flat surface [38]. From studying the voltammetric response of anthraquinone at a BDD electrode in both the presence and absence of dissolved oxygen it is possible to clearly elucidate the complex mechanistic process highlighting the remarkable potency of the semiquinone intermediate in the production of superoxide.

3.1.2 Theory

This section provides a theoretical model by using DIGISIM® to explore the mechanistic pathways and kinetics of the redox of a quinone centre and/or its mediated oxygen reduction in fully buffered aqueous solution. It provides fundamental understanding of electrode reactions, and the principles involved also apply in Chapter 4 and Chapter 5.

Anthraquinone derivatives (AQ) are present in a number of biological systems, and their electrochemical properties have long been studied. Under buffered acidic conditions and sufficient thermodynamic driving force, the reduction of AQ proceeds *via* a $2H^+ - 2e^-$ process:

$$AQ + 2H^+ + 2e^- \quad \rightleftharpoons \quad AQH_2$$

However, under other conditions, such as high pH (refer to Chapter 4) and non-aqueous media (refer to Chapter 5), the process can, at least in principle, stop at a lower protonated or un-protonated state. Moreover, even if the process is overall a $2H^+ - 2e^-$ system, the precise mechanism, *i.e.* the sequence of the addition of electrons and protons, can be dependent on the local pH and the pK_a values of the intermediate species.

A theoretical description of the $2H^+ - 2e^-$ system was first proposed by Jacq [39], based on a 'scheme of squares' model. Such a model is based upon the assumption that electron transfer is the rate limiting step and the protonations are at equilibrium. A generalised scheme for the anthraquinone redox system is presented in Figure 3.2, where the horizontal equilibrium represents the electrochemical reaction (**E**) and the vertical one represents the chemical protonation step (**C**).

3.1.2.1 AQ-only model

All simulations were performed by using the commercially available software package DIGISIM® (Section 2.4). Within the simulation all protonations were assumed to be fully buffered. Consequently the following equilibrium can be used within

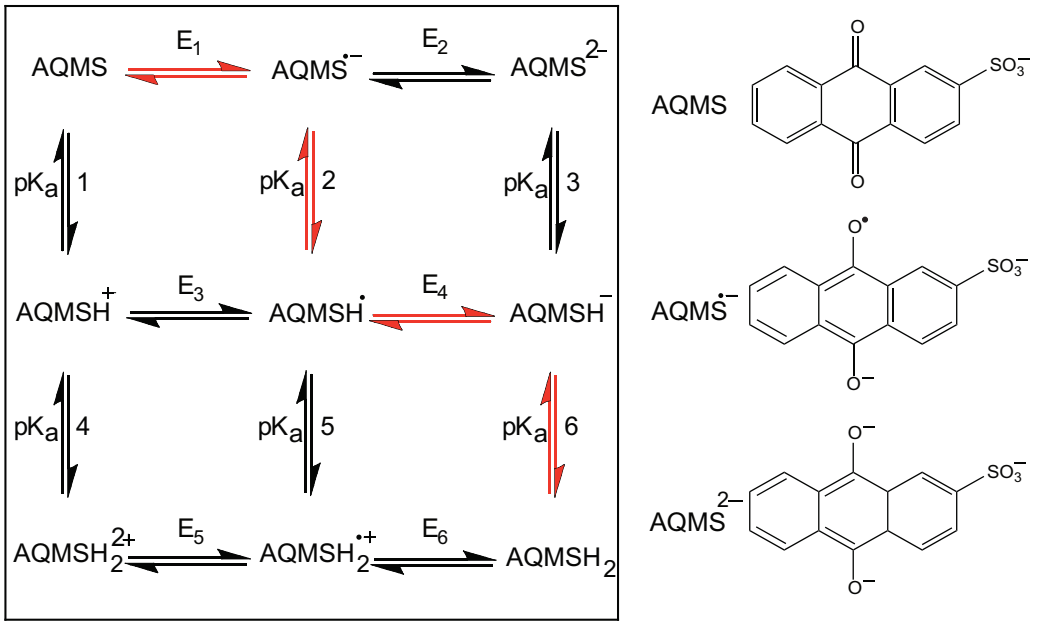

FIGURE 3.2: 'Scheme of squares' model for the reduction of AQMS with the main **ECEC** mechanistic pathway at neutral pH, highlighted red. Adjacent are the unprotonated structures of the unreduced, monoreduced and direduced forms of the anthraquinone monosulfonate species.

DIGISIM®:

$$\mathrm{HA} \overset{K_{eq}}{\rightleftharpoons} \mathrm{A}^{-}$$

$$\text{where } K_{eq} = \frac{K_a}{C_{\mathrm{H}^+}}$$

Here A^{-} is the unprotonated form, HA is the protonated form, C_{H^+} is the concentration of protons, K_{eq} is the equilibrium constant of the protonation process, and K_a is the actual acid dissociation constant for the species HA. Realistic rate constants must be used within the simulation; as such the rate constant for protonation must be no larger than 1×10^{10} $\mathrm{mol}^{-1}\mathrm{dm}^{-3}\mathrm{s}^{-1}$ (diffusion limit). It can also be shown that with the equilibrium used above, the rate constant for protonation should be dependent upon the proton concentration. Within the model all diffusion coefficients were set as equal and values taken were those measured

from the steady-state current at a microdisk electrode as reported by Batchelor-McAuley *et al.* as being 4.74×10^{-6} cm^2 s^{-1} [40]. Further to this all electron transfer coefficients, α, were set as 0.5.

At the studied experimental pH of 6.74 the dominant pathway for the reduction of AQMS is an **ECEC** type mechanism, as highlighted in Figure 3.2 [40]. The current investigation utilises a BDD working electrode; it is fair to assume that the thermodynamic properties of the system (pK_a values and potentials) are intrinsic to the AQMS and are not perturbed by the BDD surface (outer-sphere electron transfer mechanism). Consequently, these data are taken directly from literature reported on a gold electrode [40]. However the kinetic parameters, *i.e.* the rates of electron transfer, will be altered. The density of states for a BDD electrode is known to be significantly lower than for gold electrodes; as such the electron transfer kinetics observed on BDD electrodes (k_s) is commonly far slower than that measured on a metallic electrode [41–43].

Redox couple	Standard Potential (V *vs.* SCE) [40]	Electron Transfer Rate (cm s^{-1})
E_1	−0.6061	10
E_2	−0.62101	0.3
E_3	−0.3995	10
E_4	−0.22681	5
E_6	+0.03813	10

TABLE 3.1: Parameters used in the anthraquinone-only model, where values of standard potentials are taken from literature and the electron transfer rates were obtained from the optimised simulation for AQMS.

In order to achieve a suitable model of the anthraquinone system in the absence of oxygen it was necessary to fit the simulation to the experimental data. The system

was successfully fitted with attention to voltammetric peak height and position through variation of the rates of electron transfer for E_1 and E_4 steps. The pK_a values are pK_{a1} = 0.84, pK_{a2} = 4.3, pK_{a3} = 11, pK_{a5} = 3.12, and pK_{a6} = 7.6 [40, 44]. Values for the standard potentials were taken from the literature [40] and electron transfer rates were obtained from the optimized fitting with simulation, tabulated in Table 3.1.

3.1.2.2 Electrocatalytic pathway model

Modelling of the catalytic reduction of oxygen at neutral pH was based in part upon the following mechanistic steps:

$$\mathrm{AQMS}^{-\bullet} + \mathrm{O_2} \xrightarrow{k_{f1}} \mathrm{AQMS} + \mathrm{O_2}^{\bullet-} \tag{3.1}$$

$$\mathrm{AQMSH}^{-} + \mathrm{O_2} \xrightarrow{k_{f2}} \mathrm{AQMS} + \mathrm{HO_2}^{-} \tag{3.2}$$

where Reaction 3.1 is the $1e^-$ reduction of oxygen to form superoxide *via* the semiquinone intermediate ($\mathrm{AQMS}^{\bullet-}$). It is important to recognise that the $1e^-$ reduction of oxygen by the di-protonated form of the AQMS is not thermodynamically favourable and hence is not included within the reaction scheme (as will be shown in next section). The Reaction 3.2 is the $2e^- - 1\mathrm{H}^+$ reduction of $\mathrm{O_2}$ to the monoprotonated peroxide ion *via* reaction with the monoprotonated dire-duced form of anthraquinone (AQMSH^-). The superoxide radical ($\mathrm{O_2}^{\bullet-}$) species is able to undergo series of reactions, including protonation and disproportionation, which leads to the reformation of $\mathrm{O_2}$ and the production of $\mathrm{H_2O_2}$. The following

reaction schemes were used as the basis for all thermodynamic calculations:

$$O_2 + e^- \rightleftharpoons O_2^{\bullet -} \qquad E_{O1} = -0.4212\text{V } \textit{vs.}\text{ SCE}$$

$$O_2^{\bullet -} + H^+ \rightleftharpoons HO_2^{\bullet} \qquad pK_a = 4.88$$

$$HO_2^{\bullet} + e^- \rightleftharpoons HO_2^- \qquad E_{O2} = +0.5369\text{V } \textit{vs.}\text{ SCE}$$

$$HO_2^- + H^+ \rightleftharpoons H_2O_2 \qquad pK_a = 11.62$$

The above thermodynamic values were obtained from the literature where they have been corrected at the studied experimental pH and against a SCE reference electrode [45]. Note that no direct reduction of oxygen species is possible on the BDD electrode such that for E_{O1} and E_{O2}, $k_s = 0.0$ cm s^{-1}. The following pathway was also included so as to allow disproportionation of the superoxide species to occur:

$$2HO_2^{\bullet} \rightarrow O_2 + H_2O_2 \tag{3.3}$$

This disproportionation was set to occur at a diffusion limited rate. Using this full model the experimental voltammetric response was fitted through varying the values of the forward rate constants for the rates of Reaction 3.1 (k_{f1}) and Reaction 3.2 (k_{f2}). Note that the thermodynamic values for the formal potentials and pK_a values associated with the reduction of AQMS were the same as in the AQ-only model. The concentration of a saturated O_2 solution was found to be 1.24 mM [46] and has an associated diffusion coefficient of 1.77×10^{-5} cm^2 s^{-1} in aqueous solution [47].

3.1.3 Results and discussion

The cyclic voltammetric response of 50 μM anthraquinone monosulfonate (AQMS, chemical structure shown in Figure 3.2) was investigated at a BDD electrode in an aqueous solution saturated with N_2 (pH 6.74) at various scan rates. Figure 3.3(a) depicts a representative experimental voltammogram for 50 μM AQMS. A clear pair of voltammetric redox waves was recorded at -0.45 V (*vs.* SCE). The variable scan rates data of only AQMS responses were modelled through use of a commercially available software package DIGISIM®.

At the experimental pH (6.74) the dominant pathway for the reduction of AQMS is an **ECEC** type mechanism, as highlighted in Figure 3.2. In order to deconvolute the stepwise mechanistic steps, the experimental voltammetries were fitted as described in the previous section. Figure 3.3(b) depicts a 'trumpet plot' of variation in the AQMS peak potentials (experimental and simulated) as a function of scan rate. Excellent agreement was achieved. Consequently, the fitted rates of electron transfer (k_s) for E_1 and E_4 steps were 10 and 5 cm s^{-1} respectively, tabulated in Table 3.1.

The voltammetric response for the reduction of AQMS is markedly different in an oxygen saturated solution. The comparison between the reduction of AQMS (50 μM and 500 μM) in the presence and absence of oxygen is depicted in Figure 3.4. As can be seen from Figure 3.4, the observed voltammetric response shows a single irreversible wave at -0.55 V (*vs.* SCE), which does not change with respect to the concentration of AQMS. This voltammetric feature is attributed to the electrocatalytic reduction of O_2 *via* the reduced anthraquinone intermediates. Further, over the potential range of study there is no significant reduction of either oxygen or hydrogen peroxide on the BDD electrode, as shown in Figure 3.5. It is

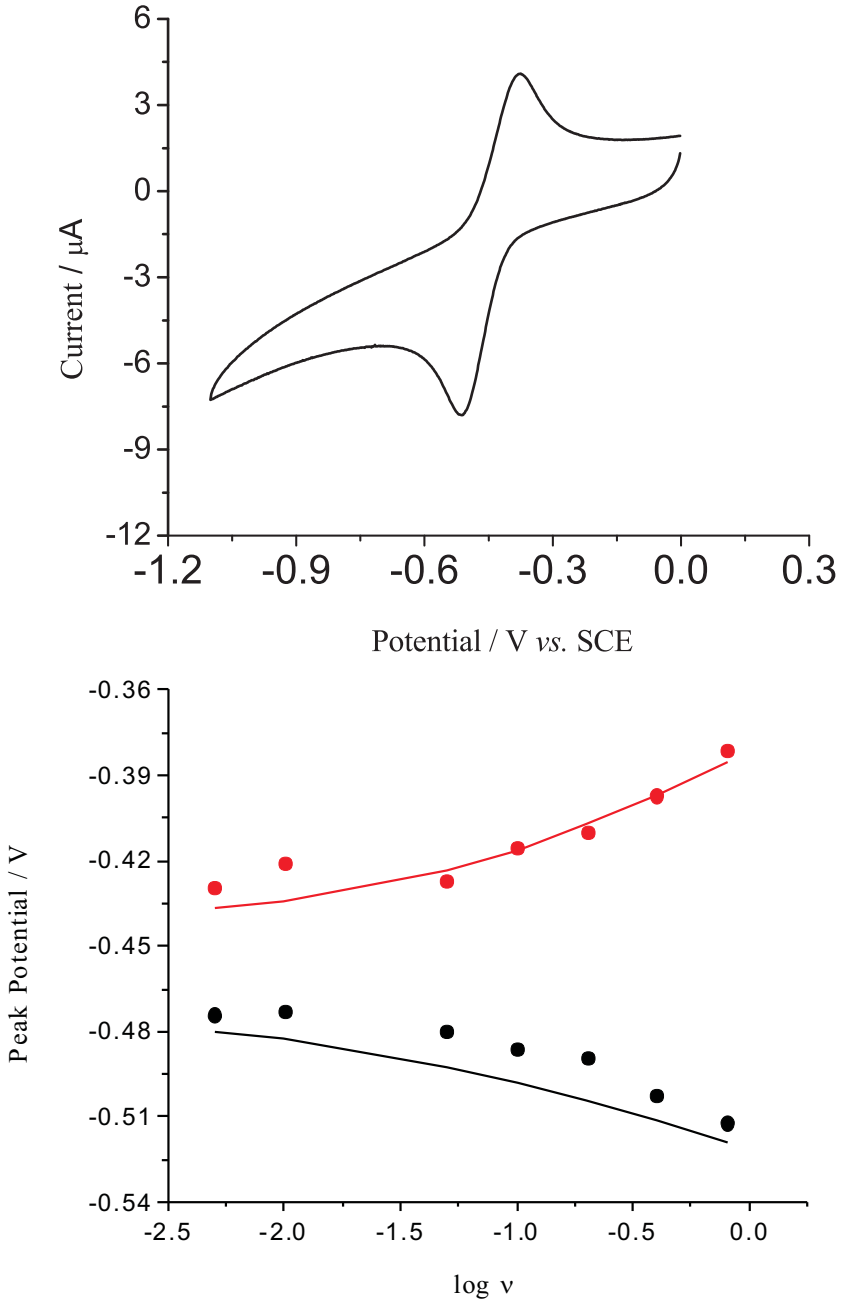

FIGURE 3.3: (a) Cyclic voltammetry of 50 μM AQMS in N_2-PBS; (b) A plot of variation of peak potentials with scan rates for both experimental (scatters) and simulated (lines) results.

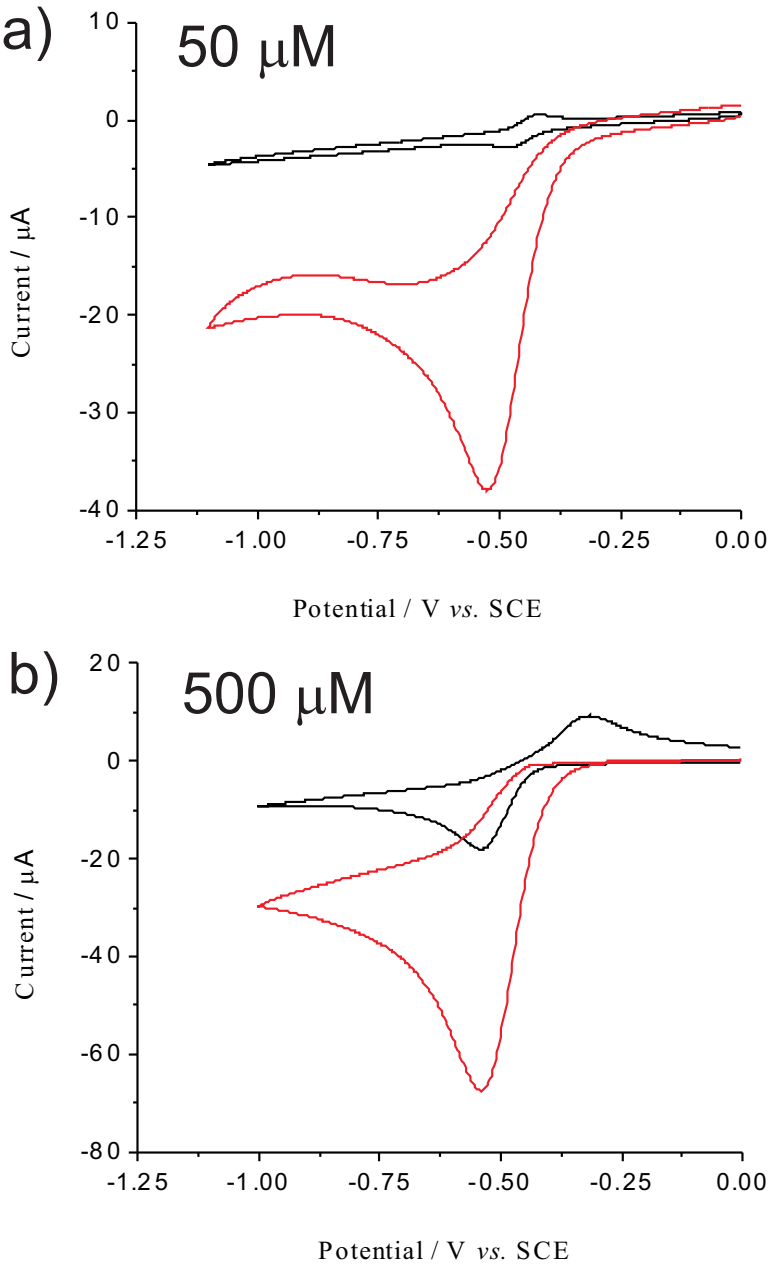

FIGURE 3.4: Comparison of the voltammetries of (a)50 μM and (b)500 μM AQMS in the absence (black) and presence (red) of saturated O_2 at scan rate of 100 mV s^{-1}.

of importance that at a concentration of 50 μM AQMS *not* all of the oxygen has been consumed, as evidenced by the lower electrocatalytic peak current than that found for the 500 μM AQMS. Additionally, the electrocatalytic peak potential for 500 μM AQMS appears unperturbed despite of increased AQMS concentration (in contrast to Section 3.2). Hence, the reduction of oxygen undergoes 'partial catalysis', and the rate limiting step is related to the redox of AQMS species.

In general the adsorption of species to BDD electrodes is reported to be weak, in part due to the 'low polarizability of the material' [42]. Through the analysis of peak current and scan rate variation (a plot of I *vs.* $\nu^{0.5}$ is linear, not shown), the voltammetric response of the anthraquinone is found to be purely diffusional in nature. Subsequently, it is assumed that the influence of adsorption upon the catalytic response is *minimal*. Hence, it is not inappropriate to approximate the electron transfer as being an outer sphere mechanism. This assumption is further corroborated by the fact the redox potentials for the anthraquinone species are found to be unaltered from those measured on a gold electrode [40]. Consequently, adsorption processes were *not* considered within the simulation model.

The AQMS mediated electrochemical reduction of O_2 is known but the mechanistic pathway is not [48, 49]. Overall, at pHs below ~ 8, the process is known to lead to the $2H^+ - 2e^-$ reduction of O_2 leading to the formation of H_2O_2. Figure 3.6 depicts the voltammetric response of 50 μM AQMS in an oxygen saturated solution at two different scan rates, (a) 100 mVs^{-1} and (b) 800 mVs^{-1}. Of particular significance is the experimentally observed 'reverse' peak on the backward scan (as highlighted *via* the red square in Figure 3.6(b)). This feature is highly unusual and indicates a pathway for O_2 reduction which is non-operational at high overpotentials.

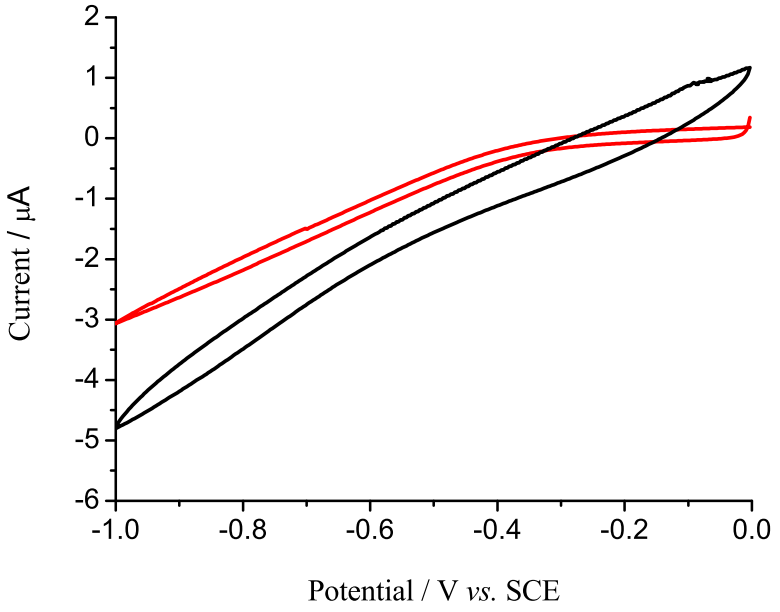

FIGURE 3.5: Voltammetries of saturated O_2 direct reduction in PBS (red) and 1 mM H_2O_2 reduction in N_2-PBS on a BDD electrode.

For multi-electron transfers it is often assumed that the subsequent electron transfers after the first electron are highly driven and hence it is possible to analyse the obtained results using the well known classical equations [6]. In the case of many organic molecules this assumption does not necessarily hold, and as demonstrated for anthraquinone the potentials for the first and second electron transfer are likely comparable [40]. As a direct result of this, at lower overpotentials significant levels of the intermediate species (for example semiquinone) are produced and are able to diffuse away from the electrode surface. During a voltammetric experiment, as the overpotential is increased the driving force increases such that at high overpotential minimal levels, if any, of the intermediate will be produced. Hence, from the above results it is reasonable to conclude that the observed 'reverse' peak (red square in Figure 3.6) is related to the formation of the semiquinone species at lower overpotentials and its catalytic reduction of oxygen.

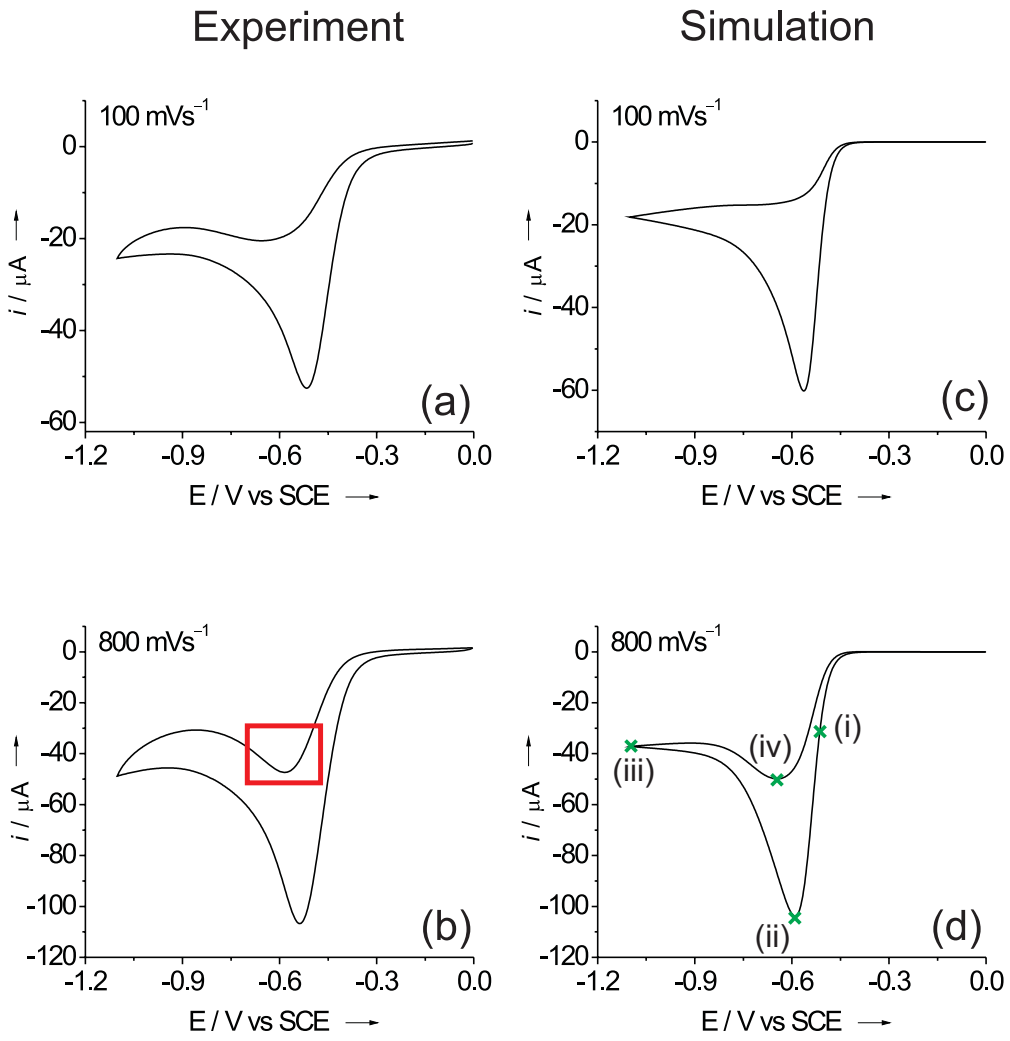

FIGURE 3.6: Comparison of the experimental (a, b) and simulated (c, d) voltammetries of 50 μM AQMS in the presence of oxygen at two different scan rates. The red square in inset (b) highlights the observed unusual 'reverse' peak. Inset (d) is the voltammogram used for concentration profiles in Figure 3.9 and Figure 3.10, where (i) to (iv) indicate the selected potentials at recorded concentration profiles.

In order to understand the kinetic role of the quinone intermediate species, the electrocatalytic system was modelled through the use of a commercially available software package DIGISIM®, as seen in Section 3.1.2. Within the full reaction scheme outlined, it is possible to examine the likely reaction pathways and reactive intermediates at the studied pH.

The same PBS solution was adjusted to pH 3.13 and the voltammetric responses

were obtained, shown in Figure 3.7. The reduction of the anthraquinone moiety occurs at −0.21 V *vs.* SCE. It can clearly be seen that in the presence of O_2 there is no influence on the anthraquinone redox response. However, a large voltammetric feature at −0.85 V ascribed as being due to the direct reduction of oxygen can be seen at the BDD electrode, *i.e. no* catalytic oxygen reduction is observed. At pH 3.13, both pK_{a6} and pK_{a2} (as defined on Figure 3.2) will lie heavily towards the production of $AQMSH_2$ and $AQMSH^{\bullet}$ respectively. Consequently, within this reaction scheme the di-reduced di-protonated form of anthraquinone ($AQMSH_2$) and the protonated semiquinone ($AQMSH^{\bullet}$) are *not* reactive towards oxygen. Therefore, it is proposed that protonation of the intermediate species disfavours the electrocatalytic reduction of oxygen.

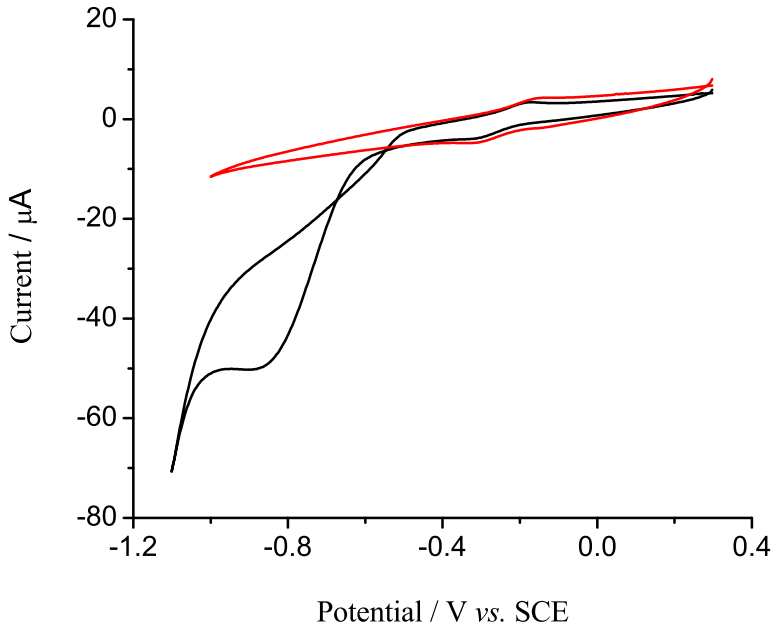

FIGURE 3.7: The voltammetric responses of 50 μM AQMS in pH 3.13 PBS in the presence (black) and absence of oxygen (red).

Applying the mechanism above to that for the reduction of anthraquinone at neutral pH, it is possible to obtain a high level of agreement between experiment and simulation, where the homogeneous rate constants for Reaction 3.1 (k_{f1}) and

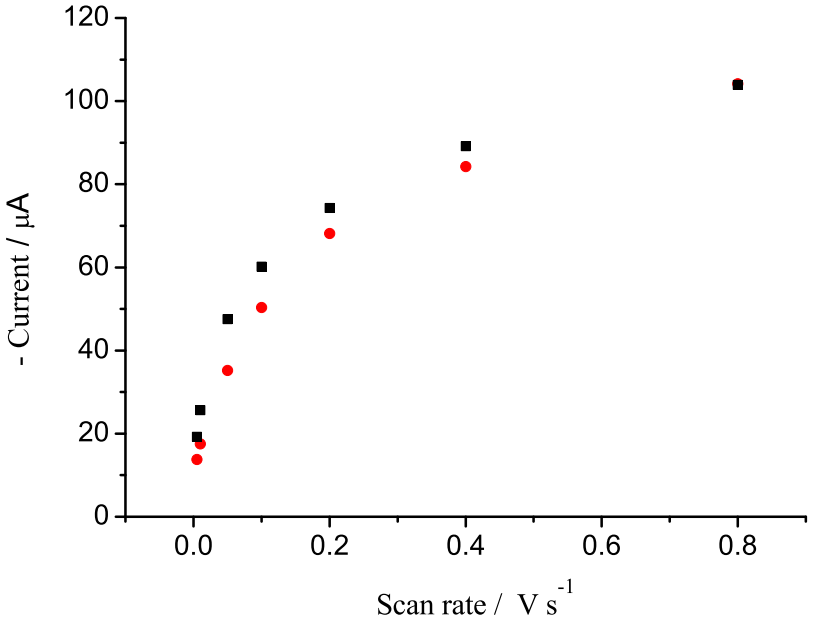

FIGURE 3.8: Comparison of the experimental (red) and simulated (black) peak currents for the reduction of AQMS in the presence of oxygen.

Reaction 3.2 (k_{f2}) are $(4.8 \pm 0.2) \times 10^9$ mol^{-1} dm^3 s^{-1} and $(1 \pm 0.5) \times 10^7$ mol^{-1} dm^3 s^{-1} respectively. Therefore, it can be highlighted that the homogeneous rate of reaction between the semiquinone and oxygen is over two orders of magnitude greater than the corresponding reaction between the di-reduced form and oxygen. Using the simulated results of k_{f1} and k_{f2}, Figure 3.8 depicts how the variation in the catalytic peak height varies with scan rate for both experimental and simulated results. It can be seen that a good agreement of both experimental and simulation results was obtained.

Figure 3.9 and Figure 3.10 depict the simulated concentration profiles at selected potentials during the electrocatalytic process for oxygen and anthraquinone species respectively. The concentration of AQMS is 50 μM and the scan rate is 800 mV s^{-1}, the voltammetry for which is depicted in Figure 3.6(d). Insets (i), (ii) and (iii) are the concentration profiles for the species on the forward scan at potentials

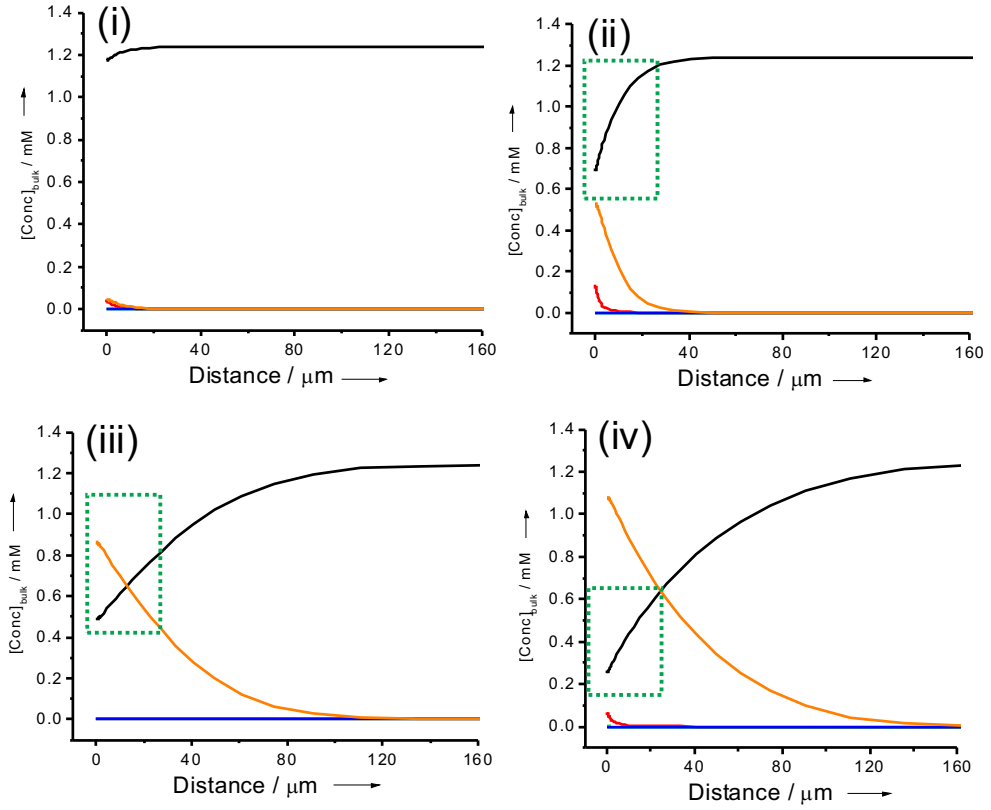

FIGURE 3.9: Concentration profiles of O_2 species in AQMS mediated O_2 reduction at selected potentials (refer to Figure 3.6(d)): (i) -0.5 V, (ii) -0.59 V, (iii) -1.1 V and (iv) -0.646 V. Black: O_2, Orange: H_2O_2, Red: $O_2^{\bullet-}$, Blue: $HO\bullet$, and Green: HO_2^- (almost zero). The green squares highlight point of interest.

-0.5 V, -0.59 V and -1.1 V respectively. Inset (iv) depicts the concentration profiles of the species at the 'reverse' peak (-0.646 V on the backward scan). The main points of significance are the fact that the concentration of oxygen at the forward peak (-0.59 V) is non-zero indicating that the peak observed in the voltammetry is related to redox cycling of the anthraquinone species and not due to the total consumption of the oxygen (highlighted in green boxes). The second point of interest is that the concentration of the reactive semiquinone intermediate is predicted by the model to have a concentration of 1.2 μM at the 'reverse' peak, as highlighted in the green box. Moreover, such a maximum concentration of semiquinone intermediate is only seen at low overpotentials, shown in both insets

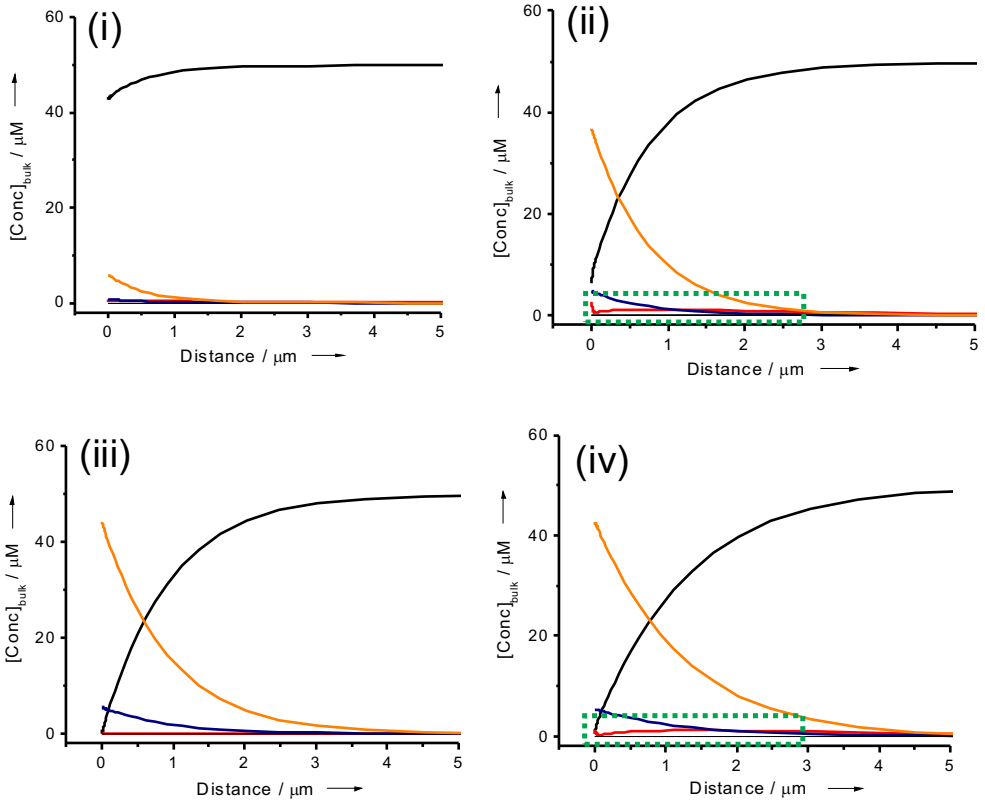

FIGURE 3.10: Concentration profiles of AQMS species in AQMS mediated O_2 reduction at selected potentials (refer to Figure 3.6(d)): (i) −0.5 V, (ii) −0.59 V, (iii) −1.1 V and (iv) −0.646 V. Black: AQMS, Orange: $AQMSH_2$, Red: $AQMS^{\bullet -}$(semiquinone), Blue: AQH^-. The green square highlights point of interest. Note that the concentrations of all other anthraquinone species remain insignificant at all potentials.

(ii) and (iv) in Figure 3.10.

3.1.4 Conclusions

The simulation results directly demonstrate that the observed 'reverse' peak is a result of the higher reactivity of the semiquinone intermediate. The concentration of the semiquinone intermediate being produced is at a maximum at low overpotentials. Hence the mechanistic pathway mediated by semiquinone is observed to switch off at higher voltages but returns at low overpotentials on the backward

voltammetric sweep. The search for optimal oxygen reduction catalysts can be seen to be dependent on finding a quinone/semiquinone/hydroquinone system in which the semiquinone is formed over a wide potential window and hence in which the two-electron reductions are relatively more widely separated in aqueous solution. Similar conclusions may relate to the toxicity of anthracycline antibiotics, allowing the minimisation of the production of reactive oxygen species in biological systems.

In the second part of this chapter, another oxygen reduction mediator will be introduced. Its non-catalytic, as well as electrocatalytic kinetics and thermodynamics will be elaborated in the next section.

3.2 'Split waves' measurement for methyl viologen electrocatalysis

3.2.1 Introduction

The electrocatalytic reduction of molecular oxygen (O_2) has received continuous interest, specifically due to its importance in many physio-chemical biological processes [50]. Various redox *mediators* can catalyse oxygen reduction under physiological conditions with the reduction potential window ranging from about −840 mV to +260 mV *vs.* saturated calomel electrode (SCE) [51]. Examples are prevalent in biological systems, such as the participation of ferredoxin [52], plastocyanin [53] and plastoquinone [54] in light dependent photosynthetic pathways. Furthermore, bipyridinium compounds are some of the most widely occurring mediators involved in the electrocatalytic reduction of oxygen [55]. Methyl viologen (or 1,1'-dimethyl-4,4'-bipyridinium dichloride or paraquat) belongs to the viologen family,

as shown in Figure 3.11. It is known to be an effective and non-selective herbicide. Its herbicidal activity on plants has been proposed to involve the production of reactive oxygen species (ROS) which initiate peroxidation of an unsaturated lipid constituent to produce malondialdehyde [56–61]. As a final outcome the plants become desiccated leading to necrosis. This process is initiated by the photosynthetic pathways, and the mediator only involves the one-electron reduction of the doubly charged nitrogen quaternary cation (MV^{2+}) to its radical cation counterpart ($MV^{\bullet+}$). Moreover, the major product of this process in aqueous solution is proposed to be hydrogen peroxide (H_2O_2) [55]. Therefore, the study of the methyl viologen mediated electrocatalytic reduction of oxygen has wider significance beyond the kinetic characterisation of reaction intermediates and chemical synthesis.

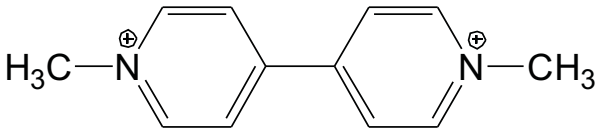

FIGURE 3.11: Molecular structure of methyl viologen (MV^{2+}).

Usually, kinetic characterisation of intermediates, such as radical cation $MV^{\bullet+}$, with lifetime less than 0.1 μs can be challenging [62]. The rate constants of homogeneous reactions can potentially reach the diffusion controlled limit. Consequently the study of this process commonly requires methods such as laser flash photolysis (nanosecond) [63], pulse radiolysis [64, 65], spectrophotometry[66], hydrodynamic voltammetry [67–69], fast-scan ultramicroelectrode cyclic voltammetry [63], and cyclic voltammetry *via* redox catalysis[62, 70]. There have been several attempts to measure the fast homogeneous rate constants of MV^{2+} mediated O_2 reduction in aqueous solution. The most relevant work was reported by Farrington *et al.* using radiolysis equipment in 0.1 M sodium formate solution, and several mechanistic

steps were proposed to explain the redox catalysis process. Values were reported to be $(4-9) \times 10^8$ dm^3 mol^{-1} s^{-1} and 6.5×10^8 dm^3 mol^{-1} s^{-1} for the second-order rate constants for the reaction of $MV^{\bullet+}$ with molecular O_2 and superoxide ($O_2^{\bullet-}$) respectively [64, 65]. Rauwel and Thevenot used ring-disc electrodes and cited Farrington's work in support of their findings [69]. Thorneley utilised an anaerobic stopped-flow spectrophotometric apparatus to report the kinetics of O_2 with $MV^{\bullet+}$ as being greater than 5×10^6 dm^3 mol^{-1} s^{-1} at pH values in the range 7.5 to 9.0 [66]. Later some electrochemical methods were developed, mainly exploiting redox catalysis. Savéant *et al.* reported kinetic studies in acidic dimethyl sulfoxide (DMSO) mixtures by using their classically derived equations *via* cyclic voltammetry [70]. Other developments include surface coated poly(xylylviologen) and solution phase dipentyl viologen studied *via* cyclic and hydrodynamic voltammetric methods, and the measured kinetics were estimated to be $10^6 - 10^7$ dm^3 mol^{-1} s^{-1} [67, 68]. These values are significantly slower than the spectroscopic data, signalling the need for caution in adopting theses results.

An electrocatalytic (EC') mechanism may be described by the equations:

$$\mathrm{A} + n\mathrm{e}^- \rightleftharpoons \mathrm{B} \tag{3.4}$$

$$\mathrm{B} + \mathrm{X} \rightleftharpoons \mathrm{A} + \mathrm{Y} \tag{3.5}$$

The voltammetric response of such an electrocatalytic process can yield a variety of different waveshapes [62]. For the case in which the heterogeneous electron transfer (Eqn. 3.4) and the homogeneous rate of reaction (Eqn. 3.5) are both fast and thermodynamically driven, the mediated reduction of X to Y may occur significantly below the formal potential ($E_{f(A/B)}$) for reduction of the mediating species [71]. Such cases lead to a split voltammetric peak. Figure 3.12 shows a

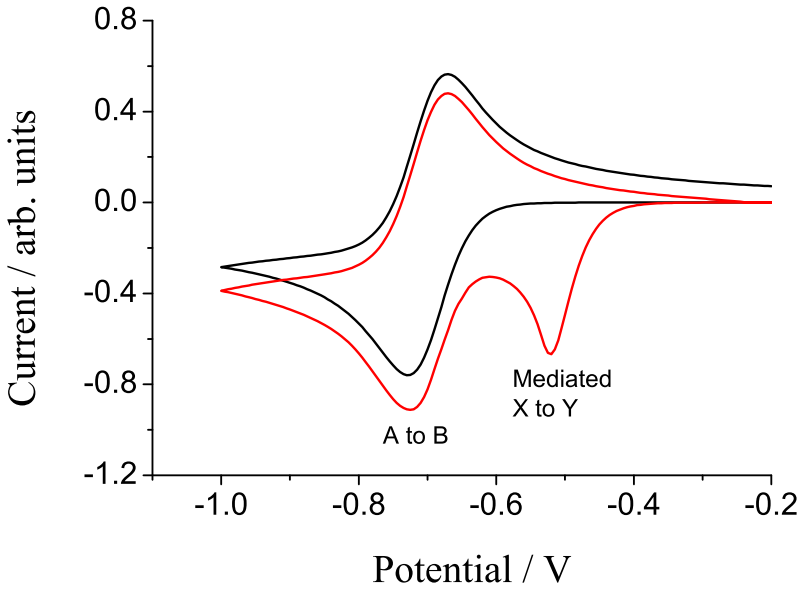

FIGURE 3.12: Simulated cyclic voltammgrams for the EC' mechanism, in the presence (red) and absence (black) of species X, depicting the analytically useful 'split waves' system. The mediated redox process (peak at ~ -0.3 V) occurs at a significantly lower potential than that of the mediator (~ -0.6 V).

generic example, highlighting the decreased potential at which the X/Y redox couple undergoes mediated electron transfer. Compton and co-workers have reported the kinetic characterisation of 'split waves' *via* simulation at channel electrodes [72], rotating disc electrodes [73], hemispherical particles and their arrays [33]. Savéant *et al.* have also reported the kinetic characterisation involving the 'total catalysis' situation for various redox couples [63]. Note that all these works took the assumption of either the homogeneous electron transfer or the follow-up chemical reaction being the rate determining step. Recently, work reported by Batchelor-McAuley and Compton showed that in some cases due to the finite nature of the rate of heterogeneous electron transfer, the overall kinetics may be shifted to that of the heterogeneous rate of the electron transfer step [74]. In the following chapter, the use of 'split waves' analysis for electrocatalytic kinetic characterisation is developed experimentally.

Recall the merit of a boron-doped diamond electrode (BDD) from the previous section; such an electrode is also used here. It is exploited to slow down the rates of heterogeneous electron transfer and 'split waves' analysis is employed to resolve the catalytic wave from its background current. Consequently, the simulation model is significantly simplified [75]. In the following section, cyclic voltammetry is used as the diagnostic electrochemical tool for kinetic characterisation of MV^{2+} mediated O_2 reduction in fully buffered aqueous solution. The current study is combined with one-dimensional simulation software DIGISIM® (introduced in Section 2.4) to deconvolute complex catalytic steps, which involves a full consideration of reaction pathways for superoxide species. The resulting kinetic parameters agree well with previously reported values measured *via* non-electrochemical methods. The underestimated kinetics from hitherto reported electrochemical methods is attributed to be due mainly to the oversimplified mechanistic pathways involved. Thereafter, the cyclic voltammetry demonstrates a convenient and powerful diagnostic tool for the study of redox catalysis. The catalytic mechanism is a viable approach to the study of kinetics, which potentially provides a justification of kinetic information which may be used in the study of biological mimetic pathways.

3.2.2 Results and discussion

3.2.2.1 Methyl viologen diffusional response

Before carrying out the investigation of methyl viologen (MV^{2+}) mediated oxygen (O_2) reduction, the thermodynamics and kinetic parameters of the electroreductions of MV^{2+} and O_2 must first be determined.

Although the one-electron reduction of MV^{2+} does not involve the consumption of protons, in the mediated pathway some of the formed reactive oxygen species (ROS) are likely to be present in their protonated forms as dictated by the associated pK_a values [45]. Additionally, despite the *minimal* interference of supporting electrolyte counter ions with electroactive species, as controlled experiments the ionic environment should be maintained the same. Therefore a fully buffered phosphate buffer solution (PBS) of pH 6.7 was used throughout all experiments reported below to maintain a constant local pH and ionic strength within the diffusion layer.

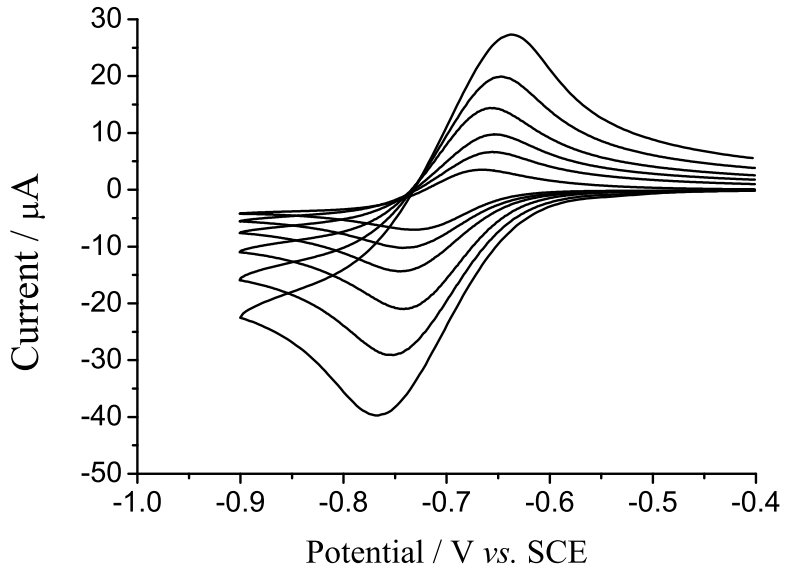

FIGURE 3.13: Cyclic voltammogramms of 1 mM MV^{2+} in pH 6.7 PBS supported with 0.1 M KCl N_2-saturated solution. Scan rate = 20, 50, 100, 200, 400 and 800 mV s^{-1}.

The one-electron electrochemical redox response of 1.0 mM MV^{2+} was studied in a N_2-saturated PBS. The cyclic voltammetry (CV) was recorded at a BDD electrode at variable scan rates ranging from 20 to 800 mV s^{-1}, as shown in Figure 3.13. It is a fair assumption that the thermodynamics, viz. formal potentials, are intrinsic to the MV^{2+} and O_2 and are not perturbed by the boron-doped diamond

(BDD) surface (outer-sphere electron transfer mechanism). However, the kinetic parameters, namely rates of electron transfer, may be altered from that measured on purely metallic electrode substrates. This decrease in the measured heterogeneous electron transfer rates likely arises due to the intrinsically low density of electronic states present within the material [41].

The experimental results in Figure 3.13 were recorded and a plot of $\log_{10}$ of reductive peak current (I_p, A) against $\log_{10}$ of scan rate (ν, V s^{-1}) is depicted in Figure 3.14 (a). A line of best-fit for experimental data points gives a slope of 0.48. Such a value is close to the expected gradient for a diffusion only process (slope of 0.5), as predicted by the Randles-Ševčík equations for a reversible process [1].

$$I_p = (2.69 \times 10^5) n^{1.5} A D_{MV^{2+}}^{0.5} C_{MV^{2+}} \nu^{0.5} \tag{3.6}$$

where n is the number of electrons transferred, A is the electrode surface area (cm^2), $C_{MV^{2+}}$ is the bulk concentration of MV^{2+}(mol dm^{-3}), $D_{MV^{2+}}$ is the diffusion coefficient of MV^{2+} (cm^2 s^{-1}), and ν is the scan rate (V s^{-1}). The $D_{MV^{2+}}$ can be calculated to be 7.7×10^{-6} cm^2 s^{-1}, from the experimentally obtained slope (Figure 3.14(a)). It should be noted that this value is only an approximation. As it can be seen from Figure 3.14(b) the reductive and oxidative peak-to-peak separation (ΔE_p) increases with ν from 58 mV to 116 mV. Such a voltammetric feature suggests that the electrochemical behaviour of MV^{2+} redox on a BDD electrode potentially exhibits quasi-reversibility, and encounters system resistance (R, Ω). In order to obtain a more accurate value of $D_{MV^{2+}}$, one way to bypass this issue is *via* simulation fitting by taking into account the system resistance to match both I_p and ΔE_p.

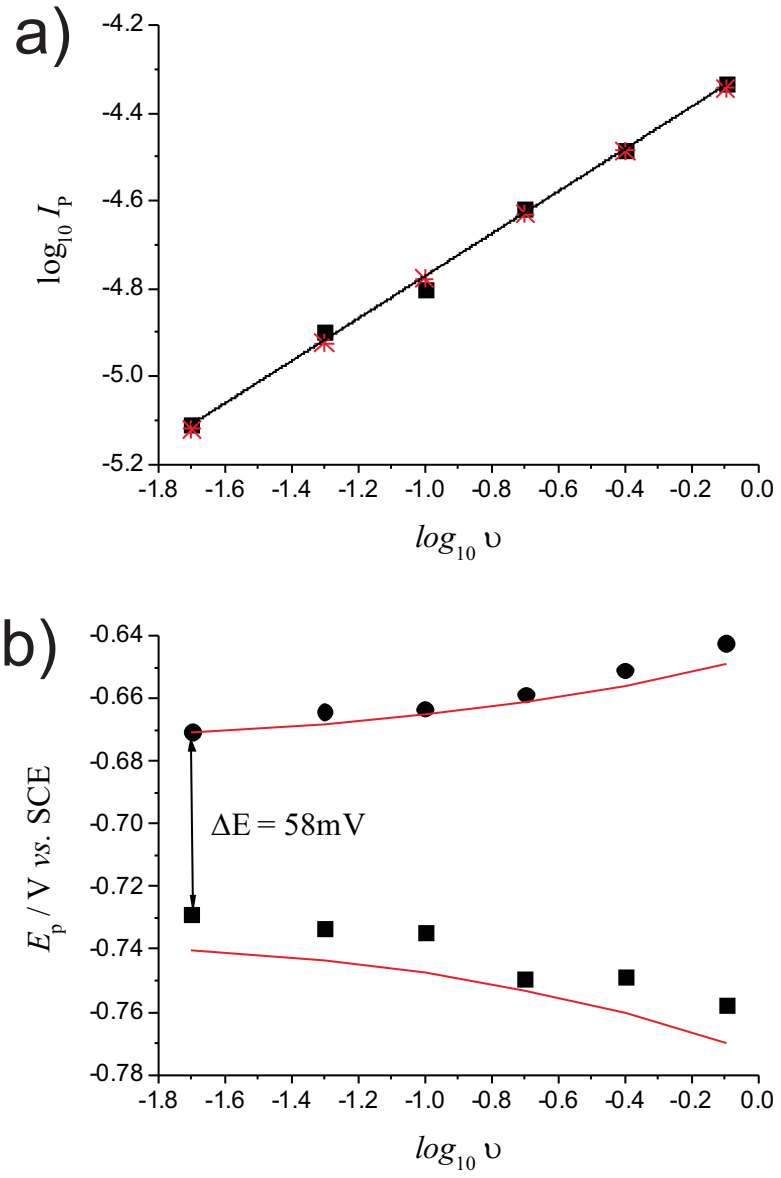

FIGURE 3.14: Comparison of 1 mM MV^{2+} experimental and simulated results: (a) plot of $\log_{10}$ of reductive peak current (I_p) against $\log_{10}$ of scan rate (ν). Both experimental (black) and simulated (red) data are shown. A line of best fit (black line) of the experimental data has a gradient of 0.48. (b) The variation of peak potentials (E_p) with $\log_{10}$ of scan rate. The experimental reductive (square) and oxidative (dot) peak potentials are compared with the simulated results (black lines).

The simulation was carried out using a commercial software package DIGISIM® based on Butler-Volmer kinetics. A simple one-electron reduction step was set up.

$$MV^{2+} + e^- \rightleftharpoons MV^{\bullet+} \tag{3.7}$$

The transfer coefficient, α, and the heterogeneous electron transfer rate (k_s) were set to be 0.5 and 10 cm s^{-1} respectively. Note that the rate of heterogeneous electron transfer was set at the reversible limit. The formal potential for the redox couple $MV^{2+}/MV^{\bullet+}$ ($E_{MV^{2+/\bullet+}}$) was approximated to be the mid-point potential, -0.7055 V *vs.* saturated calomel electrode (SCE). This value is in a good agreement with the reported $E_{MV^{2+/\bullet+}}$ ranged from -0.69 V to -0.73 V *vs.* SCE obtained by using glassy carbon and boron-doped diamond electrodes [55, 76, 77]. The diffusion coefficients of both MV^{2+} and $MV^{\bullet+}$ were assumed to be the same within the model.

By varying both $D_{MV^{2+}}$ and R (system resistance, a parameter contained in DIGISIM®), the fitted plots of $\log_{10} I_p$ and ΔE_p against $\log_{10} \nu$ are shown in Figure 3.14(a) and (b) respectively. The resulting $D_{MV^{2+}}$ was $(8.1 \pm 0.5) \times 10^{-6}$ cm^2 s^{-1}, which was close to the value that was calculated from the reversible Randles-Ševčík equation. Since the MV^{2+} redox responses demonstrated a near diffusional behaviour, so it is assumed that the influence of adsorption upon the catalytic response is *minimal*. Additionally, the simulated $D_{MV^{2+}}$ agrees with the previous literature reported values ranged from $(5.89 - 8.6) \times 10^{-6}$ cm^2 s^{-1} [76, 78–80]. System resistance, R of 600 Ω, was set to obtain the well fitted data. Therefore, both values of $D_{MV^{2+}}$ and R were utilised later in the simulation for MV^{2+} mediated O_2 reduction.

3.2.2.2 Methyl viologen mediated oxygen reduction

The kinetics of the direct reduction of O_2 is relatively slowed by the use of a BDD electrode. The BDD electrode has intrinsically low density of electronic states [41]. As a result, the electron transfer kinetics on the BDD surface is commonly far slower than those measured on for example gold or glassy carbon electrodes [75, 81, 82]. Depending on the level of boron dopancy, the degree of reversibility may be significantly tuned [81]. This decrease in the electron transfer rate is especially noticeable for an irreversible redox couple, such as the O_2 redox couple. An excessively high overpotential is required to drive an electrochemical reaction at a less doped electrode. Note that although there is a small irreversible wave at *ca.* -0.74 V *vs.* SCE (not shown) for the direct reduction of O_2 with a peak current of *ca.* 6 μA at 100 mV s^{-1}, by increasing the concentration ratio of $C_{MV^{2+}}/C_{O_2}$ the catalytic wave can be shifted away from it, as will be discussed later. Hence by controlling this concentration ratio to be relatively large the interference from the heterogeneous O_2 reduction to the catalytic peak can be minimised. To simplify the issue here, the direct O_2 reduction mechanism is excluded in the following discussion.

The voltammetric responses for the one-electron reduction of MV^{2+} are markedly different when the reaction solution involves oxygen. Figure 3.15 shows the cyclic voltammograms of increasing concentrations of MV^{2+} in air-equilibrated PBS at a scan rate of 100 mV s^{-1}. The concentration of O_2 in an air-equilibrated solution is constant with a value of (0.248 ± 0.002) mM [46]. In Figure 3.15 the concentration ratio of $C_{MV^{2+}}/C_{O_2}$ approximately increases according to values of 1/30, 1/3, 10/3, to 10 as shown from wave (a) to (d). When $C_{MV^{2+}}$ is significantly smaller than C_{O_2} (*i.e.* $C_{MV^{2+}}/C_{O_2} = 1/30$) only one irreversible catalytic peak is shown, *i.e.* wave

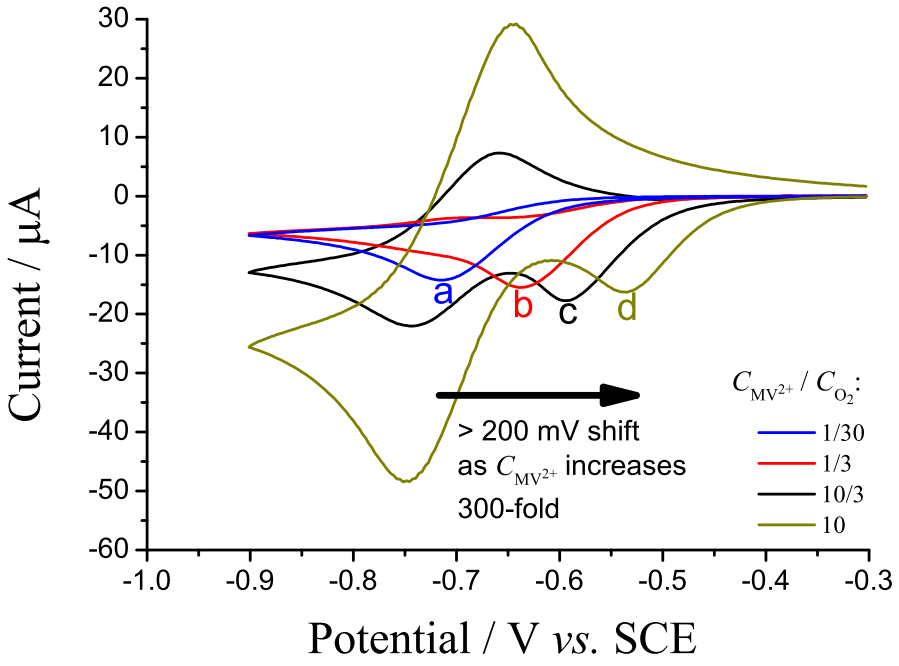

FIGURE 3.15: Comparison of cyclic voltammograms of different concentrations of MV^{2+} mediated O_2 reduction in air-equilibrated PBS (pH 6.7) under atmospheric pressure (C_{O_2} is 248 μM). The concentrations of MV^{2+} are (a) 8.263 μM, (b) 82.63μM, (c) 826.3 μM and (d) 2478.9 μM. The legend shows each corresponding concentration ratio. Scan rate = 100 mV s^{-1}.

(a). This voltammetric feature is attributed to the catalytic reduction of O_2 *via* the reduced MV^{2+} species. The following EC' catalytic mechanism is proposed:

$$MV^{2+} + e^- \rightleftharpoons MV^{\bullet+} \tag{3.8}$$

$$MV^{\bullet+} + O_2 \xrightarrow{k_{f9}} MV^{2+} + O_2^{\bullet-} \tag{3.9}$$

where $MV^{2+}/MV^{\bullet+}$ serves as the electrocatalyst for the reduction of O_2, and k_{f9} (dm^3 mol^{-1} s^{-1}) is the homogeneous rate constant of Reaction 3.9. The heterogeneous electron transfer process (Reaction 3.8) is assumed to be electrochemically reversible throughout. Instead of taking place at the electrode surface, electron transfer to O_2 occurs in solution *via* the reduced form of the electrocatalyst, $MV^{\bullet+}$,

generated at the electrode surface at a potential that is less reducing than the potential at which the direct reduction of O_2 occurs. The outcome of the catalysis shows an increased reductive wave, accompanied by a loss of reversibility.

As the concentration of MV^{2+} increases, as shown from wave (a) to (b), the catalytic peak potential ($E_{p,cat}$) shifts to the more positive potential. This positive shift takes place only when a tiny conversion of MV^{2+} to $MV^{\bullet+}$ is effective. In other words, due to the fast homogeneous kinetics, as soon as the radical cation ($MV^{\bullet+}$) is formed at the electrode interface, the catalytic process is so efficient to re-produce the MV^{2+} species. It is this homogeneous step and other possible follow-up electron transfer reactions and chemical reactions, such as superoxide ($O_2^{\bullet-}$) disproportionation and the protonation of ROS, which drive the equilibrium (Reaction 3.9) forward within the diffusion layer.

Figure 3.15 shows there is a gradual split of the reductive wave at the concentration ratio $C_{MV^{2+}}/C_{O_2}$ of 1/3 (depicted as wave(b)). The 'split wave' becomes more apparent at the concentration ratio of 10/3 and 10 (depicted as wave (c) and (d)). The first reductive wave shifts to more positive potentials with the increase of the $C_{MV^{2+}}/C_{O_2}$ ratio; whereas the second stays unperturbed. The peak potential shift from wave (c) to (d) was measured experimentally to be +55 mV. These 'split' voltammetric features can be related to a classically derived equation by Savéant [62]. The catalytic peak potential ($E_{p,cat}$) is described as,

$$E_{p,cat} = E^o_{MV^{2+/\bullet+}} - 0.409\frac{RT}{F} + \frac{RT}{F}\ln\left(\frac{RTk_{f9}}{F\nu}\frac{{C_{MV^{2+}}}^2}{C_{O_2}}\right) \tag{3.10}$$

where R is the gas constant, F is the Faraday constant, and T is the absolute temperature (K) in the bulk solution.

The equation is based on a Nernst diffusion layer model for the description of EC' processes, assuming the homogeneous electron transfer to be the rate determining step (Reaction 3.9). Under the experimental conditions in Figure 3.15, the only variable is the change of concentration of MV^{2+}, *i.e.* $\Delta C_{MV^{2+}}$. From Eqn. (3.10), it is predicted that the peak potential *versus* $\ln(\Delta C_{MV^{2+}})$ will shift with $+\frac{2RT}{F} \ln \Delta C_{MV^{2+}}$. Consequently, by increasing threefold of $C_{MV^{2+}}$, a +56 mV shift in $E_{p,cat}$ can be predicted for the 'split waves' from (c) to (d). This result shows an excellent agreement of the theoretical prediction with the experimental measurement. Moreover, a calculated value of k_{f9} from Eqn 3.10 was $(1.4 \pm 0.1) \times 10^5$ $dm^3\ mol^{-1}\ s^{-1}$, obtained from waves (c) and (d) taking into account $E_{MV^{2+/\bullet+}}$ of -0.7055 V.

The voltammetric feature of the 'split waves' can be rationalised as follows. As soon as the potential reaches a level where the electrochemical reduction of $MV^{2+/\bullet+}$ is kinetically viable, species O_2 will be rapidly consumed in the vicinity of the electrode. The consumption of O_2 is so rapid that the diffusion of O_2 from the bulk solution to the electrode interfacial surface becomes rate limiting. The $C_{MV^{2+}}$ is not perturbed dramatically from its bulk value. Therefore, the more positive reduction peak corresponds to the exhaustion of O_2 within the diffusion layer near the electrode surface. When the potential approaches $E_{MV^{2+/\bullet+}}$, the unreacted MV^{2+} within the diffusion layer gets heterogeneously reduced at the electrode surface [73, 83]. Voltammetrically, it can be seen while the first reductive wave shifts to the more positive potential whereas the second peak is unperturbed. In terms of peak current, the first peak is almost unaltered while the second seems increases proportionally to $C_{MV^{2+}}$. This is to say that the 'split waves' demonstrate 'total catalysis' process [62] where the peak current for the first wave is governed by the diffusion of molecular O_2.

There is a transition from 'partial catalysis' to 'total catalysis' as shown from waves (a) and (b) to (c) and (d), where Eqn. 3.10 describes the latter situation. However, this classic equation is too much of a simplification, evidenced by its underestimated rate of reaction. There are often a large variety of follow-up homogeneous reactions and chemical reactions according to the nature of the homogeneous electron transfer step (Reaction 3.9) [62]. For example additional reaction pathway for $MV^{\bullet+}$ species, follow-up reactions of superoxide ($O_2^{\bullet-}$), and protonation reactions. Therefore, the classic analysis is insufficient to deconvolute the rates of these catalysis steps. Consequently, the use of DIGISIM® simulation becomes one way to circumvent this issue by embedding the follow-up homogeneous reactions and the protonation steps. All of the following simulation is based upon or near 'total catalysis' situation. As such the results can be compared with those predicted from the classic equation (Eqn. 3.10). More importantly, the interference from heterogeneous O_2 reduction can be avoided in the potential region where the 'total catalysis' takes place. Subsequently, the simulation model can be significantly simplified.

The simulation was in part based upon the one-electron redox of MV^{2+} provided in the previous section. The heterogeneous electron transfer step was set to be electrochemically reversible. The homogeneous catalytic pathways taken include a full consideration of the possible reaction pathways of $O_2^{\bullet-}$ species. Modelling of the EC' catalytic mechanism was based upon Reaction 3.8 and Reaction 3.9, and the following mechanistic steps:

$$MV^{\bullet+} + O_2^{\bullet-} + 2H^+ \xrightarrow{k_{f11}} MV^{2+} + H_2O_2 \tag{3.11}$$

$$2O_2^{\bullet-} + 2H^+ \xrightarrow{k_{f12}} O_2 + H_2O_2 \tag{3.12}$$

where k_{f11} and k_{f12} are the homogeneous rate constants of the radical reactions (Reaction 3.11) and disproportionation reaction (Reaction 3.12). At the studied pH (6.7 buffer solution) $O_2^{\bullet-}$ exists as the major species due to the low pK_a value of $HO_2^{\bullet}$ (hydroperoxy radical, pK_a 4.8) [45].

The reaction pathway of the radical cation $MV^{\bullet+}$ with formed hydrogen peroxide (H_2O_2) is not included though a rate of 2.3 $\times$ 10^3 dm^3 mol^{-1} s^{-1} was reported previously [66]. It can be argued that a very low concentration ratio of $C_{MV^{2+}}/C_{O_2}$ exists in the studied reaction solution so that reaction with H_2O_2 is much less important [58, 59].

Additionally, the MV^{2+} reduction demonstrated a near pure diffusional process, as described in the previous section. Hence, the adsorption of MV^{2+} was assumed to be *minimal* and not considered within the model. All protonations were assumed to be at equilibrium. Parameters used in the simulation, such as $D_{MV^{2+}}$, R, D_{O_2}, solubility of O_2 and C_{O_2} in air-equilibrated PBS, were tabulated in Table 3.2. All oxygen related species were assumed to have the same diffusion coefficient as molecular oxygen. The reactions shown in Table 3.2 for the O_2 species were used in part as the basis for thermodynamic calculations. Taking into account the $E_{MV^{2+/\bullet+}}$ of -0.7055 V, the equilibrium constants (K_{eq}), can be calculated from the standard Gibbs energy, $\Delta G^{\ominus} = -RT/\ln K_{eq}$ and $\Delta G^{\ominus} = -nFE^o$, and the resulting K_{eq} values are tabulated in Table 3.3 at pH of 6.7.

Utilising the mechanisms above, the voltammetric waveshape fitting was possible to obtain a high level of agreement between the experimental and simulated results. The simulated rate constants for the homogeneous solution electron transfer steps, k_{f9}, k_{f11}, and k_{f12} are listed in Table 3.3. The resulted values are in excellent agreement with literature reported ones (also tabulated in Table 3.3). Both the

simulated and literature reported values of k_{f9} are in large contrast with that calculated from the classic equation derived value of (1.4 ± 0.1) $\times 10^5$ dm^3 mol^{-1} s^{-1}. The oversimplified mechanism used in Eqn. 3.10 contributes mainly to this underestimated rate of reaction,where only the first homogeneous electron transfer step is considered.

Parameters	Values	Ref.
$O_2 + e^- \rightleftharpoons O_2^{\bullet -}$	$E_1 = -0.4212$ V	Ref.45
$O_2^{\bullet -} + e^- + 2H^+ \rightleftharpoons H_2O_2$	$E_2 = +0.705$ V	Ref. 45
$D_{MV^{2+}}$ ($\times 10^{-6}$ cm^2 s^{-1})	8.1 ± 0.5	Section 3.2.2.1
R_u (Ω)	600	Section 3.2.2.1
D_{O_2} ($\times 10^{-6}$ cm^2 s^{-1})	19.6 ± 0.6	Ref. 47
Solubility of O_2 in PBS (mM)	1.24 ± 0.06	Ref. 46
$C_{MV^{2+}}$ in air-equilibrated PBS (mM)	0.248 ± 0.002	Ref. 46

TABLE 3.2: Parameters used in the EC' catalysis model. All data are corrected against a SCE reference electrode at (298 ± 0.2) K in a 0.1 M KCl supported pH 6.7 PBS under atmospheric pressure.

Reactions	Calculated K_{eq} (unitless)	Simulated k_f (dm^3 mol^{-1} s^{-1})	Literature reported k_f (dm^3 mol^{-1} s^{-1})	Ref.
(3.9)	6.7×10^4	6×10^9	$(4-9) \times 10^8$	Ref. 64, 65
(3.11)	6.9×10^{23}	6.5×10^8	6.5×10^8	Ref. 64
(3.12)	2.9×10^{18}	1.3×10^6	$(1.0-1.3) \times 10^6$	Ref.64, 84

TABLE 3.3: Calculated equilibrium constants (K_{eq}) and simulated rates of reactions (k_f) in comparison with their literature reported values in 0.1 M KCl supported pH 6.7 PBS. The standard state is taken to be 1 mol dm^{-3}.

Utilising all the parameters above, Figure 3.16 depicts the comparison of fitted voltammetric responses with their experimental data for different concentration ratios of $C_{MV^{2+}}/C_{O_2}$ at 800mV s^{-1}. Figure 3.16(a) and (c) shows a tripled $C_{MV^{2+}}$ in an air-equilibrated PBS solution (with concentration ratios of $C_{MV^{2+}}/C_{O_2}$ of

10/3 and 10 respectively). Figure 3.16(b) has the same $C_{MV^{2+}}$ as (a) but is the response in an O_2-saturated solution (equivalent to a concentration ratio of 2/3). To scrutinize the comparison of experimental and simulated data, plots of $E_{p,cat}$, $I_{p,MV^{2+}}$, and $I_{p,cat}$, as a function of either $\log_{10}\nu$ or the square root of the scan rate are depicted in Figure 3.17. General and good agreement of the simulated data with the experimental results is shown within the experimental error bars, without any systematic error.

In Figure 3.17(a), it can be seen that at all scan rates the catalytic peak potentials are shifted to the more positive potentials as the concentration ratio of $C_{MV^{2+}}/C_{O_2}$ increases from 2/3, 10/3 to 10. There is almost a parallel increase (*ca.* +56 mV shift) at all scan rates from the ratio of 10/3 to 10, as expected in the 'total catalysis' situation. However, an obvious distortion of $E_{p,cat}$ for the ratio of 2/3 at higher ν is shown. Such a feature is likely related to the increased solution resistance. At all concentration ratios, the overall $E_{p,cat}$ trend can be seen to increase with decrease of scan rates. It can be rationalised that at slower scan rates the diffusional layer thickness becomes greater as the experimental timescale becomes longer. Therefore more efficient O_2 flux is expected in the vicinity to the electrode surface, and consequently O_2 can be depleted at more positive potentials.

Figure 3.17(b) shows an excellent correlation of the MV^{2+} reductive peak current ($I_{p,MV^{2+}}$), *i.e.* the second reductive peak, at all scan rates for both experimental and simulated results. There are two further points to note. First, the Randles-Ševčík equation for reversible electron transfer predicts the slope of peak current against square root of scan rate to be linearly proportional to bulk concentrations (Eqn. 3.6). However, by tripling the amount of $C_{MV^{2+}}$ the slope obtained from the plot of experimental data for a concentration ratio of 10 is only just above twice as much as that for the ratio of 10/3. It potentially suggests that the uncompensated

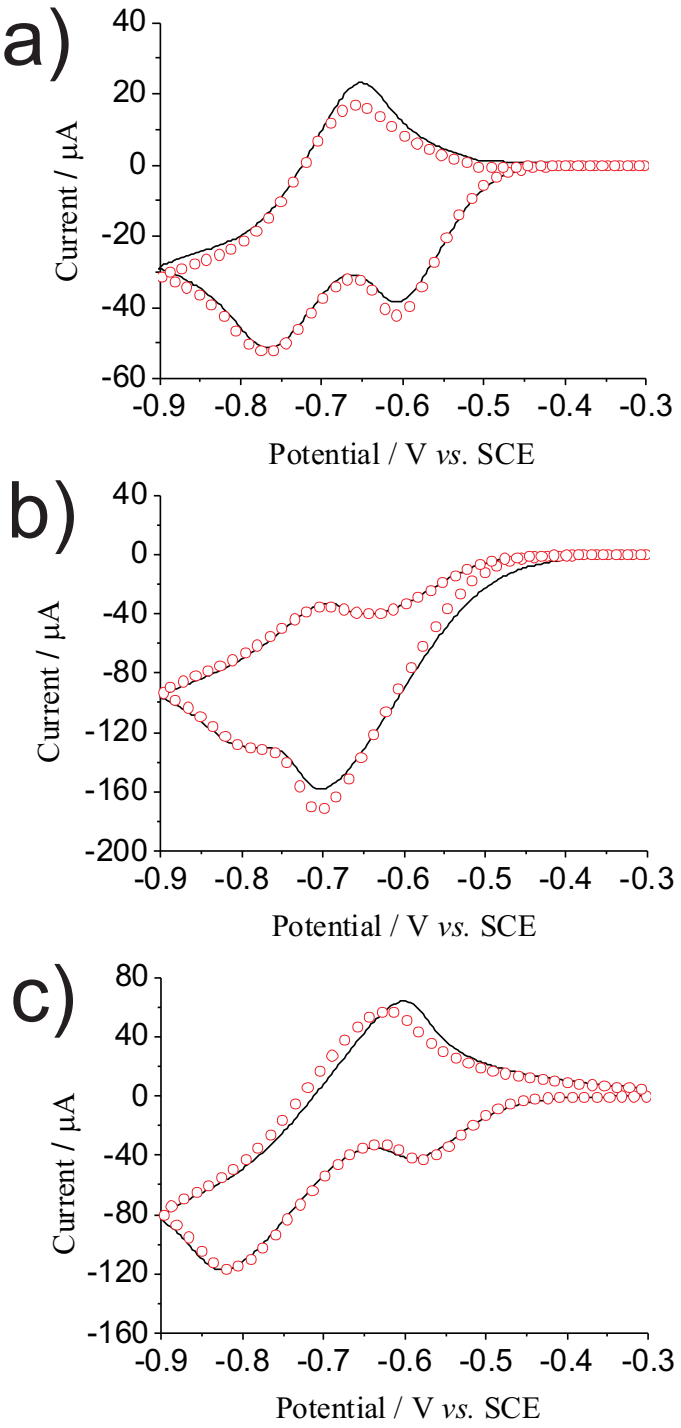

FIGURE 3.16: Cyclic voltammograms of MV^{2+} mediated O_2 reduction in pH 6.7 PBS at different concentration ratios of $C_{MV^{2+}}/C_{O_2}$: (a) 10/3, (b) 2/3, and (c) 10 under atmospheric pressure. (a) and (c) were under air-equilibration; (b) was saturated with O_2. Solid lines are experimental data, and circled lines are simulated voltammograms. Scan rate = 800 mV s^{-1}.

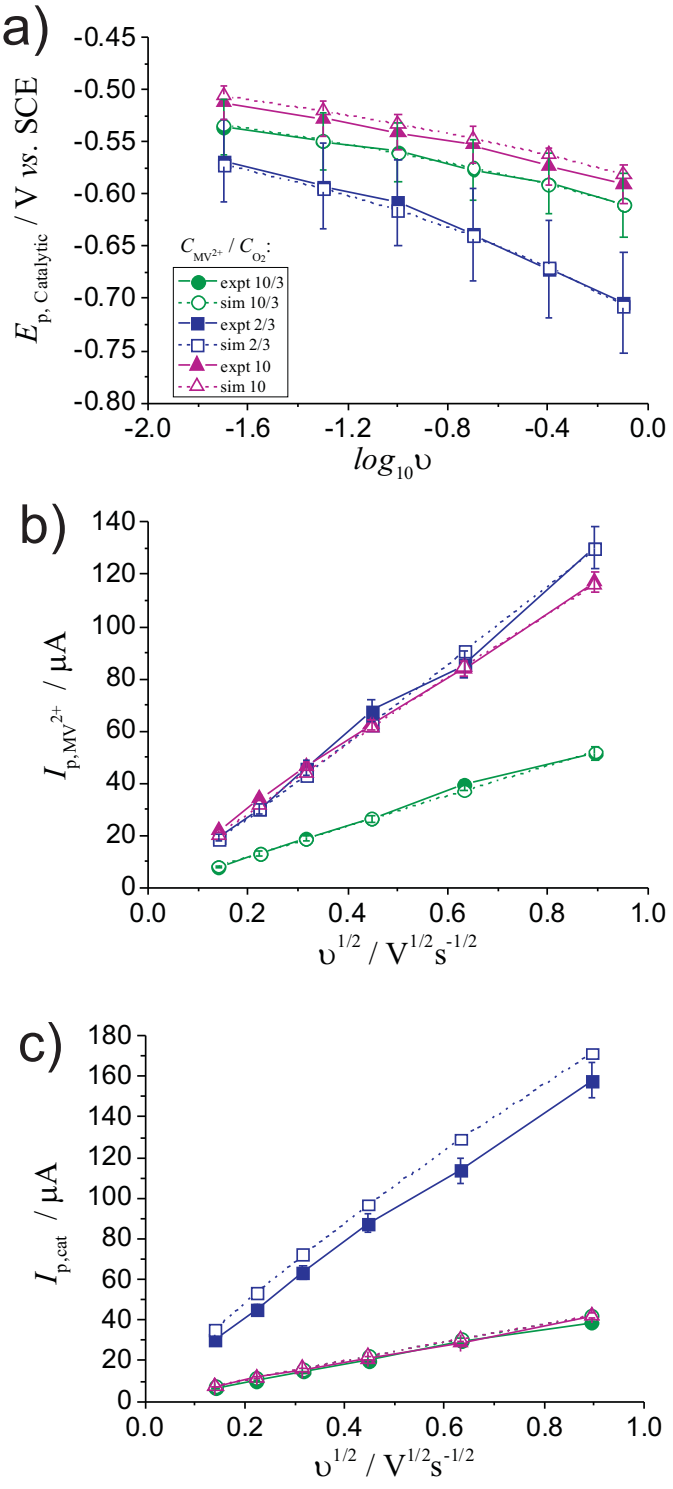

FIGURE 3.17: Comparison of experimental (filled scatter lines with error bars) and simulated (empty scatter lines) data: (a) catalytic peak potential against $\log_{10}\nu$, (b) diffusional MV^{2+} peak current against square root of ν, and (c) catalytic peak current against square root of ν. The depicted scatters represent: (green) 826.3 μM MV^{2+} and air-equilibrated solution (248 μM), (blue) 826.3 μM MV^{2+} and O_2-saturated solution (1240 μM), and (magenta) 2478.9 μM MV^{2+} and air-equilibrated solution. The error bars are obtained by reproducing the cyclic voltammetric measurements at least eight times.

solution resistance is likely to contribute to the factor difference compared with that would be predicted from the reversible Randles-Ševčík equation. Secondly, the $I_{p,MV^{2+}}$ for the concentration ratio of 2/3 and 10/3 should be expected to be the same as the $C_{\mathrm{MV^{2+}}}$ are the same in both cases. However, the $I_{p,MV^{2+}}$ for the ratio of 2/3 at all scan rates are higher. This outcome is attributed to the interference from the catalytic diffusional tail current onto the MV^{2+} diffusional only reductive peak currents. The accidental overlap of slopes for ratios 2/3 and 10 should not be confused here.

Figure 3.17(c) shows an excellent correlation in the catalytic peak current ($I_{p,cat}$), *i.e.* the first reductive peak, of the ratio of 10/3 and 10 (air-equilibrated solutions). Under both conditions, 'total catalysis' takes place at where the first reduction wave is limited by the diffusion of O_2, viz. the peak current is dependent only on the diffusion and the amount of O_2 present in the bulk solution. Hence, under the 'total catalysis' situation of exact same $C_{\mathrm{O_2}}$ the catalytic peak currents are the same regardless of $C_{\mathrm{MV^{2+}}}$. As the $C_{\mathrm{O_2}}$ increases to O_2-saturated solution ($C_{\mathrm{MV^{2+}}}/C_{\mathrm{O_2}}$ ratio of 2/3), the $I_{p,cat}$ increases dramatically at all scan rates. However, a rather poor fitting with the experimental data potentially suggests that the direct O_2 reduction contribution to the peak current can no longer be discarded.

3.2.2.3 Mediation at Various pH

The above model was further examined to investigate the pH dependency upon catalysis. It is of significance to study the influence of protonation processes upon the electrocatalytic rates of reactions. On the other hand, the above model may be self-justified.

pH	Calculated K_{eq} of Reaction (3.13) (unitless)	Calculated K_{eq} of Reaction (3.12) (unitless)	Calculated E_f of Reaction (3.11) (V *vs.* SCE)
8.5	4169	2.9×10^{15}	+0.493
6.5	41.69	2.8×10^{19}	+0.729
4.5	0.4169	2.9×10^{23}	+0.966
2.5	4.2×10^{-3}	2.7×10^{27}	+1.201
pH	$E_{p,cat}$ (experimental results) (V *vs.* SCE)	$E_{p,cat}$ (simulated results) (V *vs.* SCE)	k_{f12} for Reaction (3.12) (simulated results) (dm^3 mol^{-1} s^{-1})
8.5	−0.600	−0.605	1.25×10^6
6.5	−0.606	−0.605	1.25×10^6
4.5	−0.603	−0.598	4×10^7
2.5	−0.601	−0.593	1.1×10^{11}

TABLE 3.4: Thermodynamic and kinetic parameters involved in the study of the pH-dependent model in a 0.1 M KCl supported PBS at 800 mV s^{-1} (298 ± 0.2) K under atmospheric pressure.

All mechanistic steps are kept the same, except an extra chemical equilibrium reaction is added:

$$\mathrm{HS} \overset{K_{eq}}{\rightleftharpoons} \mathrm{S} \tag{3.13}$$

$$\text{where} \quad K_{eq} = \frac{K_a}{C_{\mathrm{H^+}}}$$

where S is the deprotonated form of superoxide ($O_2^{\bullet -}$), HS is the protonated form ($HO_2^{\bullet}$), and K_a is the acid dissociation constant for the species $HO_2^{\bullet}$ (pK_a 4.8) [45]. Realistic rate constant for the protonation must be used within the simulation. As such, a value of 1×10^{10} dm^3 mol^{-1} s^{-1} is set for protons to be at the diffusion limited regime [85]. Under the operation of equilibrium Reaction 3.13, it is expected that the rate constants for both homogeneous electron transfers of Reaction 3.11 and Reaction 3.12 should be dependent upon the proton concentrations.

The model was then optimized to give the best fit by considering both the catalytic

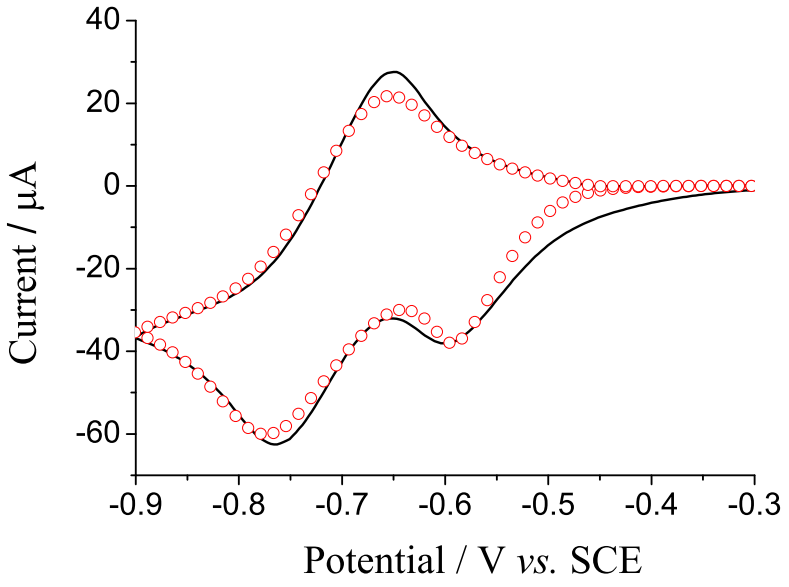

FIGURE 3.18: Comparison of experimental (line) and simulated (circle) cyclic voltammograms of 1 mM MV^{2+} mediated O_2 (air) reduction in pH 2.5 PBS. Concentration ratio of $C_{MV^{2+}}/C_{O_2}$ is 10/3, scan rate = 800mV s^{-1}.

peak current and potential. It was realized that the change of k_{f11} is almost insensitive to the change of proton concentration. However, the rate constant of Reaction 3.12 appears to be dominant upon change of pH.

Hence, by variation of the value of k_{f12} and the corresponding thermodynamic paramters and keeping all other parameters the same, a good correlation of experimental and simulated voltammetric waveshapes can be achieved at pH values ranged from 2.5 to 8.5. Table 3.4 gives the optimized values for the potentials and rate constants of Reaction 3.12; together also tabulated the calculated thermodynamic parameters with the corresponding pH. Take a representative example, Figure 3.18 shows an overlap of a simulated voltammogram onto an experimental one at the pH of 2.5. It can be seen that the simulation model works well after embedding the variation of protonation reaction. A general good agreement between the experimental and simulated catalytic peak potentials and peak current is shown in both Figure 3.18 and Table 3.4. Interestingly, the catalytic peak

potentials across six pH units appear to be insensitive upon the change of pH of the local environment. It can be attributed mainly to the extremely fast rate constant of Reaction 3.9, k_{f9}, (or irreversible reaction) which acts as the major kinetic control in the overall catalysis.

3.2.3 Conclusions

This section has voltammetrically studied the methyl viologen mediated reduction of oxygen in aqueous solutions of varied pH. Such a study has been facilitated by the use of a boron-doped diamond electrode allowing the mediated and direct oxygen reduction pathways to be clearly delineated. Through the use of simulation software the electrocatalytic oxygen reduction mechanism has been fully modelled. The homogeneous one-electron reduction of oxygen to superoxide, by the mono-reduced form of methyl viologen, is found to have an associated rate constant of 6×10^9 dm^3 mol^{-1} s^{-1}.

Importantly, it has been demonstrated how, if classical type analysis is used, over-simplification of the homogeneous reactions results in an underestimation of the associated electron transfer rate. These studies were extended further by considering the variation in the catalytic reduction as a function of pH, where it was found that the voltammetric response was relatively insensitive to the environment. This result likely reflects the high rate of electron transfer associated with the one-electron homogenous reduction of oxygen.

In this chapter, the study of kinetics, thermodynamics, and mass transport of two electrocatalytic mediators have been achieved. Exceptionally high reactivities of

semiquinone intermediate species and methyl viologen radical cations have been obtained through simulation of distinctive voltammetric features associated with the mediated oxygen reduction responses, *i.e.* 'reverse' peak and 'split waves'. In the case when the redox mediator involves multi-electron transfers, the subsequent electron transfers after the first one is *not* highly driven. The consequence is that no 'split waves' response can be observed in the AQMS mediated oxygen reduction upon change of concentration ratios. Thereafter, the rate limiting step is the reduction/oxidation of the AQMS species rather than the bimolecular reaction in this complex process.

The search for optimal oxygen reduction catalysts can be seen to be dependent on the reactive intermediate being formed over a wide potential window. Such a point shall be extended in the next chapter, where a change of ionic environment will show an effect towards the reactivity of intermediate species.

Chapter 4

Electrolyte tuning effect on intermediate reactivity towards oxygen reduction

This chapter investigates the reactivity of an active intermediate species on change of ionic environment in aqueous solution of high pH. In particular semiquinone species are carried out. The change of reactivity consequently influences the electrocatalytic reduction of oxygen. Through the use of simulation software the relevant electrode potentials can be fully deconvoluted; this provides fundamental understanding of thermodynamics of the multi-electron transfer process of the quinone/oxygen reaction. The work presented herein was published in the article '*Chem. Commun. 2011, 47, 11426-11428*'.

4.1 Introduction

Anthraquinone derivatives (AQ) are particularly interesting to study in part due to their ability to mediate oxygen reduction [86]. Such a catalytic process is encountered in a number of fields, including biological systems [87] and industrial-scaled chemical synthesis [88], as mentioned in the previous chapter. Therefore,

understanding electron transfer processes associated with quinone redox centres is an important task.

The reduction of anthraquinone-2-monosulfonic acid sodium salt (or anthraquinone monosulfonate, abbreviated as AQMS) at high pH (above $\sim$ 12) in aqueous solutions or aprotic solvents involves two sequential electron transfer steps:

$$\mathrm{AQMS} + \mathrm{e}^- \rightleftharpoons \mathrm{AQMS}^{\bullet -} \qquad E_1 \tag{4.1}$$

$$\mathrm{AQMS}^{\bullet -} + \mathrm{e}^- \rightleftharpoons \mathrm{AQMS}^{2-} \qquad E_2 \tag{4.2}$$

where E_1 and E_2 are the formal potentials of the first and second electron transfers. The separation between these two potentials, $\Delta E = E_2 - E_1$, determines whether one or two pairs of redox waves may be observed [62]. It is widely accepted that the solvent has a great effect on the electrochemical response of a redox species. For example, the hydration effect has recently been proposed to be responsible for at least a +300 mV shift in the electrochemical reduction potential of iron-sulphur cluster proteins in ferrodoxin reactive sites [51]. The voltammetric responses of AQ vary significantly between protic and aprotic media. In protic solvents, the electrochemical redox process of the quinone centre may be described through the use of a 'scheme of squares' model (mechanistic pathways refer to Figure 3.2), as proposed by Jacq in 1971 [39]. Under fully buffered pH solutions, a single $2e^-$ reductive wave is commonly observed. Such a voltammetric feature can be referred to both Figure 3.3(a) (**ECEC** mechanistic pathway) and Figure 4.1 (**EE** mechanistic pathway). Recent work by Costentin *et al.* discussed the importance of concerted proton-electron transfer mechanisms within a number of electrochemical systems [89, 90]. Nevertheless, under conditions of limited buffering in protic solvent it is possible to observe two reduction waves, where the wave at the more

negative potential is a result of a change in local pH caused by the consumption of protons in close proximity to the electrode surface [91]. In contrast, two $1e^-$ reductive waves are obtained in aprotic solvents *via* **EE** mechanistic pathway [92] (refer to Chapter 5). This difference in voltammetric responses between the two solvent systems is primarily due to hydrogen bonding [93]. In aprotic solvents, it is recognised that a number of other factors can also govern the relative positions of E_1 and E_2, for instance ion pairing, nonspecific solvation, and molecular structures *etc.* [92]. However, the importance of the supporting electrolyte in an aqueous solution has hitherto been largely overlooked.

This chapter demonstrates the significant importance of supporting electrolyte in 'tuning' electrode potentials of the AQ redox centre in aqueous solution; consequently, 'tuning' the intermediate reactivity towards oxygen reduction. The manipulation can be achieved *via* stabilisation of the semiquinone intermediate species due to ion pairing with the supporting electrolyte cation, which is proved through the reduced activity of the semiquinone intermediate towards the catalytic reduction of oxygen. This work provides fundamental insights into the electrochemistry of quinones in aqueous media.

4.2 Results and discussion

The influence of supporting electrolyte upon reduction of anthraquinone-2-sulfonate (AQMS) in aqueous media is here investigated. The electrochemical reduction of AQMS was carried out in a fully supported (0.1 M electrolyte) and oxygen-free aqueous solution on a gold (Au) electrode (r_e of 0.09 cm). The electrode potential was measured against a saturated calomel electrode (SCE). This work was performed at high pH (pH 12.9) to ensure a simple **EE** mechanism with no coupled

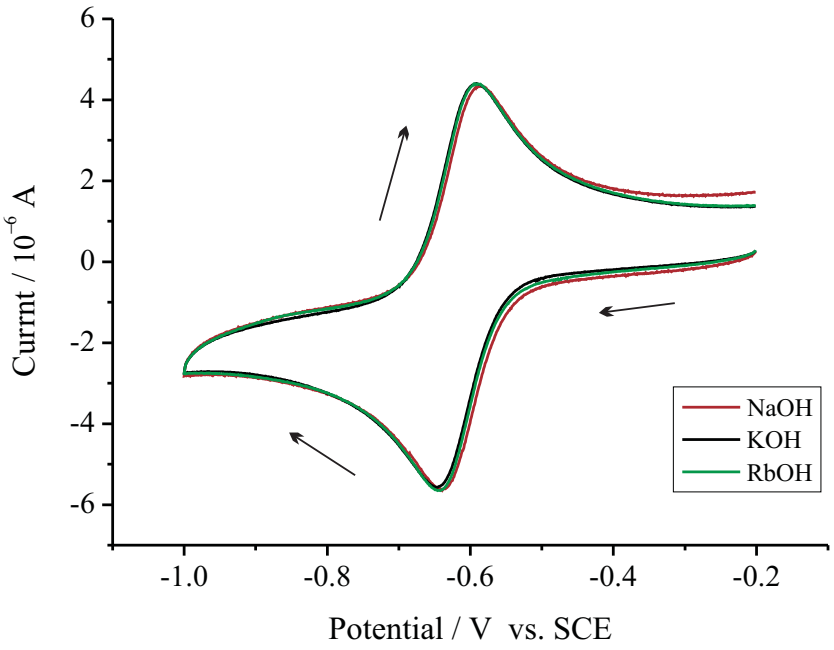

FIGURE 4.1: Cyclic voltammograms of 500 μM AQMS/ H_2O supported with various alkali metal cations of increasing size from Na^+, K^+ to Rb^+ at 100 mV s^{-1} on a Au electrode.

protonations [40]. Alkali metal cations are most commonly used as part of the buffering media and/or as supporting electrolyte. Figure 4.1 depicts the AQMS redox signals in aqueous solutions supported with various alkali metal cations (ionic strength = 0.1 M) on the Au electrode. In the presence of 0.1 M alkali hydroxide ranging from sodium (Na^+) to rubidium (Rb^+) cations, a single reductive wave was measured at -0.65 V, corresponding to the $2e^-$ reduction of AQMS [40]. Upon increasing the electrolyte cation sizes from Na^+ to Rb^+ (less commonly used as the supporting electrolyte/buffer cation), the voltammetric signals demonstrate *no* significant differences in the resulted AQMS redox waves. This likely suggests that the alkali metal cations have an insignificant degree of ion-paring with either the parent or the reduced AQMS species. Consequently a single $2e^-$ reduction wave was obtained. The formal potential of the reaction, E_f, is approximated as

the mid-point potential, and occurs at (-0.62 ± 0.005) V (298 ± 2) K for all three reaction systems. Hence, the alkali metal cations do not significantly influence the AQMS redox system in aqueous solution.

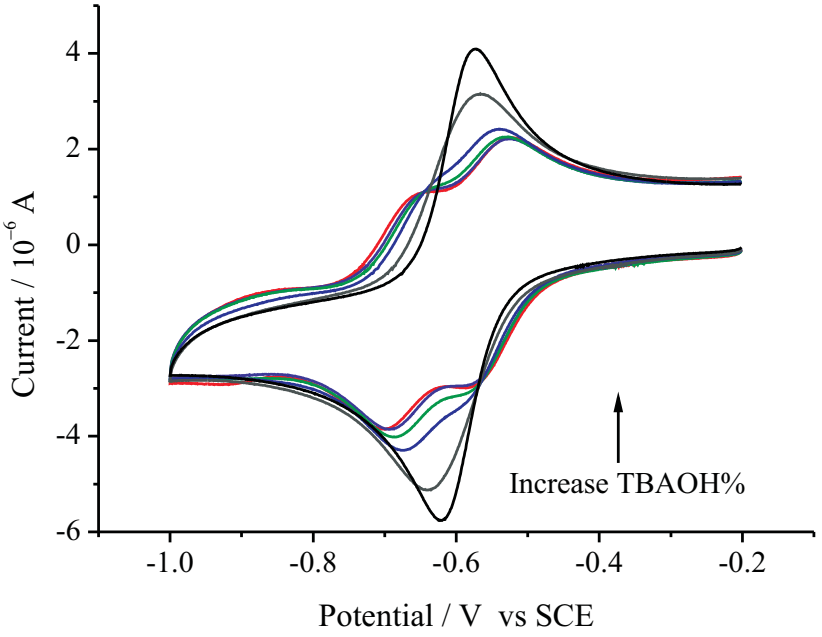

FIGURE 4.2: Cyclic voltammograms of 500 μM AQ/ H_2O supported with $(C_{(\mathrm{TMAOH})} + C_{(\mathrm{TBAOH})}) = 0.1$ M at 100 mV s^{-1} on a Au electrode. The proportion of TMAOH decreases from 100, 80, 40, 20, 10 to 0%.

In comparison, the situation is likely to change when the size of the electrolyte counter ions increases further. Commonly, tetraalkylammonium cations are widely used in aprotic solvents due to the negligible degree of ion pairing [94]. The following section studies the influence of these organic cations in aqueous solution upon the change of electrode potentials. A 500 μM AQMS aqueous solution supported with varying proportion of the tetra-n-butylammonium hydroxide (TBAOH) and tetra-methylammonium hydroxide (TMAOH) was investigated. The total concentration of TBAOH ($C_{(\mathrm{TBAOH})}$) and TMAOH ($C_{(\mathrm{TMAOH})}$) adds up as 0.1 M, *i.e.*

constant ionic strength. The cyclic voltammetric responses in Figure 4.2 demonstrate a trend of splitting one wave into two when the proportion of TBAOH increases from 0 to 100%. In the presence of 100% TMAOH, the relatively small ΔE results in a single $2e^-$ reduction wave. While keeping the pH environment and ionic strength unchanged, the increased proportion of TBA^+ cations gradually causes E_1 and E_2 to separate; consequently resulting in two resolvable $1e^-$ reduction waves. Furthermore, depending on the length of the alkyl chain, $TMA^+ < TEA^+ < TBA^+$, the voltammograms vary from one $2e^-$ wave to two $1e^-$ waves with gradual peak broadening, *i.e.* larger values of ΔE, shown in Figure 4.3.

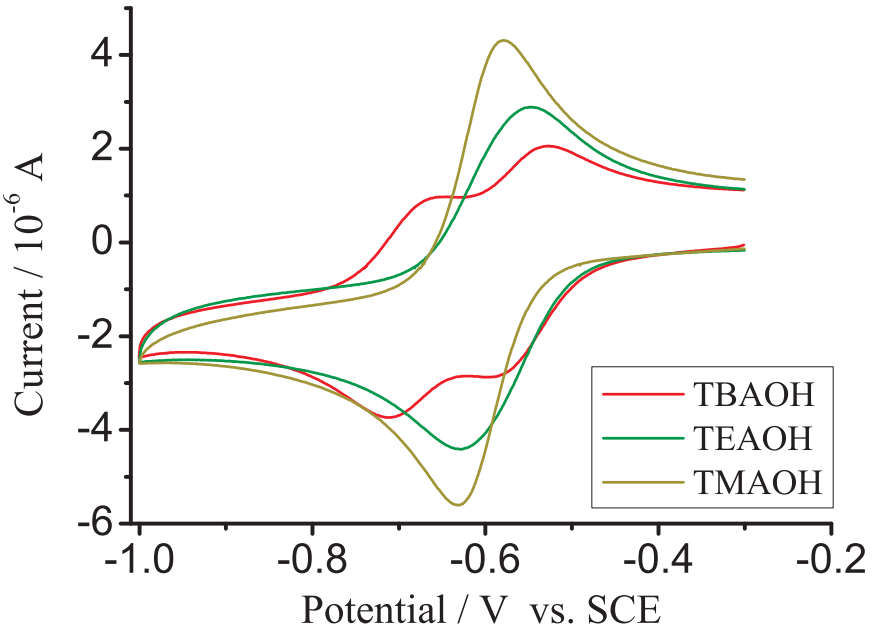

FIGURE 4.3: Cyclic voltammograms of 500 μM AQMS/ H_2O supported by 0.1 M tetraalkylammonium hydroxide salts with increasing alkyl chain from methyl-, ethyl- to n-butyl- groups at 100 mV s^{-1} on a Au electrode.

The voltammetric signals of the AQMS redox centre can be characterized *via* variation of scan rate over a range of $20 - 800$ mV s^{-1} on the Au electrode. Figure 4.4 depicts the AQMS voltammetric responses in aqueous solutions supported with 0.1 M (a) TMAOH and (b) TBAOH respectively. It is obvious to see that

the formal potentials of the first and second electron transfers are independent with scan rate variation. This is characteristic of an **EE** mechanistic reaction [6].

In addition, the reductive peak current was plotted against the square root of scan rate for the TMAOH supported reaction solution system. As shown in Figure 4.4(a), a linear relationship was obtained ($R^2 = 0.9997$). From the Randles-Ševčík equation, Eqn 4.3, for a reversible n electron diffusional process, it was possible to obtain an *apparent* diffusion coefficient, D_o, from the gradient of the line [1].

$$I_p = (2.69 \times 10^5) n^{1.5} A D_o^{0.5} C_o \nu^{0.5} \tag{4.3}$$

The symbols have been defined previously. The gradient obtained was 1.7×10^{-5} A (V s$-1)^{-0.5}$, and consequently the *apparent* D_o was calculated as 4.8×10^{-6} cm^2 s^{-1}. This value is in contrast to the one obtained *via* a micro-Au electrode (5.3×10^{-6} cm^2 s-1), as shown later (Table 4.1). The underestimation caused by applying Randles-Ševčík equation is due to the assumption of concerted two-electron transfers, *i.e.* the second electron transfer is sufficiently driven. Nevertheless, consecutive electron transfer steps are commonly encountered for organic molecules where the second electron transfer is *not* sufficiently driven [95].

In order to elucidate how E_1 and E_2 have changed with respect to the increasing proportion of TBAOH, the electrochemical system was modelled through the use of the commercially available software package DIGISIM®. Procedures were similar to those described in the previous chapter, except only a simple two-electron redox system (**EE**) was set up. Within this chapter, the electrochemical systems involve no protonation equilibrium due to high pH environment (above $\sim$ 12) [40]. All electron transfer rates were 10 cm s^{-1}, representing fast heterogeneous electron

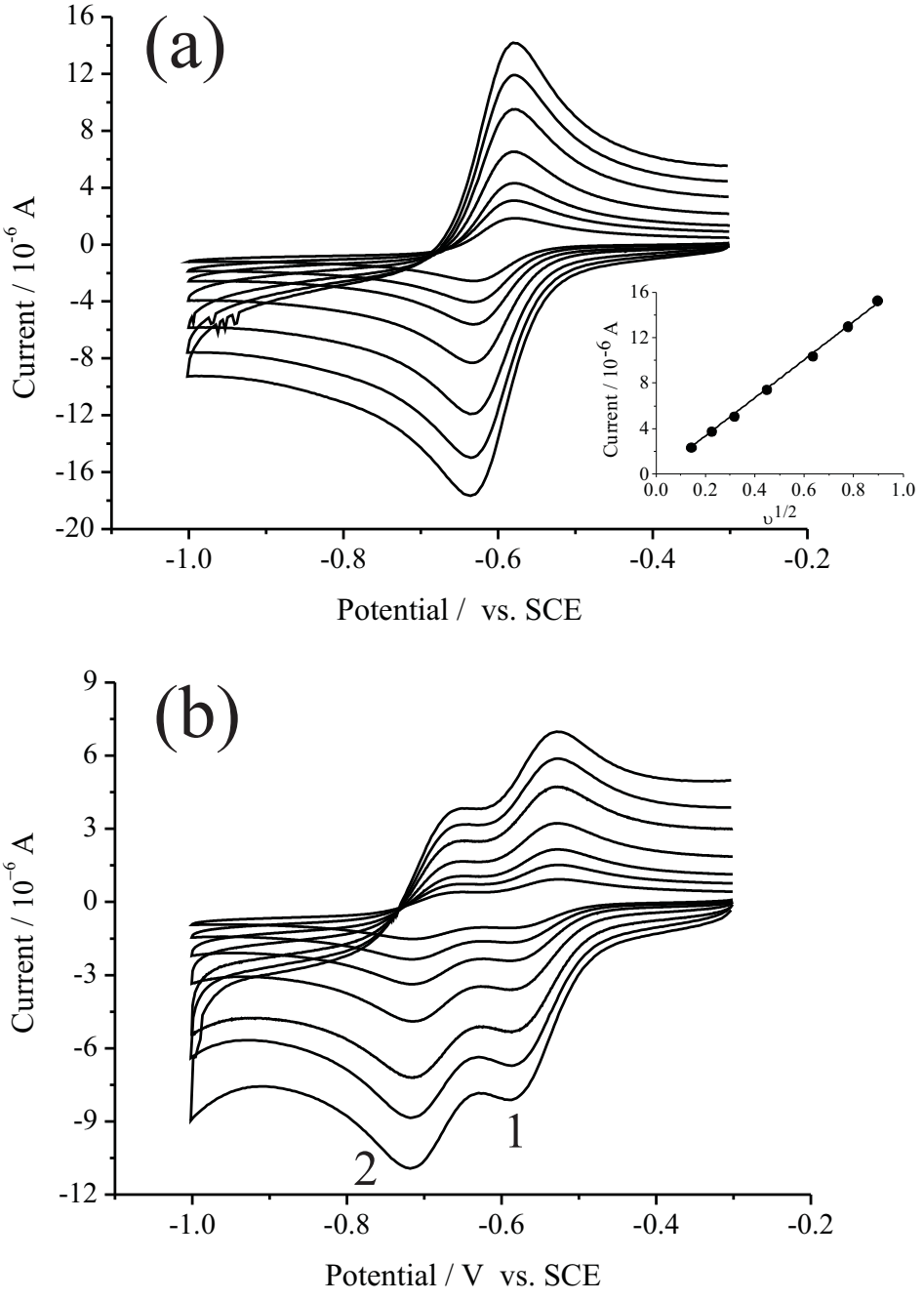

FIGURE 4.4: Variable scans of AQMS redox signals in aqueous solutions supported with 0.1 M (a) TMAOH and (b) TBAOH electrolyte at $20 - 800$ mV s^{-1} on a Au electrode. The inset is a plot of reductive peak current against square root of scan rate (ν) ($R^2 = 0.9997$).

transfer processes. The transfer coefficient, α, is 0.5 in all simulations, which assumes that the first electron transfer is the rate determining step.

In order to obtain the diffusion coefficients of AQMS and fit them in simulations, they were experimentally measured in solutions supported by various sizes of electrolyte cations. The more accurate diffusion coefficients were measured by using a micro-electrode. Such a method is not affected by the associated electron transfer kinetics or separation between two redox potentials, since a true limiting current is measured rather than a peak current (compared to the result obtained earlier by using Randles-Ševčík equation). Accordingly, the limiting current is controlled by the diffusion of AQMS and at sufficiently negative potentials is a full two-electron process.

A gold microdisc electrode was pre-calibrated *via* chronoamperometry (refer to Section 2.3). Then the calibrated electrode was scanned by using cyclic voltammetry at 10 mV s^{-1} in a 500 μM AQMS aqueous solution supported by 0.1 M hydroxide salt with various electrolyte cation sizes. A steady-state current, I_{ss}, at a microdisc electrode was obtained, described in Equation 4.4 [6].

$$I_{ss} = 4nFD_iC_ir_e \tag{4.4}$$

where parameters have been defined previously. The experimentally obtained steady-state currents and their calculated diffusion coefficients were recorded in Table 4.1. It is clearly seen that as the proportion of TBAOH rises, D_i decreases. This is attributed to the association of electrolyte cations with the negatively charged monosulfonate group ($pK_a = -9$) in the parent molecule in aqueous solution [44].

Electrolyte (I = 0.1 M)	100% TBAOH	(60+40)% TBAOH + TMAOH	(20+80)% TBAOH + TMAOH	100% TMAOH	100% KOH
I_{ss} / nA	1.62	1.89	2.22	2.86	3.05
D_i / 10^{-6} cm^2s^{-1}	3.0	3.5	4.1	5.3	5.7

TABLE 4.1: Experimentally obtained diffusion coefficients of AQMS *via* steady-state currents.

These diffusion coefficients were set in the simulation model. The parent and reduced quinone species were assumed to have the same values. In reality, the solvation sphere is different for unequally charged anions. However it is a fair assumption here, evidenced by the excellent fitting of simulated and experimental results. The simulation has discarded the comproportionation mechanism, *i.e.* combination of the parent molecule and the di-reduced species to form semiquinone intermediate. This assumption is valid as comproportionation mechanism is unobservable in conventional voltammograms when the diffusion coefficients of parent and reduced species are equal and electron transfer rates are fast [96].

Electrolyte (I = 0.1 M)	100% TBAOH	(60+40)% TBAOH + TMAOH	100% TMAOH	100% KOH
E_f / V	−0.624	−0.616	−0.606	−0.619
$\mid \Delta E \mid$ / V	0.138	0.098	0.030	0.030

TABLE 4.2: DIGISIM® data, for a simple **EE** process, of the formal potential of reaction (E_f) and the difference in the sequential formal potentials of the first and second electron transfers ($\mid \Delta E \mid$) of the electrochemical reduction of 500 mM AQMS / H_2O in various supporting electrolytes

The simulated voltammograms were aimed to match with the experimental peak currents and potentials. Figure 4.5 shows the overlaid simulated and experimental results for AQMS (500 μM) redox reaction in aqueous solutions supported by

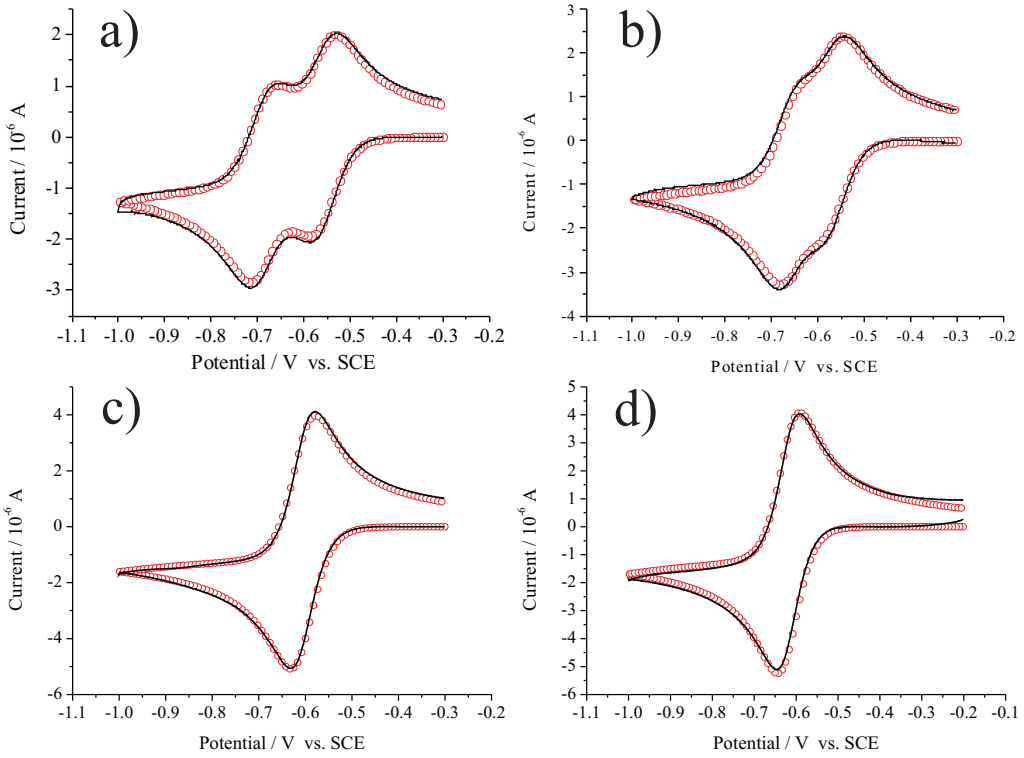

FIGURE 4.5: Overlaid experimental (black line) and simulated (red circles) cyclic voltammograms of 500 μM AQMAS redox signals in aqueous solutions at 100 mV s^{-1} supported with various supporting electrolyte (ionic strength = 0.1 M) cations: (a) TBAOH, (b) 60%TBAOH + 40%TMAOH, (c) TMAOH and d) KOH.

four different supporting electrolytes. The excellent fittings, therefore, enable E_1 and E_2 being determined explicitly. Table 4.2 shows the simulated results of the formal potentials of the reaction, E_f and $\mid \Delta E \mid$. By switching the supporting electrolyte from TMAOH to TBAOH, E_f is shifted by a mere 20 mV to the more negative potential whereas ΔE varies by over 100 mV. Consequently, the increasing ΔE results in two $1e^-$ waves. This large change in the $\mid \Delta E \mid$ can be attributed to the ion pairing effect of the intermediate species with the bulky TBA^+ cations, more specifically the $AQMS^{\bullet -}$ radical anion. The effect is not seen with other smaller electrolyte cations, such as TMA^+ and alkali metal cations (as evidenced by the similar diffusion coefficients in TMAOH and KOH solutions).

Such a preferential interaction is likely due to the large stabilisation of the $AQMS^{\bullet-}$ forming an ion pair with the electrolyte counter cation. The proposed ion pair structure, $[TBA^+][AQMS^{\bullet-}]$, is illustrated in Figure 4.6. The bulky TBA^+ cation is likely to form ionic interaction with the mono-reduced quinone centre and the substituted 2-sulfonate group. This stablised semiquinone intermediate species become thermodynamically less favorable to reduce, *i.e.* E_2 is shifted to a more negative potential. Hence, by varying the proportion of TBA^+ cations it is possible to 'tune' the electrode potentials of the AQMS reduction in buffered solutions.

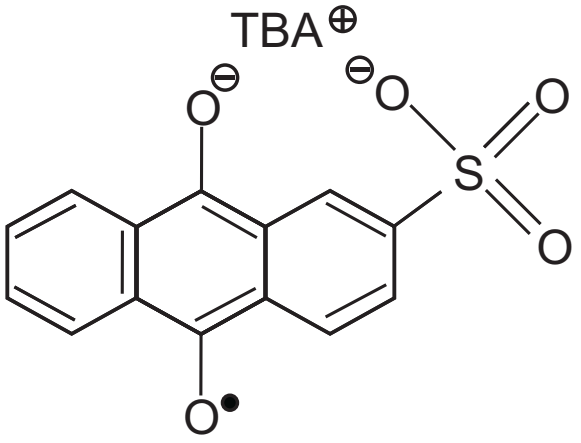

FIGURE 4.6: Proposed ion pair structure of $[TBA^+][AQMS^{\bullet-}]$.

To further demonstrate the decreased reactivity of $AQMS^{\bullet-}$ intermediate species upon ion pair formation, the study of the AQMS mediated reduction of oxygen is next discussed. A boron-doped diamond (BDD) electrode was necessitated because the electrocatalytic response shall not be masked by the oxygen reduction signal, as discussed in the previous chapter. Low concentrations of AQMS were used to ensure the rate limiting step was the AQMS redox process so that the formation of the $AQMS^{\bullet-}$ intermediate can be explicitly shown.

The electrochemical reduction of saturated oxygen was carried out in a 5 μM AQMS aqueous solution supported by 0.1 M hydroxide salt with various counter

cation sizes. The voltammetric responses, depicted in Figure 4.7, show one irreversible wave for all three supporting electrolyte systems with peak potentials of TMAOH and KOH at *ca.* −0.61 V, and that of TBAOH at −0.65 V. The possible mechanism is proposed as follows:

$$\mathrm{AQMS}^{\bullet-} + \mathrm{O_2} \rightleftharpoons \mathrm{AQMS} + \mathrm{O_2^{\bullet-}} \tag{4.5}$$

$$\mathrm{AQMS}^{2-} + \mathrm{O_2} + \mathrm{H_2O} \rightleftharpoons \mathrm{AQMS} + \mathrm{HO_2^-} + \mathrm{OH^-} \tag{4.6}$$

In contrast to Section 3.1, here the active intermediate is AQMS^{2-} instead of AQMSH^-. The existing forms of the intermediate species are dependent on their pK_a values. The pK_a of AQMSH^- is 11 [44]; consequently, it exists as the deprotonated form at pH 12 solution. The superoxide radical species is present in its un-protonated form due to low pK_a of $\mathrm{HO_2^{\bullet}/O_2^{\bullet-}}$ being 4.88 [45]. The pK_a of $\mathrm{H_2O_2}$ is 11.62 [45], and its successive dissociation of another proton (pK_a of $\mathrm{HO_2^{\bullet-}}$) is expected to be much larger. That is to say, in 0.1 M hydroxide aqueous solution (pK_a of $\mathrm{H_2O}$ = 15.7) the peroxide anion is most likely present in its mono-protonated form.

As proved in Section 3.1, $\mathrm{AQMS}^{\bullet-}$ intermediate demonstrates much greater reactivity compared to its parent and di-reduced molecules. Consequently, it results in a large irreversible reduction peak at relatively low overpotentials [75]. As the overpotential increases (beyond −0.6 V), electrocatalytic current decreases accordingly due to further reduction of semiquinone intermediate. One prominent feature in the redox process is the observed 'reverse' peak on the backward scan. It can be explained as the regeneration of $\mathrm{AQMS}^{\bullet-}$ intermediate at low overpotentials and hence 'switches on' the effective catalytic oxygen reduction.

Here, the TBA^+ cation supported solution has shown a significant decline in the

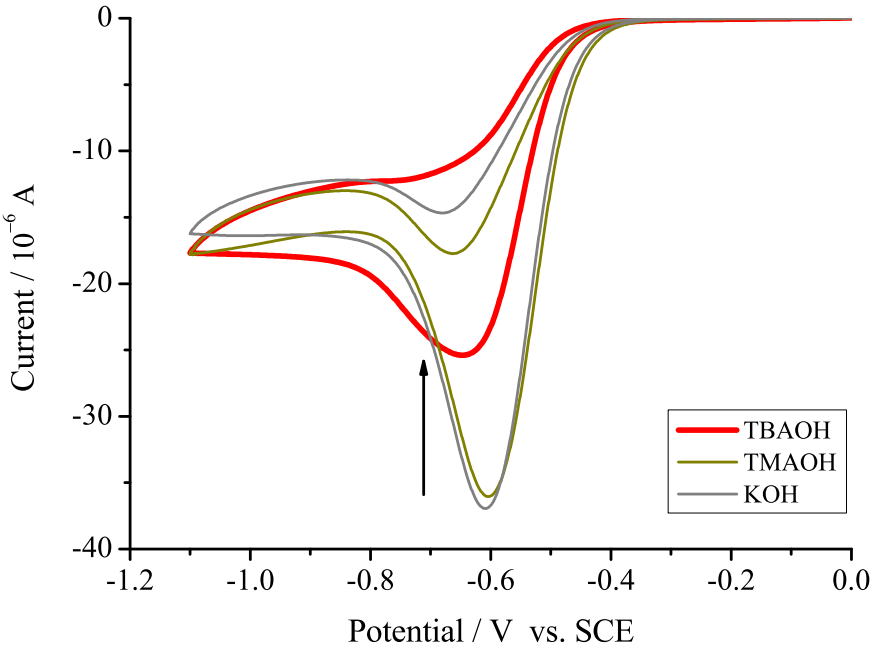

FIGURE 4.7: Cyclic voltammograms of oxygen reduction (C_{O_2} = 1.24 mM [75]) on BDD electrode (r_e=0.155 cm) at 50 mV s^{-1} in the presence of 5 μM AQMS/H_2O with various 0.1 M supporting electrolytes: TBAOH (red), TMAOH (yellow), and KOH (grey).

electrocatalytic peak current. Can this voltammetric response alone support the proposition of decreased activity of semiquinone intermediate? Such the voltammetric feature can be ascribed to two potential factors:(a) the decreased reactivity of semiquinone intermediate; and (b) the decreased diffusion coefficients of reactive species. It can be seen from Table 4.1, the diffusion coefficient of AQMS has almost halved in TBAOH supported solution. As a direct consequence, the electrocatalytic peak current is anticipated to decrease by *ca.* 30% according to Eqn 4.3 (assuming the electrocatalytic peak current is proportional to the concentration of AQMS able to diffuse to the electrode surface. This is however a major oversimplification as it ignores the influence of the oxygen concentration). So the declined

current response reflects a combination of two factors. In fact, it is the disappearance of the 'reverse' peak in TBAOH supported solution shows convincing experimental evidence for the diminishing reactivity of the semiquinone intermediate. As the stablised ion pair being formed, on the backward scan *no* 'free' $AQMS^{\bullet-}$ intermediate is available; hence disappeared 'reverse' peak. Similar deactivated voltammetric response has been reported by Tissot and Huissoud in AQ derivatives mediated oxygen reduction [97, 98]. The use of tetra-n-butylammonium hydroxide in dimethoxyethane/5% H_2O media did not provide satisfying conditions for the use in preparative electrolysis of hydrogen peroxide. The cause was claimed to be due to a low conductivity through Nafion® membrane [97]. In later work Huissoud *et al.* proved the use of tetraethylammonium salt immediately provided good conditions for the preparative electrolysis of hydrogen peroxide; yet no explanation was given [98].

Furthermore, the more negative electrocatalytic potential in TBAOH supported solution in Figure 4.7 also implies the formation of a more stablised form of intermediate over the course of reaction. Moreover, all three voltammograms showed similar limiting currents at high overpotential (beyond −0.8 V). This flat region represents the limiting rate of solution phase reaction, *i.e.* Reaction 4.6.

4.3 Conclusions

This chapter has demonstrated the significant importance of supporting electrolyte in tuning the electrode potentials of AQMS redox species in aqueous solutions. Consequently, the thermodynamic difference of E_1 and E_2 can be tuned by varying the ionic environment of the solution. Such thermodynamic parameters were successfully obtained through simulation model. The bulky TBA^+ cation is proposed

to ion-pair with the $AQMS^{\bullet -}$ intermediate species, evidenced by disappearance of the 'reverse' peak in electrocatalytic response of oxygen reduction. The electrocatalytic peak current also declined, which is a result of not only the decreased activity of semiquinone species but also the abatement of diffusion coefficient of parent molecule. Hence, in order to promote electrocatalytic activity, ion pairing effect should be minimised.

So far, Chapter 3 has studied the kinetics of electrocatalytsis for oxygen reduction; and Chapter 4 has highlighted the role of supporting electrolyte towards the reactivity of the redox mediator. Next, the influence of solvent will be discussed upon both oxygen reduction and its electrocatalytic mediators.

Chapter 5

Solvent effects on both oxygen reduction and its electrolysis

This chapter investigates the thermodynamics, homogeneous rates of reaction, and mass transport during the electro-reduction of oxygen and its mediated pathways in various organic solvent media. Due to the high solubility of oxygen in non-aqueous solvents, the objective is to find a synthetic route using electrochemical methods to produce hydrogen peroxide, which is of potential importance in industry. The three solvent media investigated are anhydrous acetonitrile, acetonitrile/water mixtures, and anhydrous ethanol. Simulation programs have been used to extract the homogeneous rate of reaction from experimental voltammograms. The work presented herein was published in three articles *'J. Electroanal. Chem. 2013, 688, 328-335'*, *'J. Electroanal. Chem. 2012, 681, 44-48'*, and *'J. Electrochem. Sci. Tech. 2013, 4, 71-80'*. The assistance of Ms R. Nissim in collection of the experimental data is acknowledged. Moreover, some work was completed through partnerships with Dr C. Batchelor-McAuley and Ms Q. Lin.

5.1 Mass transport and anomalous solubility of oxygen in acetonitrile/water mixtures

5.1.1 Introduction

The oxygen reduction reaction (ORR) is fundamental to a number of biological and industrial systems, such as respiration [87], photosynthesis [87], fuel cells [92], corrosion [92], and chemical synthesis [88]. Such processes are dependent on the thermodynamics and kinetics of the redox chemistry of oxygen, as well as the concentration of oxygen under the relevant reaction conditions. The oxygen redox processes involve multiple electron transfers. In particular, the electrochemical reduction of oxygen demonstrates one to four electron transfers dependent on conditions such as the solvent media and electrode material [99]. Usually in aprotic non-aqueous solvents, such as acetonitrile (MeCN) [100, 101], N,N-dimethylformamide (DMF) [101], dimethyl sulfoxide (DMSO) [101–103], acetone (AcT) [104], and room-temperature ionic liquids (RTILs) [105–108], a stable superoxide radical anion ($O_2^{\bullet -}$) is formed on most electrode substrates, as shown in the following equation:

$$O_2 + e^- \rightleftharpoons O_2^{\bullet -} \tag{5.1}$$

Moreover, the further reduction of $O_2^{\bullet -}$ radical anion in MeCN/H_2O and DMF/H_2O mixtures has been suggested to be the first case study of an electrochemical concerted proton-electron transfer (CPET) reaction. The mechanism was first proposed by Savéant *et al.* [89, 109], shown in the following equation:

$$O_2^{\bullet -} - - - H_2O + e^- \rightarrow {}^-O_2H - - - OH^- \tag{5.2}$$

where water acts as a reactant as well as a hydrogen bond donor to stabilise the radical anion. More recently, the presence of the radical anion has been observed in high concentration of aqueous sodium hydroxide solution *via* infrared spectroscopy [110] and scanning electrochemical microscopy [111] on platinum electrodes, as well as on modified gold and glassy carbon electrodes [112, 113]. The overall reaction pathway could further follow a rapid disproportionation reaction to form hydrogen peroxide (H_2O_2), resulting in an overall two-electron process, shown in the following equation:

$$2O_2^{\bullet -} + H_2O \rightleftharpoons O_2 + HO_2^- + OH^- \tag{5.3}$$

In comparison, the four electron pathway involves further reduction of H_2O_2 into water in fuel cells [114]. The overall reaction is reported in Equation (5.4), although the exact mechanism hitherto remains elusive.

$$O_2 + 4H^+ + 4e^- \rightarrow 2H_2O \tag{5.4}$$

Therefore, it can be seen that the mechanistic pathway can vary significantly among different experimental conditions, especially with or without the presence of water. Consequently, the electrochemical ORR in mixed-solvent involving water is of distinct scientific interest.

Among the many processes in which the ORR is involved, the industrial production of H_2O_2 *via* the quinone catalysed process is of major industrial significance [88]. Given the possible explosive reactivity of H_2O_2 with a range of organic materials, significant safety issues arise, concerning both the transportation and storage of the chemical. The at-point-of-use synthesis of H_2O_2 *via* electrochemical reduction

of oxygen in an aqueous solution has become an attractive alternative to sidestep these issues [115]. However, one of the main limiting factors is the relatively low solubility of oxygen in aqueous media, *i.e.* 1.24 mM saturated oxygen at 25 °C [46]. In comparison aprotic solvents show much increased solubility of oxygen (an almost five-fold increase in MeCN) [116], Therefore, the use of aprotic solvents or mixtures of aprotic solvent with water may provide a solution to attain a relatively concentrated H_2O_2 solution.

In solvent mixtures a knowledge of the rate of mass transport is important in determining the rate of the electron transfer kinetics of a chemical reaction [117, 118]. That said an accurate knowledge of the diffusion coefficients of a redox couple (oxidised and reduced species) is crucial to analyse the reaction kinetics and mechanism. Therefore, in this chapter, single and double potential step chronoamperometry are applied for the measurement of the diffusion coefficients of O_2 (D_{O_2}) and $O_2^{\bullet-}$ ($D_{O_2^{\bullet-}}$), independently at microelectrodes [24, 25]. The Shoup and Szabo equation[17] is used to analyse the current-time transient response. Herein, the electrochemical behaviour of oxygen in 0.1 M tetra-n-butylammonium perchlorate containing anhydrous and water-mixed (mole fraction of MeCN: $0.72 < \chi_{MeCN} < 1$) MeCN solution is investigated on both platinum and glassy carbon electrode substrates respectively. The change of electrode substrate is mainly to avoid possible adsorption of reactive oxygen intermediate (ROS). The use of supporting electrolyte is important to elevate the conductivity of the solution and suppress electric fields [1]. In contrast to Chapter 4, the tetraalkylammonium salt in MeCN/H_2O mixtures here show negligible ion pairing. Hence, the influence of solvation will be exclusively explored. The diffusional activation energies of oxygen (E_{a,O_2}) and superoxide ($E_{a,O_2^{\bullet-}}$) are studied for the first time in anhydrous MeCN electrolyte containing solution at a temperature range of $298.5 - 313.0$ K by using

a μ-Pt electrode. The chronoamperometric method also provides the first measurement of solubility of O_2 (C_{O_2}) in such experimental conditions. Consequently, the thermodynamic parameters, such as the standard enthalpy change of solvation ($\Delta H^{\ominus}_{solv}$), the standard entropy change of solvation ($\Delta S^{\ominus}_{solv}$), and the standard Gibbs energy of solvation ($\Delta G^{\ominus}_{solv}$) can be experimentally evaluated. Furthermore, the diffusion coefficients and concentrations of dissolved oxygen in MeCN/H_2O mixtures are independently determined by using a μ-C electrode. An anomalous increase in O_2 solubility after the initial water addition ($0.72 < \chi_{MeCN} < 1$) was observed, although the $\Delta G^{\ominus}_{solv}$ in pure water indicates unfavourable dissolution. This study could be of importance in future investigation on oxygen electrolysis in solvent-mixture systems, as it sets foundation in the near pure MeCN limits which has not been studied previously.

5.1.2 Results and discussion

The thermodynamics and mass transport process of oxygen reduction will first be studied in anhydrous acetonitrile, followed by studies in acetonitrile/water mixtures.

5.1.2.1 Temperature effects in anhydrous acetonitrile

Within this section, the reduction of dissolved oxygen in air-equilibrated anhydrous acetonitrile (MeCN) containing 0.1 M tetra-n-butylammonium perchlorate at a temperature range of $298.5 - 313.0$ K has been studied by both cyclic voltammetry and double potential step chronoamperometry. The diffusion coefficients of oxygen and superoxide, as well as the concentration of dissolved oxygen in air are measured as a function of temperature. The Stokes-Einstein relationship is

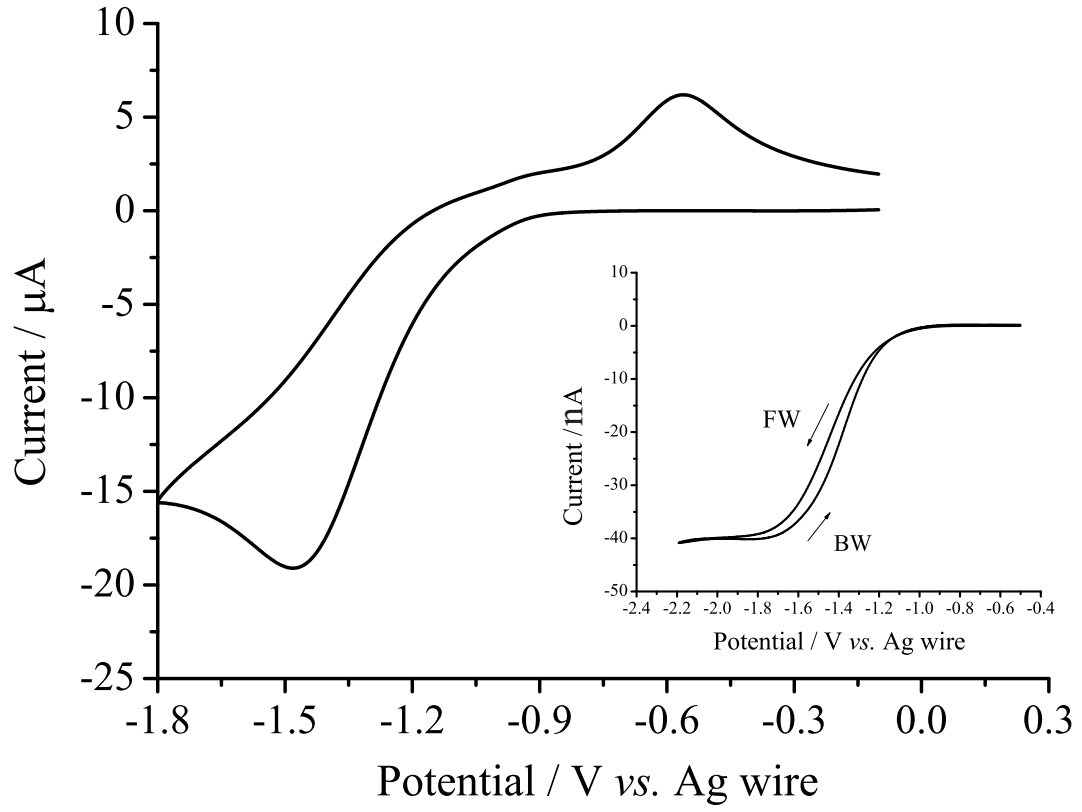

FIGURE 5.1: Cyclic voltammograms of oxygen reduction in air-equilibrated anhydrous MeCN/ 0.1 M TBAP at 298.5 K on a macro-Pt electrode at 100 mV s^{-1} and a μ-Pt electrode at 25 mV s^{-1} (inset). FW and BW represent the forward and backward wave directions.

then discussed after the measurement of diffusion coefficients. The measurement of oxygen concentration reveals the standard entropy change of solvation of oxygen in anhydrous MeCN.

First of all, the oxygen reduction in air-equilibrated anhydrous MeCN at 298.5 K was investigated. The electrochemical reduction of dissolved oxygen in air-equilibrated anhydrous MeCN / 0.1 M tetra-n-butylammonium perchlorate (TBAP) electrolyte solution was carried out at a macro-Pt electrode at 298.5 K. A cyclic voltammogram was obtained for dissolved oxygen at a scan rate of 100 mV s^{-1} running from -0.1 V to -1.8 V (*vs.* Ag wire) as shown in Figure 5.1. The redox waves correspond to a one-electron transfer to form the superoxide radical anion species ($O_2^{\bullet -}$) with a peak potential of 1.48 V and $O_2^{\bullet -}$ re-oxidation at a

potential of −0.56 V [99–101]. It should be noted that on a macro-Pt electrode there was no clear second reductive wave observed at more negative potentials, which is in contrast to the response on a glassy carbon electrode (Section 5.1.2.2). Such voltammetric feature is comparable to that obtained on a BDD electrode (seen next section, Section 5.2). The reason for the absence of the second peak is likely related to a combination of competing processes of both the organic solvent molecule adsorption and oxygen dissociative adsorption on the platinum surface at overpotential beyond −2.0 V [101, 102]. In addition, a μ-Pt disk electrode was also used for cyclic voltammetry under the same conditions (Figure 5.1 inset, 25 mV s^{-1}) to demonstrate that only one steady-state current was observed and occurred at *ca.* −1.9 V. Note that the half-wave potential obtained from the μ-Pt electrode is shifted over 400 mV to the more negative direction as compared to the formal potential of the macro-Pt (approximated mid-point potential of −1.02 V). That said the electrochemical reduction of oxygen is an electrochemical irreversible process on a platinum substrate.

Double potential step chronoamperometry was performed to determine the diffusion coefficients of both the dissolved oxygen and the superoxide radical anion. The experimental procedures are described in Section 2.3. After a 2 second pretreatment period of holding the potential at 0 V, the first part of the current-time transient was obtained by stepping to a transport-limited current at −2.0 V for 0.5. Immediately after the second current-time transient was obtained by stepping back to 0 V for another 0.5 s. In another words, the first and second steps correspond to the reduction of O_2 and oxidation of formed $O_2^{\bullet-}$ respectively. The experimentally obtained reductive part of the transient was analysed by using the Shoup and Szabo expressions (refer to Equations 1.27 to 1.29). Values of (1.26 ± 0.05) mM and (9.2 ± 0.36) $\times 10^{-9}$ $m^2 s^{-1}$ were obtained, corresponding

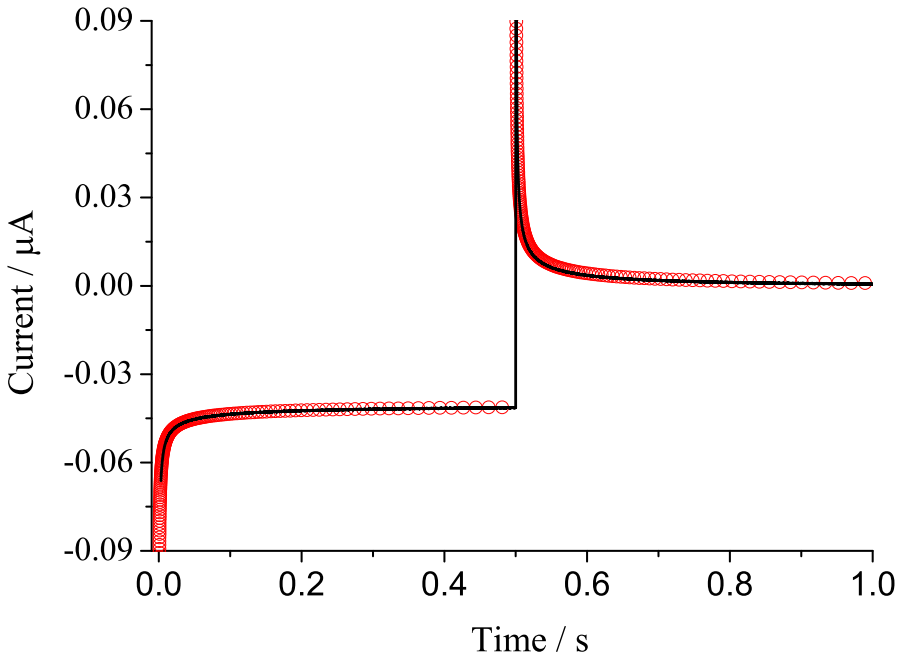

FIGURE 5.2: The experimental (line) and theoretical (circle) double potential step chronoamperometric transients for dissolved oxygen (1e transfer) in air-saturated anhydrous MeCN / 0.1 M TBAP on a μ-Pt electrode at 298.5 K. The potential was stepped from 0 V to 2.0 V and back to 0 V *vs.* Ag wire.

to the concentration (C_{O_2}) and diffusion coefficient (D_{O_2}) of O_2 in air-equilibrated anhydrous MeCN containing 0.1 M TBAP at 298.5 K. These two values were then fixed in an in-house developed simulation program, described in Section 2.4, to determine the diffusion coefficient of superoxide radical anion, $D_{O_2^{\bullet-}}$, during the implementation of the simulation program, described by Klymenko *et. al.* [26]. A value of $(2.73 \pm 0.35) \times 10^{-9}$ m^2s^{-1} was thereafter obtained for the $D_{O_2^{\bullet-}}$. The experimental and theoretical fittings are depicted in Figure 5.2.

The diffusion coefficient of molecular oxygen is in excellent agreement with the literature reported data, *i.e.* $(7.1 \sim 11.0) \times 10^{-9}$ m^2s^{-1} in anhydrous MeCN at 298.0 K [101, 102]; whereas the present study reveals a hitherto undocumented value for the diffusion coefficient of superoxide radical anion species. Discussion of

the magnitude of these two values will be discussed later. In contrast, the experimentally measured solubility of oxygen, (calculated as (6.3 ± 0.3) mM, noting oxygen takes up 20% of air), is significantly smaller as compared with previous literature, as summarized in Table 5.1. This discrepancy falls well outside the literature reported uncertainties in the experiments, and is not due to a systematic error as evidenced by the good agreement of the measured D_{O_2}. A self-consistent experiment was further conducted by bubbling pure oxygen gas into the anhydrous MeCN supported by 0.1 M TBAP solution for 10 minutes. The steady-state current obtained for the saturated oxygen solution (not shown) was exactly five times as much as that was shown in Figure 5.1 inset. Thus, the deviation may be surmised to be due to the 'salting-out' effect relating to the presence of tetraalkylammonium salt in the anhydrous MeCN solution [119]. Work reported by Pierotti [120] based on a proposed scaled particle theory suggested that the 'salting out' effect is especially pronounced for systems in which the solute was nonpolar and its molecular diameters were small in nonaqueous solutions.

C_{O_2} (mM)	Method of measurement	Ref.
8.1 ± 0.6	Gas chromatography	[116]
12.1 ± 0.7	Photochemistry	[121]
$9.6 \pm 0.5^*$	PSRK group contribution equation of state	[122]

TABLE 5.1: The saturated oxygen solubility at 1 atm in nonelectrolytic acetonitrile solvent at 298.0 K. (* The value is obtained from the simulated result at 298.0 K utilizing the optimisation group interaction parameters for the predictive SoaveRedlichKwong (PSRK) group contribution equation of state based on the experimental data obtained from a static synthetic method.)

Next, the temperature effect upon the diffusion coefficients and solubilities of oxygen are discussed as follows. Double potential step chronoamperometry was performed to determine the diffusion coefficients and solubilities of both dissolved oxygen and superoxide radical anion in anhydrous MeCN supported by 0.1 M

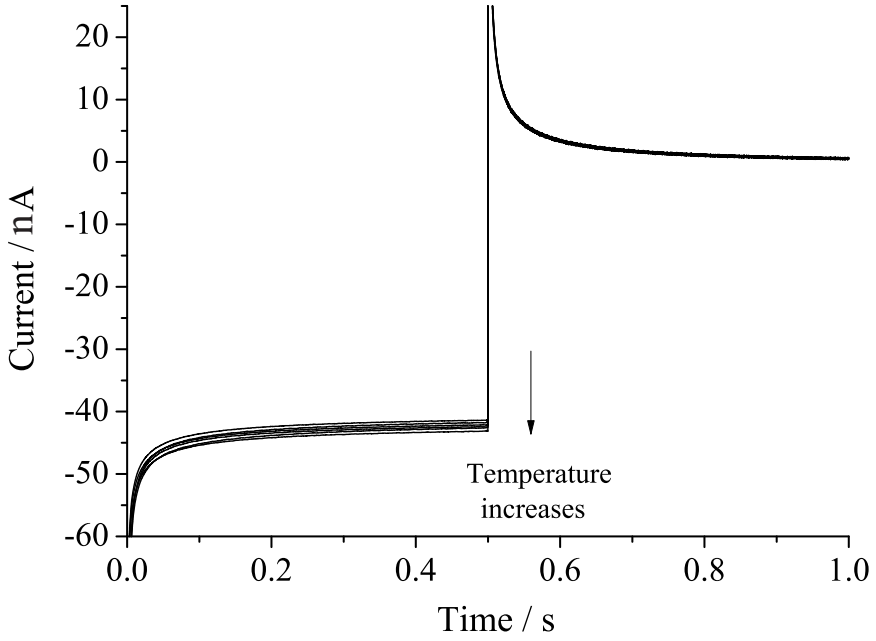

FIGURE 5.3: The experimental double potential step chronoamperometric transients for dissolved oxygen ($1e^-$ transfer) in air-saturated anhydrous MeCN/0.1 M TBAP on a μ-Pt electrode at the temperature range of $298.5 - 313.0$ K on a μ-Pt electrode.

TBAP salt in the temperature range of $298.5 - 313.0$ K by using a μ-Pt electrode. Experimental procedures are the same as described earlier. The experimental transients are illustrated in Figure 5.3, and the analysed data at elevated temperatures are shown in Table 5.2. Although the limiting currents of the first transient have a greater apparent increase with temperature, the change in the experimentally measured D_{O_2} is less than 4%. In contrast, the measured $D_{O_2^{\bullet-}}$ values are found to vary over 20% despite of the apparent minimal changes on the second part of the transients. The simulated $D_{O_2^{\bullet-}}$ values are the outcomes of a combination of dependency on both D_{O_2} and $D_{O_2^{\bullet-}}$.

The derived diffusion coefficients were then analysed in terms of the Arrhenius-type behaviour [106]. To calculate the diffusional activation energy of oxygen and superoxide, the diffusion coefficients were analysed in terms of the Arrhenius

T(K)	C_{O_2} (mM)	error (±)	D_{O_2} (10^{-9} m^2 s^{-1})	error (±)	$D_{O_2^{\bullet-}}$ (10^{-9} m^2 s^{-1})	error (±)	$D_{O_2^{\bullet-}}/D_{O_2}$
298.5	1.26	0.05	9.20	0.36	2.73	0.11	0.297
302.8	1.27	0.06	9.32	0.42	2.84	0.13	0.305
304.3	1.27	0.06	9.35	0.48	2.98	0.15	0.319
305.8	1.27	0.06	9.38	1.02	2.94	0.31	0.313
309.0	1.27	0.07	9.47	0.81	2.89	0.24	0.305
313.0	1.27	0.05	9.56	0.37	3.25	0.12	0.340

TABLE 5.2: Concentrations, diffusion coefficients and their ratio were obtained from Shoup and Szabo analysis[17] of double potential step chronoamperometry for the reduction of oxygen in air-equilibrated anhydrous MeCN/TBAP (0.1 M) solution at elevated temperatures on a μ-Pt electrode.

equation:

$$D = D_\infty \exp\left(\frac{-E_{a,i}}{RT}\right) \tag{5.5}$$

where R is the gas constant, D_∞ is a constant corresponding to the hypothetical diffusion coefficient at infinite temperature, $E_{a,i}$ is the diffusional activation energy of the electroactive species, and T is the temperature in the bulk solution. Plots of $\ln D$ *vs.* T^{-1} for both oxygen and superoxide are shown in Figure 5.4. Values of both E_{a,O_2} and $E_{a,O_2^{\bullet-}}$ being (2.07 ± 0.05) kJ mol^{-1} ($R^2 > 0.997$) and (8.01 ± 2.24) kJ mol^{-1} ($R^2 > 0.702$) were determined respectively. To the best knowledge of the authors, there is no previous literature reported for these values in anhydrous aprotic solutions containing electrolyte. In comparison, the E_{a,O_2} measured in room temperature ionic liquids are much larger as compared with that in MeCN, which spans a range of $21 - 34$ kJ mol^{-1} [105]. The observation reflects the difference in viscosities of MeCN being 0.344 cP, in contrast to the highly associated and viscous ionic liquids with values from 50 to 250 cP at 298.15 K [123].

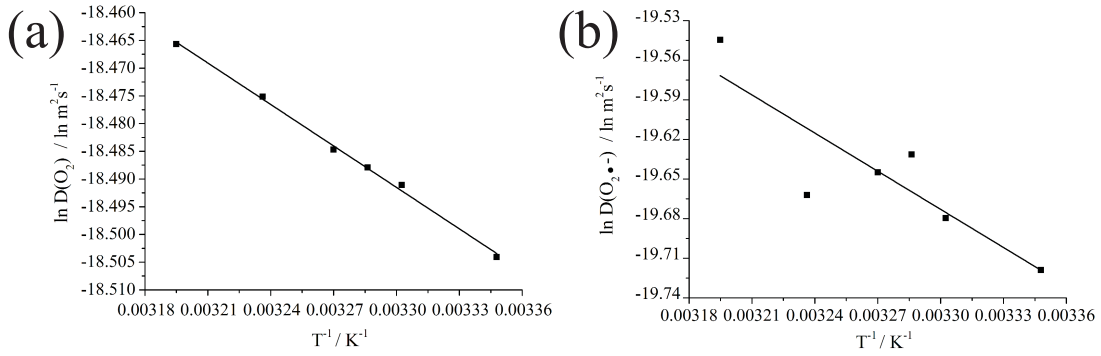

FIGURE 5.4: Arrhenius plot of $\ln D$ *vs.* T^{-1} for both (a)oxygen and (b)superoxide over the temperature range of $298.5-313.0$ K on a μ-Pt electrode in air-equilibrated anhydrous MeCN/0.1 M TBAP.

The Stokes-Einstein relationship [1] may be used to describe the idealised temperature dependence of the diffusion coefficient for a sufficiently large solute:

$$D = k_B T/6\pi\eta\alpha \tag{5.6}$$

where

$$\eta = \eta_\infty \exp\left(\frac{E_{a,MeCN}}{RT}\right) \tag{5.7}$$

k_B is the Boltzmann constant, η is the macroscopic dynamic viscosity of the solution, and α defines the molecular 'effective' radius. For a particle or molecule of sufficient size the E_{a,O_2} is solely dependent upon the solvent properties reflecting the change in viscosity as a function of temperature [111, 118]. Accordingly, the activation energy of viscous flow of MeCN, $E_{a,MeCN}$, was calculated from the published data for the temperature-dependent viscosity of pure MeCN, which has a value of 5.9 kJ mol^{-1} [123]. This value is in close agreement to that was found experimentally *via* measurements by using ferrocene [108] and N,N,N,N-tetramethyl-para-phenylenediamine (TMPD) [118] where the resulted values range

from $6.9 - 10.7$ kJ mol^{-1} in electrolytic MeCN solution. The small positive discrepancy between the values likely represents the increase in the viscosity after the addition of supporting electrolyte in MeCN solution [124]. Hence, due to the comparatively low value of E_{a,O_2} ((2.07 ± 0.05) kJ mol^{-1}) the diffusion of molecular oxygen in anhydrous MeCN solution containing 0.1 M TBAP is concluded *not* to follow the Stokes-Einstein relationship. This is ascribed as being due to the smaller size of molecular oxygen compared with that of the solvent molecules [118]. In such a case, the small oxygen molecules are able to diffuse 'around' the MeCN solvent molecules and supporting electrolyte without being much affected by the solvent viscosity. Consequently, the simple macroscopic hydrodynamic theory becomes quantitatively inadequate to describe the behaviour. Conversely, the diffusional behaviour of fully hydrated molecular oxygen has been reported to be described accurately by the Stokes-Einstein relationship in aqueous sodium hydroxide solution with concentration ranging from 1 to 12 M [111]. In addition, the diffusion coefficients of the $O_2^{\bullet-}$ radical anion are less than a third compared to its parent neutral molecule at all temperatures, suggesting ion pairing effects are likely taking place between the radical species and the tetraalkylammonium cation, or strong interactions of $O_2^{\bullet-}$ with the solvent dipoles. The corresponding value of $E_{a,O_2^{\bullet-}}$ being (8.01 ± 2.24) kJ mol^{-1} lies within the range that the Stoke-Einstein relationship applies. This confirms the importance of the size of solute, where the diffusional species must be at least comparable in size to that of the solvent molecule in order to follow the Stoke-Einstein relationship.

So far we have been focusing on the discussion of the diffusion coefficients; next the solubilities of oxygen will be considered. Hitherto a very limited amount of work has been published on the solubility of molecular oxygen at elevated temperatures

in only nonelectrolyte containing MeCN solution. Horstmann *et al.* experimentally obtained three Henry coefficient data points at 305.51 K, 323.12 K and 353.13 K [122], which converted to concentration to give 9.52 mM, 10.10 mM, and 10.90 mM respectively. In the same work, simulated Henry coefficients against a temperature range of $250 - 400$ K have indicated an overall endothermic process for the dissolution of oxygen in ***pure*** MeCN.

The relationship between the change of solubility and temperature can be interpreted through the use of the Van't Hoff equation,

$$\frac{d \ln \chi_{O_2}}{dt} = \frac{\Delta H^{\ominus}_{solv}}{RT^2} \tag{5.8}$$

where χ_{O_2} is defined as the mole fraction of oxygen solubility [125], which can be approximated as $\chi_{O_2} = \frac{C_{\mathrm{O_2}}}{C_{\mathrm{MeCN}}}$ ($C_{\mathrm{O_2}}$ and C_{MeCN} are the concentrations of saturated O_2 and MeCN respectively), and $\Delta H^{\ominus}_{solv}$ is the standard enthalpy change of the solvation of oxygen at elevated temperatures. It can be seen from Table 5.2 the concentrations of oxygen were almost invariant under the temperature range, *i.e.* $\Delta H^{\ominus}_{solv}$ is close to zero. To obtain a more accurate value of $\Delta H^{\ominus}_{solv}$, the Van't Hoff equation can be integrated, viz.,

$$\ln \chi_{O_2} = -\frac{\Delta H^{\ominus}_{solv}}{RT} + \text{Constant} \tag{5.9}$$

By plotting $\ln \chi_{O_2}$ versus T^{-1}, the $\Delta H^{\ominus}_{solv}$ can be calculated as $+0.33$ (error: $+4.69/-3.86$) kJ mol^{-1}. The relatively large error is ascribed as being due to the limited temperature range applied. This experimental restriction originated from the volatility of the solvent and distortion of chronoamperogram at higher temperatures. Such an experimentally measured value can be justified in comparison with previous literatures [122, 126]. From careful analysis of the experimental

values obtained by Horstmann *et al.* [122] spanning a temperature range of 50 K, the $\Delta H^{\ominus}_{solv}$ in ***pure*** MeCN can be estimated as + 2.55 kJ mol^{-1}. Additionally, the experimentally obtained value has a reasonable agreement with the $\Delta H^{\ominus}_{solv}$ of oxygen in pure acetone, being + 0.13 kJ mol^{-1}, noting the similar polarities of these two solvents [126].

The standard entropy change of the solvation, $\Delta S^{\ominus}_{solv}$, hereafter can be evaluated *via* the standard Gibbs energy of solvation, $\Delta G^{\ominus}_{solv}$, by

$$T\Delta S^{\ominus}_{solv} = \Delta H^{\ominus}_{solv} - \Delta G^{\ominus}_{solv} \tag{5.10}$$

where $\Delta G^{\ominus}_{solv} = -RT \ln \chi_{O_2}$. Hence, the calculated $\Delta G^{\ominus}_{solv}$ is +19.9 (error: $+0.12/-0.11$) kJ mol^{-1} and the $\Delta S^{\ominus}_{solv}$ is - 65.5 (error: $+15.25/-12.62$) J mol^{-1} K^{-1} at 298.5 K in anhydrous MeCN supported by 0.1 M salt. These values are tabulated in Table 5.3. The experimentally measured $\Delta G^{\ominus}_{solv}$ has a good agreement with the previous reported results of oxygen dissolved in nonelectrolytic MeCN being +19.2 kJ mol^{-1} [125]. Furthermore, these thermodynamic parameters are contrasted with ones found in pure water, shown in Table 5.3. The less positive value of $\Delta G^{\ominus}_{solv}$ in electrolytic MeCN suggests that the solvation of oxygen is less unfavourable. Although the $\Delta H^{\ominus}_{solv}$ in water is an exothermic process, probably mainly due to the energy released for the hydrogen-bond formation during solvation shell reformation [120], the entropic term plays an dominant role in making the overall process less favoured.

	$\Delta H^{\ominus}_{solv}$ / kJ mol^{-1}	$\Delta S^{\ominus}_{solv}$ / J mol^{-1} K^{-1}	$\Delta G^{\ominus}_{solv}$ / kJ mol^{-1}
MeCN / 0.1 M TBAP	+0.33 (error: +4.69 / − 3.86)	−65.5 (error: +15.25 / − 12.62)	+19.9 (error: +0.12 / − 0.11)
Pure H_2O [126]	−12.1	−129.5	+26.5

TABLE 5.3: Thermodynamic parameters *via* experimental determination in this work and of cited values from literature at 298.0 K.

5.1.2.2 Dependency of diffusion coefficients and solubilities of oxygen upon water addition

Within this section, the reduction of dissolved oxygen in air-equilibrated MeCN/H_2O mixtures containing 0.1 M TBAP at 298.5 K has been studied by both cyclic voltammetry and single potential step chronoamperometry. Consequently, the diffusion coefficients and concentrations of dissolved oxygen are measured as a function of water content.

A glassy carbon (GC) substrate is used in the following experiments instead of platinum electrodes. There is no steady-state current on a μ-Pt electrode when water is involved. Such phenomenon is accounted by the adsorption of produced reactive oxygen species (ROS) in the complex mechanism, most likely to be the hydroxyl radicals (OH•) [127]. Literature reports that the reactivity of hydroxyl radicals can be triggered dramatically in the presence of hydrogen bond donors as opposed in dipolar aprotic MeCN solvent [128]. Hence, a carbon electrode was used as an alternative when water was involved in further studies.

The electrochemical reduction of dissolved O_2 in air-equilibrated solvent mixtures of MeCN/H_2O was carried out by using a macro-GC electrode at 298.5 K. Aliquots

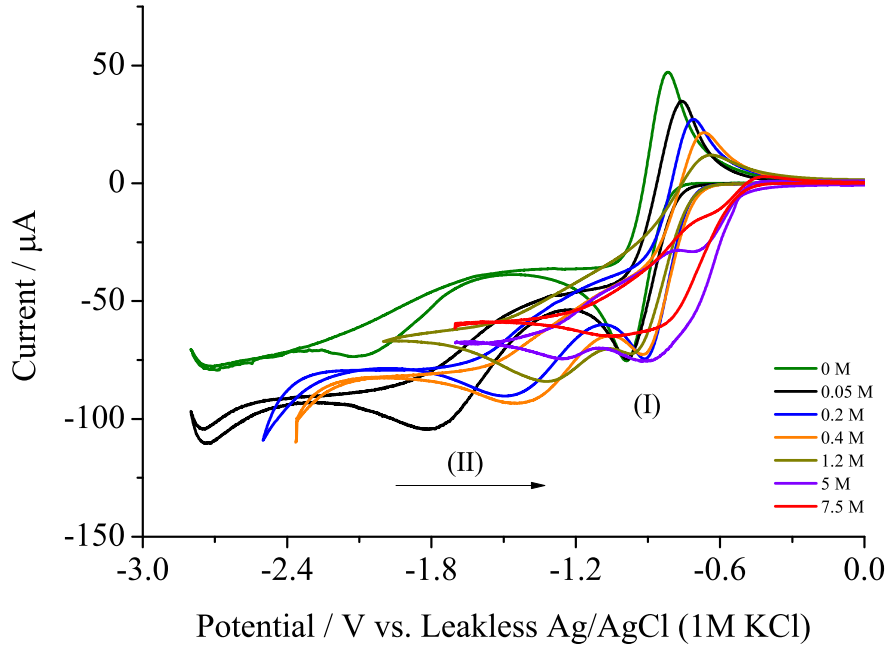

FIGURE 5.5: Cyclic voltammograms (subtracted by blank) of dissolved oxygen redox in air-equilibrated solvent mixtures of MeCN/H_2O supported by 0.1 M TBAP on a macro-GC electrode at 298.5 K. Initial anhydrous MeCN volume was 10 mL. Aliquots of water was successively added to make up reaction solutions with increasing water content from $0, 0.05, 0.2, 0.4, 1.2, 5$ to 7.5 M.

of deionised water were successively added into a 10 mL electrolytic MeCN reaction solution. The MeCN solution was maintained at a constant concentration of 0.1 M TBAP over the range of various water contents *via* the addition of salt. Figure 5.5 shows the cyclic voltammograms of dissolved O_2 in solvent mixtures with water concentration varying from $0-7.5$ M at 100 mV s^{-1}. An entire cycle was completed by scanning from 0 V to the negative potential direction until the occurrence of the second reductive wave, after which the scan was reversed back to 0 V. All the voltammograms are shown after blank scan subtraction, and front baselines were corrected to zero current.

In anhydrous MeCN, a reversible redox wave occurs at -1.0 V and -0.85 V (*vs.* Ag/AgCl - 1 M KCl). It is reported that the reversible wave corresponds to the one

electron reduction of O_2 to form the $O_2^{\bullet -}$ [99, 101]. The second irreversible wave correlates to a further electron reduction to form the peroxide dianions [99]. Upon gradual H_2O addition, the reductive waves shift to more positive potentials without a significant change in wave shape. The subtle media effect can be ascribed as being due to both kinetic and thermodynamic outcome related to the water content. Here, water is not only the reactant *via* a proposed concerted proton and electron transfer (CPET) mechanism, but also a participant through the hydrogen bonding stabilisation with the reduced anions (Reaction 5.2) [89, 109, 129]. The di-reduced species interacts with water to a greater extent, therefore a larger positive potential shift is observed. This tendency continues until the water concentration reaches approximately $7-7.5$ M, at which point the two reductive waves coalesce into one. A plot of the first and second reductive peak current density against log concentration of water ($\log_{10} C_{H_2O}$) is shown in Figure 5.6. It is interesting to note that up to 5 M of water concentration, the peak current densities of the first reductive wave are almost unchanged. This experimental observation seemingly suggests at first sight that the product of $D^{0.5}C_o$ for molecular oxygen is independent of H_2O concentration up to 5 M (according to the Randles-Ševčík equation). This result is unexpected given that each parameter is known to be around a factor of five times lower in pure water than in MeCN [121]. Consequently, this abnormity led us to further investigate the relationship of D_{O_2} and C_{O_2} under the variable H_2O concentrations.

The dependency of the diffusion coefficients and concentrations of oxygen upon water content is now further analysed. Single potential step chronoamperometry is used to independently and simultaneously measure the diffusion coefficients and concentrations of dissolved oxygen in air-equilibrated solvent mixtures at 298.5 K by using a μ-C electrode. It should be noted that the current-time transient

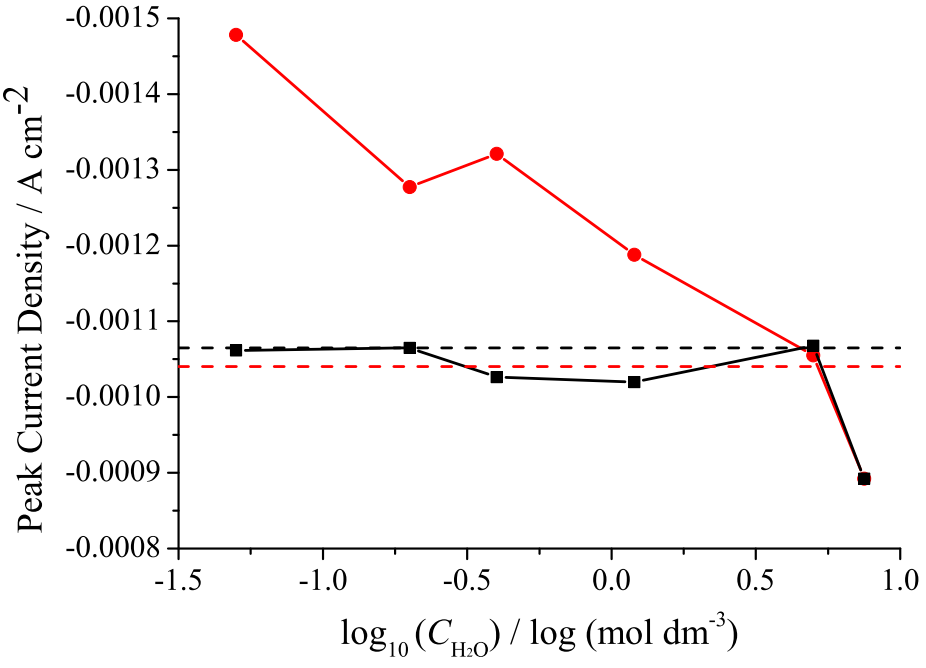

FIGURE 5.6: Plot of the first (squares) and second oxygen reductive (dots) peak current density *vs.* $\log_{10}$ concentration of water in MeCN/H_2O mixtures supported by 0.1 M TBAP on a macro-GC electrode at 298.5 K. The water content varies from $0, 0.05, 0.2, 0.4, 1.2, 5$ to 7.5 M. The two straight lines represent the peak current densities in anhydrous MeCN.

obtained by stepping the potential after the first electron reduction incurred extra current at short-time scale (not shown). This outcome is likely due to the thermodynamically favourable disproportionation mechanism involving superoxide radical anions, referring to Reaction 5.3. Alternatively, the reductive transients can be obtained by stepping after the second electron transfer, where the product of which showed no interference with the carbon surface. A longer time scale (2 s) was required in order to achieve a steady-state current profile involving the two electron reduction of O_2. The experimental transients were analysed as described in Section 2.3.

The resulting diffusion coefficients and concentrations of oxygen with variation of H_2O content are shown in Figure 5.7, where the C_{H_2O} has been converted in terms

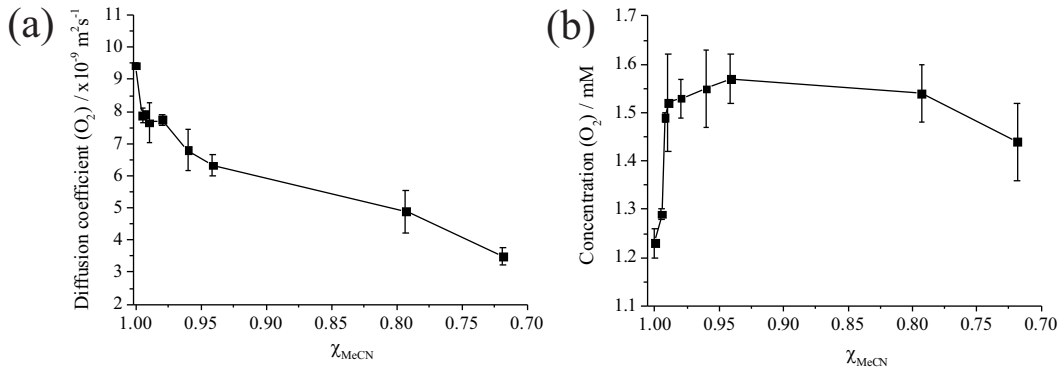

FIGURE 5.7: (a) Experimental diffusion coefficients of oxygen as a function of mole fraction of MeCN (χ_{MeCN}). (b) Experimentally measured concentration of dissolved oxygen *vs.* χ_{MeCN} in air-equilibrated MeCN/H_2O mixtures supported by 0.1 M TBAP on a μ-C electrode. All the experiments were repeated at least five times, and the errors are obtained from the square root of the variance of all data points.

of mole fraction of MeCN, χ_{MeCN}. In anhydrous MeCN solution, the D_{O_2} and the C_{O_2} measured by using the μ-C electrode were $(9.43 \pm 0.07) \times 10^{-9}$ m^2 s^{-1} and (1.23±0.03) mM respectively. These values are within the errors obtained from the utilisation of the μ-Pt electrode, as described in Section 5.1.2.1. The experimentally measured diffusion coefficients for oxygen are found to decline throughout the studied range of water mixing, shown in Figure 5.7 (a), in particular in the range of $0.94 < \chi_{MeCN} < 1$. Concurrently, the concentration of oxygen is found to increase by *ca.* 28%. Both the decrease in the D_{O_2} and the increase in the C_{O_2} suggest that the dissolved O_2 is preferentially solvated by the H_2O molecules rather than the MeCN molecules at relatively low water content. This preferential solvation arises possibly due to the existence of hydrogen-bonding between the dissolved molecular O_2 and H_2O molecules. Such hydrogen bonding might contribute both to a decrease in enthalpy of mixing, resulting in the observed increase in solubility and lead to an effective increase in the solvated radius; hence causing a decrease in the measured diffusion coefficients. However, as water content increases further

the hydrogen bonding can introduce short range dipole-dipole interactions in the reaction solution, and results in the decreased in entropy of solvation. It is clearly shown that when $\chi_{MeCN} < 0.94$, the entropic term is dominant over the dissolution process. Therefore, at higher water content the unfavourable entropy of solvation plays the dominant role; consequently resulting in the observed decrease in the oxygen solubility.

Hence to resolve the previously posed paradox that on the macro-GC electrode the first electron reduction peak current is independent of the H_2O concentration up to 5 M ($0.94 < \chi_{MeCN} < 1$), it can be seen that the initial increase in the C_{O_2} offsets the decrease in the D_{O_2} at low water content. Hence the invariance of the peak current to water concentration was observed. Beyond this threshold, *i.e.* $\chi_{MeCN} < 0.94$, the decrease in both the diffusion coefficients and solubilities of oxygen result in an overall peak currents to decline at higher water content.

5.1.3 Conclusions

This section has been focused upon the electrochemical behaviour of oxygen reduction and the measurement of D_{O_2}, $D_{O_2^{\bullet-}}$ and C_{O_2} of dissolved oxygen in air-equilibrated MeCN solution containing 0.1 M tetra-n-butylammonium salt under two experimental conditions: (1) anhydrous MeCN at elevated temperature from $298.5 - 313.0$ K on platinum electrodes; (2) solvent mixtures of MeCN / H_2O ($0.72 < \chi_{MeCN} < 1$) at 298.5 K on glassy carbon electrodes. The D_{O_2} and C_{O_2} were found to be $(9.20 \pm 0.36) \times 10^{-9}$ m^2 s^{-1} and (1.26 ± 0.05) mM at 298.5 K and were determined through the use of a μ-Pt electrode. The resulted concentration value shows a negative discrepancy from literatures, possibly due to the 'salting-out' effect in the presence of the bulky tetraalkylammonium cation. The diffusional

activation energies of O_2 (E_{a,O_2}) and $O_2^{\bullet-}$ ($E_{a,O_2^{\bullet-}}$) were determined. The small value of E_{a,O_2}, (2.07±0.05) kJ mol^{-1}, suggests the diffusional behaviour of molecular oxygen lies outside the classical description of Stokes-Einstein relationship due to the relative smaller effective size of the solute molecule to that of the solvent. This finding could be of importance in the development of oxygen gas sensing in MeCN solution over a large temperature range. The change of solubilities over the temperature range was shown to be almost invariant. A more quantitative analysis found the $\Delta H^{\ominus}_{solv}$ to be + 0.33 (error: $+4.69/-3.86$) kJ mol^{-1}. Other thermodynamic parameters, such as $\Delta G^{\ominus}_{solv}$ and $\Delta S^{\ominus}_{solv}$, were determined as +19.9 (error: $+0.12/-0.11$) kJ mol^{-1} and - 65.5 (error: $+15.25/-12.62$) J mol^{-1} K^{-1} respectively. The value of $\Delta G^{\ominus}_{solv}$ indicates the solubility of O_2 is greater in MeCN as compared to that in H_2O. However, the experimental results showed an anomalous greater solubility of O_2 in solvent mixtures at the initial addition of H_2O ($0.94 < \chi_{MeCN} < 1$). Combined with the observed decrease in D_{O_2}, such behaviour can be tentatively explained by the preferential solvation of molecular O_2 by H_2O molecules *via* hydrogen bonding at lower water content. Consequently, the thermodynamic terms in the mixing process were altered, and therefore favour the dissolution of O_2. At higher water content, the decrease in both the D_{O_2} and C_{O_2} were shown in a predicted manner. To the best knowledge of the authors, this is the first time that the diffusion coefficients and solubilities of oxygen are reported in electrolyte containing MeCN/ H_2O mixtures.

Having studied the electrochemical behaviour of oxygen reduction in acetonitrile, the electrocatalytic response is next discussed. Some of the parameters obtained from this section, such as diffusion coefficients and concentration of oxygen in air-equilibrated anhydrous acetonitrile, are utilised in the next section.

5.2 Anthraquinone mediated oxygen reduction in anhydrous acetonitrile

5.2.1 Introduction

The production of hydrogen peroxide in industry is *via* the chemical hydrogenation of oxygen, utilising 2-alkyl-anthraquinone as a catalyst [88]. However, this process is complex and is only economically feasible on a large scale [34]. Consequently, it has been proposed that it would be desirable to find a method by which small scale hydrogen peroxide production could be achieved [130]. To date, a number of approaches towards the electrochemical production of hydrogen peroxide have been pursued, either focussing on direct [131, 132] or mediated reduction pathways [49, 133]. A significant gain in the use of a mediated redox system, such as anthraquinone, is the greater limitation of the rate of undesirable side reactions, such as the further reduction of the produced hydrogen peroxide to water.

For many applications only reasonably dilute peroxide solutions are required ($3-8\%$) [130]. However, producing even a moderately concentrated solution ($\geq 2\%$) [88] *via* electrochemical methods poses a significant challenge. It has been recognised that one of the main limiting factors is the relatively low solubility of oxygen in aqueous media (sat. 1.24 mM at 25 °C) [46]. The low oxygen solubility is problematic primarily due to the fact that, as higher hydrogen peroxide concentrations are attained, the direct reduction of the product (hydrogen peroxide) becomes competitive, thus leading to significant decreases in the system's efficiency. Although the use of higher pressure may render the desired results, this is inherently problematic due to the associated safety risks. One alternative approach to increasing the reactant concentration has been to use a flow of pure oxygen across

a porous carbon cathode, hence increasing the local concentration and causing the oxygen reduction to occur at the three-phase boundary. This experimental procedure resulted in the continuous formation of 7 wt% hydrogen peroxide in a sodium hydroxide solution [115]. Although this represented a significant improvement, outside of the paper industry most applications (medical and chemical) require a solution of a lower pH. Moreover, purification of the highly basic working solution is non-trivial. Consequently, more recent work has focused upon the production of hydrogen peroxide at neutral pH. These systems are able to achieve comparatively highly concentrated solutions (13.5 wt%); however, the conversion efficiency can be as low as 31% [134, 135]. Therefore, alternative electrochemical synthetic routes, and specifically systems in which the oxygen concentration at the cathode is improved, are still desirable.

One such alternative may be to use an aprotic solvent. The solubility of oxygen within acetonitrile is found to be significantly higher (roughly by a factor of five) [116]. However, the thermodynamics of the oxygen and quinone reduction are significantly altered within this medium. Importantly, in contrast to an aqueous solution, in acetonitrile the superoxide species is thermodynamically stable [99]. Disproportionation of this superoxide species into oxygen and hydrogen peroxide is readily achievable through addition of a sufficiently strong proton source [129]. Consequently, the work presented within this section aims to investigate the one-electron anthraquinone mediated reduction of oxygen to form superoxide, in an *anhydrous* acetonitrile solution. This investigation is enabled, first, through the use of a boron-doped diamond electrode (BDD) and second, through the selection of an optimal anthraquinone derivative. Utilising software DIGISIM® the anthraquinone mediated reduction of oxygen is successfully modelled.

5.2.2 Results and discussion

5.2.2.1 Selection of substituted quinone species

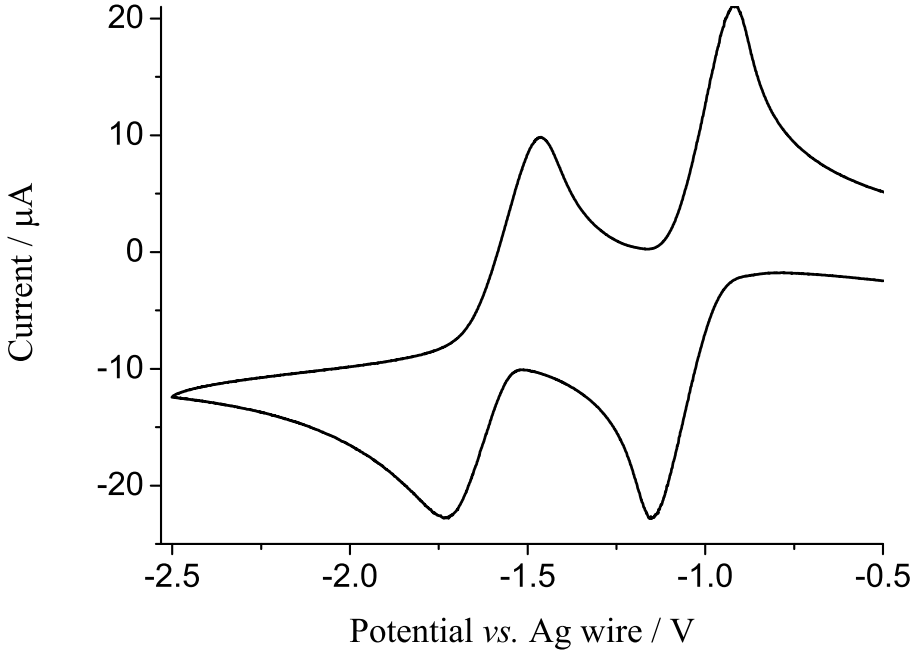

FIGURE 5.8: The reduction of anthraquinone (1 mM AQ, 0.1 M TBAP in acetronitrile), at a BDD macroelectrode, at 100 mV s^{-1}. The two quasi reversible one-electron reductive waves are observed at −1.16 V and −1.74 V (*vs.* Ag wire).

The cyclic voltammetric response of anthraquinone (AQ, 1 mM) in a 0.1 M tetra-n-butylammonium perchlorate (TBAP) acetonitrile solution was investigated at a BDD electrode with an experimental scan rate of 100 mV s^{-1} (Figure 5.8). Two quasi-reversible $1e^-$ reduction waves are observed at −1.16 V and −1.74 V (*vs.* Ag wire). These two waves are ascribed as being due to the first and second $1e^-$ reductions of the anthraquinone to the mono- and di-anion species respectively (**EE** mechanistic pathway, refer to Figure 3.2) [136]. This voltammetric behaviour of the quinone moiety is significantly different from that observed in aqueous media (Section 3.1 and Chapter 4), where a single $2e^-$ wave is observed. This difference

in response is commonly interpreted in terms of the influence of both the hydrogen bonding ability of the solvent [93] and the nature of the supporting electrolyte [74].

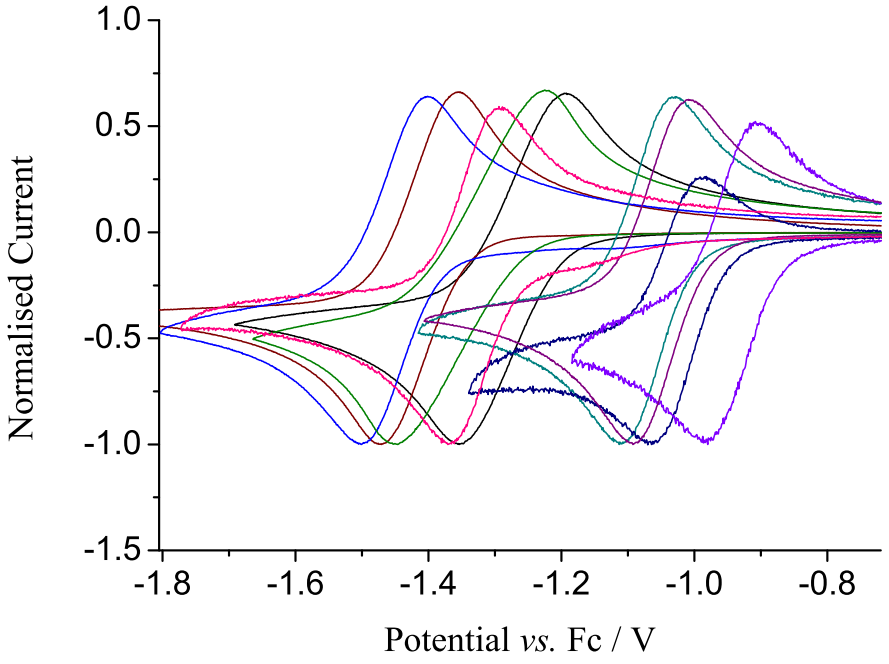

FIGURE 5.9: The first $1e^-$ reductions for a series of anthraquinone species in an acetonitrile solution, at a BDD macroelectrode, at 100 mV s^{-1}. From left to right, 2AAQ, 1AAQ, AQ, 2-HM-AQ, 1CAQ, 1,4-DH-AQ, 1,8-DH-AQ, 1,5-DH-AQ and 6,7- DC-1,4-DH-AQ (see Table 5.4 for formal potentials).

Beyond the solvent influence, the formal potential at which the first electron reduction occurs may also be 'tuned' through the variation of the substituent groups present upon the anthraquinone. Figure 5.9 depicts the first $1e^-$ reductions for a series of anthraquinone derivatives, in acetonitrile, where the position of the voltammetric wave is found to vary over 500 mV. Table 5.4 reports the formal potentials for these first $1e^-$ reductions against the ferrocene/ferrocenium redox couple. Of interest is the fact that the reduction potential becomes more positive by the inclusion of both oxygen and chlorine functionalities onto the aromatic structure; it is hence surmised that these moieties, due to their electronegativity,

result in the stabilisation of the LUMO relative to that of an unsubstituted anthraquinone. Conversely, the presence of amine substituents is found to increase the magnitude of the formal potential, shifting it to more negative values. For the above examples, the reductions of the anthraquinone species are found to be quasi-reversible, where the peak-to-peak separations vary between 220 and 63 mV.

Next, the eletro-reduction of oxygen is explored. The reduction of oxygen (1.26 mM air-equilibrated solution) in an anhydrous acetonitrile solution was studied, both at a glassy carbon (GC) and a BDD electrode, at a scan rate of 100 mV s^{-1}, the results of which are depicted in Figure 5.10. For the response at the GC electrode, a clear quasi-reversible redox wave is observed at -1.30 V (*vs.* Fc) (mid-point potential = -1.25 V (*vs.* Fc)), this corresponds to the $1e^-$ reduction of the oxygen species to superoxide. At higher overpotentials, a second irreversible wave is observed relating to the second $1e^-$ transfer, corresponding to the formation of the peroxide species [89] (as discussed in Section 5.1). In comparison, on the BDD electrode only a single poorly defined reduction wave is observed which exhibits a large peak-to-peak separation of 1.14 V. It is of interest to note that the influence of the BDD electrode upon the electron transfer rate is voltammetrically more prominent (*i.e.* induces a larger shift in peak potential) for irreversible species. This experimental observation is to be expected and relates to the insensitivity of voltammetric procedure towards differences in high electron transfer rates (as defined relative to the scan rate).

The significantly larger peak-to-peak separation for the reduction of oxygen observed on the BDD electrode, as compared to the GC substrate, leads to the potential ability of studying the anthraquinone mediated reduction of oxygen within the non-aqueous media. Comparable experiments have been performed under aqueous conditions, where the semiquinone species was observed to be highly reactive

Anthraquinone derivatives	Formal potentials *vs.* Fc (V)	Peak-to-peak separation (mV)
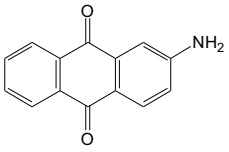 (2AAQ)	−1.45	97
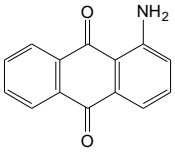 (1AAQ)	−1.41	114
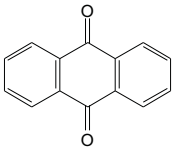 (AQ)	−1.34	22
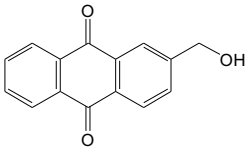 **(2-HM-AQ)**	**-1.33**	**72**
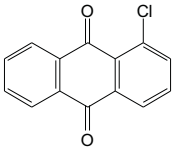 (1CAQ)	−1.28	158
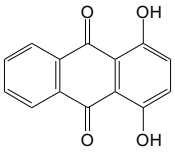 (1,4-DH-AQ)	−1.08	100
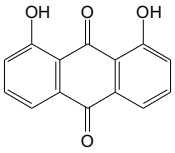 (1,8-DH-AQ)	−1.05	81
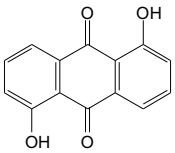 (1,5-DH-AQ)	−1.03	74
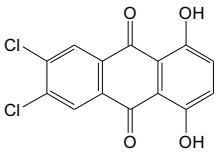 (6,7-DC-1,4-DH-AQ)	−0.95	63

TABLE 5.4: The formal potentials for the first electron reduction of anthraquinone derivatives against the ferrocene/ferrocenium redox couple.

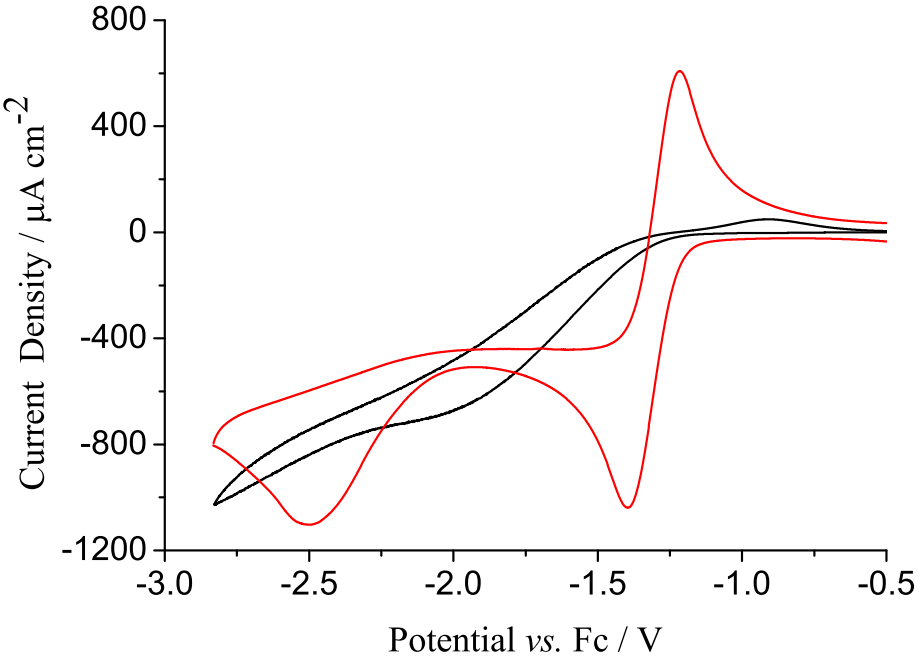

FIGURE 5.10: The direct reduction of oxygen (1.26 mM O_2, 1 mM Fc, 0.1 M TBAP in acetonitrile) at a BDD (black) and a GC (red) macroelectrode, at 100 mV s^{-1}.

towards the reduction of oxygen, as discussed in Section 3.1. However, due to the smaller potential range available for study in the present case (relative to that in aqueous media), careful selection of the electrocatalyst is required. The mediated reduction pathway is taken to be:

$$AQ + e^- \rightleftharpoons AQ^{\bullet -} \tag{5.11}$$

$$AQ^{\bullet -} + O_2 \xrightarrow{k_f} AQ + O_2^{\bullet -} \tag{5.12}$$

The above is an EC' mechanism, where the anthraquinone acts as an electrocatalyst and k_f is the homogeneous rate of reaction. If the formal potential for the anthraquinone species is more positive than −1.25 V (mid-point potential for the

first electron transfer in oxygen reduction), then Reaction 5.12 will not be thermodynamically favourable. Furthermore, if the formal potential for the AQ reduction is significantly more negative than this value, then the direct reduction of oxygen at the BDD surface will likely be the dominant reduction pathway.

Of the quinones presented within Table 5.4, 2-HM-AQ presents itself as a prime candidate for the study of the mediated reduction pathway. Figure 5.11 depicts the variable scan rate study ($25-400$ mV s^{-1}) of the first $1e^-$ reduction of the 2-HM-AQ species (0.1 mM). Its inset depicts the variation of the peak height as a function of the square-root of scan rate, where the linearity of this plot indicates that the process is purely diffusional in nature [6]. Moreover, the diffusion coefficient of $(2.40 \pm 0.04) \times 10^{-5}$ cm^2 s^{-1} was obtained through the measurement of the steady-state current at a gold microdisc electrode (not shown, same analysis as discussed in Chapter 4). The voltammetric response of this species was successfully modelled through DIGISIM®. A simple $1e^-$ reduction model was set up, as described in Chapter 4, where the heterogeneous rate of electron transfer was found to be 0.028 cm s^{-1}. It should be noted that this simulation is based upon a one-dimensional model and hence, due to the heterogeneous BDD surface, it is only a first approximation.

5.2.2.2 Electrocatalytic reduction of oxygen

The voltammetric response of 2-HM-AQ in the presence of oxygen was subsequently investigated, at a BDD electrode, as a function of scan rate, and a representative experimental result is depicted in Figure 5.12. Importantly the peak current for the catalysed reaction is found to occur at a potential where the direct

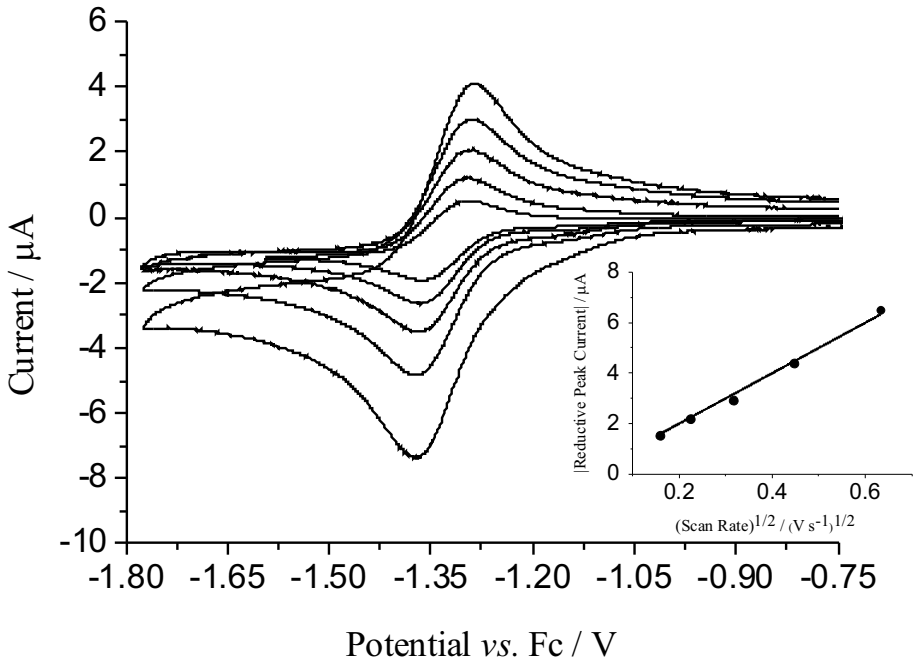

FIGURE 5.11: The first $1e^-$ reduction of 2-HM-AQ (0.1 mM 2-HM-AQ, 1 mM Fc, 0.1 M TBAP in acetonitrile), at a BDD electrode, variable scan rates ($25 - 400$ mV s^{-1}). The inset shows variation of the peak height as a function of the square-root of scan rate.

reduction of oxygen at the BDD surface is *minimal*. Hence, we are able to unambiguously study and determine the rate for the mediated reduction pathway (*i.e.* k_f).

The proposed EC' mechanism (Reactions 5.11 and 5.12) was modelled *via* DIGISIM® with the aim of elucidating the rate of transfer between the semiquinone and oxygen. It should be noted that analysis of this voltammetric response *via* classical procedures (*i.e.* not through simulation) was not feasible due to the anthraquinone species exhibiting quasi-reversible electron transfer kinetics upon the BDD surface. For the modelling, it was assumed that the diffusion coefficients of the species were unaltered upon reduction, where the transfer coefficient value for the reductions

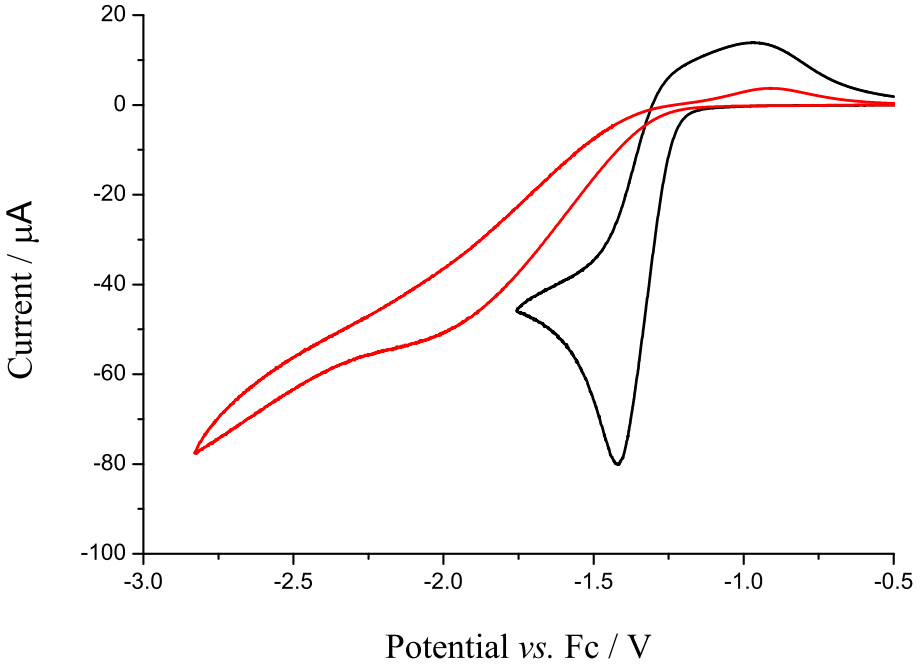

FIGURE 5.12: Representative result for the response of the 2-HM-AQ in the presence of oxygen (black, 1 mM 2-HM-AQ, 1.26 mM O_2, 1 mM Fc, 0.1 M TBAP in acetonitrile), at a BDD electrode, 100 mV s^{-1}, overlaid with the direct O_2 reduction (red, 1.26 mM O_2, 1 mM Fc, 0.1 M TBAP in acetonitrile) on the BDD surface. The direct O_2 reduction, at the potential where the peak current for the catalysed reaction is found to occur, is minimal.

was taken to be 0.5. Further, values for the diffusion coefficient and concentration of oxygen were taken to be 9.2×10^{-5} cm^2 s^{-1} and 1.26 mM respectively, as obtained from previous section (Section 5.1). Having modelled the direct O_2 reduction on the BDD surface, the electron transfer was found to be irreversible and the rate being of the order of 10^{-6} cm s^{-1}, which was taken into account within the simulations. Given that the formal potentials for the two redox species are also known, from experimentation, then the only unknown remaining in the simulation was the rate of reaction between the semiquinone and oxygen. This parameter was varied such that a best fit was achieved between the peak height of the experimental and simulated voltammogram as a function of scan rate, the results of which are depicted in Figure 5.13. As can be seen, a close agreement

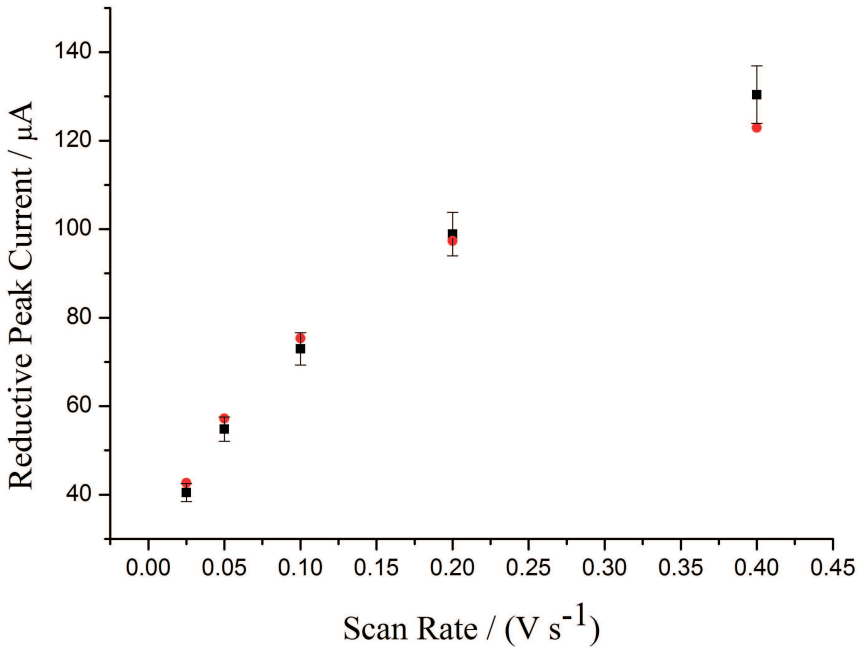

FIGURE 5.13: Peak height vs scan rate for experimental (black, 1 mM 2-HM-AQ, 1.26 mM O_2, 1 mM Fc, 0.1 M TBAP in acetonitrile) and simulated (red) responses of 2-HM-AQ in the presence of O_2.

between the simulated and experimental results was obtained; consequently, the rate of k_f was $(7 \pm 3) \times 10^6$ mol^{-1} dm^3 s^{-1}. Such a value, in comparison, is less than three orders of magnitude lower to that obtained in an aqueous media, *i.e.* $(4.8 \sim 6) \times 10^9$ mol^{-1} dm^3 s^{-1}, simulated in Section 3.1. Despite of the same electrode material and minimum ion pairing effect (as highlighted in Chapter 4), the major difference in these two systems is the solvent. In aprotic solvent, both superoxide and semiquinone radical anions are stable, evidenced by their distinct $1e^-$ redox waves. Although semiquinone is formed over a wide potential window in acetonitrile, the rate of solution reaction is constrained by the stablised nature of the reactive intermediates.

5.2.3 Conclusions

The study of oxygen reduction in acetonitrile systems is of significance due to the higher oxygen solubility within this medium as compared to aqueous environments. Hence, this may prove to be a beneficial synthetic route towards the electrochemical production of hydrogen peroxide. However, the thermodynamics of the electrochemical system is significantly altered as compared to that of protic (aqueous) environments, where importantly in the present experimental example the superoxide species is stable. Work in this section has been focussed upon the study of the mediated oxygen reduction pathway in anhydrous acetonitrile. It has been successfully demonstrated that, first, the formal potential for the one-electron reduction of anthraquinone may be controlled through varying the substituent groups upon the aromatic system and second, that the direct oxygen reduction at the electrode, in aprotic media, to form the superoxide species may be experimentally 'slowed' through the use of a BDD electrode (in comparison to Section 5.1). Consequently the anthraquinone mediated reduction of oxygen can be unambiguously studied within the aprotic environment. Through modelling of the electrochemical system, it was possible to show that the one-electron reduction of oxygen, mediated by the 2-HM-AQ semiquinone species, has a bimolecular reaction rate of $(7 \pm 3) \times 10^6$ M^{-1} s^{-1}.

The above results provide the basis upon which future investigations may be initiated, where work will look towards the use of a mixed solvent (water/acetonitrile) for electrocatalytic reduction of oxygen in which high solubility of oxygen and fast rate of solution reaction with semiquinone is sought to be balanced.

In the next section, kinetic studies of the electrocatalysis of oxygen reduction in ethanol media will be discussed. Oxygen is expected to dissolve to a greater extent

in *pure* ethanol than acetonitrile (*e.g.* 10.04 mM and 8.1 mM reported by Che *et al.* [125]).

5.3 Methyl viologen mediated oxygen reduction in ethanol

5.3.1 Introduction

Methyl viologen (MV^{2+}) has been studied as a redox mediator in biological systems and as a component for LEDs and LCDs due to marked colour difference between its oxidation states [55, 56, 137]. As shown in Figure 5.14, methyl viologen exhibits three main oxidation states, viz. MV^{2+}, $MV^{\bullet+}$ and MV^{0}. Its electrochemical redox behaviour has been investigated in various electrolytic solvents, such as dimethyl sulfoxide, dimethylformamide, dichloromethane, *etc.* using hanging mercury drop, gold, platinum, glassy carbon, pyrolytic graphite carbon, boron-doped diamond electrodes [70, 137–139]. In most cases, the rates of electron transfer for both the first and second reductions demonstrate fast kinetics.

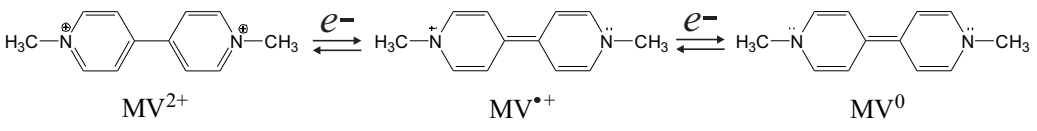

FIGURE 5.14: Structures of three oxidation states of methyl viologen.

The methyl viologen mediated reduction of oxygen can be described as an electrocatalytic EC' mechanism. The product of this process is hydrogen peroxide (see Section 3.2). The need for small scale synthesis of dilute peroxide solutions ($3-8\%$) has been highlighted in the previous section. The drawback often relates to the low oxygen concentration in aqueous solution. The use of organic solvents,

such as acetonitrile, dimethyl sulfoxide, dimethylformamide and ethanol [125], is able to offset the limitation of low oxygen solubility; thereafter increase the product concentration. The objective is to find a 'react-then-use' solution without further processing. Hence, within this section, ethanol was used as the reaction solvent to study the methyl viologen mediated oxygen reduction. Chronoamperometry was used to independently determine the precise values of the diffusion coefficient and concentration of oxygen independently in the electrolytic ethanol solution. Prior to electrocatalytic analysis, both oxygen and methyl viologen were studied independently. For the first time methyl viologen mediated oxygen reduction in ethanol is shown to be feasible on both boron-doped diamond electrodes and carbon microdisc electrodes. The electrocatalytic behaviour is in contrast with that found in aqueous solution. The resulting electrocatalytic steady-state currents were successfully modelled for both air-equilibrated and oxygen-saturated conditions.

5.3.2 Results and discussion

5.3.2.1 Solubility and diffusion coefficient of oxygen

The O_2 electrochemical redox response in an air-equilibrated anhydrous EtOH solution supported with 0.1 M tetra-*n*-butylammonium chloride (TBACl) was studied to obtain the concentration of oxygen (C_{O_2}) and diffusion coefficient of O_2 (D_{O_2}) using a carbon microdisc electrode (μ-C).

First, cyclic voltammograms were recorded at a scan rate of 25 mV s^{-1}, as shown in Figure 5.15. The scan was run from -0.5 V to -2.0 V (*vs.* Ag/AgCl - 1 M KCl). The formal potential of $O_2/O_2^{\bullet-}$ ($E_{O_2/O_2^{\bullet-}}$) in EtOH has not been reported

in the literature. However, a range of −0.825 V to −0.965 V (vs. Ag/AgCl - 1 M KCl) were previously reported in various other organic solvents [99]. At the potential range of *ca.* −1.2 V to −1.5 V, a steady-state current (I_{ss}) is achieved, corresponding to the reduction current of O_2. As the overpotential increases, further reduction is shown until it reaches solvent breakdown region beyond *ca.* −2.0 V. As can be seen in Figure 5.15 the current crosses over at high overpotential; this likely suggests a change of the electrode surface resulting from attack by the formed reactive oxygen species. A voltammogram of same scan rate reversed at −1.3 V is also shown in Figure 5.15, the inset of which illustrates scan rates variation from 5 to 1000 mV s^{-1}.

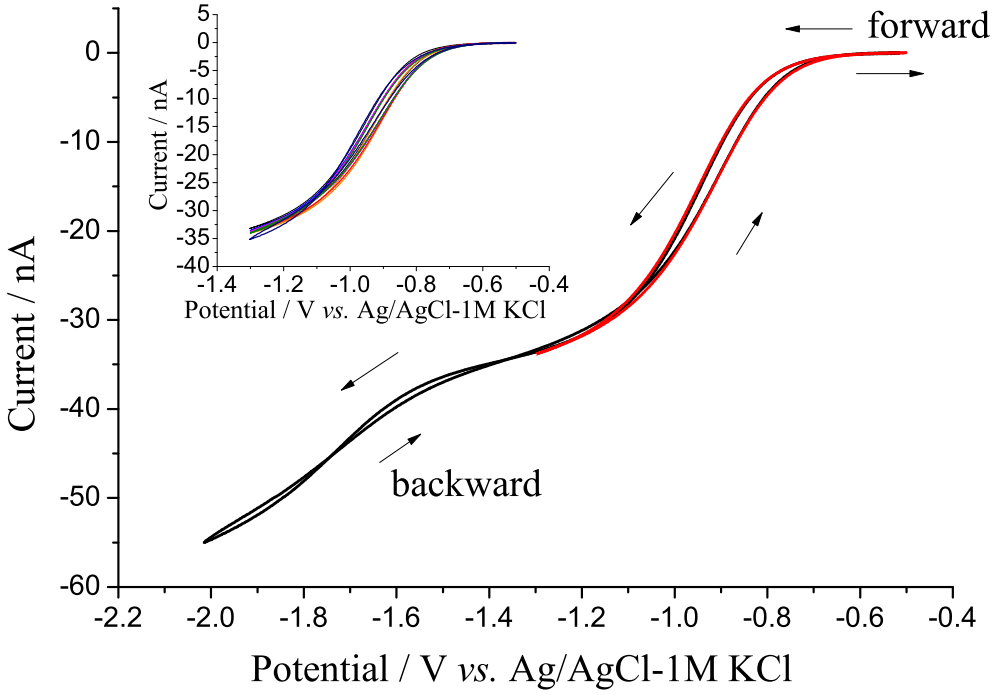

FIGURE 5.15: (Cyclic voltammogram for the direct O_2 reduction in an air-equilibrated EtOH / 0.1 M TBACl solution on a μ-C electrode at 25 mV s^{-1} (black line). A repeated scan reversed at −1.3 V is overlapped in red, and its scan rate variation of 5, 10, 25, 50, 100, 200 and 1000 mV s^{-1} are shown in inset.

Once the reduction potential was known, single potential step chronoamperometry

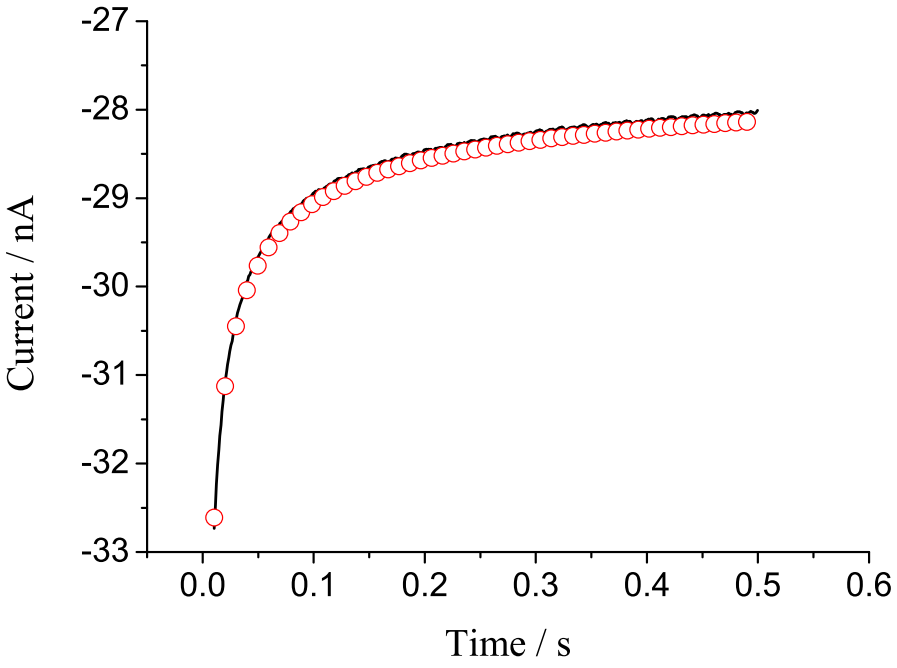

FIGURE 5.16: The experimental (line) and simulated (circle) single potential step chronoamperometric transients for O_2 reduction in air-equilibrated EtOH / 0.1 M TBACl solution on a μ-C electrode. The potential was stepped from 0 V to -1.25 V and back to 0 V *vs.* leakless Ag/AgCl - 1 M KCl electrode.

was performed to determine nC_i and D_i independently. Please refer the procedure in Section 2.3. Figure 5.16 shows the chronoamperomogram obtained in the same reaction solution by stepping a potential from -0.5 V to -1.25. In order to determine precise values of nC_i and D_i, the lowest mean scaled absolute deviation (MSAD) method was used (Section 2.4). The MSAD defines as the average error per point over the entire chronoamperometric transitents:

$$\text{MSAD}\% = \frac{1}{N}\sum_{N}\left|\frac{I_{sim} - I_{exp}}{I_{exp}}\right| \times 100 \tag{5.13}$$

where N is the number of experimental data points, I_{exp} is the experimental current and I_{sim} is the simulated current from Shoup and Szabo equation (Eqn. 1.27−1.29) [24]. This procedure can be computed and repeated by narrowing down the value

ranges for nC_i and D_i for the same chronoamperomogram. Figure 5.17 shows a two-dimensional contour plot of MSAD from the depicted chronoamperomogram in Figure 5.16, where x and y axes corresponding to nC_i and D_i respectively. The MSAD contour plot gives a minimum, as shown in Figure 5.17, correspond to the precise values of nC_i and D_i. It can be seen that there are also a wide range of nC_i and D_i values that satisfy the fitting criteria of a maximum error of less than 0.5% (MSAD % $<$ 0.5 %).

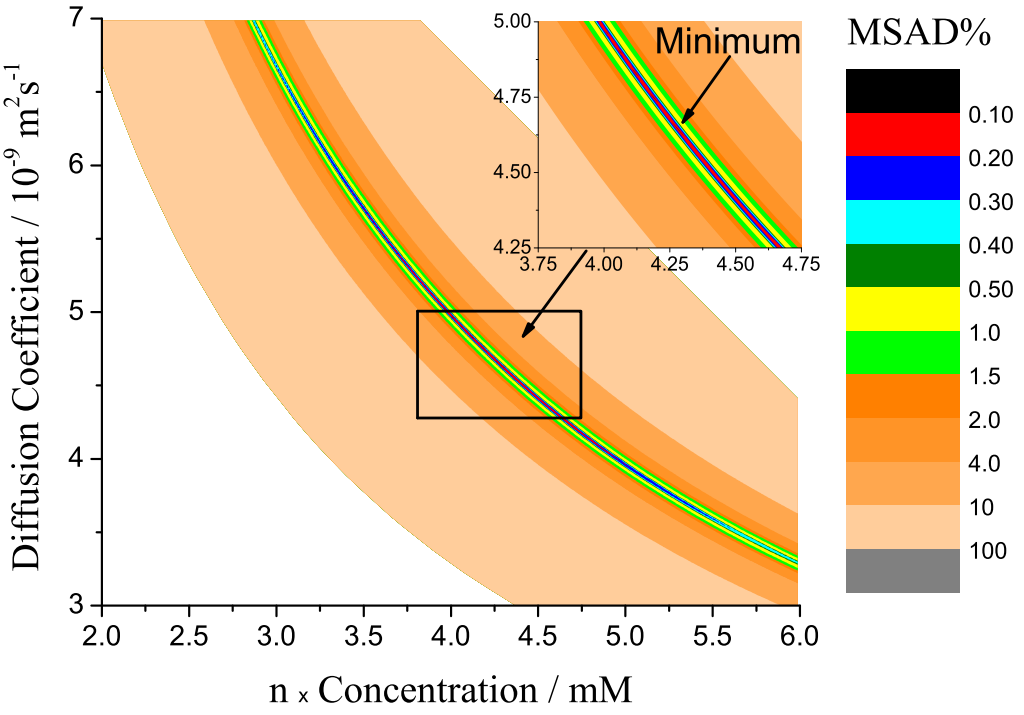

FIGURE 5.17: The two-dimensional contour plot of mean scaled absolute deviation (MSAD), where x axis corresponds to the product of concentration and the number of electron transferred, and y axis corresponds to the diffusion coefficient of O_2 in air-equilibrated EtOH / 0.1 M TBACl solution. The scale of MSAD is listed on the right. This is obtained from the chronoamperometry for the reduction of O_2 at a transient time of 0.5 second.

The final results of D_{O_2} and nC_{O_2} in an air-equilibrated EtOH were evaluated, by taking the mean of four sets of data with lowest MSAD%, to be $(4.70 \pm 0.41) \times 10^5$ $cm^2\ s^{-1}$ and (4.25 ± 0.39) mM respectively. The optimum fitting of simulated result is also shown in Figure 5.16. The experimentally obtained diffusion coefficient is

found to be comparable with the literature. Values for D_{O_2} range from $(1.64-4.0) \times 10^5$ cm^2 s^{-1}, despite the fact that all previously reported experiments were in the absence of supporting electrolyte [140–143]. To the best of the authors knowledge, it is the first time that D_{O_2} is determined in an electrolytic EtOH solution. Moreover, the C_{O_2} in an air-equilibrated EtOH can be determined by the evaluation of n, the number of electrons involved in the I_{ss}. The electrochemical reduction of O_2 demonstrates one to four electron transfers, dependent on conditions such as solvent media and electrode materials [99, 101, 144, 145]. However, the number of electrons transferred in electrolytic EtOH solution has not yet been identified. The value of n herein could be 1, 2, or 4. Che *et al.* reported the solubility of O_2 in pure EtOH being 10.04 mM [125]. Therefore, knowing that air contains 21% of O_2 [146, 147], only the value of n being 2 gives the most sensible solubility of O_2 in electrolytic EtOH solution, *i.e.* (10.14 ± 0.95) mM. Both values of C_{O_2} and D_{O_2}, as given in Table 5.5, are utilised later in the simulation for MV^{2+} mediated O_2 reduction.

Parameters	Values
C_{O_2} in air-equilibrated EtOH (mM)	2.13 ± 0.20
Solubility of O_2 (mM)	10.14 ± 0.95
$C_{MV^{2+}}$ (mM)	1.00
D_{O_2} ($\times 10^{-6}$ cm^2 s^{-1})	47.0 ± 4.1
$D_{MV^{2+}}$ ($\times 10^{-6}$ cm^2 s^{-1})	4.65 ± 0.04
k_s (cm s^{-1})	1
$E_{MV^{2+/\bullet+}}$	−0.352 V (*vs.* Ag/AgCl - 1 M KCl)
$\alpha_{MV^{2+}}$	0.79

TABLE 5.5: Parameters used in the EC' catalysis model. All data are corrected against a leakless Ag/AgCl - 1 M KCl reference electrode at (298 ± 0.2) K in a 0.1 M TBACl supported EtOH.

5.3.2.2 Methyl viologen redox response and kinetics

Before further elaboration of mediated redox response of MV^{2+} upon O_2 reduction, the MV^{2+} redox reaction in the absence of oxygen is first investigated.

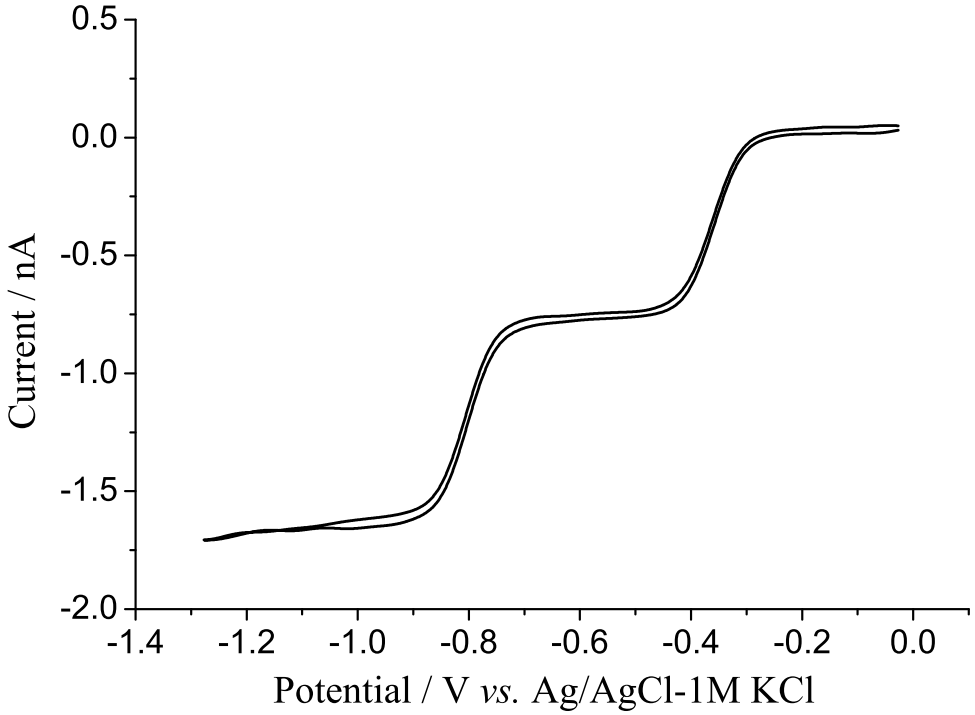

FIGURE 5.18: Cyclic voltammogram for the two $1e^-$ redox of 1 mM MV^{2+} in a N_2-saturated EtOH/0.1 M TBACl solution on a μ-C electrode at 25 mV s^{-1}.

The 1.00 mM MV^{2+} electrochemical responses were carried out in a N_2-saturated EtOH solution supported with 0.1 M TBACl salt on a μ-C electrode. The two $1e^-$ redox signal was first obtained at 25 mV s^{-1} and is shown in Figure 5.18. Two steady-state currents were achieved, corresponding to the first and second electron reduction of MV^{2+} to form $MV^{\bullet+}$ and MV^0 respectively. Similar responses were also reported in other solvents, namely dimethyl sulfoxide [70], dimethylformamide [138] and aqueous systems (see later in Figure 5.21) [64, 139]. These two electron transfers are well separated by over 200 mV. As a result, at lower overpotentials there is substantial amount of radical cations produced, which are able

to diffuse away from the electrode surface and participate in the electrocatalysis. The electrocatalytic mechanism herein is focused mainly on the mediator couple $MV^{2+/\bullet+}$.

Accordingly the first electron reduction of MV^{2+} is studied. Cyclic voltammetries were recorded on a μ-C electrode at variable scan rates ranging from 5 to 1000 mV s^{-1}, shown in Figure 5.19. The diffusion coefficient of MV^{2+} ($D_{MV^{2+}}$) in EtOH supported with 0.1 M TBACl solution can be calculated from Eqn. 5.14 *via* I_{ss} at low scan rate (5 mV s^{-1}) [1]:

$$I_{ss} = 4nFr_eD_{MV^{2+}}C_{MV^{2+}} \tag{5.14}$$

where n is the number of electrons transferred, r_e is the radius of the electrode (cm) and $C_{MV^{2+}}$ is the concentration (mol dm^{-3}) of MV^{2+}. A value of (4.65±0.04) $\times 10^6$ cm^2 s^{-1} was obtained for $D_{MV^{2+}}$. The transfer coefficient, α, can be obtained from a Tafel plot. The representative Tafel plot is shown as inset in Figure 5.19(a) at 5 mV s^{-1}, and the corresponding α value is 0.79. $E_{MV^{2+/\bullet+}}$ in EtOH solution is assumed to be the same as the half-wave potential, being −0.352 V (*vs.* Ag/AgCl - 1 M KCl).

Utilising all the parameters obtained above, the heterogeneous electron transfer rate constant (k_s) can be obtained by a microdisc simulation model developed by Klymenko (Section 2.4) [32]. The simulated CVs were optimized by fitting both the wave shape and I_{ss} at scan range from 5 to 1000 mV s^{-1}. The fitted data are shown in Figure 5.19 at 5, 100, and 1000 mV s^{-1}. It can be seen that as the scan rate increases, the convergent diffusional regime gradually switches to linear diffusion due to the reduced experimental time scale. Note that the experimental CVs were blank subtracted and baseline corrected. Excellent agreement is achieved between

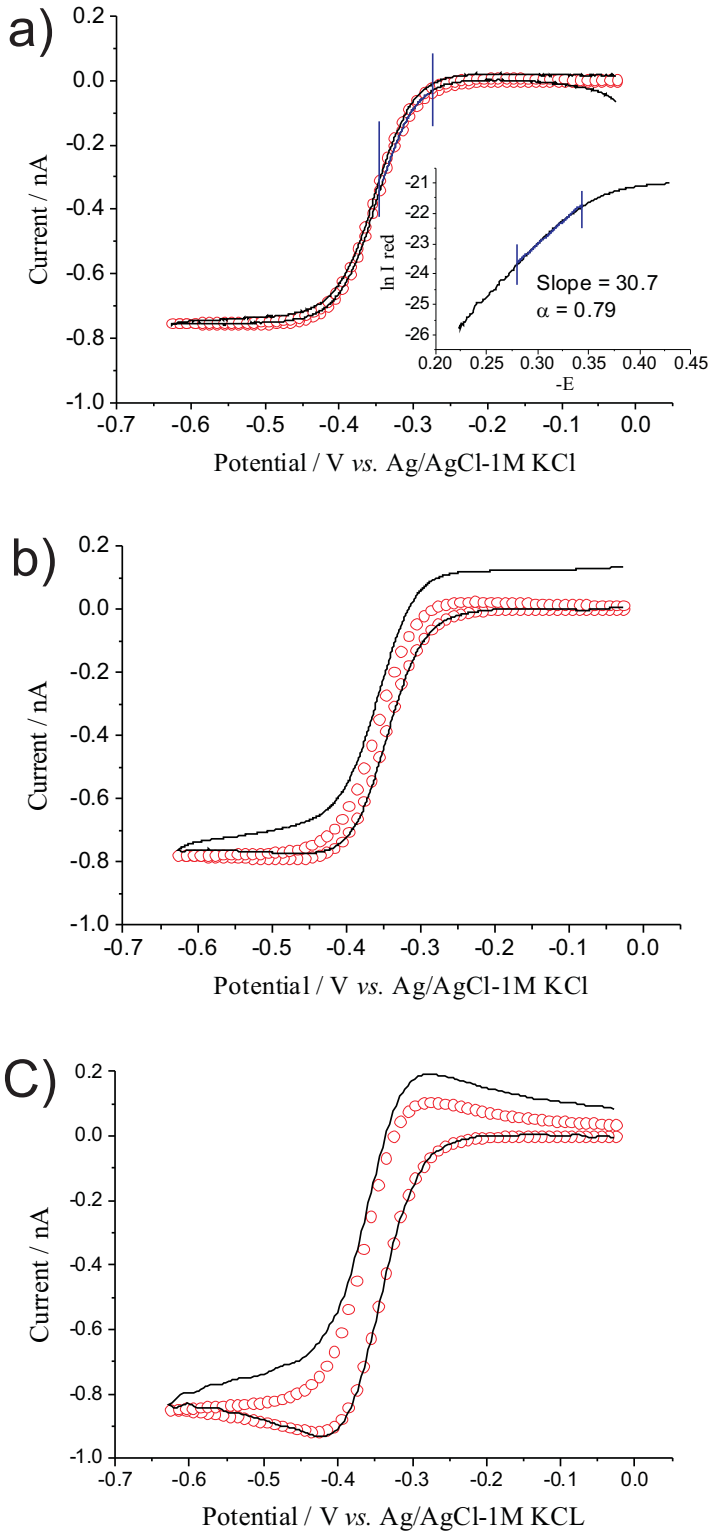

FIGURE 5.19: The experimental (line) and simulated (circle) cyclic voltammograms for the $1e^-$ transfer of 1 mM MV^{2+} in a N_2-saturated EtOH / 0.1 M TBACl solution on a μ-C electrode at scan rates of (a) 5 mV s^{-1} (The forward scan highlighted in blue was selected as Tafel analysis region. Inset is the Tafel plot of α being 0.79); (b) 100mV s^{-1}; (c) 1000mV s^{-1}.

experimental and simulated results. The simulated CVs become unchanged when $k_s \geq 1$ cm s^{-1}.

After having obtained the parameters for both MV^{2+} and O_2 necessary for the simulations reported below, the mediated responses are now further discussed.

5.3.2.3 Methyl viologen mediated oxygen reduction

The electrocatalytic EC' mechanism of MV^{2+} mediated O_2 reduction is proposed as follows,

$$MV^{2+} + e^- \overset{k_s}{\rightleftharpoons} MV^{\bullet+} \qquad E_{MV^{2+/\bullet+}} \tag{5.15}$$

$$MV^{\bullet+} + O_2 \overset{k_f}{\longrightarrow} MV^{2+} + O_2^{\bullet-} \tag{5.16}$$

where $E_{MV^{2+/\bullet+}}$ is the formal potential of $MV^{2+/\bullet+}$ redox couple, k_s is the heterogeneous electron transfer rate constant (cm s^{-1}), and k_f is the homogeneous rate of electron transfer (dm^3 mol^{-1} s^{-1}). In the EC' mechanism, MV^{2+} acts as the mediator to reduce O_2 to superoxide ($O_2^{\bullet-}$) *via* reduction to $MV^{\bullet+}$.

First, the electrocatalytic response of O_2 reduction in an air-equilibrated EtOH solution supported with 0.1 M TBACl on a boron-dope diamond (BDD) macroelectrode is shown in Figure 5.20. The cyclic voltammogram of MV^{2+} reduction in N_2-saturated solution represents two $1e^-$ reduction waves. The direct O_2 reduction only takes place at high overpotentials. The catalytic peak at -0.71 V corresponds to the $MV^{\bullet+}$ mediated O_2 reduction. There is a second reductive wave at *ca.*-1.0 V at the electrocatalytic diffusional current tail. It may correlate to nonelectrocatalytic reduction of $MV^{\bullet+}$ to MV^0. However, the overlap between the

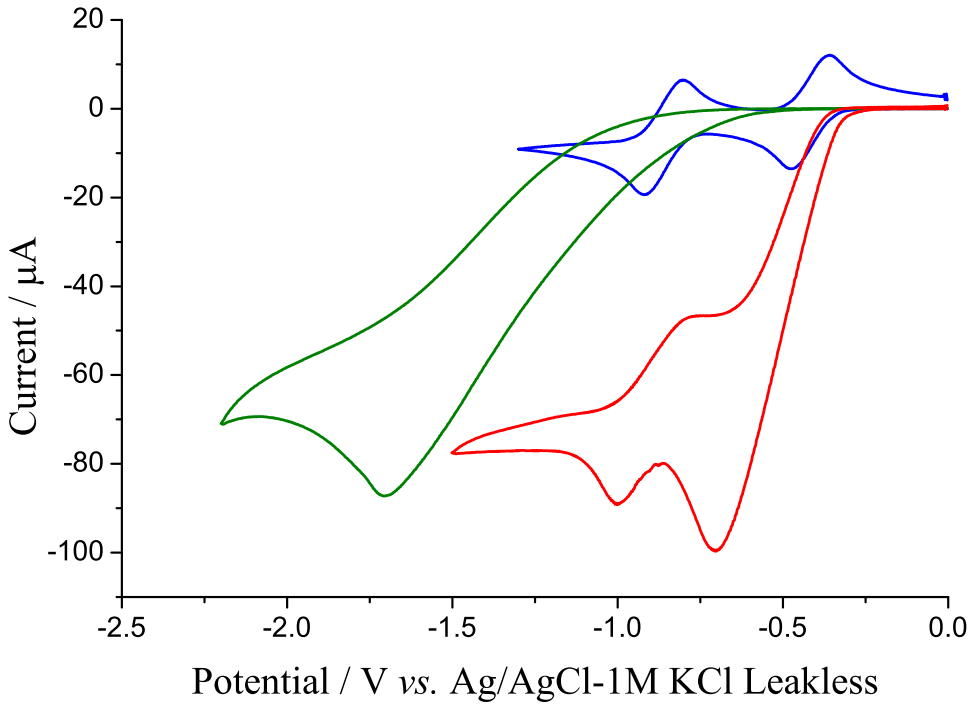

FIGURE 5.20: Comparison of cyclic voltammograms in EtOH / 0.1 M TBACl solution on a BDD electrode at 100 $mV{\cdot}s^{-1}$. Blue: two $1e^-$ transfer waves of 1 mM MV^{2+} in N_2-saturated solution; Green: direct reduction of O_2 in air-equilibrated solution; Red: 1 mM MV^{2+} mediated O_2 reduction in air-equilibrated solution.

$MV^{\bullet+/0}$ redox response and direct O_2 reduction complicates any definitive analysis upon gaining electrocatalytic kinetics information. Therefore, the following study in ethanolic solution is mainly focused on the radical cation mediated O_2 reduction.

Voltammetric responses in are markedly different in aqueous solution as compared to that in EtOH solution. Figure 5.21 shows the same redox couples were run in aqueous phosphorous buffer solution (PBS, pH 6.7) supported with 0.1 M potassium chloride on a μ-C electrode. The cyclic voltammograms demonstrate 1.00 mM MV^{2+} redox only, O_2 direct reduction, and MV^{2+} redox in the presence of air O_2. The consecutive two $1e^-$ reduction I_{ss} waves are clearly shown for redox couples of $MV^{2+/\bullet+}$ and $MV^{\bullet+/0}$. The direct O_2 reduction commences at *ca.* 300

mV more positive in potential as compared to the first electron transfer of MV^{2+}.

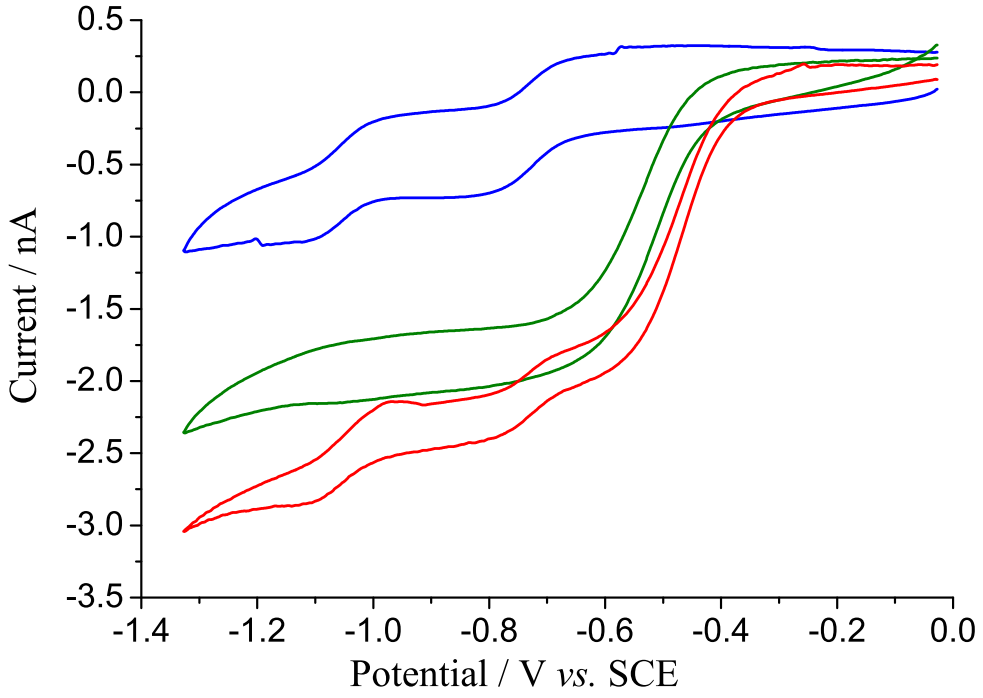

FIGURE 5.21: Comparison of cyclic voltammograms in aqueous PBS / 0.1 M KCl (pH 6.7) on a μ-C electrode at 25 mV s^{-1}. Blue: two 1-electron transfer waves of 1 mM MV^{2+} in N_2-saturated PBS; Green: direct reduction of O_2 in air-equilibrated PBS; Red: presence of both 1 mM MV^{2+} and air O_2.

Unsurprisingly, when combining both redox species in the aqueous solution, *no* electrocatalytic response is seen (Figure 5.21). The three redox waves correlate to the O_2/H_2O_2, $MV^{2+/\bullet+}$ and $MV^{\bullet+/0}$ responses. In order to achieve a favourable homogeneous electron transfer process (Eqn. 5.16), the formal potential of $O_2/O_2^{\bullet-}$ should be at more positive potential as compared to that of the $MV^{2+/\bullet+}$ redox couple. Knowing the $E_{O_2/O_2^{\bullet-}}$ of -0.4212 V and $E_{MV^{2+/\bullet+}}$ of -0.7055 V in aqueous solution *vs.* standard calomel electrode (SCE) [45, 139], the homogeneous electron transfer process (Eqn. 5.16) is expected to be thermodynamically favourable. However, the direct O_2 reduction takes place with much lower driving force. Therefore, no electrocatalytic reduction is seen here. The fact that the $E_{O_2/O_2^{\bullet-}}$ exhibits a much more positive potential in water than in anhydrous solvents as against

$E_{MV^{2+/\bullet+}}$ is presumably related to the stronger solvation of $O_2^{\bullet-}$ by water as compared with organic solvents.

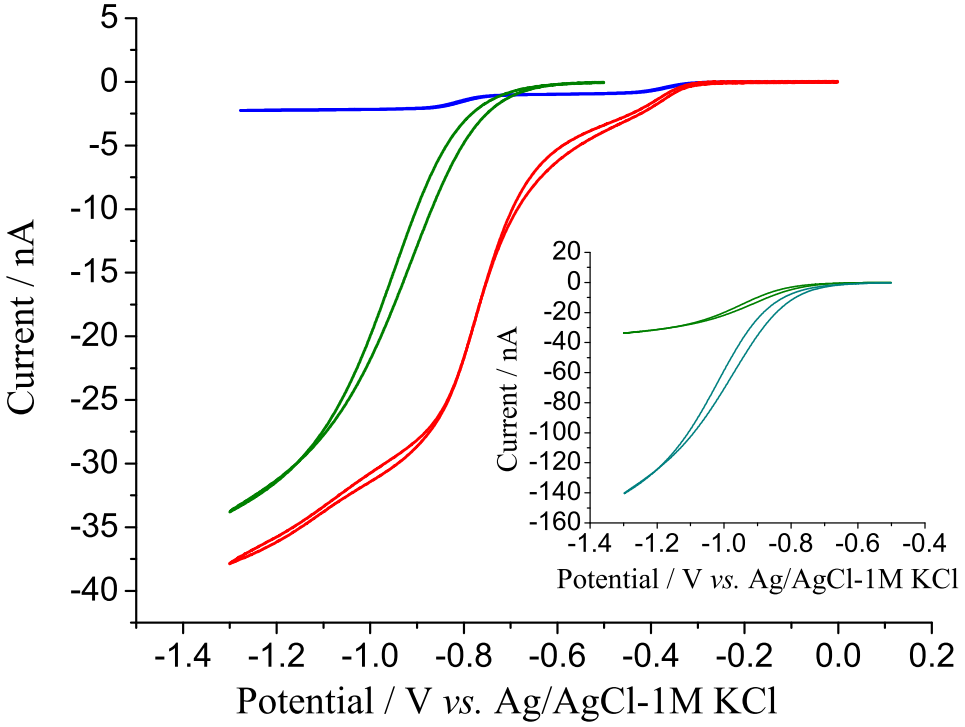

FIGURE 5.22: Comparison of cyclic voltammograms in EtOH / 0.1 M TBACl solution on a μ-C electrode at 100 mV s^{-1}. Blue: two 1-electron transfer waves of 1 mM MV^{2+} in N_2-saturated solution, Green: direct reduction of O_2 in an air-equilibrated solution; Red: 1 mM MV^{2+} mediated O_2 reduction in air-equilibrated solution. Inset depicts the direct reduction of O_2 in air-equilibrated (green) and O_2-saturated (cyan) EtOH solution.

Voltammetric responses in electrolytic EtOH media is next discussed. Figure 5.22 shows the corresponding cyclic voltammograms at a scan rate of 25 mV s^{-1} for 1.00 mM MV^{2+} mediated O_2 reduction signal, direct two $1e^-$ MV^{2+} redox and direct $2e^-$ air O_2 redox, respectively, where the inset shows a comparison of direct O_2 reduction in both air-equilibrated and pure O_2-saturated EtOH solution. It is evident that within the region of the first electron reduction of $MV^{2+/\bullet+}$ ($E_{MV^{2+/\bullet+}}$ is -0.352 V) there is no heterogeneous current contribution from O_2 reduction, where the latter only occurs after *ca.* -0.6 V. Therefore, on the mediated signal response the current contribution prior to -0.6 V accounts for the electrocatalytic

reduction of O_2 *via* $MV^{\bullet+}$ intermediate species (Eqn. 5.16), and beyond −0.6 V the background current contribution is mainly from direct O_2 reduction.

The important feature of zero-current from heterogeneous O_2 reduction on a μ-C electrode enables an unambiguous study of the electrocatalytic process of MV^{2+} mediated O_2 reduction. An attempt to study the homogeneous step is carried out here. The proposed EC' mechanism was modelled *via* an in-house developed program by Ward *et al.* (Section 2.4) [33]. Parameters used in the simulation, such as C_{O_2} in air-equilibrated EtOH, solubility of O_2, D_{O_2}, $C_{MV^{2+}}$, $D_{MV^{2+}}$, k_s, $E_{MV^{2+/\bullet+}}$ and $\alpha_{MV^{2+}}$ are tabulated in Table 5.5. $MV^{\bullet+}$ is assumed to have the same diffusion coefficient as MV^{2+}, and $O_2^{\bullet-}$ is assumed to have the same diffusion coefficient as O_2. By utilising the simple EC' mechanism, the model was optimized to give a best fit by considering both the wave shape and steady-state current.

The air-equilibrated response was first simulated. Figure 5.23 depicts both the experimental (line) and simulated (circle) data of electrocatalytic responses of O_2 reduction in an air-equilibrated EtOH solution. An excellent correlation of experimental and simulated results is shown at *ca.* −0.4 V. The simulated homogeneous rate of electron transfer is (1.0 ± 0.1) $\times 10^5$ dm^3 mol^{-1} s^{-1}. If taking Eqn. (5.14) and known C_{O_2} and D_{O_2} for $2e^-$ reduction of O_2, the estimated I_{ss} for complete reduction is about 15 nA. It is in contrast to the experimentally obtained I_{ss} of *ca.* 2.5 nA. Hence, it can be concluded that the homogeneous electron transfer step (Eqn. 5.16) is the rate determining step. This was further proved *via* simulation by increasing k_f until 1 $\times 10^8$ dm^3 mol^{-1} s^{-1} when current limits at about 15 nA (not shown). Moreover, the much smaller I_{ss} suggests that only partial catalysis is achieved. As previously discussed in Section 3.2, in an aqueous system the concentration ratio of the mediator against O_2 can directly relate to a switch

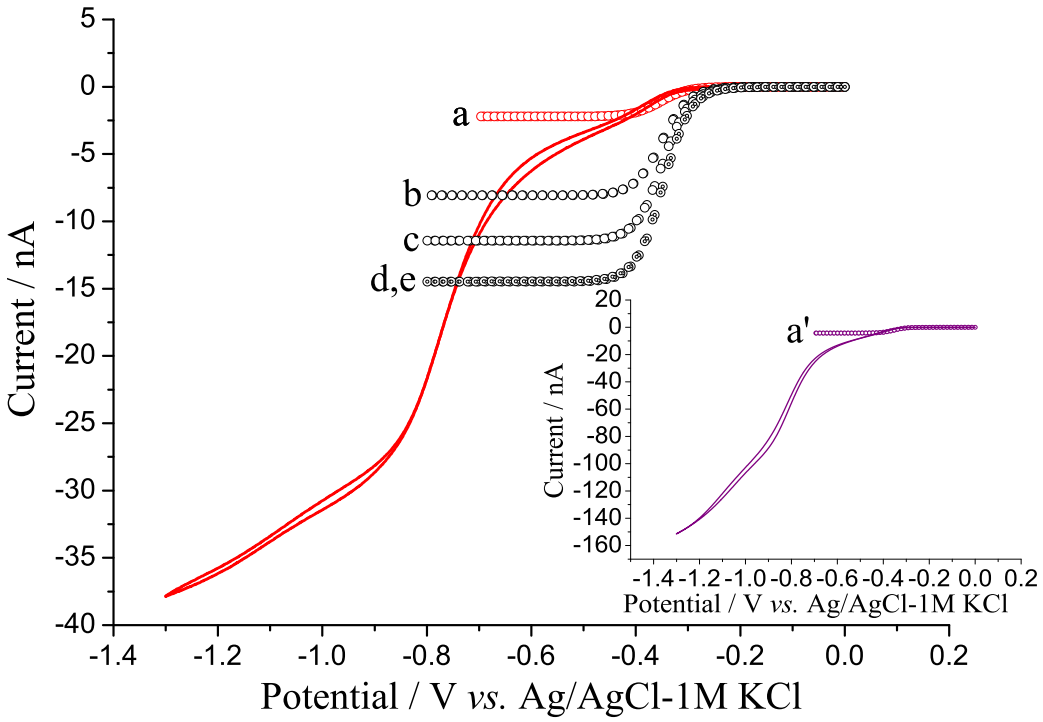

FIGURE 5.23: The experimental (line, 1mM MV^{2+}) and simulated (circle, various concentration of MV^{2+}) steady-state currents of MV^{2+} mediated O_2 reduction in both air-equilibrated (red) and O_2-saturated (purple, inset) EtOH / 0.1 M TBACl solution on a μ-C electrode at 100 mV s^{-1}. (a) and (a') 1mM MV^{2+}; (b) 4mM MV^{2+}; (c) 6mM MV^{2+}; (d) 8mM MV^{2+}; (e, smaller circle) 10mM MV^{2+}, where k_f is 1 $\times 10^5$ dm^3 mol^{-1} s^{-1} for all simulations.

between partial catalysis to 'total catalysis' [139]. By increasing this concentration ratio, it is predicted that the partial catalysis can also be tuned towards the 'total catalysis' regime [62, 63, 139]. This can be further proved *via* simulation by increasing $C_{MV^{2+}}$ from 1 mM to 4, 6, 8 and 10 mM (Figure 5.23), keeping C_{O_2} and k_f unchanged. As $C_{MV^{2+}}$ approaches *ca.* 8 mM the I_{ss} limits at about 15 nA. Oxygen reduction 'total catalysis' now takes place. The same parameter of k_f being 1 $\times 10^5$ dm^3 mol^{-1} s^{-1} is then used to simulate the O_2-saturated case, shown in Figure 5.23. Again, a good agreement was achieved.

Moreover, it is of interest to note that there is an elevation after the predicted steady-state currents for both air-equilibrated and O_2-saturated cases. This is

likely due to the migration current in the presence of MV^{2+} molecules. As migration of MV^{2+} molecules requires an electric field, the potential of zero charge (PZC) for the μ-C electrode was estimated, and a migration current would be observed at more negative potential than PZC. Moreover, a quantity of dielectric constant, ϵ_i, is an indicator here, which measures the extent to which a solvent can reduce the energy of interaction of ions dissolved in it. Under the studied conditions, the low dielectric constant of ethanol ($\epsilon_{EtOH} = 24.6$) [148] compared to water ($\epsilon_{H_2O} = 78.4$) or acetonitrile ($\epsilon_{CH_3CN} = 36.0$) [149] is suggested to lead to a more significant migration contribution.

Information about the PZC comes from the investigation of interfacial capacitance at low concentrations of supporting electrolyte [6]. The specific capacitance of the system was estimated by cyclic voltammetry as a function of potential, in an EtOH solution supported with only 1.00 mM TBACl. Each cyclic voltammogram was recorded over a limited potential range of 50 mV at a high scan rate of 2 V s^{-1}, shown in Figure 5.24(a). The difference in current between the forward and backward scan (I_{cap}, A) can be correlated to the specific capacitance of the electrode (C_{sp}, μF cm^{-2}) by the following equation:

$$I_{cap} = 2\ \nu\ C_{DL} \tag{5.17}$$

where $C_{DL} = A \times C_{sp}$. Parameters are defined as ν being the scan rate (V s^{-1}), C_{DL} being the double layer capacitance (μF) and A being the area of the electrode surface (cm^2). Hence, given the measured I_{cap} and A, C_{sp} can be plotted in Figure 5.24(b). The distinct minimum observed at *ca.* 0 V likely corresponds to the PZC [150–152]. A significant increase in C_{sp} is observed specifically when the potential becomes more negative than -0.4 V. It suggests that at potentials

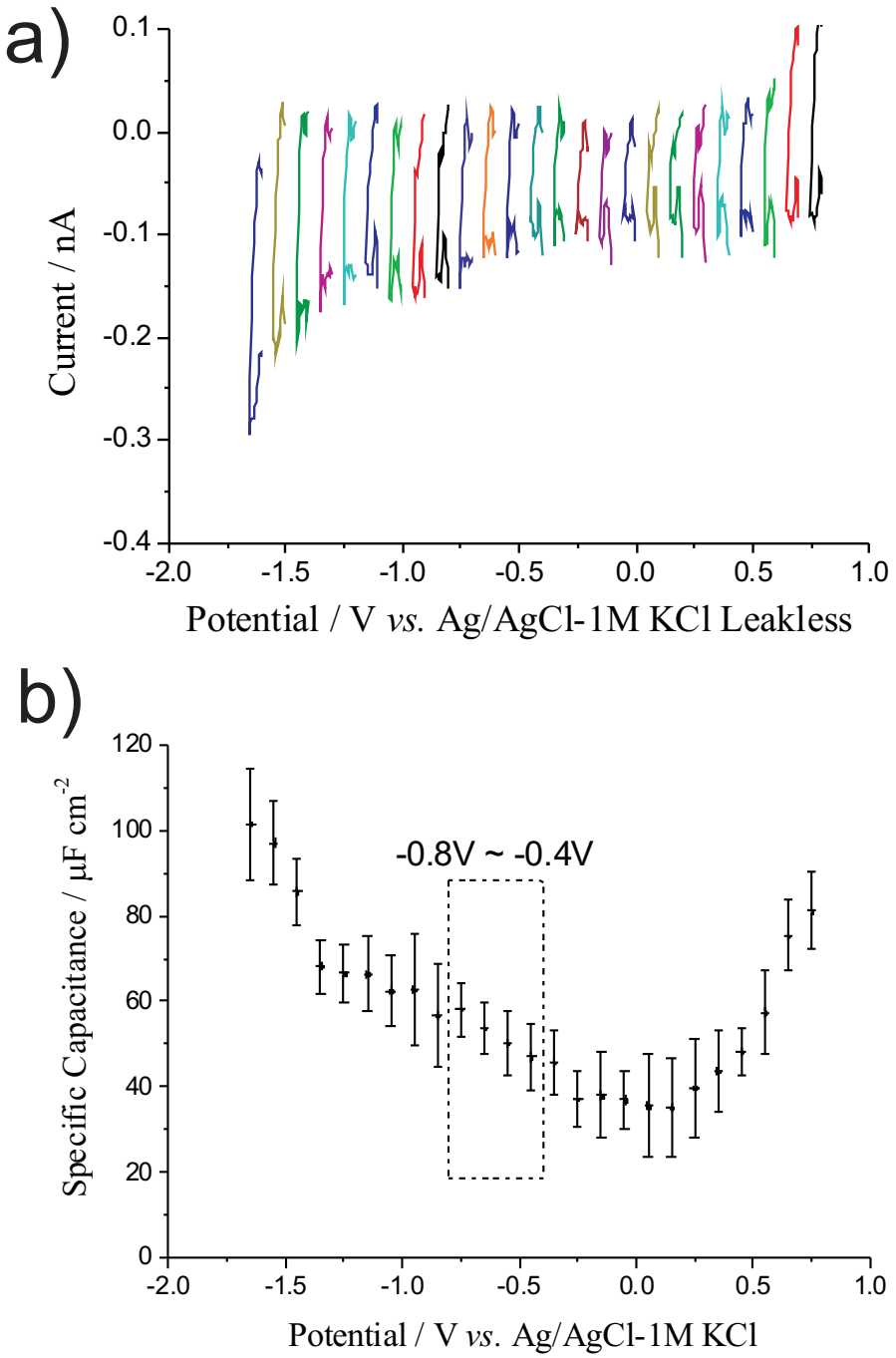

FIGURE 5.24: (a) Overlap of cyclic voltammograms containing no electro-active species in a N_2-saturated EtOH supported with only 1 mM TBACl over a limited potential range of 50 mV at a high scan rate of 2 V s^{-1} at a μ-C electrode. (b) The variation of specific capacitance for a μ-C electrode as a function of potential in N_2-saturated EtOH / 1 mM TBACl solution.

negative of the PZC, the charged molecules are more inclined to be attracted towards the electrode surface. The boxed region can account for the difference in current in the corresponding potential range between experimental and simulated voltammograms. This *migration* contribution, in fact, is arguably useful because it is enhancing the mass transport again over above diffusion in electrocatalytic O_2 reduction. It should be noted that migration effects are only apparent for the mediated and not the MV^{2+} only reduction. This likely arises due to the relatively small size of the reaction layer under electrocatalysis as compared to the unperturbed diffusion layer in the absence of O_2. Upon contraction of the reaction layer to dimensions comparable to that of the electric field the mass transport of the positively charged MV^{2+} towards the electrode will be increased. This greater mass transport may result in the observed potential dependent enhancement of the electrocatalytic responses.

5.3.3 Conclusions

The study of oxygen reduction in ethanol systems is of significant importance due to the higher oxygen solubility in this solvent as compared to aqueous and other organic solvent environments. Hence, this may prove to be a beneficial route towards the electrochemical synthesis of hydrogen peroxide. This section has been focussed upon the study of the mediated oxygen reduction in ethanol solution. However, the thermodynamics, kinetics and mass transport of the electrochemical system are significantly altered as compared to that of aqueous environment. To the best knowledge of the authors, it is the first time that these data have been obtained electrochemically in an electrolytic ethanol solution. The diffusion

coefficient and solubility of oxygen were determined *via* chronoamperometry using Shoup and Szabo analysis and mean scaled absolute deviation method in an electrolytic ethanol solution to be $(4.70 \pm 0.41) \times 10^{-5}$ cm^2 s^{-1} and (10.14 ± 0.95) mM. The number of electrons involved in the first steady-state current was evaluated to be 2, showing H_2O_2 to be the reaction product. Moreover, the diffusion coefficient of methyl viologen was obtained from the steady-state current, being $(4.65 \pm 0.04) \times 10^{-6}$ cm^2 s^{-1}. Fast electrode kinetics was shown by simulation fitting. The heterogeneous electron transfer rate constant is $k_s \geq 1$ cm s^{-1} with the obtained transfer coefficient of 0.79.

For the first time methyl viologen mediated oxygen reduction in ethanol has been proved to be feasible *via* both boron-doped diamond and micro-carbon disc electrodes. The electrocatalytic response is demonstrated to be due to the radical cation, $MV^{\bullet+}$, mediated oxygen reduction. Successful modelling of the experimental data results in a homogeneous rate constant of $(1.0 \pm 0.1) \times 10^5$ dm^3 mol^{-1} s^{-1}, of which step was shown to be the rate determining step. Under the studied experimental conditions, only partial catalysis was obtained. With the aid of simulation program, it can be seen that by increasing the concentration ratio of MV^{2+} to O_2 a 'total catalysis' regime can be achieved. Moreover, a potential dependent electrocatalytic steady-state current is likely resulted from the migration current contribution, which can be arguably useful because it is enhancing the mass transport again over above diffusion in electrocatalytic O_2 reduction.

Hitherto, the electro-reduction of oxygen and its mediated pathways have been studied in three solvent media, *i.e.* anhydrous acetonitrile, acetonitrile/water mixtures, and anhydrous ethanol. Although the solubility of molecular oxygen is

much higher in non-aqueous solvents, the bimolecular reaction rates prove to be 3 $\sim$ 4 orders of magnitude lower than these in the aqueous solution, primarily due to the decreased reactivity of intermediate species. Therefore, a balanced solubility and reaction rate will need to be reached when seeking any beneficial synthetic route towards electrochemical production of hydrogen peroxide. Such a question can be approached in future studies by a mixture of water and organic media, where water enhances the reactivity of intermediate species and organic media is able to increase the solubility of molecular oxygen.

So far, the mediator towards oxygen reduction has been studied under a diffusional regime. In the next chapter, a surface bound mediator will be investigated.

Chapter 6

Anthraquinonyl modified graphite surfaces

This chapter proposes a novel surface modification methodology for a 2-anthraquinonyl sub-monolayer formation. The modified layer is characterised with the aid of a simulation program showing near ideal behaviour. The work presented herein was published in the article *'New J. Chem. 2011, 35, 2462-2470'*.

6.1 Introduction

Carbon is an attractive electrode substrate due to its low cost, high electrical conductivity, and wide voltammetric potential window [153, 154]. There are a large variety of carbon forms bearing different chemical and physical properties, such as pyrolytic graphite, glassy carbon, carbon black, boron doped diamond, and carbon nanotubes (CNTs) *etc.* [155]. Graphitic carbon electrodes are of particular interest, not only because they can provide structurally well-defined models as compared with other more disordered carbon materials, but also because they exhibit different surface electroactivities. Depending upon how the graphite layers are cut, either perpendicular or parallel to the graphene layers, an electrode

can be predominantly either edge plane or basal plane in nature, shown in Figure 6.1. It is generally accepted that the rate of electron transfer is much greater at the edge plane sites/defects as compared with basal plane sites for both diffusional [156–158] and diffusionless systems [159, 160]. Moreover, adsorption onto graphitic surfaces can also be influenced by the density of edge plane sites. It has been shown that the electron transfer rates and adsorption on graphitic surfaces are highly dependent on factors including the density of states (DOS) of the graphite surface, the presence of surface functional groups, and the nature of the redox couple in respect to the mechanism of electron transfer [161]. Furthermore the electrochemical response of CNTs may be understood by analogy with graphite, where the side walls are related to basal plane sites and the tube ends are comparable to edge plane sites/defects [162, 163].

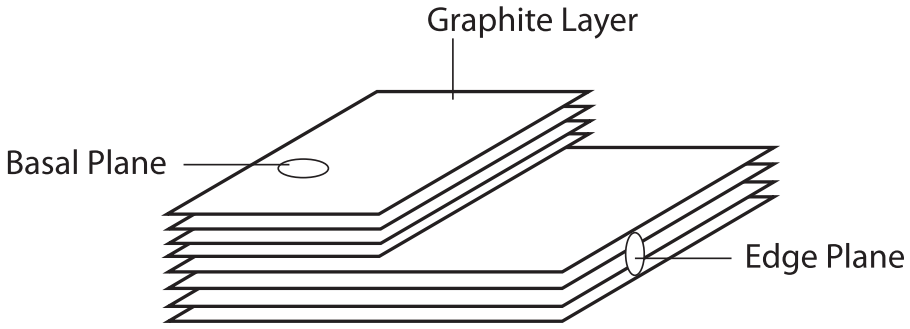

FIGURE 6.1: Schematic structure of graphite material, indicating the edge and basal plane sites on the graphitic layered structure.

Due to the relative ease of modification as compared to metal based materials, carbon electrodes are often derivatised to enable tailor-made properties and hence further extend their applications [42]. The modification procedures of carbon surfaces include but are not limited to the physisorption of polyaromatic hydrocarbons [164], chemical reaction of amine compounds [165], acid chloride reagents [166], aryl diazonium salts [167–169], and 'click' cycloaddition chemistry [170]. Among all, the modification by using aryl diazonium salts has drawn the greatest

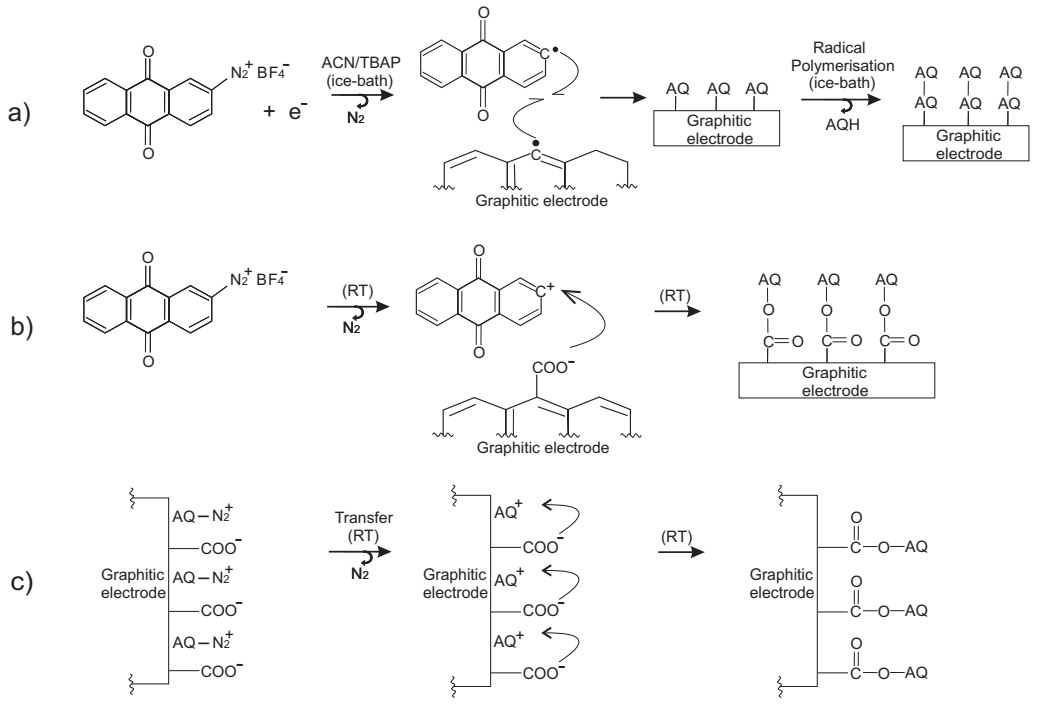

FIGURE 6.2: Illustration of derivatising graphitic electrodes *via* (a) radical generated in electrochemical reduction method, (b) carbocation after spontaneous diazonium salt thermo-decomposition and (c) adsorption-transfer method. Room temperature is abbreviated as RT within the scheme; AQ = 2-anthraquinonyl; MeCN = acetonitrile.

attention in recent years [48, 133, 171–175]. This common usage of aryl diazonium salts is in part due to the stability of the aryl layer formed, and also because of the control over the surface coverage of the grafted species *via* the fine control of the charge passed afforded by electrochemical reduction [109]. The modification process involves irreversibly covalently bonding either aryl radicals ($Ar^{\bullet}$) or cationic species (Ar^{+}) onto the graphitic substrate [167]. The mechanistic pathways are illustrated in Scheme 6.2(a) and (b) respectively. A variety of methods have been used to generate these reactive intermediates from aryl diazonium salts, including electrochemical reduction, thermolysis, photolysis and chemical reduction [176]. Beyond modification, the modified carbon electrodes have been widely used for a range of sensing applications, which allow complex analyses to be rapidly and sensitively performed. These applications include reagentless pH sensors [177, 178],

water purification [153, 179, 180], development of oxygen gas sensors *via* quinone-mediated catalysis [181–184], drug delivery [185], and a large number of biosensors [171, 186].

The derivatised aryl layer often exhibits complex voltammetric responses due to polymer formation, often resulting in broadened peak signals. The full width at half maximum (FWHM) is one of the diagnostic criteria for ideal behaviour of surface bound species, where a value of $90.6/n$ mV (25 °C, n is the number of electrons transferred) corresponds to an ideal case [187]. The possible causes for deviation from an ideal voltammetric peak signal have been modelled and explained by Honeychurch *et al.*, and more recently Henstridge *et al.* [188, 189]. To overcome these problems, previous work has attempted to develop methods for the production of near-ideal aryl layers upon the electrode surfaces. For example, a near-atomically flat pyrolyzed photoresist film was produced and used in microfabrication as a molecular level supporting substrate [190]. A near-monolayer thickness can be achieved by using a sterically hindered diazonium salt [191, 192] and alkyl hydrazone grafting precursors *via* a two step 'formation-degradation' procedure [193, 194]. More recently, Randriamahazaka and co-workers demonstrated the formation of a thin and densely packed layer *via* electrochemical reduction of *in situ* generated diazonium cations in viscous ionic liquids as the grafting media [195–200]. However, a relatively simple methodology to develop a thin film of monolayer is urgently desired. Furthermore, the majority of electrochemical reduction procedures involving the diazonium salt are conducted at room temperature [201–204], where it is known that the aryl diazonium salt decomposes spontaneously into the carbocation [205] and the dinitrogen molecule. A consequence of using such methodologies is that a mixture of both the thermo-decomposed cation and electrochemically reduced radical [206] intermediate species are likely to be

produced at the same time. The voltammetric responses are inevitably influenced by the different reactivities of the intermediates towards the attachment to the heterogeneous graphite surface. In this chapter, it is aimed to minimise the generation of such a mixture of reaction intermediates, which can be achieved with careful control over the experimental conditions.

This chapter investigates the feasibility and characterisation of the formation of thin sub-monolayer films of 2-anthraquinonyl groups bound onto an edge plane pyrolytic graphite electrode. As illustrated in Scheme 6.2(a), the commonly applied electrochemical reduction method has shown a high propensity of to form multilayers *via* radical intermediate species. At even very low surface coverage, randomly distributed AQ polymer clusters are likely to initiate at the edge plane sites/defects. In order to obtain a thin film sub-monolayer, a methodology involving pre-adsorption of anthraquinone-2-diazonium salt onto graphite surface was devised, illustrated in Scheme 6.2(c). The surface coverage is limited by the maximum adsorption of a monolayer of unreacted diazonium salt. After transfer to a buffer solution containing no diazonium salt, the adsorbed material undergoes thermal decomposition at room temperature to form carbocations. The entire derivatisation process involves no electrolysis. The reaction pathway was inferred to involve the carbocation intermediate species, shown in Scheme 6.2(b), which would bond to surface carboxylate groups present on the edge regions to form ester linkages. To the best knowledge of the authors, it is the first case that an adsorption-transfer method has been applied to obtain thin sub-monolayer films of 2-anthraquinonyl on a graphite electrode. The desired thin aryl film formation has significant importance especially in sensor design and electroanalysis.

6.2 Results and discussion

This section discusses two different methods of electrode modification, namely electrochemical reduction and adsorption transfer. The work then represents the comparative voltammetric characterisation of the derivatised layers. Finally the influence of the carbon electrode structure upon the measured voltammetric signal is investigated, with the aim of further elucidating the possible mechanistic pathways for the surface modification.

6.2.1 Surface modification with 2-anthraquinonyl groups

6.2.1.1 Electrochemical modification

The electrochemical reduction of anthraquinone-2-diazonium tetrafluoroborate salt was carried out in various diazonium salt concentrations ranging from 15 μM to 800 μ M in cold acetonitrile (MeCN)/ 0.1 M tetra-n-butylammonium perchlorate (TBAP) electrolyte solution onto an edge plane pyrolytic graphite (EPPG) electrode. The reaction cell was wrapped with foil to prevent diazonium salt decomposition *via* photolysis, and kept in an ice-bath (0 °C) throughout the whole set of experiments. The electrochemical modification was achieved *via* cyclic voltammetry running from +1 V to −0.4 V for 5 consecutive scans at a scan rate of 100 mV s^{-1}. As shown in Figure 6.3(a) at a low concentration of diazonium salt (30 μM), all 5 consecutive modification scans exhibited a chemically irreversible diazonium reduction peak at *ca.*+0.4 V (*vs.* Ag wire). This corresponds to a one-electron reduction step leading to the formation of an aryl radical intermediate and a dinitrogen molecule [206], shown in Scheme 6.2(a). The reduction current in 800 μM diazonium/MeCN solution (Figure 6.3(b)) became negligible virtually by the

second cycle after which only the background current remained. This behaviour seen at high diazonium surface concentrations is indicative of the formation of an organic layer, which after the first scan blocks off further diazonium reduction at the surface [172, 207]. Note that after formation the modified electrode was immediately removed from diazonium stock solution and rinsed with cold MeCN and cold water to remove unreacted material so that the thermo-decomposition pathway for the production of carbocation intermediate species was minimised.

Once the electrochemical modification had been achieved, the redox modified EPPG electrode was characterised *via* variation of scan rate over a range of $100 - 800$ mVs^{-1}. Figure 6.4 shows the voltammetric responses of a 30 μM diazonium solution modified EPPG electrode in a deaerated buffer solution containing 0.1 M NaOH/ 0.1 M KCl scanned from -0.5 V to -1.2 V. After five consecutive scans the redox signal stabilised. All data were recorded using the 6th scan. The cyclic votammetries exhibit an electrochemically quasi-reversible redox signal with a mid-point potential at *ca.* -0.82 V (*vs.* SCE), which has previously been shown to be $2e^-$ redox of the surface bound AQ group [91]. The plot of peak current of both forward and backward waves against scan rate was found to be linear ($R^2 = 0.999$ and $R^2 = 0.998$ respectively) passing through the origin as shown in the inset of Figure 6.4, indicating that the redox species was surface-bound. Upon repetitive scanning of this wave, less than 5% loss of material was seen after comparing the peak area of the last scan with the 6th scan.

Once the surface had shown voltammetric modification, the influence of the diazonium stock solution concentration on the surface coverage was investigated. The surface coverage, Γ_{AQ} (mol cm^{-2}), of the 2-anthraquinonyl groups bound to the graphite surface can be estimated from the area under the reduction peak with

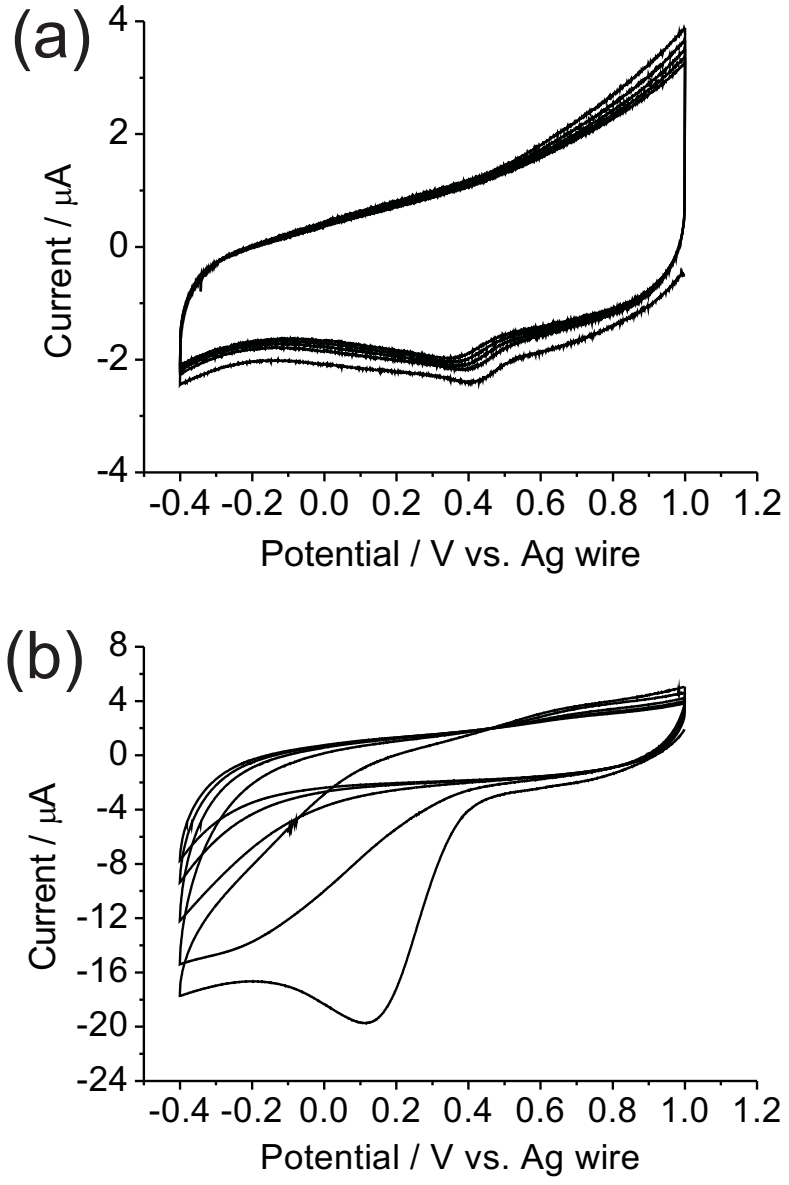

FIGURE 6.3: Electrochemical reduction of anthraquinone-2-diazonium salt at low and high concentrations in a cold MeCN / 0.1 M TBAP electrolyte solution onto a EPPG electrode: (a) 30 μM, (b) 800 μM.

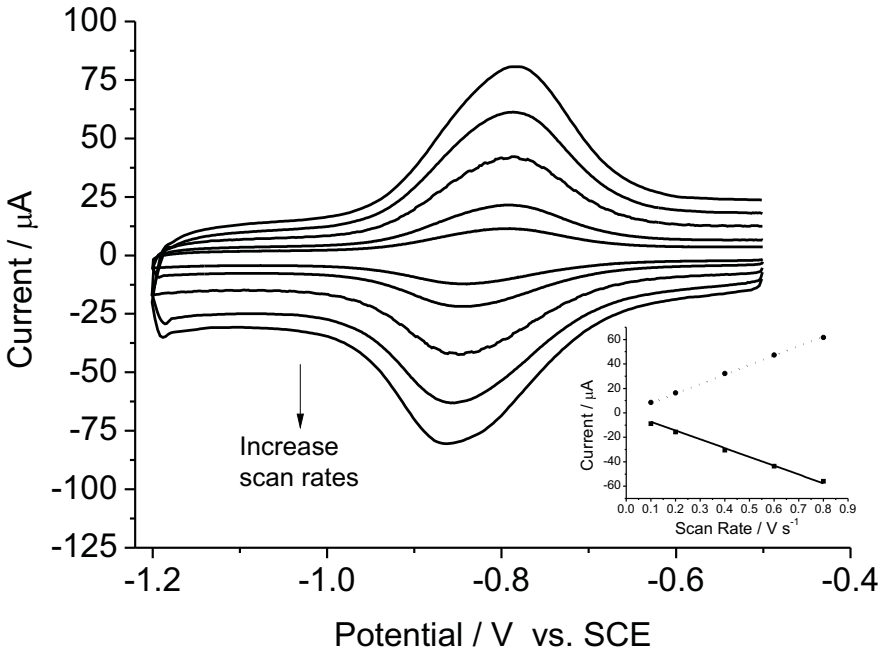

FIGURE 6.4: Characterisation of the electrochemically modified EPPG electrode in a 0.1 M NaOH/ 0.1 M KCl aqueous buffer solution by varying scan rates from $100 - 800$ mV s^{-1},(diazonium stock solution concentration being 30 μM). Inset: plot of both forward (■, solid line, $R^2 = 0.999$) and backward (•, dotted line, $R^2 = 0.998$) peak currents against scan rates.

use of the following equation:

$$\Gamma_{\mathrm{AQ}} = \frac{Q}{nF\pi r_e^2} \tag{6.1}$$

where Q is the charge passed (C), F is the Faraday constant (96485 C mol^{-1}), r_e is the radius of the graphite electrode, and n is the number of electrons transferred (n=2).

The EPPG electrode was modified in diazonium stock solutions of increasing concentration from 15 to 800 μM. Cyclic voltammetry was carried out in aqueous buffer solution with a freshly prepared surface for each measurement, the corresponding voltammograms are shown in Figure 6.5(a). The peak areas of both the

forward and backward waves increase as a function of the diazonium salt concentration. At high concentrations, the surface coverage was found to be effectively constant. The corresponding plot of Γ_{AQ} against diazonium salt concentration is shown in Figure 6.5(b). From the geometric area of the EPPG electrode it is calculated that the Γ_{AQ} was found to limit at *ca.* 2.5×10^{-9} mol cm^{-2}. A previously reported value for a close-packed monolayer (Γ_{CPML}) of phenyl groups was estimated as $\Gamma_{CPML} = 1.35 \times 10^{-9}$ mol cm^{-2} from molecular models [172]. The value of the measured Γ_{AQ} is larger than the Γ_{CPML} for phenyl groups despite the fact that the AQs is more than twice as large as the phenyl moiety. This suggests that multilayer formation upon the electrode surface has occurred at high diazonium salt concentrations.

6.2.1.2 Adsorption-transfer modification

Next, a methodology was devised in which the diazonium salt was pre-adsorbed to the electrode surface. The thermally modified graphite surface was achieved by this novel adsorption-transfer method. Pre-adsorption of diazonium salt was accomplished by exposure of an EPPG electrode to a 100 μM diazonium salt/H_2O stock solution, wrapped with foil and placed in an ice-bath, for various adsorption times (t_{ad}) ranging from $5 - 720$ s. After adsorption, the electrode was rinsed with room temperature water to remove residual materials. The electrode was then transferred to a buffer solution containing no diazonium salt, where the adsorbed material was allowed to thermally decompose and hence chemically modify the graphitic surfaces without electrolysis taking place. The EPPG surface was renewed *via* polishing for each modification.

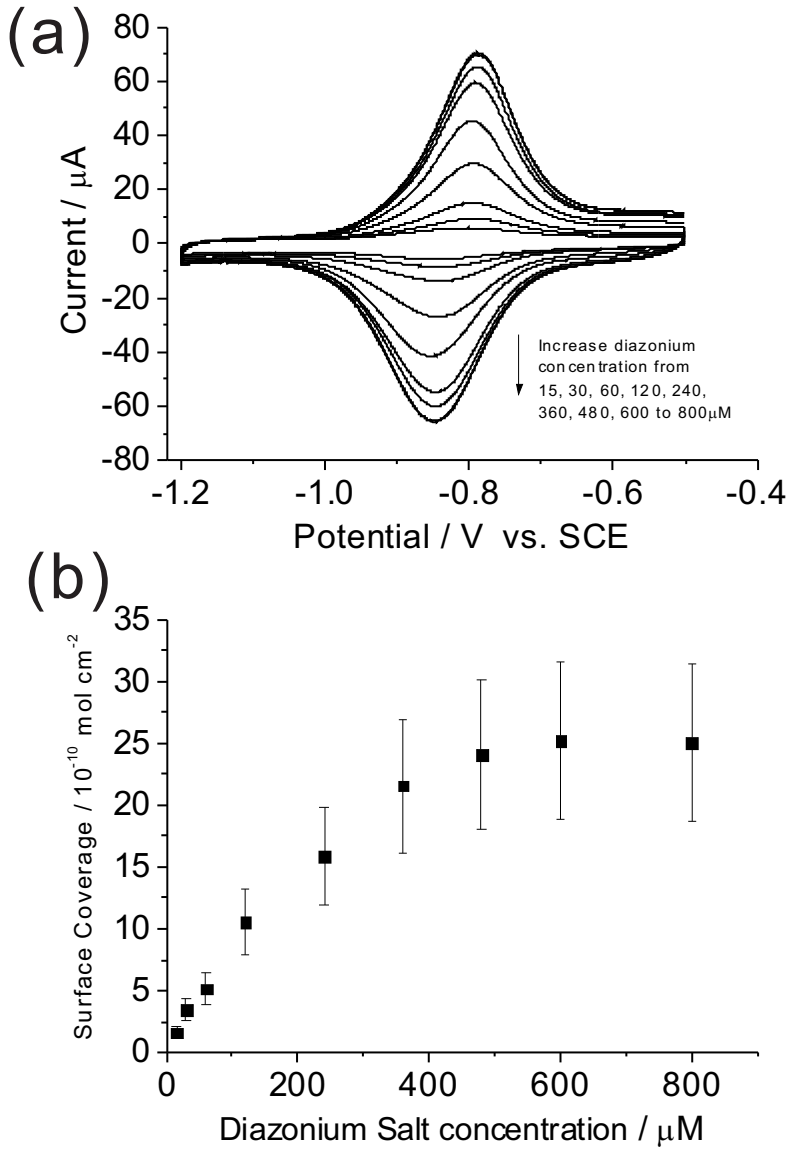

FIGURE 6.5: Voltammetric responses of modified EPPG electrodes *via* electrochemical reduction method in a blank aqueous buffer solution. The concentrations of diazonium stock solution varied from $15 - 800$ μM. (b) Plot of the corresponding surface coverages of the forward wave against concentration of diazonium stock solutions. Error bars were determined by conducting the experiments eight times.

In order to characterise the modified electrode, cyclic voltammetry was carried out in deaerated 0.1M NaOH / 0.1M KCl buffer solution and scanned from −0.5 V to −1.2 V. The voltammogram was recorded after ten consecutive scans for which the voltammetric signals reached an equilibrium. The scan rate variation experiment was conducted with a chosen t_{ad} of 30 s in order to characterise the derivatised EPPG electrode. A linear plot for both the reduction and oxidation peak currents against scan rate was obtained (not shown), indicating a surface modified redox species. The organic layer was observed to form a strong attachment to the carbon surface, with less than 5% decrease in the overall voltammetric signals upon repetitive scanning.

Once the electrode was shown to be modified, the influence of voltammetric responses with varying t_{ad} (from 5 s to 720 s) was studied. Figure 6.6(a) shows the increasing peak area with t_{ad}. The formation of the aryl layer may be rationalised as two sequential steps, as illustrated in Scheme 6.2(c). Initially, a film of unreacted diazonium salt is adsorbed onto the graphite surface. The Γ_{AQ} is limited by monolayer formation, which is confirmed by AFM images on graphite surface for such systems [208–210]. After transfer of the electrode to a buffer solution containing no diazonium salt, the surface adsorbed material thermally decomposes at room temperature and results in carbocation intermediate species [205] which can form ester links with the carboxylate groups on edge plane sites [155, 176]. Throughout the modification process, no electrolysis is involved. The corresponding plot of the surface coverage with increasing t_{ad} is shown in Figure 6.6(b). The Γ_{AQ} levelled off at a plateau value of 7.4×10^{-10} mol cm^{-2}, as calculated from the geometric area of the EPPG electrode. This plateau value is likely to be limited by the maximum adsorption of the unreacted diazonium salt on the electrode surface. As a result, the possibility of forming polymers with the adsorbed monolayer is

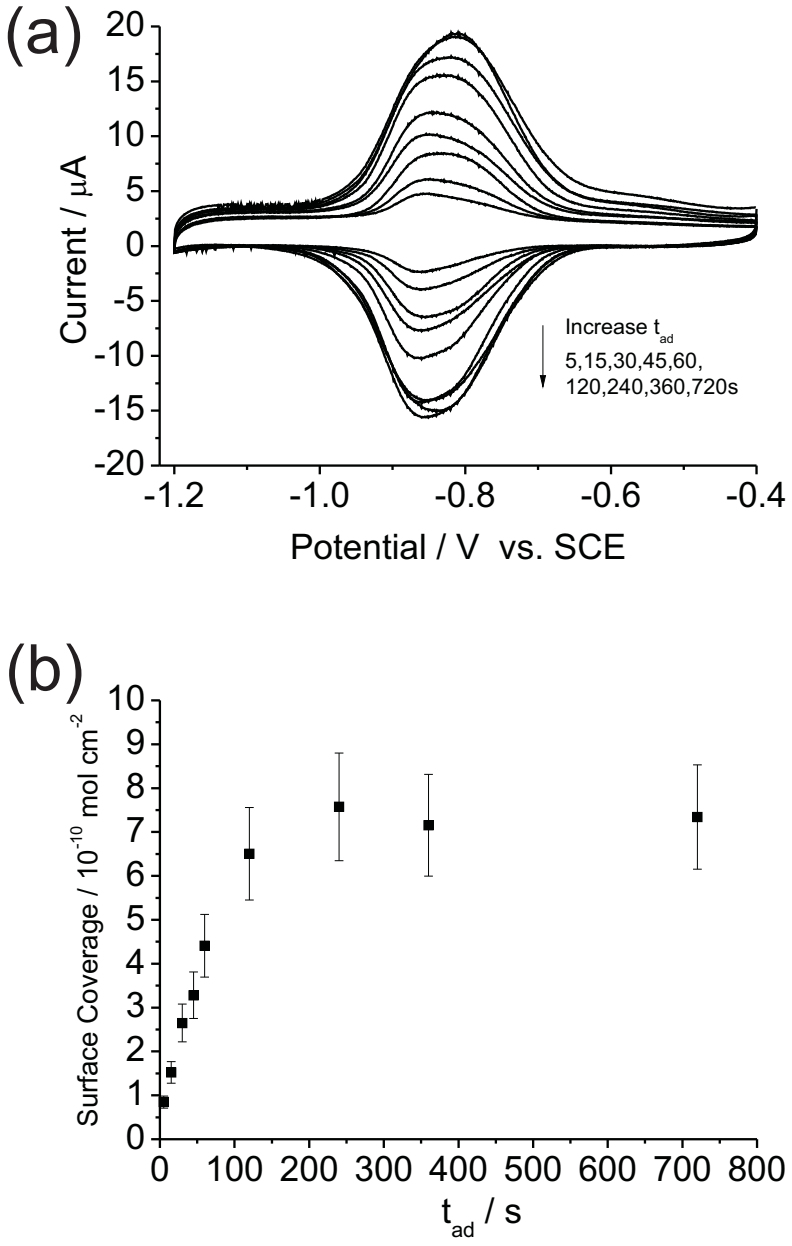

FIGURE 6.6: Voltammetric responses of modified EPPG electrodes *via* adsorption-transfer method in a blank aqueous buffer solution. The pre-adsorption time (t_{ad}) of EPPG electrode in a 100 μM cold diazonium/H_2O stock solution increased from $5 - 720$ s. (b) Plot of the corresponding surface coverages of the forward wave against t_{ad}. Error bars were determined by conducting the experiments eight times.

much reduced. A theoretical value of 3.2×10^{-10} mol cm^{-2} was calculated for the maximum surface coverage of vertically aligned close-packed monolayer of AQs. This value is approximised based on the crystal structure data (assuming $a = 2c$, space group $P2_1/a$) [211] and molar volume of 159 cm^3 mol^{-1} [212], where one anthraquinone molecule occupies the area of 51.2 ± 0.5 Å^2 (taken the projection of an AQ crystal with its $ab-$plane 30 ° away from the electrode surface). However, the surface coverage determined by voltammetry is about a factor of two higher than theoretically predicted value. This may be rationalised on the basis of the surface roughness, where the real electroactive area is larger than that of the geometric area of the electrode surface [201]. Therefore, a 2-anthraquinonyl monolayer was believed to be formed at the limiting plateau of surface coverage.

6.2.1.3 Variation of surface coverage on EPPG surfaces

A variation in Γ_{AQ} was observed for both the electrochemical reduction and adsorption-transfer methods during repetition on an edge plane pyrolytic electrode. This variation is closely related to both the electrode surface roughness and the electrode history. The polishing procedure inevitably varies the surface morphology (and therefore the actual electoactive surface area) in each electrode preparation. Moreover, surface carboxylic groups are believed to form spontaneously upon exposure of carbon to air, so that a variation of surface oxygenated functionality is expected on exposed edge plane sites/defects [208, 213]. In order to achieve reasonable reproducibility, the experiments were repeated eight times and the observed variability was 25.2% and 16.2% for electrochemical and adsorb-transferred methods respectively. It was possible to effectively control the amount of materials grafting on the graphitic surface.

6.2.2 Characterisation of the surface-bound AQ layer

Theoretically for an 'ideal' system the full width at half maximum (FWHM) of a surface bound voltammetric peak has a value of $90.6/n$ mV (25 °C), where n is the number of electrons transferred [187]. However, a discrepancy is commonly found in the experimental voltammograms as compared with theory. Primarily, the value of $90.6/n$ assumes that all electron transfer steps subsequent to the first are highly driven in nature. In reality, for many electroactive organic molecules this is found not to be the case [95, 160, 214]. Consequently, larger FWHM are often encountered experimentally. Beyond the issue relating to the separation of the formal potentials, numerous models provided by Honeychurch *et al.* and more recently by Henstridge *et al.* have attempted to explain possible causes for non-ideal broadening of voltammetric peaks [188, 189], mainly include the lateral interactions of the adsorbate molecules, and the heterogeneous environment of the electrode surface.

The ideal behaviour of the voltammetric responses of the modified surfaces for both methods, *i.e.* electrochemical reduction and adsorption-transfer, was examined in closer detail by using a simple two-electron redox model. The simulation of the voltammetric responses for a covalently bound AQ layer was achieved through the use of the commercially available software package DIGISIM®. A thin-layer cell model was applied under conditions where the concentration profiles of all the species present are uniform with respect to the distance from the electrode. The resulting response can be equivalent to that for an adsorbed species in which there are no interactions between adsorbate molecules [160]. Within the model the separation between the formal potentials of the two electron transfers, $\mid E_1 - E_2 \mid$ (where E_1 and E_2 are the sequential formal potentials of the first and second

electron transfers), was set to be as far apart as possible, so that a largest FWHM was obtained without splitting the redox peak into two.

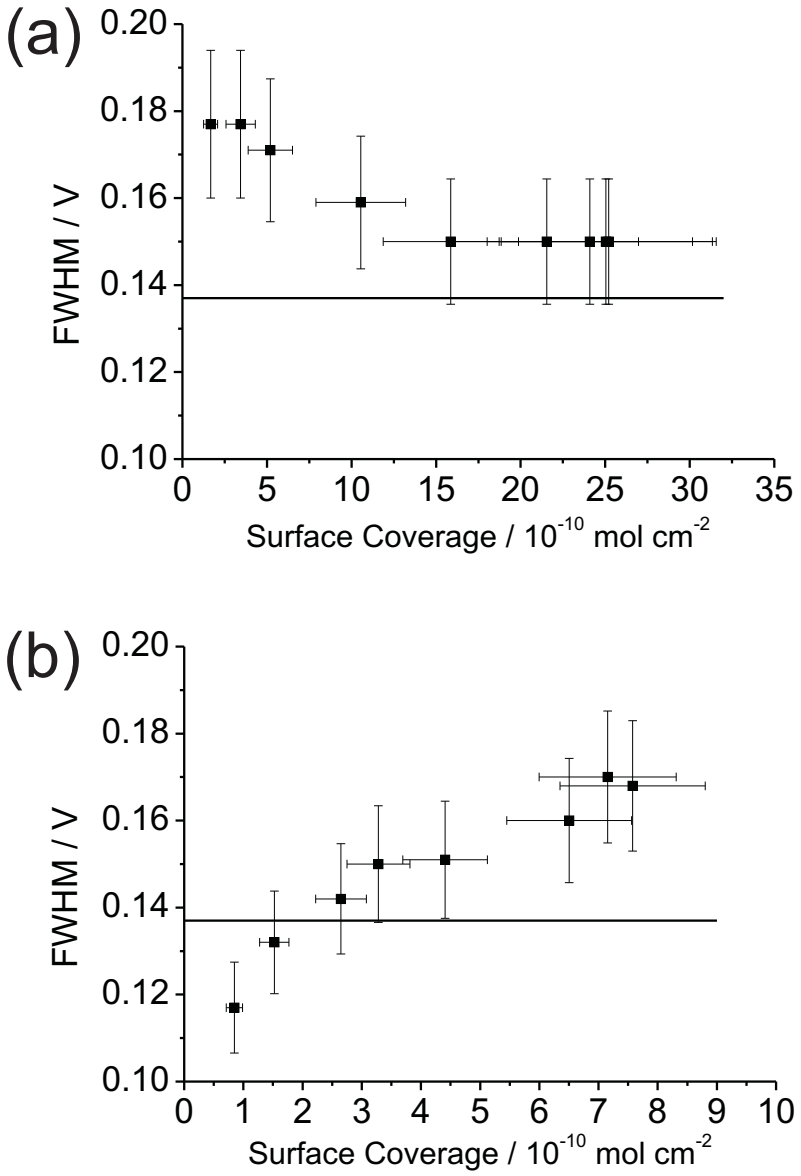

FIGURE 6.7: Plots of the experimentally measured (■) and simulated maximum value (0.137 V, solid line) of FWHM for the reductive waves against surface coverage for both (a) electrochemical and (b) adsorb-transferred modification methods. Error bars were determined by conducting the experiments eight times.

Figure 6.7 depicts the plots of experimentally measured FWHM against surface coverage for both electrochemical (a) and adsorption-transfer (b) methods. The

horizontal line at 137 mV represents the maximum simulated result of the FWHM for an ideal system, where $\mid E_1 - E_2 \mid$ is 65 mV. In Figure 6.7(a), the FWHMs of the peak measured for all surface coverages obtained *via* the electrochemical method are found to be above 137 mV. At high Γ_{AQ}, the non-ideality is mainly attributed to the polymeric layers of AQs present on the electrode surface. It should be noted that it may be possible to improve the voltammetric response of the multilayer *via* electrochemical activation in order to obtain a more ideal response [215]. Symmetrical peak broadening was also observed at even the lowest Γ_{AQ} where the diazonium salt concentration was only 15 μM. The experimentally measured FWHM for the electrochemical method was 40 mV greater than the maximum simulated value for an ideal system. At low Γ_{AQ} this large deviation from ideality is likely due to the initial nucleation of AQ radicals forming polymers at the edge plane sites/defects upon modification. Similar conclusions have been made for other carbon surfaces [202, 210, 216]. Techniques such as AFM and XPS have proved an initial nucleation of AQ radicals at the randomly distributed edge plane sites/defects to form a less compact but thicker aryl layer on carbon surfaces [172]. Hence there is a high propensity for the formation of non-ideal layers at even very low surface coverage *via* the electrochemical modification method.

In comparison, the adsorption-transfer method exhibited non-broadened peak signals at low surface coverage ($\Gamma_{AQ} < 2 \times 10^{-10}$ mol cm^{-2}). As shown in Figure 6.7(b), the experimentally measured FWHMs for both t_{ad} of 5 s and 15 s were below that of the simulated maximum value of 137 mV for an ideal case. This near-ideal voltammetric response may be rationalised as the carbocation intermediate species forming ester links with the carboxylate functional groups on edge plane sites/defects [155, 176]. These linkages may be sufficiently distant from the surface so that the thermodynamic properties of the organic redox layer is not

significantly altered from that of an ideal solution phase species. As Γ_{AQ} increases from 8.5×10^{-11} mol cm^{-2} ($t_{ad} = 5$ s) to 7.4×10^{-10} mol cm^{-2} ($t_{ad} = 720$ s), there is a trend of increasing FWHM, as shown in Figure 6.7(b). The peak responses clearly indicate non-ideal voltammetric behaviour under these conditions. For an ideal system, the adsorbate is expected to form a spatially homogeneous layer and the measured FWHM will be independent of the change in surface coverage. It is known that the FWHM may be viewed as a direct measurement of the extent of lateral interactions among adsorbate molecules [217]. When more AQs are grafted on the surface, the average inter-molecular distances decrease. As a consequence, lateral interactions are likely to become greater. Other factors, such as the inherent heterogeneity of graphitic surfaces, could also contribute to the broadened voltammetric peak signals. Nevertheless, it can be concluded that at sufficiently low Γ_{AQ} a sub-monolayer of 2-anthraquinonyl likely exhibited a near-ideal voltammetric response on an EPPG surface *via* the adsorption-transfer methodology.

A control experiment where the adsorbed diazonium layer is electrochemically reduced is not possible to carry out due to the rapid thermal decomposition of the adsorbed layer upon exposure to air.

6.2.3 Reactivity of radicals and cations towards edge plane sites/defects and basal planes

Carbon surfaces are heterogeneous; the basal and edge plane sites are known to exhibit differing electrochemical and chemical properties [176]. It is likely that the diazonium modification at these two sites will differ. As a result, carbon surfaces containing varying proportions of edge and basal plane sites are of interest for investigation. Therefore, three different carbon surfaces, namely edge plane

(EPPG), basal plane (BPPG) and highly ordered (HOPG) pyrolytic graphites, were modified *via* both the electrochemical and the adsorption-transfer methods. Low surface coverages were chosen to simplify the analysis. The bulk concentration of diazonium stock solution for the electrochemical method was 30 μM; whereas for the adsorption-transfer methodology a stock solution of 100 μM and an adsorption time of 30 s was applied.

The cyclic voltammetry was carried out in a deaerated 0.1 M NaOH / 0.1 M KCl buffer solution as described earlier. Figure 6.8 shows the normalized voltammetric responses of the surface modified 2-anthraquinonyl redox centre on EPPG, BPPG, and HOPG electrodes for both electrochemical (a) and adsorption-transfer (b) methods at a scan rate of 100 mV s^{-1}. All voltammograms were baseline corrected by subtracting the background current. It is clearly seen that within both methods, the surface coverage varied with the different carbon surfaces, suggesting there is a correlation between the Γ_{AQ} with the density of edge plane sites/defects on the graphitic surfaces. The surface coverages and corresponding ratios (as measured from the forward waves) for all three carbon surfaces *via* both modification methods are shown in Table 1. Two likely scenarios may be considered as causing the observed correlation between the edge plane sites/defects and the voltammetrically measured Γ_{AQ} in both methods: (I) the intermediate species (radical and carbocation) are only attached at the edge plane sites/defects; (II) the intermediate species attack at not only edge plane sites/defects, but also at basal plane sites, however only the AQs attached at edge regions are electrically connected. We will discuss the possible reaction pathways for both methods in turn.

In the electrochemical modification method, the Γ_{AQ} ratios of BPPG/EPPG and HOPG/EPPG were found to be 0.66 and 0.18 respectively. Literature reports that electron transfer rates are greater at the edge plane sites/defects than that at the

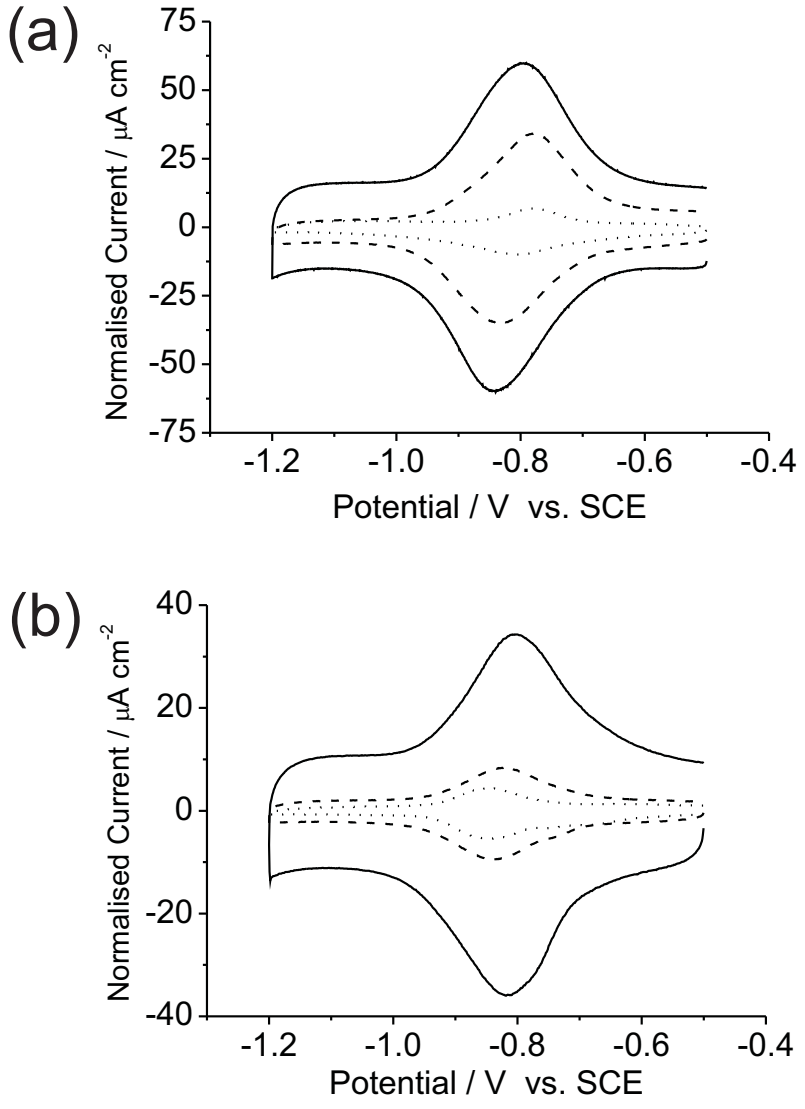

FIGURE 6.8: Normalised voltammetric responses of three modified surfaces, namely EPPG (solid line), BPPG (dashed line) and HOPG (dotted line), in blank aqueous buffer solution *via* (a) electrochemical (diazonium concentration being 30 μM) and (b) adsorb-transferred ($t_{ad} = 30$ s) modification methods. All voltammograms are baselined corrected.

	Electrochemical		Adsorbed-transferred	
	$\Gamma_{AQ}/ \times 10^{-10}$ mol cm^{-2}	Ratio	$\Gamma_{AQ}/ \times 10^{-10}$ mol cm^{-2}	Ratio
EPPG	4.13 ± 0.045	1	2.39 ± 0.179	1
BPPG	2.71 ± 0.004	0.66	0.64 ± 0.001	0.27
HOPG	0.73 ± 0.003	0.18	0.22 ± 0.004	0.09

TABLE 6.1: The surface coverages (Γ_{AQ}) of the forward wave for all three modified electrodes *via* both electrochemical and adsorption-transfer methods are shown. The ratios were calculated by dividing the Γ_{AQ} of EPPG by that of the BPPG and HOPG values respectively. Errors were obtained by repeating the experiment eight times.

basal plane sites [157, 159]. As a result, the AQ radical intermediate species will be predominantly formed at the edge regions. Furthermore, edge plane sites/defects are known to be more reactive due to the chemical sites present [156]. Hence, it can be concluded that the diazonium modification *via* radical formation is more likely to occur at the edge plane sites/defects. However, the Γ_{AQ} ratio for the HOPG/EPPG is comparatively large (0.18) given that the average defect coverage on a HOPG electrode is roughly 1% [218]. This discrepancy may either be due to the AQ radical attachment at non-edge sites or more likely in light of the previous discussion it is probable that the electrochemical reduction method leads to the formation of electroactive polymers at the edge plane sites/defects. This hypothesis can be further confirmed by the large positive deviation of FWHM measured on HOPG electrodes from the simulated value of 137 mV for an ideal system, where an average value of *ca.* 43 mV difference was measured experimentally. Moreover, this interpretation is supported by work from McDermott who demonstrated that the initial nucleation induced from electrochemically generated diethylaniline radicals in solution attacking at the aryl moieties bound to the HOPG surface; the deposition layer was tracked by using infrared reflectance absorption spectroscopy and scanning force microscopy [216].

In the adsorption-transfer methodology, the surface coverage ratios of BPPG/EPPG and HOPG/EPPG were found to be 0.27 and 0.09 respectively. Both values are lower relative to those obtained by using the electrochemical reduction method. The anthraquinone diazonium salt bears the same redox moiety as compared with the anthraquinone disulfonate (AQDS) molecule, whose adsorption behaviour was reported previously [218]. It is surmised that the diazonium salt behaves in the same way as AQDS. It was recognised that the AQs adsorbed on both the basal and edge plane sites/defects *via* $\pi - \pi$ interactions (planar adsorption) and dipole-dipole interactions (vertical attachment) respectively [218]. Possibly due to the higher density of states (DOS) at edge regions [208], the diazonium salt adsorbed on the edge plane sites/defects with greater density than that at the basal plane sites. This variation in density of adsorbates is unlikely to be enough to explain the observed trend of decrease in surface coverage with the number of edge plane sites/defects. It is known that carbocation intermediate species were produced *via* thermo-decomposition to attack at the oxygenated functional groups on the edge plane sites/defects [176]. Therefore, it is concluded that although a layer of diazonium adsorbate was formed during the pre-adsorption step at both sites on the heterogeneous graphite surface, the carbocation intermediate species produced are likely to attack the reactive chemical sites and form ester linkages with the carboxylate groups at the edge regions and thereafter contribute to the redox signal. An unexpected high adsorption response occurred on the HOPG electrode where the charge density ratio showed a value of 0.09. This ratio is relatively large given that the average defect coverage on a HOPG electrode is often stated as 0.01 ± 0.004 [218]. However, Bard and co-workers also reported the number of edge defects on the HOPG electrode could vary up to 10% of the surface [219]. From earlier discussion, it is known that physisorption takes place on both basal

and edge plane sites/defects, but higher density of adsorbed material occurs on the edge regions. The amount of pre-adsorbed diazonium salt is relatively large as compared to the edge densities on the surface. Therefore, a higher Γ_{AQ} will be expected after the thermo-decomposition at the HOPG surface.

6.3 Conclusions

This chapter has investigated aryl diazonium salt modification onto edge plane (EPPG), basal plane (BPPG), and highly ordered (HOPG) pyrolytic graphite surfaces. Using the electrochemical reduction method it has been inferred that polymerization might occur even at very low surface coverages on the EPPG electrode, even though the concentration of the diazonium/acetonitrile stock solution was as low as 15 μM. Polymer formation is supported by the observed broadened voltammetric responses. It is proposed that the aryl radicals are more likely to polymerise at the edge regions of graphitic carbon, which are more reactive and the rate of electron transfer is known to be faster as compared with the basal plane sites. The modification methodology is successfully improved by using an adsorption-transfer method in order to obtain sub-monolayer films of 2-anthraquinonyl groups on an EPPG electrode surface. The surface coverage is limited by the maximum adsorption of unreacted diazonium salt, which is then subject to thermal decomposition at room temperature to form covalent bond with the graphite surfaces. A 2-anthraquinonyl monolayer was formed and found to plateau at a value of 7.4×10^{-10} mol cm^{-2}. When the surface coverage is lower than *ca.* 2×10^{-10} mol cm^{-2}, non-broadened voltammetric peak responses were observed, with the measured full widths at half maximum (FWHM) being below

the maximum simulated value for an ideal system. This near-ideal voltammetric response is further corroborated with the reaction pathway. It is concluded that although the diazonium salt will likely adsorb on both basal and edge plane sites/defects, only the materials attached on the edge regions may form ester linkages after decomposition with the surface carboxylate groups. As a result, the sub-monolayer is covalently bound at a distance away from the electrode. Hence there is less interaction between the redox moiety and the surface, leading to a near-ideal voltammetric response. Although there is variation in the surface coverage possibly due to the surface roughness and electrode history, through the use of the adsorption-transfer method one is able to effectively control the amount of material modified onto the graphitic surface.

Up to this point within the thesis, the electrochemical reduction of oxygen has been studied under static reaction solutions. Next, an enhanced mass transport system within a gravity-feed hydrodynamic flow cell will be discussed. Two carbon substrates, tubular glassy carbon and reticulated vitreous carbon, will be modified by using the adsorption-transfer method developed in this chapter. The advantages of the modified redox mediator will also be highlighted.

Chapter 7

Prototype hydrodynamic system for H_2O_2 production

This chapter investigates oxygen reduction under a gravity-feed flow system using both tubular glassy carbon and reticulated vitreous carbon electrodes. It utilises all the knowledge obtained from the previous chapters, including conclusions about the thermodynamics of oxygen reduction, the kinetics of oxygen electrocatalysis, the minimisation of ion pairing, the enhancement of intermediate reactivity in aqueous solutions, and the surface modification by 2-anthraquinonyl groups. A theoretical model is also developed to explore the conditions of volume flow rate and electrode geometry for which near-full electrolysis may be achieved. The objective is to design and develop a prototype reactor for continuous production of hydrogen peroxide at relatively high fractional current conversion of oxygen. The work presented herein was published in two articles *'Phys. Chem. Chem. Phys. 2013, 15, 7854-7865'*, and *'J. Solid-State Electrochem. 2013, DOI: 10.1007/s10008-013-2250-9'*. Dr M. C. Henstridge should be recognised for the production of the simulation program. Further thanks are necessary to C. J. V. Jones for valuable help towards the flow cell final design and fabrication.

7.1 TGCEs for oxygen reduction

7.1.1 Introduction

The industrial production of hydrogen peroxide (H_2O_2) has received continuous interest due to its increasing demand each year [34]. According to a recent report from Global Industry Analysts, the annual capacity of H_2O_2 is approaching almost five million metric tons in 2017 [220]. Mass-produced H_2O_2 is primarily used in the paper and pulp bleaching industry, chemical synthesis, environmental protection and fuel for rocket propulsion [34]. However, for the majority of medical uses, such as sterilisation, only relatively low H_2O_2 concentrations are required (*cf.* 3% w/w) [130]. For such antiseptic applications the strong oxidative abilities of H_2O_2 are utilised. One of the significant advantages of the use of H_2O_2 as a chemical oxidiser both medically and industrially is its potentially low environmental impact. Currently any environmental gains from its use are heavily mitigated by the utilisation of large amounts of organic solvents in energy expensive syntheses [88].

The most popular method to synthesize H_2O_2 is *via* a chemical pathway, viz. the anthraquinone auto-oxidation (AO) process [34, 88]. This process involves the catalytic reduction of oxygen by anthrahydroquinone to H_2O_2 and anthraquinone, which then returns to the catalytic cycle. Other commercial methods to reduce oxygen to H_2O_2 include the oxidation of isopropyl alcohol and secondary alcohols in general by the Shell Chemical and Lyondell Chemical respectively. The mass-produced product is commonly consumed a long way from the source. As such both the transportation and storage of the H_2O_2 must be considered in evaluating the economics of the H_2O_2 generating process. Further concerns relate to its possible explosive reactivity with a range of organic materials and inorganic compounds

[88]. Consequently, the at-point-of-use synthesis of H_2O_2 *via* an electrochemical or other pathway is much desired. One of the well-developed electrochemical methods is the 'Dow process', which is an on-site alkaline peroxide generation system [221, 222]. However, this procedure has been limited to high pH [88]. Other electrochemical attempts include solid polymer electrolyte electrolysis cell [134, 223], gas diffusion electrodes (GDE) [224, 225], micro-fluidic electrochemical reactors [226], power ultrasound assisted electrosynthesis [131], and the hydrodynamic tubular flow cell [227]. The use of three-dimensional electrodes, such as reticulated vitreous carbon, merits particular attention, and will be discussed in the next section.

This section explores the use of a tubular glassy carbon electrode (TGCE), as a method for the continuous production of hydrogen peroxide. The schematic for this tubular electrode setup is shown in Figure 7.1. The main attributes of this cell design include the wide range over which mass transport can be varied, enhanced current signals that minimise the inaccuracy arising from double-layer charging and reproducible conditions where natural convection effects become masked [20–22]. A laminar flow pattern in which smooth and separated layers of solution possessing velocities characteristic of their position within the tube, is used throughout.

To realise this aim of continuous H_2O_2 production *via* a tubular electrochemical cell, first, a theoretical model is developed to explore the conditions, such as volume flow rate and geometry, for which near-full electrolysis may be achieved. Second, the characteristics of the system are studied experimentally, utilising the theoretical model to provide physical insight into the electron transfer kinetics on the glassy carbon interface. Since direct O_2 reduction is an irreversible process,

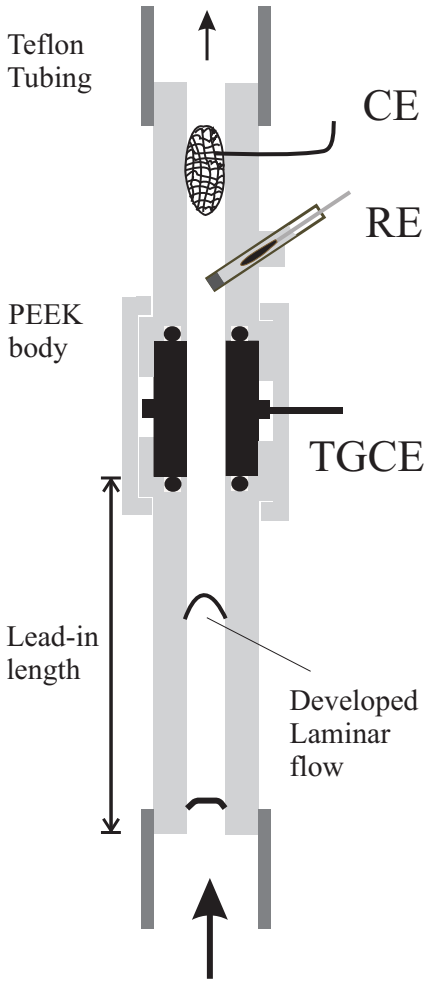

FIGURE 7.1: Tubular electrode flow cell cross-section. TGCE stands for the tubular glassy carbon working electrode; RE is reference electrode; and CE is the counter electrode. The lead-in length is *ca.* 5 cm. PEEK represents polyether ether ketone.

the reduction voltage is expected to move to significant overpotentials as the volume flow rates increase [228]. Consequently, problems involving increased power demand and ohmic drop issues may become significant drawbacks. Third the use of a 2-anthraquinonyl surface modified tubular electrode is developed to help mitigate the above problems. The operative catalytic reaction mechanism is as shown in Figure 7.2. To the best of the authors knowledge this is the first time that a quinone modified tubular glassy carbon electrode has been utilised to study the electrochemical production of H_2O_2.

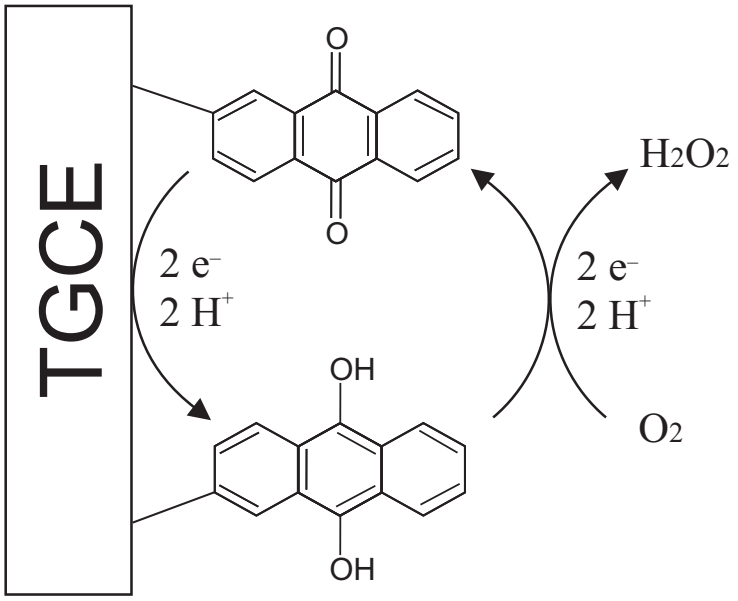

FIGURE 7.2: Reaction scheme for surface bound 2-anthraquinonyl groups mediated oxygen reduction.

7.1.2 Theory

This section seeks to discover the optimal conditions (*i.e.* solution flow rate and electrode geometry) for the electrolysis of a species dissolved in a solution flowing through a tubular electrode. Specifically, a theoretical model enables the study of this problem *via* numerical simulation.

7.1.2.1 Model

Given a solution containing an electroactive analyte, A, undergoing laminar flow through a tubular electrode with radius r_e and length x_e (cm), as shown in Figure 7.3. It is aimed to determine the conditions under which near-full conversion of analyte to product may be achieved.

At the electrode surface the analyte undergoes a one-electron reduction: $A + e^- \rightleftharpoons B$. The solution is assumed to contain sufficient supporting electrolyte that migration

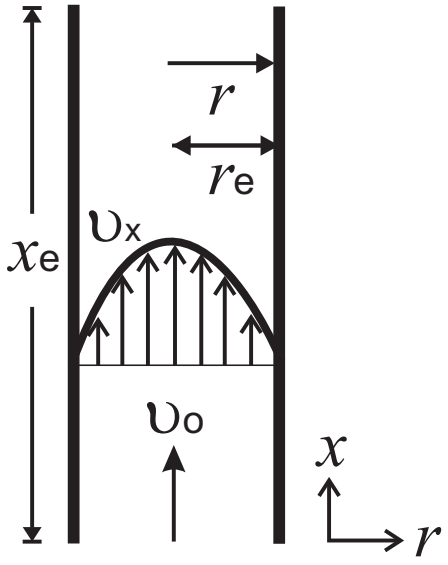

FIGURE 7.3: Laminar flow profile in a tubular electrode, showing the maximum flow velocity at the centre of the tube.

may be neglected [229] and so the mass transport in this system is fully described by:

$$\frac{\partial c}{\partial t} = D\left[\frac{\partial^2 c}{\partial r^2} + \frac{1}{r}\frac{\partial c}{\partial r} + \frac{\partial^2 c}{\partial x^2}\right] - v_x \frac{\partial c}{\partial x} \tag{7.1}$$

where c (mol cm^{-3}) is concentration, t (s) is time, D (cm^2 s^{-1}) is the diffusion coefficient, r (cm) is radial distance, x (cm) is axial distance and v_x (cm s^{-1}) is the axial velocity of the solution given by:

$$v_x = v_o\left[1 - \left(\frac{r}{r_e}\right)^2\right] \tag{7.2}$$

where v_o (cm s^{-1}) is the velocity through the centre of the electrode (shown in Figure 7.3), more conveniently expressed in terms of a volume flow rate, V_f (cm^3 s^{-1}):

$$V_f = \frac{1}{2}\,\pi\, r_e^2\, v_o \tag{7.3}$$

We consider this system at steady-state such that $\frac{\partial c}{\partial t} = 0$. The model is also greatly simplified by neglecting axial diffusion such that $\frac{\partial^2 c}{\partial x^2} = 0$. This assumption has

been studied previously and has been shown to be valid when the convective mass transport is much faster than the diffusive mass transport, *i.e.* for high solution velocities such that $2v_o x_e^2 \gg Dr_e$ [230].

The following dimensionless variables shall be introduced in order to generalise the solution:

$$\text{Radial distance :} \qquad R = \frac{r}{r_e} \tag{7.4}$$

$$\text{Axial distance :} \qquad X = \frac{x}{r_e} \tag{7.5}$$

$$\text{Concentration :} \qquad C = \frac{c}{c^*} \tag{7.6}$$

where c^* is the concentration of species A in bulk solution. Substituting these dimensionless variables into Equation (7.1) and rearranging yields:

$$0 = \frac{\partial^2 C}{\partial R^2} + \frac{1}{R}\frac{\partial C}{\partial R} - \frac{v_x r_e}{D}\frac{\partial C}{\partial X} \tag{7.7}$$

Boundary conditions are required in order to solve Equation (7.7). We wish to find the limiting current and so at the electrode surface ($R = 1$) we assume complete depletion of species A ($C = 0$) and, noting that the tubular electrode is symmetrical, along the centre of the tube ($R = 0$) we apply a zero-flux condition ($\frac{\partial C}{\partial R} = 0$).

7.1.2.2 Computation

We solve this equation using the finite difference method; the resulting discretised equation is:

$$\begin{aligned} 0 \;=\; & \left\{ \frac{C_{x,\,r+1} - C_{x,\,r}}{\frac{1}{2}\Delta R_+(\Delta R_+ + \Delta R_-)} + \frac{C_{x,\,r-1} - C_{x,\,r}}{\frac{1}{2}\Delta R_-(\Delta R_+ + \Delta R_-)} \right\} \\ & + \left\{ \frac{1}{R} \cdot \frac{C_{x,\,r+1} - C_{x,\,r-1}}{\Delta R_+ + \Delta R_-} \right\} \\ & - \left\{ \frac{v_x r_e}{D} \cdot \frac{C_{x,\,r} - C_{x-1,\,r}}{\Delta X_-} \right\} \end{aligned} \tag{7.8}$$

where ΔR_+ and ΔR_- are respectively the grid spacings $R_{r+1} - R_r$ and $R_r - R_{r-1}$. Analogously ΔX_- is the grid spacing $X_x - X_{x-1}$. The radial grid spacing expands inwards from the edge of the electrode, the axial grid spacing is regular along the entire length of the electrode.

The radial derivatives in Equation (7.8) are given by a central difference approximation which is accurate to second order [231]. Notice, however, that the axial derivative is approximated using a backward difference which is accurate only to first order.

While this use of a first-order, rather than second-order, approximation reduces simulation accuracy for a given grid spacing, it enables the use of a space-marching algorithm [232, 233] which represents a great increase in simulation speed versus other methods such as the alternating direction implicit (ADI) method [231]. Simulation accuracy is maintained by using small values of ΔX.

As a consequence of the one-sided approximation to $\frac{\partial C}{\partial X}$ each term in Equation (7.8) depends solely on the concentrations at the current axial coordinate and the axial coordinate immediately upstream. In the absence of axial diffusion the

concentration immediately upstream of the electrode ($X = X_{-1}$) is simply the bulk concentration and so we may solve Equation (7.8) to find the concentrations for the 'column' of points at the upstream edge of the electrode ($X = X_0$). Once we have done this we may then calculate the concentrations at X_1, for which the upstream concentrations are given by the values at X_0. We continue this inductive process (calculating the concentrations at X_n using the values already calculated for X_{n-1}) along the entire length of the electrode until we reach the downstream edge.

The set of simultaneous equations which result from applying Equation (7.8) and the boundary conditions to each column of points may be written in the form:

$$My = z \tag{7.9}$$

where y is a vector containing the unknown concentrations to be determined, z is a vector of known quantities and M is a tri-diagonal matrix of coefficients. Such a system may be efficiently solved using the Thomas algorithm [231]. Once we have solved the concentration profile throughout the tube, we may calculate the current *via* integration of the flux across the electrode surface:

$$I = FD \int_0^{x_e} 2\pi r_e \left(\frac{\partial c}{\partial r}\right)_{r=r_e} \mathrm{d}x \tag{7.10}$$

Qualitatively, in order to achieve appreciable conversion of A to B at an experimentally achievable flow rate we require a long electrode (*vide infra*). This requirement, in combination with the requirement for the axial grid spacing to be small, dictates that there be a very large number of grid points within the tube. Through the use of an expanding radial grid, we require only $\sim$100 points in the R-direction, however a typical value for ΔX is 10^{-4}. Therefore for a given aspect

ratio

$$X_{\mathrm{e}} = \frac{x_e}{r_e} \tag{7.11}$$

the grid typically contains around $X_{\mathrm{e}} \times 10^6$ points. As such, for large values of X_{e}, it is not feasible to hold the concentrations for every point in the computer memory simultaneously.

Fortunately this is not necessary, we need only hold two 'columns' of concentrations in memory: the column to be solved (X_n) and the column immediately upstream (X_{n-1}). Once a column has been solved, we can calculate the incremental current for the portion of electrode between X_{n-1} and X_n by evaluating Equation (7.10) using the trapezium rule. We may then discard the upstream values as they are no longer required and the most recently solved column then becomes the new upstream column. In this manner we may calculate the limiting current without the need to hold the entire simulation space in memory simultaneously.

7.1.2.3 Limiting forms

The Levich equation [10] is commonly used to calculate the limiting current in convective systems:

$$I_{\mathrm{Levich}} = 5.50\ F c^* D^{2/3}\ x_e^{2/3}\ V_f^{1/3} \tag{7.12}$$

where the units of the above terms have been previously defined, and the constant is unitless. This equation is applicable in the limit $V_f \to \infty$ (or $x_e \to 0$) and is derived assuming that the diffusion layer is thin compared to the electrode radius. The derivation makes use of a linearised solution velocity profile (Equation (7.13)) in the vicinity of the electrode surface and assumes that the concentration takes

its bulk value at a large distance from the electrode.

$$v_x \simeq 2v_0 \left[1 - \frac{r}{r_e}\right] \tag{7.13}$$

Amatore *et al.* have recently published work in the limit for microfludic channels [234–236].

However, if the solution flows very slowly through the electrode (or the electrode is very long) the diffusion layer can reach the centre of the electrode and these assumptions no longer hold. In the limit $V_f \to 0$ (or $x_e \to \infty$) the analyte will be completely consumed before exiting the tube. In this limit the current, limited only by the rate at which analyte enters the electrode, is given by:

$$I_{\max} = Fc^* V_f \tag{7.14}$$

7.1.2.4 Theoretical results

We are interested in the region in between the two limits given by Equations (7.12) and (7.14), in particular the conditions of flow rate and geometry under which we begin to achieve appreciable conversion of A to B. This may be estimated by considering the conditions under which $I_{\text{Levich}} \simeq I_{\max}$. Manipulation of Equations (7.12) and (7.14) yields:

$$\frac{Dx_e}{V_f} \simeq 7.75 \times 10^{-2} \tag{7.15}$$

We may obtain a more detailed understanding of this region by employing the model described above. Figure 7.4 shows a plot of simulated $\log_{10}(I_{\text{lim}}/I_{\max})$ against $\log_{10} \frac{Dx_e}{V_f}$. The limits given in Equations (7.12) and (7.14) are also shown for comparison.

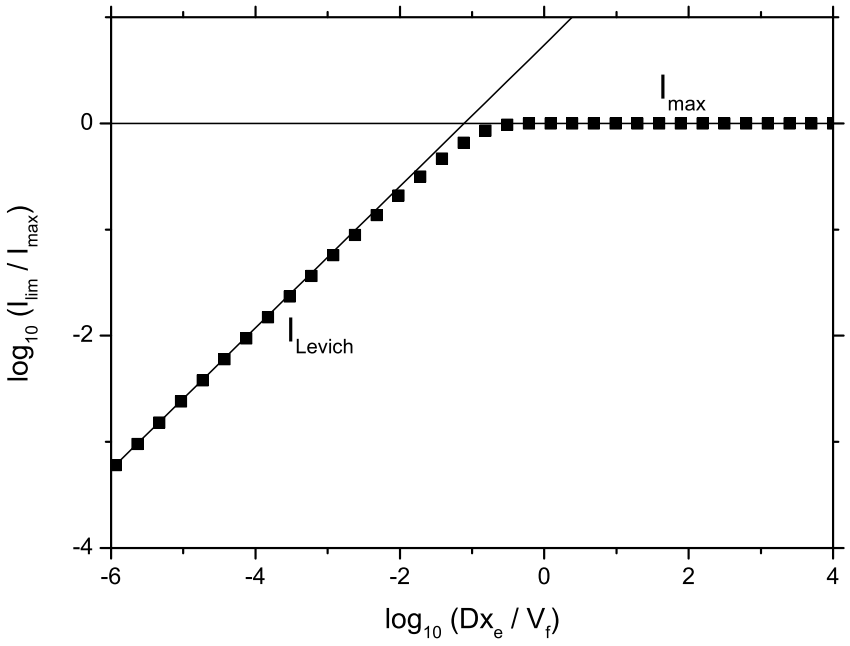

FIGURE 7.4: Variation of $\log_{10}(I_{\text{lim}}/I_{\text{max}})$ with $\log_{10}\frac{Dx_{\text{e}}}{V_{\text{f}}}$. The solid lines show Equations (7.12) and (7.14), the black squares show simulated values.

Excellent agreement between simulation and theory is observed in both limits while in the region where $I_{\text{Levich}} \simeq I_{\text{max}}$ the simulated limiting current transitions smoothly between the two limits.

The source of this transition behaviour is illustrated by the concentration profiles shown in Figure 7.5. For small values of $\frac{Dx_e}{V_f}$ the assumptions of the Levich equation hold because the diffusion layer is confined to a region close to the edge of the tube (Figure 7.5(a)). As $\frac{Dx_e}{V_f}$ increases the solution spends longer inside the tube and so the diffusion layer becomes more extensive and begins to reach across the entire width of the tube (Figure 7.5(b)). For very large values of $\frac{Dx_e}{V_f}$ the solution is within the tube for a sufficiently long time such that it is almost completely electrolysed (Figure 7.5(c)).

This problem has previously been studied using analytical methods by Chen *et*

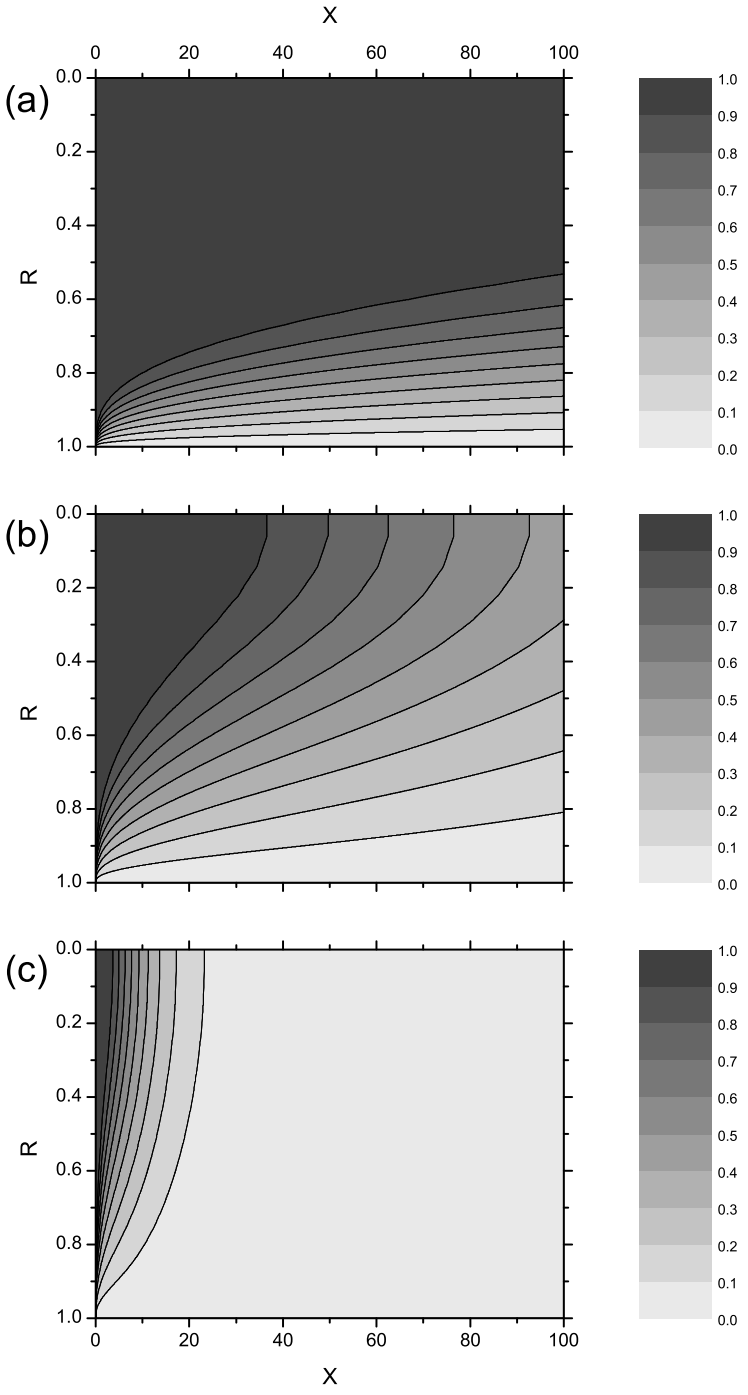

FIGURE 7.5: Simulated concentration profiles for $\frac{Dx_e}{V_f}$ = (a) 10^{-2}, (b) 10^{-1} and (c) 1 for a tubular electrode with aspect ratio $X_e = 100$.

al. [237], who also neglected axial diffusion. They presented an approximate expression for the limiting current as a series, the first terms of which are:

$$\frac{I_{\text{lim}}}{I_{\text{max}}} = 1 - 0.8191 \exp\left[-11.489\ \frac{Dx_e}{V_f}\right] - 0.09753 \exp\left[-70.058\ \frac{Dx_e}{V_f}\right] \tag{7.16}$$

the first two terms of which are sufficient to yield accurate results in the region

$$\frac{Dx_e}{V_f} \geq 4.46 \times 10^{-2} \tag{7.17}$$

A comparison of simulation against Equation (7.16) is shown in Figure 7.6. The solid line shows only the first two terms and the dotted line shows the effect of including the third term. We see that the analytical solution given by Equation (7.16) deviates from the simulated result for small $\frac{Dx_e}{V_f}$, although the inclusion of the third term of the series solution does improve the range of applicability. Nevertheless the analytical result agrees closely with the numerical simulations in the transition region.

Equation (7.16) also gives us a convenient means of calculating the how much of A is converted to B for a given flow rate and geometry. At steady state the fractional conversion, f, is given by:

$$f = \frac{I_{\text{lim}}}{I_{\text{max}}} \tag{7.18}$$

and so f is given directly by Equation (7.16). Rearranging this expression (neglecting the third term) also enables determination of the flow rate and electrode length required to achieve a given fractional conversion.

$$\frac{Dx_e}{V_f} = 0.0870\ \ln\left[\frac{0.8191}{1-f}\right] \tag{7.19}$$

Some representative values for Equation (7.19) are given in Table 7.1. The third

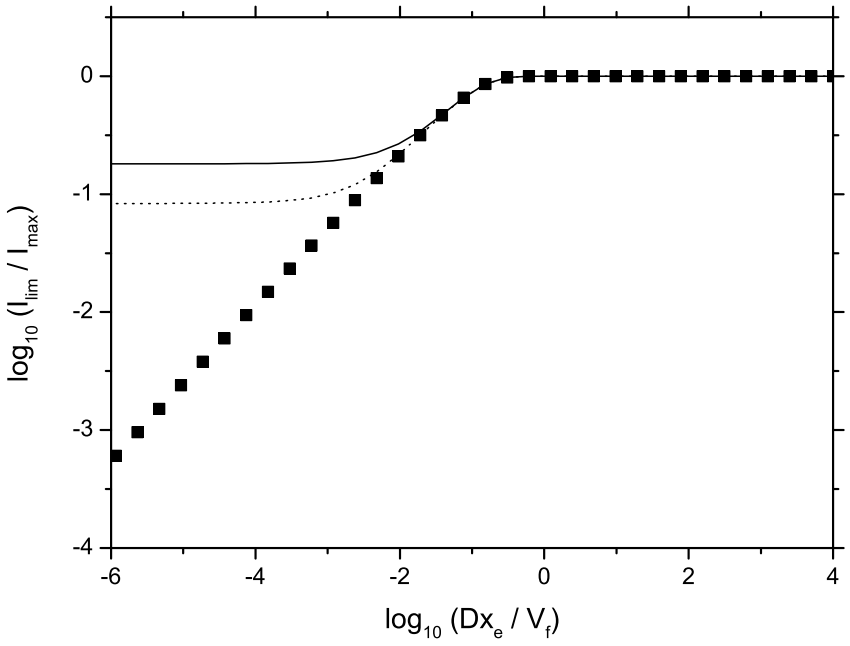

FIGURE 7.6: Variation of $\log_{10}(I_{\text{lim}}/I_{\text{max}})$ with $\log_{10}\frac{Dx_e}{V_f}$. The solid line and dotted lines show, respectively, the first two terms and the first three terms of Equation (7.16). The black squares show simulated values.

column gives a 'representative' value for x_e assuming $D = 10^{-5}$ cm^2 s^{-1} and $V_f = 0.1$ cm^3 s^{-1}.

The above results (both numerical and analytical) have been derived assuming that axial diffusion may be neglected. The results are, however, presented in terms of the ratio $\frac{Dx_e}{V_f}$ and so may be used confidently as long as the flow rate is sufficiently high to justify the approximation [230].

7.1.2.5 Simulation of experimental voltammetry

The simulations used in the fitting of experimental voltammetry in Section 7.1.3.2 were carried out using a very similar method to the simulations undertaken in this section. Equation (7.1) was discretised (without the assumption of steady-state

f	$\frac{Dx_e}{V_f}$	x_e / cm
0.5	0.043	430
0.6	0.062	624
0.7	0.087	874
0.8	0.123	1227
0.9	0.183	1830
0.95	0.243	2433
0.99	0.383	3834

TABLE 7.1: Required experimental parameters in order to achieve fractional conversion f. The third column gives a 'representative' value for x_e assuming $D = 10^{-5}$ cm^2 s^{-1} and $V_f = 0.1$ cm^3 s^{-1}.

conditions) using the backwards implicit method [231]. Each timestep was then solved in the same manner as described above with the exception that Butler-Volmer kinetics were taken to operate at the electrode surface, rather than the previous assumption of total depletion of species A at the electrode surface:

$$\left.\frac{\partial c_{\mathrm{A}}}{\partial r}\right|_{r=r_e} = \frac{k_o}{D_{\mathrm{A}}}\left(c_{\mathrm{A,o}}\exp\left[-\frac{\alpha F}{RT}(E-E_f^{\ominus})\right] - c_{\mathrm{B,o}}\exp\left[+\frac{(1-\alpha)F}{RT}(E-E_f^{\ominus})\right]\right) \tag{7.20}$$

where $c_{\mathrm{A,o}}$ and $c_{\mathrm{B,o}}$ are the concentrations of species A and B at the electrode surface, $E_f^{\ominus}$ is the formal potential of the AB couple, k_o is the standard heterogeneous rate constant and α is the transfer coefficient, in addition at $R = 0$, $\partial C/\partial R = 0$.

7.1.3 Results and discussion

In the following sub-sections, full laminar flow conditions will be experimentally characterised for three different lengths of TGCE (0.515 cm, 1.024 cm and 10.039 cm). Direct oxygen reduction was then carried out on an unmodified TGCE (1.024 cm) and the results fitted to the theoretical model developed in Section 7.1.2.5.

As discussed earlier in the introduction, due to the large overpotentials required for the reduction of an irreversible redox couple, the surface of the TGCE was then modified and the *mediated* oxygen reduction process is further explored.

7.1.3.1 Laminar flow characterisation

The hydrodynamic system was first fully characterised so as to ascertain the maximum flow rate studiable before the laminar flow regime is lost. These experiments also serves to validate the theory presented in the previous section giving insight into the percentage of the electroactive species electrochemically converted upon traversing the electrochemical cell. Linear sweep voltammetry (LSV) was conducted for all hydrodynamic studies. A well studied redox couple of ferrocyanide/ferricyanide was utilised as a model compound to calibrate the laminar flow profile.

First, the TGCE of length 0.515 cm was housed within a flow cell. The experimental procedures are described in Section 2.2. An aqueous solution of 1.20 mM $K_4[Fe(CN)_6]$ supported with 0.1 M KCl was transported through a gravity-feed hydrodynamic system. Figure 7.7(a) depicts the LSVs of the single electron oxidation of $K_4[Fe(CN)_6]$ to $K_3[Fe(CN)_6]$ at flow rates spanned over three orders of magnitudes (1.5×10^{-3} to 1.9 $cm^3\ s^{-1}$). The experimentally obtained limiting currents, I_{lim}, were measured and plotted against $V_f^{1/3}$, as shown in Figure 7.7(b). A straight line of best fit through flow rate range across 1.5×10^{-3} to 0.7 $cm^3\ s^{-1}$ is shown (the range is marked with arrows). By using the Levich equation (Equation (7.12)) diffusion coefficient of ferrocyanide was calculated to be 6.4×10^{-6} $cm^2\ s^{-1}$. This value is in excellent agreement with literature [238], which is reported to be 6.3×10^{-6} $cm^2\ s^{-1}$.

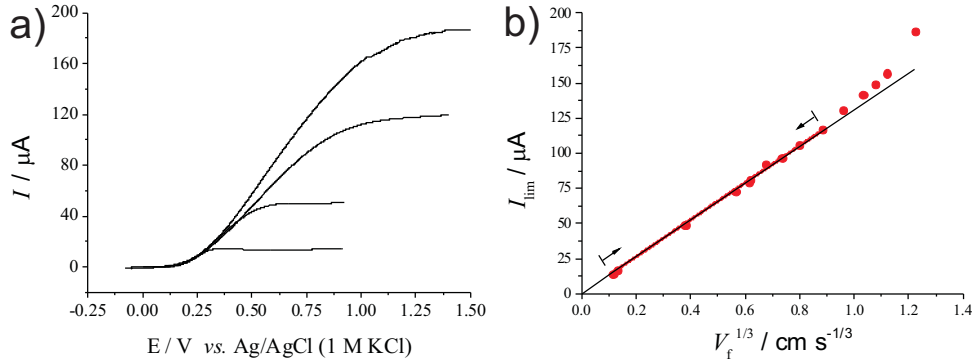

FIGURE 7.7: (a) Linear sweep voltammograms of oxidation of 1.2 mM ferrocyanide / 0.1 M KCl on a x_e = 0.515 cm TGCE at increasing flow rates, 1.5×10^{-3} cm^3 s^{-1}, 0.05 cm^3 s^{-1}, 0.7 cm^3 s^{-1} , and 1.9 cm^3 s^{-1} at scan rates ranged from 10 to 25 mV s^{-1}. (b) Experimental (red dots and red line of best fit) and Levich predicted I_{lim} (black line) as a function of $V_f^{1/3}$. The marked flow rate range is from 1.5×10^{-3} cm^3 s^{-1} to 0.7 cm^3 s^{-1}. Note the error bars are smaller than the points.

Moreover, by superimposing the Levich prediction using literature values in the plot, deviations are clearly seen at high flow rates. A parameter that determines whether flow is laminar or turbulent is the Reynolds number [20–22], Re, which for a tube can be calculated from

$$Re = \frac{V_f}{\pi r_e v} \tag{7.21}$$

where v (cm^2 s^{-1}) is the kinematic viscosity of reaction solution at the studied temperature. Herein, v was approximated as equal to that of pure water at 293 K being 10^{-2} cm^2 s^{-1} [123]. Consequently, at the maximum laminar flow rate Re was estimated to be 148, which is well within the critical value of 2000. Beyond a flow rate of 0.7 cm^3 s^{-1} deviations were seen from Levich behaviour (linear I_{lim} *vs.* $V_f^{1/3}$ behaviour). This is likely due to local turbulence at the joints of TGCE and PEEK tube which causes the extra current, rather than the fully developed turbulence predicted by Equation (7.21). Hence, it can be concluded that TGCE

electrode of length 0.515 cm demonstrates laminar flow character when the flow rate does not exceed 0.7 cm^3 s^{-1}.

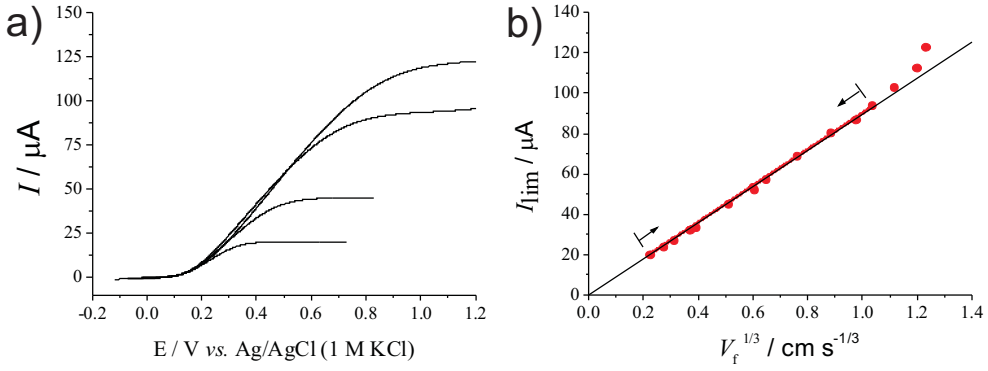

FIGURE 7.8: (a) Linear sweep voltammograms of oxidation of 0.5 mM ferrocyanide / 0.1 M KCl on a x_e = 1.024 cm TGCE at increasing flow rates, 11.1×10^{-3} , 0.1 , 1.1 , and 1.9 cm^3 s^{-1} at scan rates ranged from 10 to 25 mV s^{-1}. (b) Experimental (red dots and red line of best fit) and Levich predicted I_{lim} (black line) as a function of $V_f^{1/3}$. The marked flow rate range is from 11.1×10^{-3} to 1.1 cm^3 s^{-1}. Note the error bars are smaller than the points.

Longer tube lengths were next investigated. The reaction solution was composed of 0.5 mM $K_4[Fe(CN)_6]$ supported with 0.1 M KCl. The LSVs of TGCE of length 1.024 cm are shown in Figure 7.8(a). The flow rates range from 0.01 to 1.9 cm^3 s^{-1}. Figure 7.8(b) shows a plot of the experimentally obtained I_{lim} as a function of $V_f^{1/3}$. A theoretical Levich Equation (7.12) predicted line was also superimposed on the same plot. An excellent correlation of the experimental data compared with the Levich predicted I_{lim} was shown between the flow rate range of 0.01 to 1.1 cm^3 s^{-1}. The calculated Re at the maximum laminar flow rate was 237 ± 3. Again the deviations from the predictions of laminar flow at relatively high flow rates result from imperfections around the tube edge at the joint of TGCE and PEEK tube that causes local turbulence to the solution flow character.

The characterisation of the laminar flow was further extended to the 10.039 cm TGCE. A solution of 0.9 mM $K_4[Fe(CN)_6]$ was used. The supporting electrolyte

concentration was deliberately increased by tenfold to 1 M in order to enhance the solution conductivity. Obtained LSVs are shown in Figure 7.9(a) for increasing flow rates from 7.8×10^{-3} to 1.5 $\text{cm}^3\ \text{s}^{-1}$. Due to the substantial length of TGCE, a pronounced solution resistance (R_s) is expected. To resolve this problem experimentally, a certain amount of ohmic drop, IR_s, is allowed to set in modern potentiostat. The aim is to minimise voltammetric distortion due to solution resistance. The amount can be estimated *via* the charging current in chronoamperometry (as discussed in Section 1.4).

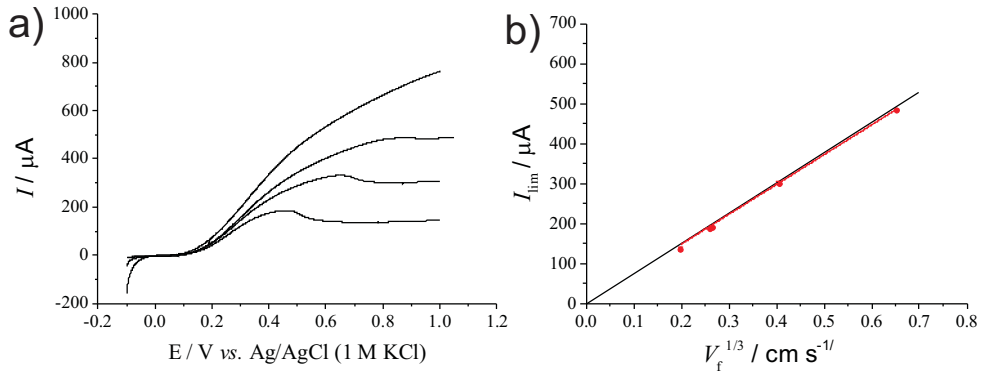

FIGURE 7.9: (a) Linear sweep voltammograms of oxidation of 0.9 mM ferrocyanide / 1 M KCl on a x_e = 10.039 cm TGCE at increasing flow rates, 7.8×10^{-3}, 0.07, 0.3 , and 1.5 $\text{cm}^3\ \text{s}^{-1}$ at scan rates ranged from 2 to 20 mV s^{-1}. (b) Experimental (red dots and red line of best fit) and Levich predicted I_{lim} (black line) as a function of $V_f^{1/3}$. The plotted flow rate range is from 7.8×10^{-3} to 0.3 $\text{cm}^3\ \text{s}^{-1}$, and error bars are embedded in the plot.

In a solution of only 1 M KCl, a potential was stepped from −0.1 V to 0 V, where no faradaic current incurred, which can cause the charging current. This charging current is derived in Appendix B [20–22]:

$$I = \frac{\Delta E}{R_{\text{s}}} \exp\left[-\frac{t}{AR_{\text{s}}C_{\text{d}}}\right] \tag{7.22}$$

where C_d is the 'average' capacitance at the double layer, A is the electrode area, and ΔE is 0.1 V in this case. By plotting $\ln I$ against t, the solution resistance was

calculated from the intersection of $t = 0$ to be $(14000 \pm 2000)\ \Omega$. Consequently, the ohmic drop was estimated to be 1.4 – 11.2 V, assuming I_{lim} lies in the range of 100 – 800 μA. This large ohmic drop is the major cause for the observed voltammetric distortion. However, the values of I_{lim} were still unambiguously measured at slow flow rates. These mass-transport limited currents were consistent with the Levich prediction (Figure 7.9(b)). Despite the added R_s at each measurement, the ohmic drop became dominant at high flow rate, *i.e.* 1.5 $\text{cm}^3\ \text{s}^{-1}$, so that no true limiting current was obtained. This is mainly due to the uncompensated resistance (R_u), some fraction of R_s, caused by the inevitable gap in solution between working and reference electrodes.

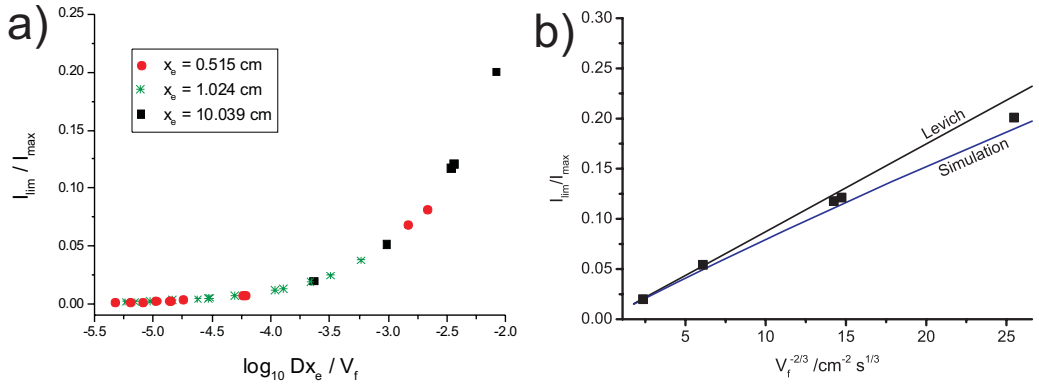

FIGURE 7.10: Plots of fractional current conversion, $I_{\text{lim}}/I_{\text{max}}$, as a function of (a)$\log_{10} \frac{Dx_e}{V_f}$ for variable lengths of TGC electrodes; and (b)flow rate ($V_f^{-2/3}$) in $x_e = 10.039$ cm TGCE. Scatters: experimental, Blue line: simulated limiting current, and Black line: Levich approximated limiting current

At lower flow rates in Figure 7.9 a significant proportion of the electroactive species have been electrochemically converted on flowing through the tubular electrode. Plots of fractional current conversion, f (Equation 7.18), as a function of $\log_{10} \frac{Dx_e}{V_f}$ and $V_f^{-2/3}$ are depicted in Figure 7.10(a) and (b) respectively. Figure 7.10(a) demonstrates the current conversion ratios of all three variable tubular lengths under laminar flow regime. It can be seen explicitly from the plot that under

the same flow rate, the conversion ratios give much higher value with longer tube length. For example, at V_f of 7.8×10^{-3} cm^3 s^{-1} almost 20% of the electroactive species were oxidised in the 10.039 cm TGCE; in contrast to only *ca.*5% and 3% for 1.024 cm and 0.515 cm TGC electrodes respectively. Under the flow in the same length tube, the conversion rate decreases at higher flow rates, such as *ca.* 4% at 0.1 cm^3 s^{-1} in the 10.039 cm TGCE. Also for comparison in Figure 7.10 is the predicted conversion ratios obtained from both the Levich equation and the current predicted by the simulation presented in Section 7.1.2. For the lowest flow rate ($V_f^{-2/3} = 35.5$) the Levich equation overestimates the current by 9%, moreover the simulation is clearly able to successfully describe this deviation away from linearity. It is of interest that the simulation marginally underestimates the current, this likely relates to the break down of the approximation of zero axial diffusion made within the theory section. It should also be noted that these relatively high conversion ratios (cf. 20%) imply that the diffusion layer within the tube is of a comparable magnitude to the radius of the cell. Consequently it is this partial 'thin-layer' regime that leads to the observed peak currents in the LSVs for the lower flow rates as evidenced in Figure 7.9 As a result, variable scan rates are used herein. At lower flow rates small scan rates were applied; in contrast to the progressively dominant peak responses at high scan rates. On the other hand, relatively higher scan rates were used at higher flow rates due to the change of time scale and reduction of analyte consumption..

For above lengths of TGCEs studied (*ca.* 0.5, 1, 10 cm), laminar flow character was seen with certain flow rate ranges. Though higher fractional current conversion could be achieved at longer length TGCE, experimental complications due to solution ohmic distortion and high potential drop correction onto the flow system limit their usage. Therefore, in the rest of this section the study of either direct

or mediated reduction of oxygen to produce H_2O_2 was carried out on the 1.024 cm TGCE, which experimentally has the largest range of flow rates available for study. Note that any successful application of H_2O_2 will require purification from the supporting electrolyte and concentration, which is beyond the scope of the discussion here.

7.1.3.2 Oxygen reduction under hydrodynamic flow

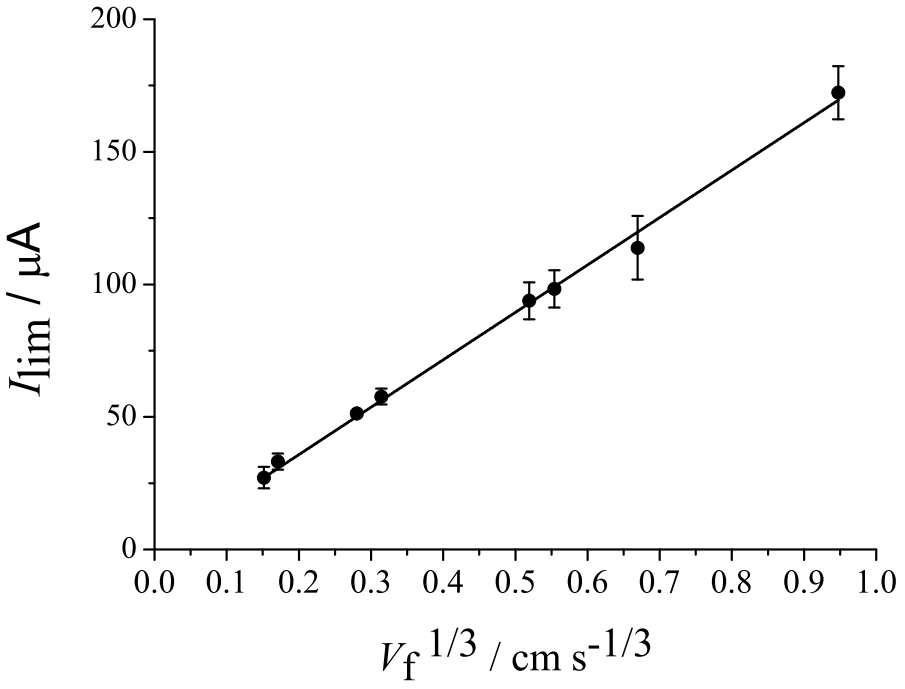

FIGURE 7.11: Plot of I_{lim} against $V_{\text{f}}^{1/3}$ from oxygen direct reduction on x_e = 1.024 cm TGCE.

Direct oxygen reduction was investigated using a bare-TGCE (x_e = 1.024 cm) under the hydrodynamic system. An air-equilibrated PBS solution of pH 6.7 was flowed through the TGCE at flow rates ranging between 3.5×10^{-3} and 0.9 cm^3 s^{-1} under laminar flow. Convection-diffusion limited steady-state currents for O_2 reduction were seen to increase with flow rates. A plot of I_{lim} and $V_f^{1/3}$ is shown in

Figure 7.11. The experimentally obtained diffusion coefficient of O_2 was 1.8×10^{-5} cm^3 s^{-1} from the slope, assuming a $2e^-$ process. This value agreed excellently with that reported previously [75]. The two-electron reduction mechanism to form hydrogen peroxide is likely to be

$$O_2 + e^- \rightleftharpoons O_2^{\bullet -} \tag{7.23}$$

$$O_2^{\bullet -} + e^- + 2H^+ \rightleftharpoons H_2O_2 \tag{7.24}$$

The experimental LSVs were then fitted with the theory model developed in Section 7.1.2.5. These simulations were carried out using a very similar method to that undertaken to examine the limiting current. Equation (7.1) was discretised (without the assumption of steady-state conditions) using the backwards implicit method [231]. The concentrations were then solved for each time-step in the same manner as described above with the exception that Butler-Volmer kinetics were taken to operate at the electrode surface, rather than the previous assumption of zero concentration at the electrode surface. Simulations were consistent with theory developed by Klatt and Blaedel [228]. A simple two-electron heterogeneous reduction was set up, with the aim of identifying the transfer coefficients, α, at each flow rate. The standard electrochemical rate constant was set to be in the irreversible limit, *i.e.* 10^{-5} cm s^{-1}. The experimental LSVs at 5×10^{-3}, 2.2×10^{-2} and 0.3 cm^3 s^{-1} were used in the fitting, shown in Figure 7.12. The experimental steady-state currents were well fitted with the theoretical model. However, immediately after the experimental steady-state current was reached, the plateau current inclined and increased rapidly. This is likely due to a breakdown of solvent in the studied potential window. Note that the direct reduction of H_2O_2 should not be observed on glassy carbon electrodes in the studied potential region [239].

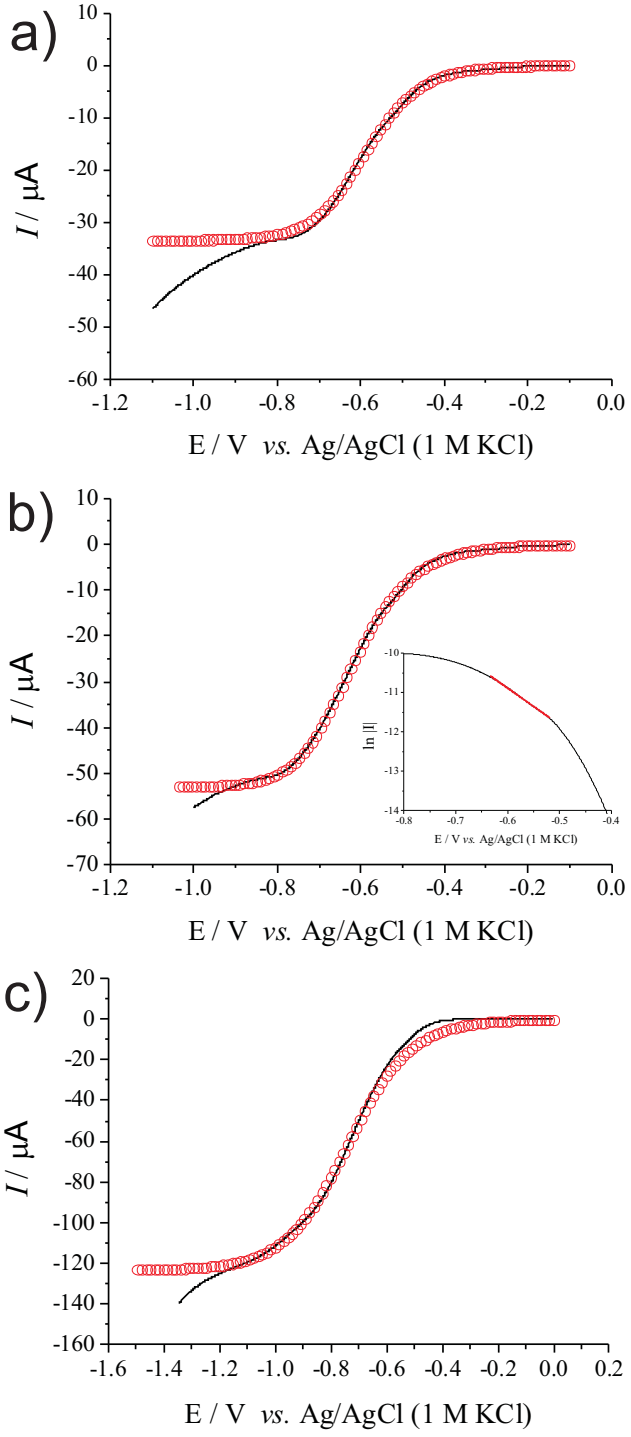

FIGURE 7.12: Experimental (black line) and theoretical (red circle) fitting of LSVs of direct oxygen reduction on $x_e = 1.024$ cm at flow rates of (a) 5×10^{-3}, (b) 2.2×10^{-2} and (c) 0.3 cm^3 s^{-1}. The inset in (b) is its corresponding Tafel plot. The transfer coefficient, α, obtained from the linear (highlighted red) slope is 0.24.

The α values inferred by best fitting the meaused voltammograms were found to be 0.21 ± 0.03. The consistency of this value was further checked with an approxiamte equation, proposed by Klatt and Blaedel [228] studied under an irreversible charge transfer at a tubular electrode under laminar flow

$$E_{\frac{1}{2},\text{irrev}} = E_f^{\ominus} + \frac{RT}{(n' + \alpha)F} \ln \left[\frac{k_o}{1.101 D^{2/3} (2V_f / \pi x_e {r_e}^3)^{1/3}} \right] \tag{7.25}$$

where $E_{\frac{1}{2},\text{irrev}}$ is the half-wave potential for the irreversible oxygen redox couple, n' is the number of electrons preceding the rate determining step, $E_f^{\ominus}$ is the formal electrode potential, k_o is the standard heterogeneous rate constant. Figure 7.13 shows a plot of $E_{\frac{1}{2},\text{irrev}}$ against $\ln V_f$. In this way, $(n' + \alpha)$ was calculated to equal to 0.22. It has been widely reported that the first electron transfer is the rate determining step [240]. Therefore, n' should equal to zero and α value attained from the halfwave dependence on flow rate is self-consistent with the results from the voltammetric waveshape theory model. Moreover, the α values were further confirmed with ones obtained from Tafel plots (a representative Tafel plot is shown in Figure 7.12(b)), being 0.24.

Furthermore, from Figure 7.13 it is shown that as the flow rates increase, the $E_{\frac{1}{2},\text{irrev}}$ for O_2 reduction requires higher overpotential to drive the process. This leads to increased power demand and greater IR_s issues. Hence, the TGCE surfaces will be modified with an oxygen reduction catalyst. Such an approach is discussed in the following sections.

7.1.3.3 TGCE surface modification

The chemical modification of 2-anthraquinonyl groups on carbon substrate can be achieved *via* the adsorption-transfer methodology, as described in Chapter 6.

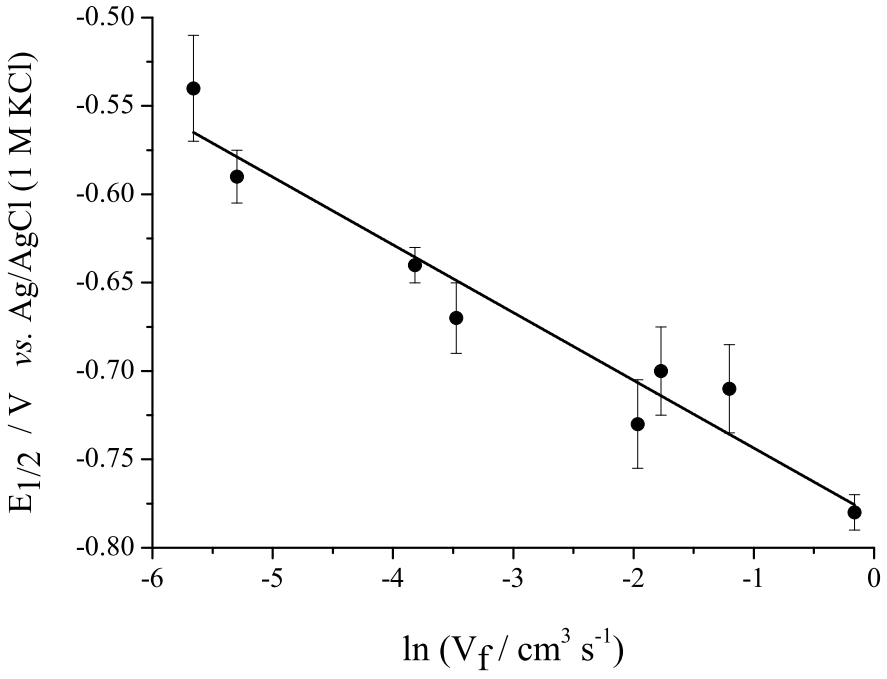

FIGURE 7.13: Plot of $E_{\frac{1}{2},\text{irrev}}$ for O_2 reduction *vs.* $\ln V_f$.

However, the reaction mechanism is different on glassy carbon electrode compared with pyrolytic graphite [203].

The TGCE surface of length 1.024 cm was modified by 1 mM anthraquinone-2-diazonium tetrafluoroborate salt aqueous solution at open circuit potential in the dark. The diazonium aqueous solution was injected into a double-end-sealed TGCE at room temperature for 5 minutes. The electrode was then sonicated in pure water for at least 1 minute to knock off any physisorbed material. The major mechanistic pathway was proposed to occur *via* spontaneous electron transfer from glassy carbon substrate to the diazonium salt with the electron being supplied from the fermi level of the carbon material, where the complementary charge transfer reaction (if any) is currently unknown [203].

The modified AQ-TGCE was characterised in an O_2-free PBS solution assembled in the flow cell set-up. The voltammetric responses were obtained in the absence

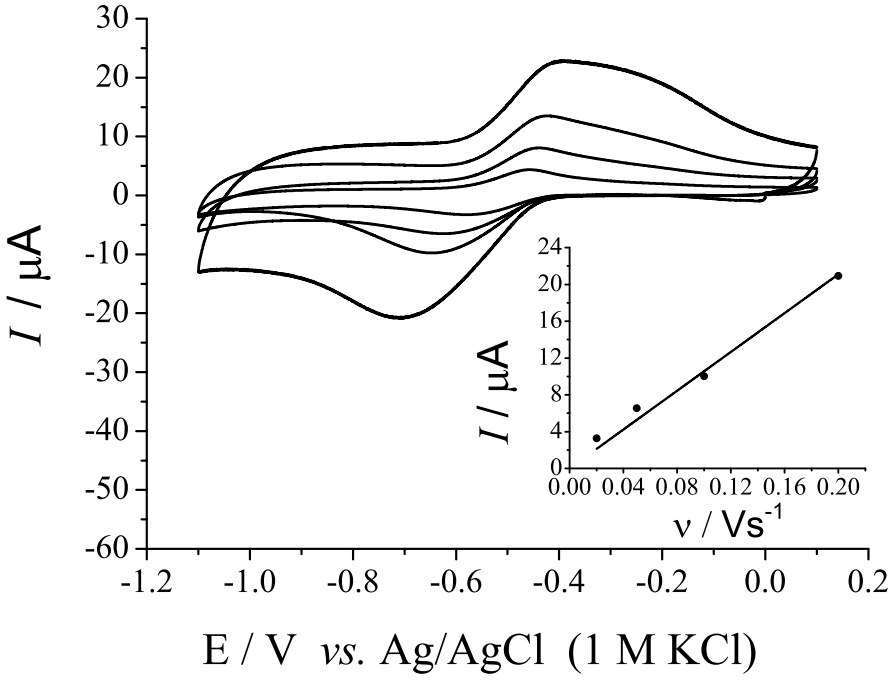

FIGURE 7.14: Redox responses of modified anthraquinonyl groups on TGC (x_e = 1.024 cm) at increasing scan rates from $20 - 200$ mV s^{-1} in N_2-degassed PBS in the absence of flow. Inset depicts the relationship between peak current and scan rates.

of flow. Note that the peak current for the surface bound species is not diffusional limited. That is to say, no flow rate dependency should be observed. The cyclic voltammograms at variable scan rates were obtained between +0.1 V and −1.1 V, as shown in Figure 7.14. A well-defined redox pair at *ca.* −0.52 V (*vs.* Ag/AgCl 1 M KCl) is ascribed due to the quasi-reversible reduction of the modified anthraquinone species. The inset depicts that the anthraquinonyl group is surface bound as the linear relationship between peak current and scan rates. The modified AQ-TGCE electrode was scanned repeatedly, by the 20th scan the signal stabilised. The cyclic voltammograms in Figure 7.14 were obtained after the 20th scan and showed little change in surface coverage throughout a range of scan rate variation. It is then possible to estimate the surface coverage of the modified AQ

molecules, Γ_{AQ} (mol cm^{-2}), taking the geometric area of the TGCE inner wall surface, as being roughly 1.3×10^{-10} mol cm^{-2}. A theoretical value of 3.2×10^{-10} mol cm^{-2} was calculated for the maximum surface coverage of vertically aligned close-packed monolayer of AQ molecules [241]. Hence the modified AQ layer suggests near monolayer formation on the TGCE surface.

7.1.3.4 Catalytic oxygen reduction on modified TGCE

The electrocatalytic activity of a surface modified AQ-TGCE was next examined in the presence of oxygen. Air-equilibrated PBS solution was gravity-fed through the above modified AQ-TGCE in a flow cell set-up. The V_f was varied from 0.01 to 1.3 cm^3 s^{-1}. Linear sweep voltammograms were scanned from 0 V to -1.3 V at 20 mV s^{-1}, as shown in Figure 7.15. The TGCE surfaces with and without modified AQ redox mediator in the absence of O_2 were also depicted for comparison (inset). It is obvious that at the similar potential of where AQ- was reduced all three hydrodynamic voltammograms showed the same steady-state currents ($E_{\frac{1}{2}} \approx -0.5$ V). This 'pre-wave' is ascribed to be due to the AQ mediated oxygen reduction. The presence of the catalyst is capable of turning over O_2 at a far less negative overpotential than that recorded on the unmodified electrode. Note that the catalytic peak current is insensitive to the flow rate, implying that the electron transfer to the oxygen species is kinetically limited.

As the overpotentials became more negative (beyond *ca.* -0.7 V), the direct reduction of oxygen commences. The mass transport limited currents increase in magnitude with an increase in flow rates. The steady-state currents agree with those predicted from the Levich equation (Equation (7.12)), and are much higher than the anthraquinone mediated responses. The kinetic hindrance of the

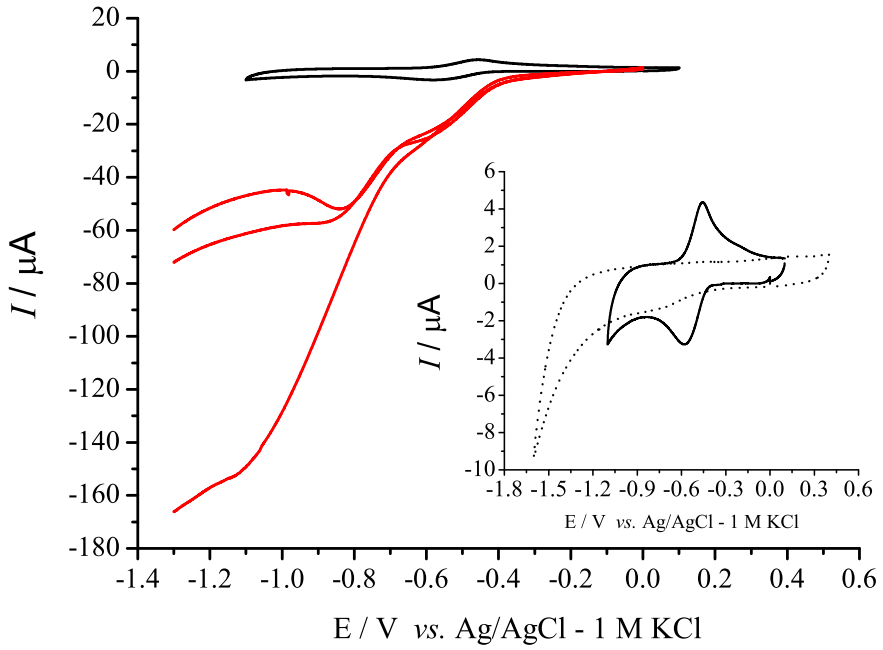

FIGURE 7.15: The red LSVs depict mediated oxygen reduction at increasing flow rates from 0.01, 0.06, to 1.3 cm^3 s^{-1}. The black LSV demonstrates AQ redox in N_2-degassed PBS. Inset shows the enlarged redox signal of AQ on TGCE as compared to unmodified TGCE. Scan rate at 20 mV s^{-1}.

catalyst, as a consequence, results in less fractional current conversion to form H_2O_2. It is interesting to note that these steady-state currents span a much wider range in potential as compared to those obtained on a bare-TGCE surface (experimental voltammograms in Figure 7.12), which is believed to be a result of the modified layer slowing down the rate of solvent breakdown. Hence, the catalysed oxygen waves can be concluded to have a reduced overpotential by almost 200 mV. This represents a valuable saving and the approach of using surface modified electron transfer mediation may be of significant generic value for the electrolysis of irreversible systems in flow.

7.1.4 Conclusions

This section has explored a novel type of flow system for continuous synthesis of hydrogen peroxide at point-of-use *via* tubular glassy carbon electrodes. Theory has been developed to quantify the flow rates and cell demensions required for significant conversion of the electroactive species (Table 7.1). Experimentally the cell setup was characterised, demonstrating that up to 20% conversion of the electroactive species may be readily obtained in a TGCE of tube length 10.039 cm at 7.8×10^{-3} cm^3 s^{-1}. Further to this oxygen reduction to H_2O_2 on the TGCE was studied under hydrodynamic flow. It is the first time such a macroscopic scale tubular flow cell has been implemented and combined with a developed theoretical model. Excellent agreement of experimental results and the simulation model was achieved. Simulation enabled the quantitative measurement of the associated alpha value ($\alpha = 0.21 \pm 0.03$) for the oxygen reduction process. Finally, by covalently modifying the TGCE surface with 2-anthraquinonyl redox mediator the overpotential required for the reduction process was successfully decreased by *ca.* 200 mV. This is promising in the reduction of any power demand of this process.

A potential scale-up of the flow cell set-up has been justified by the developed theory. However, it has shown that for current conversion to reach 50%, the length of a tubular electrode must be as long as 4.3 metres! This is simply not practically realistic. To further develop the prototype design, a reticulated vitreous carbon (RVC) substrate can be used to replace a tubular glassy carbon electrode.

7.2 Oxygen reduction on a novelly designed RVC flow cell

7.2.1 Introduction

Reticulated vitreous carbon (RVC) is a disordered glassy porous carbon material, with an open-pore foam structure [242, 243]. Its high void volume retains infused materials within controlled pore sizes. The distinct characteristics of large surface area and high porosity of the RVC material counteract the limitations of the low space velocity obtained in electrochemical processes with two-dimensional electrodes [243]. The use of a reticulated vitreous carbon electrode (RVCE) to electrochemically reduce oxygen to H_2O_2 has been studied on a trickle bed cell [244], in an ultrasound assisted RVC flow cell [131], and with both stationary and rotating RVCEs in alkaline and acidic solutions [245, 246]. However, the electrosynthesis of H_2O_2 is challenging, mainly due to the sluggishness of oxygen electroreduction, particularly in neutral and acidic solutions, and the enhanced rate of further reduction of H_2O_2 [227, 245]. Therefore, the use of an electrocatalyst becomes imperative. Previous work on such a process involved solution phase 2-ethylanthraquinone [98], the use of the cationic surfactant trioctylmethylammonium chloride [247], and oxidised RVCE [248, 249].

Within this section, a RVCE was modified with 2-anthraquinonyl groups, which can electrocatalytically reduce O_2 to H_2O_2. The advantage of the surface confined covalently modified catalyst has the benefit in terms of easy separation from the product solution. For the first time, the oxygen reduction is investigated on a novelly designed RVCE, housed in a gravity-feed flow system. Such a hydrodynamic flow system is shown in Figure 7.16, together with a RVCE cross-section. The

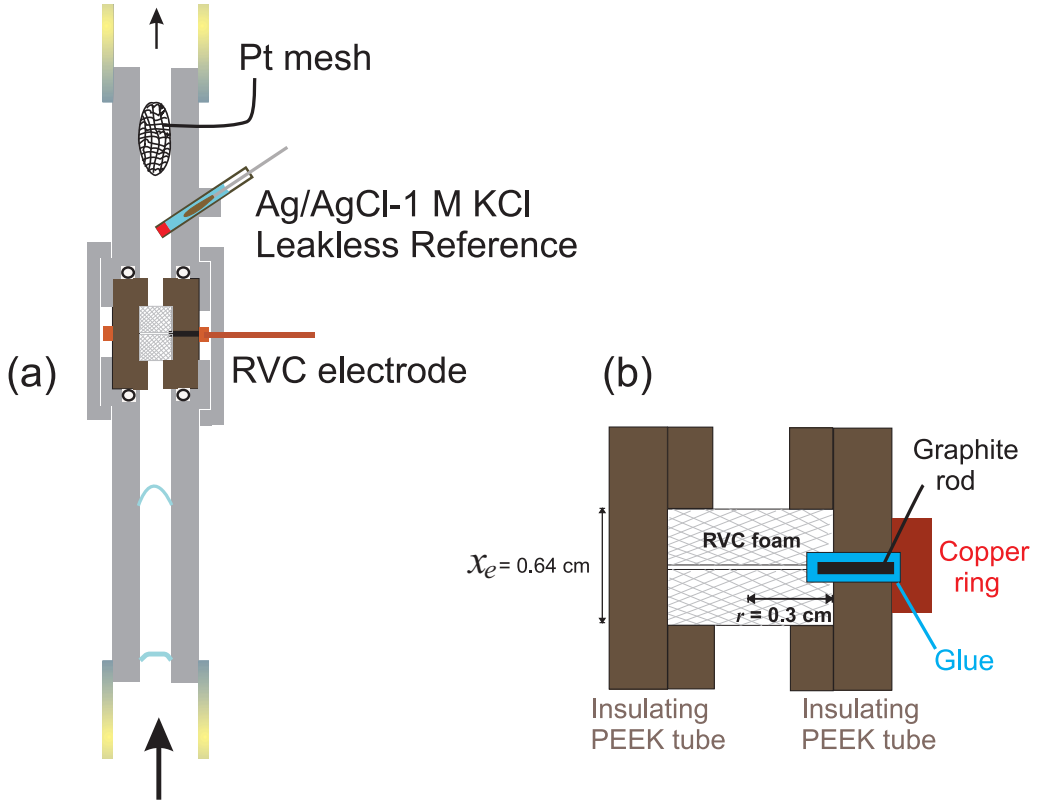

FIGURE 7.16: (a) Scheme of the hydrodynamic flow system equipped with a reticulated vitreous carbon electrode (RVCE); (b) RVCE cross-section, where PEEK represents polyether ether ketone.

dissolved oxygen in neutral aqueous solution (pH of 6.7) was continuously reduced under the applied potentials. Fractional current conversions obtained on a RVC flow cell were compared and contrasted with those on a two-dimensional electrode, viz. a tubular electrode flow cell. The *in situ* generated low concentration of H_2O_2 provides potential applications to water purification processes and disinfection for water and food.

7.2.2 Results and discussion

A model redox couple, ferrocyanide/ferricyanide ($Fe(CN)_6^{4-}$ / $Fe(CN)_6^{3-}$), was first studied. Cyclic voltammetry was conducted first under a static aqueous solution

containing 0.55 mM potassium ferrocyanide ($K_4[Fe(CN)_6]$) supported with 3 M KCl salt. After each scan fresh solution was flushed through the reticulated vitreous carbon electrode (RVCE). Figure 7.17 shows cyclic voltammograms at variable scan rates from 20 to 800 mV s^{-1}. The oxidation peak potentials range from +0.385 V to +0.633 V accordingly. A plot of percentage conversion of the reactant as a function of scan rate is shown as an inset in Figure 7.17. This term is defined as

$$\text{Percentage conversion} = \frac{\text{Charge passed}}{\text{Maximum generated charge}} \times 100\%$$

The charge passed was measured from the peak area under the oxidation waves after blank subtraction. The maximum amount of charge generated can be calculated *via* the following expression,

$$\text{Maximum generated charge} = FC_iV$$

where F is the Faraday constant (96485 C mol^{-1}), C_i is concentration of analyte (mol dm^{-3}), and V is the volume of voids (cm^3). Under the studied cell dimensions, the calculated maximum generated charge was 9.2×10^{-3} C. It can be seen that at scan rate of 20 mV s^{-1}, almost 30% of ferrocyanide was electro-oxidised to ferricyanide on the RVCE. However, as the experimental time scale decreases (at high scan rates) the percentage conversion of the reactant drops sharply.

Linear sweep voltammetry (LSV) was next conducted within flowing solutions. A reaction solution of the same composition was transported through a gravity-feed hydrodynamic system *via* the RVC flow cell. Figure 7.18 depicts the LSVs of a single electron oxidation of $Fe(CN)_6^{4-}$ to $Fe(CN)_6^{3-}$ at increasing volume flow rates (V_f) from 0.02 to 0.74 cm^3 s^{-1} at a scan rate of 5 mV s^{-1}. The half-wave potential rises as the increase of flow rates from +0.353 V to +0.565 V. The noise

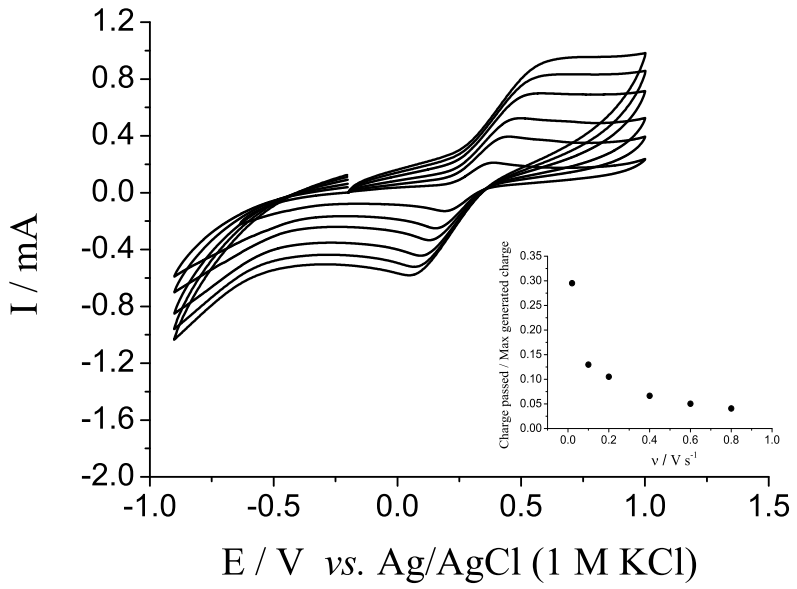

FIGURE 7.17: Cyclic voltammograms of potassium ferrocyanide redox signals under static aqueous solution supported by 3 M KCl salt on RVCE at increasing scan rates from 20, 100, 200, 400, 600, to 800 mV s^{-1}. The inset shows a plot of percentage conversion as a function of scan rate.

at higher V_f likely indicates a switch to a turbulent flow regime. A parameter that determines whether flow is laminar or turbulent is the Reynolds number, *Re*, which has been previously defined in Eqn. 7.21. The pores within RVCE can be envisaged as entangled tubes of void. Assuming the kinematic viscosity of reaction solution is 10^{-2} cm^2 s^{-1} (the value of pure water at 20 °C), the calculated *Re* value at 0.74 cm^3 s^{-1} is *ca.* 1130, which is approaching the turbulent flow limit. Moreover, local turbulence can set in before any fully developed turbulence. Hence, noise on voltammograms suggests a tendency towards turbulent flow.

Note that in the limit of $V_f \to 0$ the analyte will be completely consumed before exiting the RVC flow cell. In this limit the current (I_{max}), is determined by the rate at which analyte enters the electrode, is given by Eqn. 7.14; and the fractional current conversion, f, refers to Eqn. 7.18. The fractional current conversions for oxidative current at increasing volume flow rates for the RVC flow cell are recorded

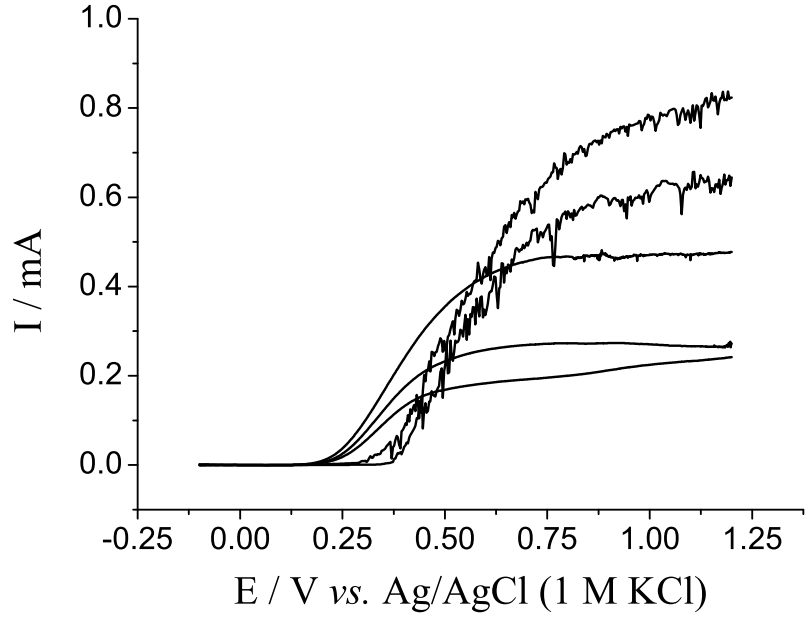

FIGURE 7.18: Linear sweep voltammograms of potassium ferrocyanide oxidation under flowing aqueous solution supported by 3 M KCl salt on RVC flow cell at increasing volume flow rates from 0.02, 0.07, 0.28, 0.44 to 0.74 $cm^3\ s^{-1}$ at 5 $mV\ s^{-1}$.

V_f / $cm^3\ s^{-1}$	f_{RVC}	f^*_{TGC}
0.02	0.24	0.021
0.07	0.09	0.008
0.28	0.04	0.003
0.44	0.03	0.002
0.74	0.02	0.002

TABLE 7.2: Comparison of fractional current conversion of potassium ferrocyanide oxidation on RVC flow cell (f_{RVC}) and TGC flow cell (f_{TGC}) at various volume flow rates (V_f) at 25 °C, 5 $mV\ s^{-1}$. Both RVC and TGC electrodes have the same geometric dimensions (cylindrical radius of 0.3 cm and length of 0.64 cm). * The I_{lim} used to calculate f_{TGC} was predicted from the Levich equation (Eqn. 7.12).

in Table 7.2. It can be seen that f_{RVC} decreases dramatically with increasing V_f. On the right hand side column, a direct comparison was made with a tubular glassy carbon (TGC) flow cell. From Section 7.1, it has shown that the I_{lim} for a tubular electrode under laminar flow can be suitably described by the Levich equation (Eqn. 7.12). Moreover, within the experimentally studied V_f range and dimensions of electrode the steady-state currents lie in the Levich predicted regime. Embracing exactly the same cell dimensions as RVCE, the f_{TGC} can be unambiguously predicted as shown in Table 7.2. It is obvious that f_{RVC} is more than one order of magnitude higher than f_{TGC}. Hence, as expected for same geometric cell dimensions the use of the porous RVCE results in far larger fractional current conversions than the TGCE. The electrochemical behaviour of RVCE is now further discussed, focussing on the reduction of dissolved oxygen.

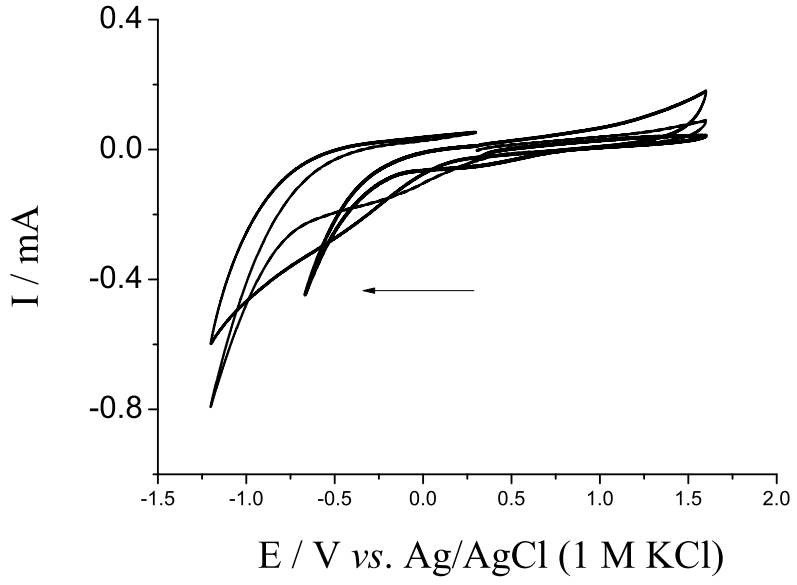

FIGURE 7.19: Cyclic voltammograms of oxygen redox signals under static air-equilibrated solution of PBS - 3 M KCl on RVCE at increasing scan rates from 20, 100, to 200 mV s^{-1}.

Direct O_2 reduction was investigated at the RVCE under static conditions with an air-equilibrated phosphate buffer solution (PBS) supported with 3 M KCl salt.

Fresh solution was flushed through after each scan. Cyclic voltammograms measured at increasing scan rates from 20 to 200 mV s^{-1} are shown in Figure 7.19. It can be seen that the irreversible peak for O_2 reduction shifts from *ca.* +0.3 V to *ca.* −0.4 V (*vs.* Ag/AgCl - 1 M KCl) as the scan rate increases. The peak potential of an irreversible redox couple is dependent on both the heterogeneous rate constant and the rate of mass transport to the electrode so that the reduction peak potential moves to greater overpotentials as the scan rate increases [1]. According to the literature [245, 246] and results from Section 7.1, the irreversible peak corresponds to the 2-electron reduction of O_2 to hydrogen peroxide (H_2O_2).

Hydrodynamic studies of O_2 direct reduction in flowing reaction solutions were then carried out. The LSVs are shown in Figure 7.20 with increasing volume flow rates. No clear O_2 direct reduction was observed at any flow rate. This outcome agrees with work reported by Alvarez-Gallegos *etc.* on a RVC flow cell in an O_2-saturated hydrochloric acid solution [246]. In order to enhance the rate of O_2 reduction, the RVCE surface was modified with a catalyst, and the corresponding electrochemical signals are discussed as follows.

The chemical modification method is similar as described in Section 7.1.3.3. An aqueous solution containing 5 mM diazonium salt was injected into a sealed compartment of RVCE to fill up the entire cavity. The RVCE surface was exposed to diazonium solution for 36 hours under room temperature and pressure in the dark. The modified 2-anthraquinonyl RVCE (AQ-RVCE) was studied electrochemically in a static PBS reaction solution. Figure 7.21 shows the cyclic voltammograms of the AQ-RVCE without and with O_2 at a scan rate of 25 mV s^{-1}. The surface bound electrochemical responses in Figure 7.21 demonstrate a $2e^- - 2H^+$ reduction process of AQ- to AQH_2^- in the absence of O_2. The reaction pathway involves only the heterogeneous redox steps. The non-zero background current is mainly related

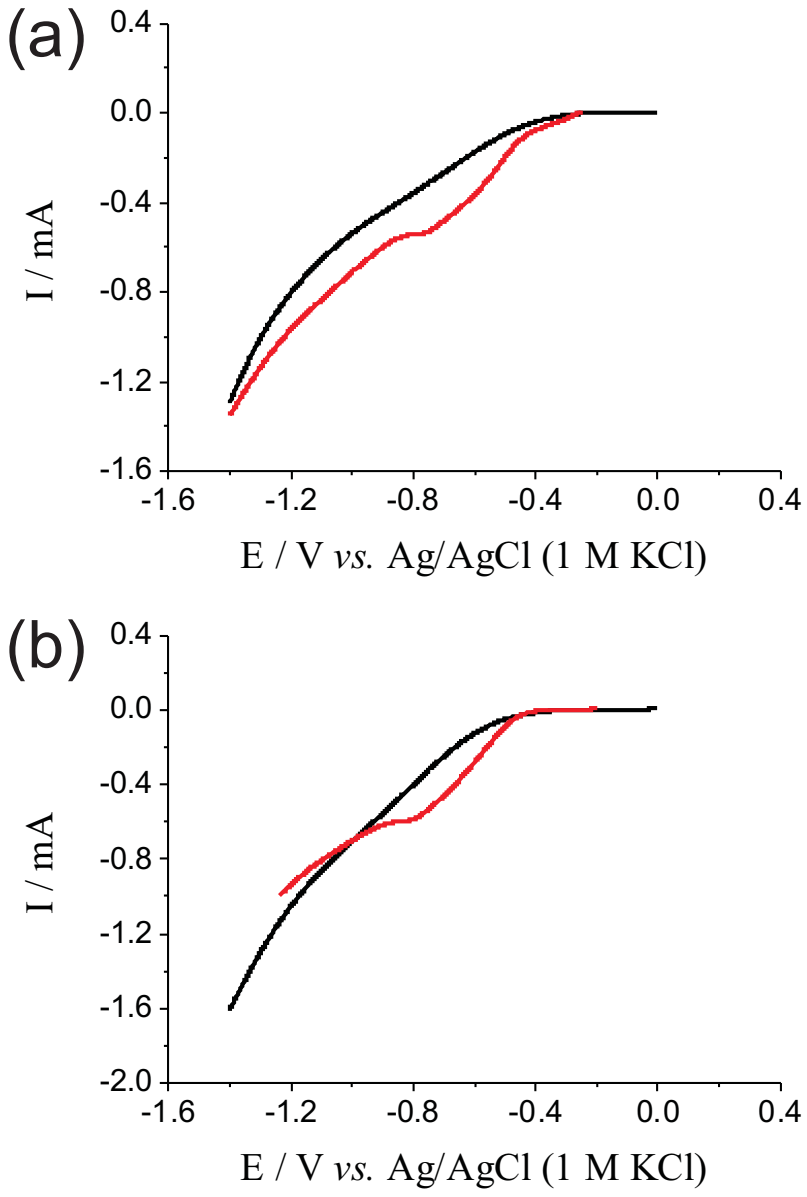

FIGURE 7.20: Linear sweep voltammograms of oxygen reduction under flowing solution of air-equilibrated PBS - 3 M KCl on both unmodified (black) and anthraquinonyl modified (red) RVC flow cell at increasing volume flow rates from (a) 0.06 to (b) 0.3 $cm^3\ s^{-1}$ at 5 $mV\ s^{-1}$.

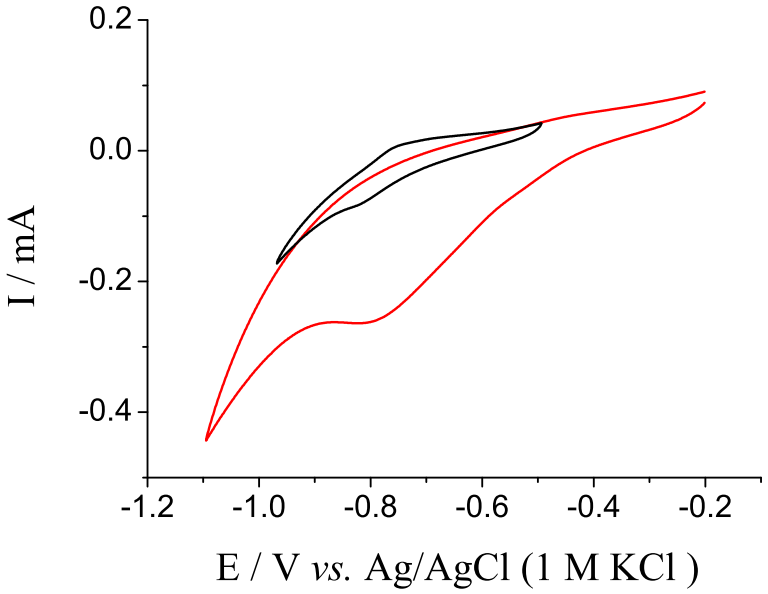

FIGURE 7.21: Redox signals of 2-anthraquinonyl modified RVCE under nitrogen saturated (black line) and air-equilibrated (red line) solution of PBS 3 M KCl at scan rate of 25 mV s^{-1}.

to the significant ohmic drop across the system. The high supporting electrolyte concentration (3 M KCl) helps to mitigate this ohmic drop distortion to a certain extent. Moreover, the high electrolyte conductivity determines the potential distribution and hence the effectiveness of the three-dimensional electrodes.

Once the electrode has been chemically modified, the surface coverage of 2-anthraquinonyl groups, Γ_{AQ} (mol cm^{-2}), can be estimated from the peak area under the redox waves (Figure 7.21) by using the following equation

$$\Gamma_{AQ} = \frac{Q}{nFA} \tag{7.26}$$

where Q is the charge passed (C), n is the number of electrons transferred (n is 2), and A is the surface area of the RVCE (cm^2).

The surface area can be estimated experimentally from the charging current on an unmodified RVCE (Section 1.4). A cyclic voltammogram can be obtained in a

solution containing *no* analyte. The blank scan shown in Figure 7.22 was obtained on the RVCE in a nitrogen saturated PBS solution, where v is the scan rate and C_d is the capacitance. It is known that the charging current is proportional to an electrode surface area (Eqn. 1.18). Additionally, the RVCE possesses similar carbon composition as a glassy carbon electrode (GCE). The former is a low volume disordered glassy porous carbon material [243]. Therefore, by relating the experimentally measured charging currents of both RVCE and GCE and the known surface area of GCE, it is possible to calculate the unknown electrode surface area for the RVCE. Consequently, the surface area of RVCE was estimated to be (4.3 ± 0.5) cm^2 per volume of a cylindrical block of RVCE with geometric radius being 0.3 cm and eletrode length (x_e) being 0.64 cm. Such a value can be justified to have a close agreement with work reported by Ponce de Leön *etc.*, where a value of 3.7 cm^2 per volume of a cylindrical block of RVCE with the same geometric cell dimensions can be estimated from their work [245]. Hence, the Γ_{AQ} was calculated to be $(1.2 \pm 0.1) \times 10^{-10}$ mol cm^{-2}. A theoretical value of 3.2×10^{-10} mol cm^{-2} was calculated for the maximum surface coverage of vertically aligned close-packed monolayer of AQ- groups [241]. Hence, the modified AQ- layer suggests a near monolayer formation on the RVCE surface.

Following the characterisation, the modified surface was then studied in an air-equilibrated solution. The electrocatalytic activity of 2-anthraquinonyl groups towards O_2 reduction becomes apparent, as shown in Figure 7.21. The large irreversible reduction wave demonstrates that the 2-anthraquinonyl groups mediate O_2 reduction process. The operative electrocatalytic mechanism is as shown in Figure 7.2, the same as that on a TGCE. With the assistance of surface bound semiquinonyl intermediate and hydroquinonyl species, O_2 is reduced to H_2O_2 [75, 250].

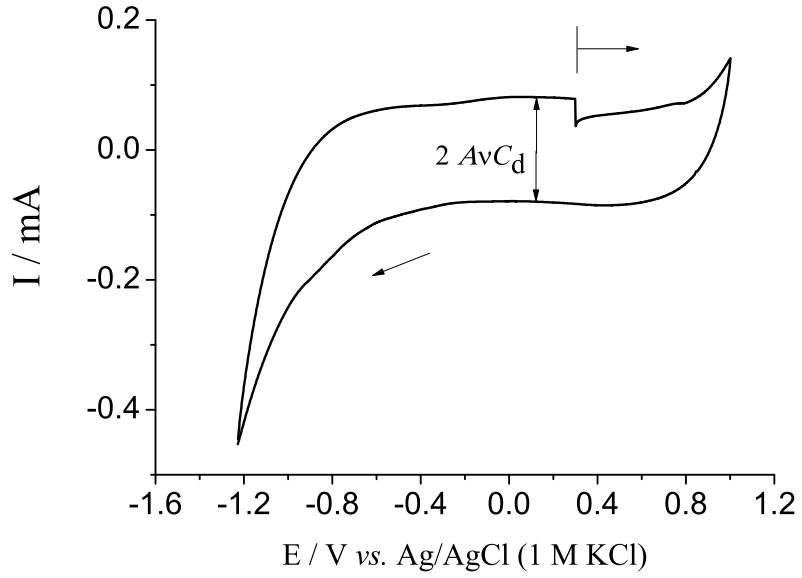

FIGURE 7.22: Cyclic voltammogram of a blank scan in nitrogen saturated PBS 3 M KCl solution on RVCE at scan rate of 100 mV s^{-1}. v is scan rate, and C_d is capacitance.

V_f / cm^3 s^{-1}	Measured I_{lim} / $\times 10^{-4}$ A	f_{AQ-RVC}	f^*_{TGC}
0.006	0.62	0.89	0.09
0.06	5.4	0.71	0.02
0.3	6.0	0.18	0.01

TABLE 7.3: Comparison of fractional current conversion of oxygen reduction on AQ-RVC flow cell (f_{AQ-RVC}) and TGC (f_{TGC}) flow cells at various volume flow rates (V_f) under air-equilibrated PBS / 3 M KCl at 25 °C, 5 mV s^{-1}. Experimentally measured limiting current (I_{lim}) on AQ-RVC flow cell is also shown. * The I_{lim} used to calculate f_{TGC} was predicted from the Levich equation (Eqn. 7.12).

The mediated O_2 reduction under hydrodynamic conditions was next investigated on the AQ-RVC flow cell. The LSVs are shown in Figure 7.20 at increasing volume flow rates from 0.06 to 0.3 cm^3 s^{-1} at 5 mV s^{-1}. The steady-state currents are shown, in comparison with direct O_2 reduction on an unmodified RVCE. In the absence of O_2, no limiting currents can be observed. Note that H_2O_2 is not active at the potentials of the steady state currents. Consequently, the limiting currents

correspond to the AQ- mediated 2-electron reduction of O_2 to H_2O_2. The limiting currents were measured against the extrapolated front baseline and were recorded in Table 7.3. It can be seen that the O_2 reduction overpotentials are significantly reduced on the modified surface. Knowing the concentration of dissolved O_2 in an air-equilibrated aqueous solution supported with 3 M KCl salt to be 0.132 mM [46], consequently the fractional current conversions in the RVC flow cell were calculated and shown in Table 7.3. The generally greater f for O_2 reduction relates to its higher diffusion coefficient as compared to that of $K_4[Fe(CN)_6]$ (1.77×10^{-5} cm^2 s^{-1} for O_2 and 6.3×10^{-6} cm^2 s^{-1} for $K_4[Fe(CN)_6]$) [227]. Similarly, as discussed earlier, the corresponding fractional current conversions on TGC flow cell can be theoretically predicted and were tabulated in Table 7.3. It can be seen that at lower V_f an almost full fractional current conversion of O_2 to H_2O_2 may be achieved on the RVC flow cell. In comparison, TGCE has a surface area of 1.2 cm^2, bearing the same geometric cell dimensions as the RVCE. Though the surface area of the RVCE is just over three times than that of the TGCE, the fractional current conversions of former demonstrate at least one order of magnitude higher. Such an outcome is mainly due to the distinct structure of the RVC material. The porous structure enhances the mass transport of analyte towards the electrochemical interface.

7.2.3 Conclusions

This section has explored the electrochemical reduction of dissolved O_2 in a neutral solution on a novelly designed RVC flow cell. A continuous synthesis of H_2O_2 at the point-of-use achieved a fractional current conversion of nearly 0.9 at a volume flow rate of 0.006 cm^3 s^{-1} on 2-anthraquinonyl groups modified RVC flow cell. The much higher fractional current conversions on RVC flow cell compared

with a two-dimensional electrode, *i.e.* tubular glassy carbon, is mainly due to its high electrode surface area and porous structure. The gravity-feed hydrodynamic system provides a promising method to produce H_2O_2 in a continuous manner at the point-of-use. It is of significant importance to have provided a bench-scale prototype for the electrochemical synthesis of H_2O_2 under continuous flow conditions.

Chapter 8

Overall conclusions

The electrochemical reduction of molecular oxygen has received continuous interest in the past decades, ranging from photosynthesis, surface corrosion, to rocket fuel synthesis. The present work started with the investigation of the electrocatalytic rates, thermodynamics, and mass transport of two oxygen reduction mediators, viz. a quinone and a viologen, in aqueous solutions. The voltammetric responses exhibited distinct features in each case, corresponding to the different rate determining steps. Through the use of simulation, very fast homogeneous rates between the semiquinone/ the viologen radical cation and molecular oxygen were identified, 10^9 M^{-1} s^{-1}, which ensure efficient redox catalysis to take place. However, the ion pairing of the semiquinone intermediate species with supporting electrolyte disfavours this electrocatalysis.

Throughout the course of this DPhil, the project has been in collaboration with Schlumberger Ltd. with the aim of developing a small scale at point-of-use generator of dilute hydrogen peroxide. This is however potentially limited by the low oxygen concentration in aqueous media. Therefore, this work further investigated the electro-reduction of oxygen and its mediated pathways in various organic

solvents. Although the solubility of oxygen is 6 – 8 fold higher in non-aqueous solvents, the bimolecular reaction rates prove to be 3 – 4 orders of magnitude lower than in aqueous solutions. Thus at the prototype flow cell stage, the aqueous solutions were used to assure high intermediate reactivities. Moreover, anthraquinonyl modified graphite surfaces were characterised with respect to surface ideality and intermediate reactivity towards reaction sites. The advantages of the surface confined catalyst has the benefit of easy separation from the product solution and much reduced power demand of the overall catalysis.

Utilising the results from earlier chapters, two gravity-feed flow cells were designed and developed, allowing continuous electrogeneration of hydrogen peroxide at point-of-use. The percentage conversion of molecular oxygen to hydrogen peroxide was shown to improve from 9% to 89% from a tubular glassy carbon to a reticulated vitreous carbon electrode at the same volume flow rate and electrode geometric dimensions. The flow cell designs were subject to two patent applications.

The modified reticulated vitreous carbon flow cell provides a promising method to produce hydrogen peroxide at point-of-use. However, the aqueous and high salt system limits the oxygen solubility and consequently lowers the product yield. Such a challenge may be approached in future studies by increasing the mole fraction of organic media in a solvent mixture, in which the reactivity of intermediate species are still retained in the aqueous part. Furthermore, knowing that the semiquinone intermediate species exhibits its highest reactivity in the non-protonated form, higher pH environment is therefore worthwhile considering. Moreover, the prototype may be further improved by separating the counter electrode with a Nafion membrane, such that a ‘collect-and-go’ reactor may hold commercial applications.

Appendix A

Fick's Laws of Diffusion

The rate of diffusion at a given point in solution is dependent upon the concentration gradient at that particular location. Fick described the diffusion mathematically by considering the simple case of linear diffusion to a planar surface (yz–plane). Consider an imaginary yz–plane with $N(x)$ molecules on one side and $N(x + \delta x)$ molecules on the other side at time t. Assuming a concentration gradient exists solely in the $x-$direction, so that diffusion occurs normal to the $yz-$plane.

Diffusion is described by the diffusion coefficient, D_i, which gives a measure of how far a molecule can travel during a period of time. The statistical view of diffusion is a random walk process that suggests the root-mean-square displacement (cm) diffused by a species in time t is

$$\sqrt{\langle x^2 \rangle} = \sqrt{2D_i t} \tag{A.1}$$

Therefore, during the interval t only half of the molecules move a distance of $\sqrt{\langle x^2 \rangle}$ towards the $x-$direction. The diffusional flux, $J_d(x)$ (mol cm^{-2} s^{-1}), is defined as

the number of moles of material diffusing through a unit area in one second and is related to the current, I, as shown:

$$I = nAFJ_d(x)$$

It is known that the total diffusive flux of i across the yz–plane is:

$$J_d(x) = \frac{\sqrt{\langle x^2 \rangle}}{2t}(C_{i,(x+\delta x)} - C_{i,x}) \tag{A.2}$$

The concentration gradient in the same direction is given by:

$$\frac{\partial C_i}{\partial x} = -\frac{(C_{i,(x+\delta x)} - C_{i,x})}{\sqrt{\langle x^2 \rangle}} \tag{A.3}$$

We can then combine Eqn. A.1 – Eqn. A.3 to obtain the expression for Fick's first law [251]:

$$J_d(x) = -\frac{\langle x^2 \rangle}{2t}\frac{\partial C_i(x)}{\partial x} = -D_i\frac{dC_i(x)}{dx} \tag{A.4}$$

where $\dfrac{\partial C_i(x)}{\partial x}$ is the local concentration gradient at point x.

Fick's first law describes the linear diffusion to a planar surface, while Fick's second law enables the prediction of concentration changes of species i close to an electrode surface as a function of time. It can be derived from Fick's first law by considering the difference in flux into and out of a volume of width dx and the area A during a time interval dt. By conservation of mass:

$$C_{i,(t+dt)}Adx - C_{i,t}Adx = J_{(x,t)}Adt - J_{(x+dx),t}Adt \tag{A.5}$$

Eqn. A.5 can be rearranged to a general relationship that is applicable to any transport:

$$\frac{\partial C_i(x)}{\partial t} + \frac{\partial J_d(x)}{\partial x} = 0 \tag{A.6}$$

Substituting Fick's first law (Eqn. A.4) into the above equation to yield Fick's second law in one dimension [252]:

$$\frac{\partial C_i(x)}{\partial t} = D_i \frac{\partial^2 C_i(x)}{\partial x^2} \tag{A.7}$$

The more general form of Fick's second law for any given geometry is:

$$\frac{\partial C_i(x)}{\partial t} = D_i \bigtriangledown^2 C_i(x) \tag{A.8}$$

where $\bigtriangledown^2$ is the Laplacian operator at any geometry.

Appendix B

The Charging Current in Electrochemical Measurement

The conditions for measuring the potential difference between a working and a reference electrode can be approximated by an electrical circuit with a resistor, R_s, representing the solution resistance and a capacitor, C_d, representing the double layer at the electrode/solution interface. Such a resistor-capacitor (RC) circuit is shown in Figure B.1. The charging current can be measured by using a voltage step or voltage ramp method.

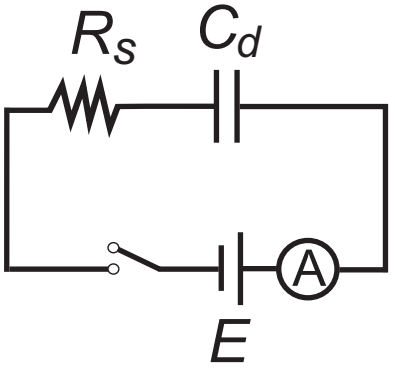

FIGURE B.1: Potential step experiment for an RC circuit.

For a general capacitor, the charge, q, is as a function of the voltage across it, E, and is linearly proportional to the electrode area, A:

$$q = AC_dE \tag{B.1}$$

At any time the sum of the voltages, E_R and E_C, across the resistor and the capacitor, respectively, must equal the applied potential:

$$E = E_R + E_C = IR_s + \frac{q}{AC_d} \tag{B.2}$$

Since $I = dq/dt$, so after rearranging Eqn. B.2, it yields

$$\frac{dq}{dt} = \frac{-q}{AR_sC_d} + \frac{E}{R_s} \tag{B.3}$$

In the initial conditions of $q = 0$ at $t = 0$, the solution of Eqn. B.3 is:

$$q = EAC_d[1 - e^{-t/AR_sC_d}] \tag{B.4}$$

By differentiating Eqn. B.4 via dq/dt, the charging current, I, can be obtained as:

$$I = \frac{\Delta E}{R_s}e^{-t/AR_sC_{DL}} \tag{B.5}$$

This equation can be used to determine the solution resistance by using chronoamperometry.

During the linear potential sweep or cyclic voltammetry experiment, the applied potential increases linearly with time at a scan rate ν (V s^{-1}):

$$E = \nu t \tag{B.6}$$

If such a ramp is applied to the RC circuit, Eqn. B.2 yields:

$$\nu t = R_s(dq/dt) + q/AC_d \tag{B.7}$$

If $q = 0$ at $t = 0$, then

$$I = \nu AC_d[1 - e^{-t/AR_sC_d}] \tag{B.8}$$

As the $t \geqslant AR_sC_d$, the charging current becomes a constant size of νAC_d. Therefore, with known values of scan rates and an electrode surface area, it is able to relate the charging current of an unknown electrode to estimate its electrode surface area, provided the capacitances of these two are approximately the same.

Appendix C

Peak Current of An Ideally Adsorbed Species

In a linear sweep voltammetric experiment, an *ideally* adsorbed species, $A_{(ad)}$, undergoes 'n'-electron reduction to form $B_{(ad)}$:

$$A_{(ad)} + ne^- \rightleftharpoons B_{(ad)}$$

The derivation below is based on the following assumptions. Fast heterogeneous electron transfer kinetics are obtained. No interactions are between the adsorbed species. All adsorption sites are equal. The surface activity is equivalent to the surface coverage, and the total surface coverage (Γ_{tot}) is independent of the applied potentials.

Since fast electrode kinetics takes place, so a Nernstian distribution of species, Γ_{tot}, is defined as:

$$\Gamma_{tot} = \Gamma_A + \Gamma_B \tag{C.1}$$

and is determined by the Nernst equation (Eqn. 1.2):

$$\frac{\Gamma_A}{\Gamma_B} = \exp(-n\theta) \tag{C.2}$$

where

$$\theta = \frac{F}{RT}(E - E_f^{\ominus})$$

which represents the normalised overpotential applied to the electrode.

Substitute Eqn. C.1 into Eqn. C.2 and rearrange to yield:

$$\Gamma_A = \frac{\exp(n\theta)}{1 + \exp(n\theta)}\Gamma_{tot} \tag{C.3}$$

The current is:

$$\frac{I}{nFA} = -\frac{\partial \Gamma_A}{\partial t}$$

and the applied potential varies with:

$$E = E_{initial} - \nu t$$

Note that minus sign represents reduction.

Next substitute the above equations into Eqn. C.3 and differentiate to give:

$$\frac{I}{nFA} = \frac{nF\nu}{RT}\Gamma_{tot}\frac{\exp(-n\theta)}{(1 + \exp(-n\theta))^2} \tag{C.4}$$

At equilibrium, *i.e.* $\theta = 0$, the peak current (I_p) can be obtained from Eqn. C.4 as:

$$\mid I_p \mid = \frac{n^2F^2A\nu}{4RT}\Gamma_{tot} \tag{C.5}$$

Bibliography

[1] Compton, R. G.; Banks, C. E. *Understanding Voltammetry*, 2nd ed.; Imperial College Press, 2011.

[2] Debye, P.; Hückel, E. *Physikalische Zeitschrift* **1923**, *24*, 185–206.

[3] Albery, W. J. *Electrode Kinetics*; Clarendon Press, 1975.

[4] Erdey-Grúz, T.; Volmer, M. *Physik. Chem.* **1930**, *150*, 203–213.

[5] Butler, J. A. V. *Trans. Fraraday Soc.* **1932**, *28*, 379–382.

[6] Bard, A. J.; Faulkner, L. R. *Electrochemical Methods: fundamentals and applications*, 2nd ed.; Wiley, 2001.

[7] Laborda, E.; Henstridge, M. C.; Batchelor-McAuley, C.; Compton, R. G. *Chem. Soc. Rev.* **2013**, *42*, 4894–4905.

[8] Compton, R. G. *Adv. Phy. Org. Chem.* **1999**, *32*, 1.

[9] Kolthoff, I. M.; Thomas, F. G. *J. Phys. Chem.* **1965**, *69*, 3049–3058.

[10] Levich, V. G. *Physicochemical hydrodynamics*; Englewood Cliffs, N.J., Prentice-Hall, 1962.

[11] Wain, A. J.; Thompson, M.; Klymenko, O. V.; Compton, R. G. *Phys. Chem. Chem. Phys.* **2004**, *6*, 4018–4027.

[12] Kittel, C. *Introduction to Solid State Physics*; Wiley Int. 8th Ed., 2005.

[13] Matsuda, H.; Ayabe, Y. *Z. Elecktrochem.* **1955**, *59*, 494–503.

[14] Compton, R. G.; Batchelor-McAuley, C.; Dickinson, E. J. F. *Understanding Voltammetry: Problems and Solutions*; Imperial College Press, 2012.

[15] Aoki, K. *Electroanalysis* **1993**, *5*, 627–639.

[16] Saito, Y. *Rev. Polarography* **1968**, *15*, 177–187.

[17] Shoup, D.; Szabo, A. *J. Electroanal. Chem.* **1982**, *140*, 237 – 245.

[18] Cottrell, E. G. Z. *Physik. Chem.* **1902**, *44*, 385.

[19] Milner, D. J. *Synthetic Communications* **1992**, *22*, 73–82.

[20] Compton, R. G.; Unwin, P. R. *J. Electroanal. Chem.* **1986**, *205*, 1 – 20.

[21] Fisher, A. C.; Compton, R. G. *J. Phys. Chem.* **1991**, *95*, 7538–7542.

[22] Cooper, J. A.; Compton, R. G. *Electroanalysis* **1998**, *10*, 141–155.

[23] Wang, Y.; Rogers, E. I.; Compton, R. G. *J. Electroanal. Chem.* **2010**, *648*, 15 – 19.

[24] Xiong, L.; Aldous, L.; Henstridge, M. C.; Compton, R. G. *Anal. Methods* **2012**, *4*, 371–376.

[25] Paddon, C. A.; Silvester, D. S.; Bhatti, F. L.; Donohoe, T. J.; Compton, R. G. *Electroanalysis* **2007**, *19*, 11–22.

[26] Klymenko, O. V.; Evans, R. G.; Hardacre, C.; Svir, I. B.; Compton, R. G. *J. Electroanal. Chem.* **2004**, *571*, 211 – 221.

[27] Rudolph, M. *J. Electroanal. Chem.* **1991**, *314*, 13–22.

[28] Rudolph, M. *J. Electroanal. Chem.* **1992**, *338*, 85–98.

[29] Newman, J. *Electrochemical Systems*; Prentice Hall, 1973; p 414.

[30] Mocak, J.; Feldberg, S. *J. Electroanal. Chem.* **1994**, *378*, 31–37.

[31] Feldberg, S.; Goldstein, C.; Rudolph, M. *J. Electroanal. Chem.* **1996**, *413*, 25–36.

[32] Rees, N. V.; Klymenko, O. V.; Compton, R. G.; Oyama, M. *J. Electroanal. Chem.* **2002**, *531*, 33 – 42.

[33] Ward, K. R.; Lawrence, N. S.; Hartshorne, R. S.; Compton, R. G. *J. Phys. Chem. C* **2011**, *115*, 11204–11215.

[34] Hage, R.; Lienke, A. *Angew. Chem. Int. Ed.* **2006**, *45*, 206–222.

[35] Minotti, G.; Menna, P.; Salvatorelli, E.; Cairo, G.; Gianni, L. *Pharmacol. Rev.* **2004**, *56*, 185–229.

[36] Singal, P. K.; Iliskovic, N. *N. Eng. J. Med.* **1998**, *339*, 900–905.

[37] Menna, P.; Salvatorelli, E.; Minotti, G. *Chem. Res. Toxicol.* **2010**, *23*, 6–10.

[38] Toghill, K. E.; Wildgoose, G. G.; Moshar, A.; Mulcahy, C.; Compton, R. G. *Electroanalysis* **2008**, *20*, 1731–1737.

[39] Jacq, J. *J. Electroanal. Chem.* **1971**, *29*, 149–180.

[40] Batchelor-McAuley, C.; Li, Q.; Dapin, S. M.; Compton, R. G. *J. Phys. Chem. B* **2010**, *114*, 4094–4100.

[41] Royea, W.; Hamann, T.; Brunschwig, B.; Lewis, N. *J. Phys. Chem. B* **2006**, *110*, 19433–19442.

[42] McCreery, R. L. *Chem. Rev.* **2008**, *108*, 2646–2687.

[43] Luong, J.; Male, K.; Glennon, J. *Analyst* **2009**, *134*, 1965–1979.

[44] Gamage, R.; McQuillan, A.; Peake, B. *J. Chem. Soc. Faraday Trans.* **1991**, *87*, 3653–3660.

[45] Koppenol, W. H.; Stanbury, D. M.; Bounds, P. L. *Free Radical Biol. Med.* **2010**, *49*, 317 – 322.

[46] Millero, F.; Huang, F.; Graham, T. *J. Solution Chem.* **2003**, *32*, 473–487.

[47] Han, P.; Bartels, D. M. *J. Phys. Chem.* **1996**, *100*, 5597–5602.

[48] Seinberg, J.-M.; Kullapere, M.; Meorg, U.; Maschion, F. C.; Maia, G.; Schiffrin, D. J.; Tammeveski, K. *J. Electroanal. Chem.* **2008**, *624*, 151 – 160.

[49] Tammeveski, K.; Kontturi, K.; Nichols, R. J.; Potter, R. J.; Schiffrin, D. J. *J. Electroanal. Chem.* **2001**, *515*, 101–112.

[50] Jones, R. D.; Summerville, D. A.; Basolo, F. *Chem. Rev.* **1979**, *79*, 139–179.

[51] Dey, A.; Jenney Jr., F.; Adams, M.; Babini, E.; Takahashi, Y.; Fukuyama, K.; Hodgson, K.; Hedman, B.; Solomon, E. *Science* **2007**, *318*, 1464–1468.

[52] Venkateswara Rao, P.; Holm, R. *Chem. Rev.* **2003**, *104*, 527–560.

[53] Raven, J.; Evans, M.; Korb, R. *Photosynth. Res.* **1999**, *60*, 111–150.

[54] Bricker, T. M.; Ghanotakis, D. F. *Adv. Photosynth.* **1996**, *4*, 113–136.

[55] Bird, C. L.; Kuhn, A. T. *Chem. Soc. Rev.* **1981**, *10*, 49–82.

[56] Monk, P.; Fairweather, R.; Ingram, M.; Duffy, J. *J. Chem. Soc., Perkin Trans. 2* **1992**, 2039–2041.

[57] Fridovich, I.; Hassan, H. *Trends Biochem. Sci.* **1979**, *4*, 113–115.

[58] Youngman, R.; Elstner, E. *FEBS Lett.* **1981**, *129*, 265–268.

[59] Winterbourn, C. *FEBS Lett.* **1981**, *128*, 339–342.

[60] Weidauer, E.; Morke, W.; Foth, H.; Bromme, H. *Arch. Toxicol.* **2002**, *76*, 89–95.

[61] Yumino, K.; Kawakami, I.; Tamura, M.; Hayashi, T.; Nakamura, M. *J. Biochem.* **2002**, *131*, 565–570.

[62] Savéant, J.-M. *Elements of molecular and biomolecular electrochemistry: an electrochemical approach to electron transfer chemistry*; John Wiley & Sons, Inc., 2006; Vol. 13.

[63] Savéant, J.-M. *Chem. Rev.* **2008**, *108*, 2348–2378.

[64] Farrington, J.; Ebert, M.; Land, E.; Fletcher, K. *Biochim. Biophys. Acta - Bioenerg.* **1973**, *314*, 372 – 381.

[65] Farrington, J. A.; Ebert, M.; Land, E. J. *J. Chem. Soc., Faraday Trans.* **1978**, *74*, 665–675.

[66] Thorneley, R. N. *Biochim. Biophys. Acta - Bioenerg.* **1974**, *333*, 487 – 496.

[67] Martigny, P.; Anson, F. C. *J. Electroanal. Chem.* **1982**, *139*, 383–393.

[68] Oh, M.-K.; Okajima, T.; Kitamura, F.; Lee, C.-W.; Tokuda, K.; Ohsaka, T. *Chem. Lett.* **1997**, *26*, 67–68.

[69] Rauwel, F.; Thevenot, D. *J. Electroanal. Chem.* **1977**, *75*, 579–593.

[70] Andrieux, C.; Hapiot, P.; Savéant, J. *J. Electroanal. Chem.* **1985**, *189*, 121 – 133.

[71] Dimarco, D. M.; Forshey, P. A.; Kuwana, T. *Chemically Modified Surfaces in Catalysis and Electroanalysis*; ACS Symposium Series 192, 1982; Chapter : Simulation of the Cyclic Voltammetric Characteristics of a Second Order EC Catalytic Mechanism, pp 71–97.

[72] Fisher, A. C.; Compton, R. G. *Electroanalysis* **1992**, *4*, 311–315.

[73] Compton, R. G.; Spackman, R. *J. Electroanal. Chem.* **1990**, *285*, 273 – 279.

[74] Batchelor-McAuley, C.; Compton, R. G. *J. Electroanal. Chem.* **2012**, *669*, 73 – 81.

[75] Li, Q.; Batchelor-McAuley, C.; Lawrence, N. S.; Hartshorne, R. S.; Compton, R. G. *ChemPhysChem* **2011**, *12*, 1255–1257.

[76] Myers, S. A.; Mackay, R. A.; Brajter-Toth, A. *Anal. Chem.* **1993**, *65*, 3447–3453.

[77] Granger, M.; Swain, G. *J. Electrochem. Soc.* **1999**, *146*, 4551–4558.

[78] Kim, J. Y.; Lee, C.; Park, J. W. *J. Electroanal. Chem.* **2001**, *504*, 104 – 110.

[79] Quan, D.; Min, D. G.; Cha, G. S.; Nam, H. *Bioelectrochemistry* **2006**, *69*, 267 – 275.

[80] Steckhan, E.; Kuwana, T. *Ber. Bunsen-Ges. Phys. Chem* **1974**, *78*, 253–259.

[81] Vinokur, N.; Miller, B.; Avyigal, Y.; Kalish, R. *J. Electrochem. Soc.* **1996**, *143*, L238–L240.

[82] Granger, M. C.; Witek, M.; Xu, J.; Wang, J.; Hupert, M.; Hanks, A.; Koppang, M. D.; Butler, J. E.; Lucazeau, G.; Mermoux, M.; Strojek, J. W.; Swain, G. M. *Anal. Chem.* **2000**, *72*, 3793–3804.

[83] Compton, R. G.; Spackman, R.; Unwin, P. R. *J. Electroanal. Chem.* **1989**, *264*, 1 – 25.

[84] Behar, D.; Czapski, G.; Rabani, J.; Dorfman, L. M.; Schwarz, H. A. *J. Phys. Chem.* **1970**, *74*, 3209–13.

[85] Berg, O.; von Hippel, P. *Annu. Rev. Biophys. Biophys. Chem.* **1985**, *14*, 131–160.

[86] Armitage, B.; Yu, C.; Devadoss, C.; Schuster, G. B. *J. Am. Chem. Soc.* **1994**, *116*, 9847–9859.

[87] Cadenas, E. *Annu. Rev. Biochem.* **1989**, *58*, 79–110.

[88] Campos-Martin, J. M.; Blanco-Brieva, G.; Fierro, J. L. G. *Angew. Chem. Int. Ed.* **2006**, *45*, 6962–6984.

[89] Costentin, C.; Evans, D. H.; Robert, M.; Savant, J.-M.; Singh, P. S. *J. Am. Chem. Soc.* **2005**, *127*, 12490–12491.

[90] Costentin, C.; Robert, M.; Saveant, J.-M. *Phys. Chem. Chem. Phys.* **2010**, *12*, 11179–11190.

[91] Batchelor-McAuley, C.; Kozub, B. R.; Menshykau, D.; Compton, R. G. *J. Phys. Chem. C* **2011**, *115*, 714–718.

[92] Izutsu, K. *Electrochemistry in Nonaqueous Solutions*; WILEY-VCH Verlag GmbH & Co. KGaA Weinheim, 2009.

[93] Quan, M.; Sanchez, D.; Wasylkiw, M. F.; Smith, D. K. *J. Am. Chem. Soc.* **2007**, *129*, 12847–12856.

[94] Wain, A.; Wildgoose, G.; Heald, C.; Jiang, L.; Jones, T.; Compton, R. *J. Phys. Chem. B* **2005**, *109*, 3971–3978.

[95] Li, Q.; Batchelor-McAuley, C.; Compton, R. G. *J. Phys. Chem. B* **2010**, *114*, 7423–7428, PMID: 20446746.

[96] Andrieux, C.; Savéant, J. *J. Electroanal. Chem.* **1970**, *28*, 339 – 348.

[97] Tissot, P.; Huissoud, A. *Electrochim. Acta* **1996**, *41*, 2451–2456.

[98] Huissoud, A.; Tissot, P. *J. Appl. Electrochem.* **1998**, *28*, 653–657.

[99] Sawyer, D. T.; Sobkowiak, A.; Roberts, J. L. *Electrochemistry for chemists*; Wiley New York, 1995; Vol. 170.

[100] Lorenzola, T. A.; López, B. A.; Giordano, M. C. *J. Electrochem. Soc.* **1983**, *130*, 1359–1365.

[101] Vasudevan, D.; Wendt, H. *J. Electroanal. Chem.* **1995**, *392*, 69 – 74.

[102] Sawyer, D. T.; Chiericato, G.; Angelis, C. T.; Nanni, E. J.; Tsuchiya, T. *Anal. Chem.* **1982**, *54*, 1720–1724.

[103] Wadhawan, J. D.; Welford, P. J.; Maisonhaute, E.; Climent, V.; Lawrence, N. S.; Compton, R. G.; McPeak, H. B.; Hahn, C. E. W. *J. Phys. Chem. B* **2001**, *105*, 10659–10668.

[104] Wei, Y.; Shao, C.; feng, H. *Russian J. Electrochem.* **2007**, *43*, 178–183.

[105] Huang, X.; Rogers, E. I.; Hardacre, C.; Compton, R. G. *J. Phys. Chem. B* **2009**, *113*, 8953–8959.

[106] Evans, R. G.; Klymenko, O. V.; Saddoughi, S. A.; Hardacre, C.; Compton, R. G. *J. Phys. Chem. B* **2004**, *108*, 7878–7886.

[107] Buzzeo, M. C.; Klymenko, O. V.; Wadhawan, J. D.; Hardacre, C.; Seddon, K. R.; Compton, R. G. *J. Phys. Chem. A* **2003**, *107*, 8872–8878.

[108] Jacob, S. R.; Hong, Q.; Coles, B. A.; Compton, R. G. *J. Phys. Chem. B* **1999**, *103*, 2963–2969.

[109] Savéant, J.-M. *J. Phys. Chem. C* **2007**, *111*, 2819–2822.

[110] Shao, M.-h.; Liu, P.; Adzic, R. R. *J. Am. Chem. Soc.* **2006**, *128*, 7408–7409.

[111] Zhang, C.; Fan, F.-R. F.; Bard, A. J. *J. Am. Chem. Soc.* **2009**, *131*, 177–181.

[112] Matsumoto, F.; Okajima, T.; Uesugi, S.; Koura, N.; Ohsaka, T. *Electrochemistry* **2003**, *71*, 266–273.

[113] Yang, H.-H.; McCreery, R. L. *J. Electrochem. Soc.* **2000**, *147*, 3420–3428.

[114] Sanchez-Sanchez, C. M.; Rodriguez-Lopez, J.; Bard, A. J. *Anal. Chem.* **2008**, *80*, 3254–3260.

[115] Yamanaka, I.; Onizawa, T.; Takenaka, S.; Otsuka, K. *Angew. Chem. Int. Ed.* **2003**, *42*, 3653–3655.

[116] Achord, J. M.; Hussey, C. L. *Anal. Chem.* **1980**, *52*, 601–602.

[117] Suárez, M. F.; Marken, F.; Compton, R. G.; Bond, A. M.; Miao, W.; Raston, C. L. *J. Phys. Chem. B* **1999**, *103*, 5637–5644.

[118] Evans, R. G.; Klymenko, O. V.; Price, P. D.; Davies, S. G.; Hardacre, C.; Compton, R. G. *ChemPhysChem* **2005**, *6*, 526–533.

[119] Battino;, R.; Rettich;, T. R.; Tominaga, T. *J. Phys. Chem. Ref. Data* **1983**, *12*, 163–179.

[120] Pierotti, R. A. *Chem. Rev.* **1976**, *76*, 717–726.

[121] Franco, C.; Olmsted, J. *Talanta* **1990**, *37*, 905 – 909.

[122] Horstmann, S.; Grybat, A.; Kato, R. *J. Chem. Thermodynamics* **2004**, *36*, 1015 – 1018.

[123] Lide, D.; Kehiaian, H. V. *CRC Handbook of Thermophysical and Thermochemical DataCRC*; CRC Press, Inc., 1994.

[124] Saha, N.; Das, B. *J. Chem. & Eng. Data* **2000**, *45*, 1125–1128.

[125] Che, Y.; Tokuda, K.; Ohsaka, T. *Bull. Chem. Soc. Jpn.* **1998**, *71*, 651–656.

[126] Abraham, M. H. *J. Am. Chem. Soc.* **1982**, *104*, 2085–2094.

[127] Noël, J.-M.; Latus, A.; Lagrost, C.; Volanschi, E.; Hapiot, P. *J. Am. Chem. Soc.* **2012**, *134*, 2835–2841.

[128] Mitroka, S.; Zimmeck, S.; Troya, D.; Tanko, J. M. *J. Am. Chem. Soc.* **2010**, *132*, 2907–2913.

[129] Singh, P. S.; Evans, D. H. *J. Phys. Chem. B* **2006**, *110*, 637–644, PMID: 16471577.

[130] Edwards, J. K.; Solsona, B.; N, E. N.; Carley, A. F.; Herzing, A. A.; Kiely, C. J.; Hutchings, G. J. *Science* **2009**, *323*, 1037–1041.

[131] González-García, J.; Banks, B., C. E. an Slijukić; Compton, R. G. *Ultrason. Sonochem.* **2007**, *14*, 405–412.

[132] Yeager, E. *Electrochim. Acta* **1984**, *29*, 1527–1537.

[133] Sarapuu, A.; Vaik, K.; Schiffrin, D. J.; Tammeveski, K. *J. Electroanal. Chem.* **2003**, *541*, 23 – 29.

[134] Murayama, T.; Yamanaka, I. *J. Phys. Chem. C* **2011**, *115*, 5792–5799.

[135] Murayama, T.; Tazawa, S.; Takenaka, S.; Yamanaka, I. *Catal. Today* **2011**, *164*, 163–168.

[136] Belding, S. R.; Limon-Petersen, J. G.; Dickinson, E. J. F.; Compton, R. G. *Angew. Chem. Int. Ed.* **2010**, *49*, 9242–9245.

[137] Tanabe, K.; Yasuda, T.; Yoshio, M.; Kato, T. *Org. Lett.* **2007**, *9*, 4271–4274.

[138] Shelepin, I.; Ushakov, O. *Zh. Fiz. Khim.* **1973**, *49*, 1736.

[139] Lin, Q.; Li, Q.; Batchelor-McAuley, C.; Compton, R. G. *Phys. Chem. Chem. Phys.* **2013**, *15*, 7760–7767.

[140] Sada, E.; Kito, S.; Oda, T.; Ito, Y. *Chem. Eng. J.* **1975**, *10*, 155 – 159.

[141] Krieger, I. M.; Mulholland, G. W.; Dickey, C. S. *J. Phys. Chem.* **1967**, *71*, 1123–1129.

[142] Ware, W. R. *J. Phys. Chem.* **1962**, *66*, 455–458.

[143] Chang, P.; Wilke, C. R. *J. Phys. Chem.* **1955**, *59*, 592–596.

[144] Li, Q.; Batchelor-McAuley, C.; Lawrence, N. S.; Hartshorne, R. S.; Compton, R. G. *J. Electroanal. Chem.* **2013**, *688*, 328 – 335.

[145] Wu, J. F.; Che, Y.; Okajima, T.; Matsumoto, F.; Tokuda, K.; Ohsaka, T. *Electrochim. Acta* **1999**, *45*, 987 – 991.

[146] Jacob, D. *Introduction to atmospheric chemistry*; Princeton University Press, 1999.

[147] Levine, I. N. *Physical Chemistry*; McGraw-Hil: Boston, 2009.

[148] Papanastasiou, G. E.; Ziogas, I. I. *J. Chem. & Eng. Data* **1991**, *36*, 46–51.

[149] Cunningham, G. P.; Vidulich, G. A.; Kay, R. L. *J. Chem. & Eng. Data* **1967**, *12*, 336–337.

[150] Nissim, R.; Batchelor-McAuley, C.; Henstridge, M. C.; Compton, R. G. *Chem. Commun.* **2012**, *48*, 3294–3296.

[151] Hahn, M.; Baertschi, M.; Barbieri, O.; Sauter, J.; K$'$otz, R.; Gallay, R. *Electrochem. Solid-State Lett.* **2004**, *7*, A33–A36.

[152] Gerischer, H.; McIntyre, R.; Scherson, D.; Storck, W. *J. Phys. Chem.* **1987**, *91*, 1930–1935.

[153] Wildgoose, G. G.; Leventis, H. C.; Davies, I. J.; Crossley, A.; Lawrence, N. S.; Jiang, L.; Jones, T. G. J.; Compton, R. G. *J. Mater. Chem.* **2005**, *15*, 2375–2382.

[154] Banks, C. E.; Compton, R. G. *Analytical Sciences* **2005**, *21*, 1263–1268.

[155] McCreery, R. L. In *Electroanalytical Chemistry a Series of Advances*; Bard, A. J., Dekker, M., Eds.; New York, 1991.

[156] Banks, C. E.; Davies, T. J.; Wildgoose, G. G.; Compton, R. G. *Chem. Commun.* **2005**, *0*, 829–841.

[157] Davies, T. J.; Hyde, M. E.; Compton, R. G. *Angew. Chem. Int. Ed.* **2005**, *44*, 5121–5126.

[158] Banks, C. E.; Moore, R. R.; Davies, T. J.; Compton, R. G. *Chem. Commun.* **2004**, *0*, 1804–1805.

[159] Cline, K. K.; McDermott, M. T.; McCreery, R. L. *J. Phys. Chem.* **1994**, *98*, 5314–5319.

[160] Neumann, C. C. M.; Batchelor-McAuley, C.; Downing, C.; Compton, R. G. *Chem. Eur. J.* **2011**, *17*, 7320–7326.

[161] McCreery, R. L.; Cline, K. K.; McDermott, C. A.; McDermott, M. T. *Colloids Surf., A* **1994**, *93*, 211 – 219.

[162] Dumitrescu, I.; Unwin, P. R.; Macpherson, J. V. *Chem. Commun.* **2009**, *0*, 6886–6901.

[163] Dudin, P. V.; Unwin, P. R.; Macpherson, J. V. *J. Phys. Chem. C* **2010**, *114*, 13241–13248.

[164] Jaegfeldt, H.; Kuwana, T.; Johansson, G. *J. Am. Chem. Soc.* **1983**, *105*, 1805–1814.

[165] Brooks, S. A.; Ambrose, W. P.; Kuhr, W. G. *Anal. Chem.* **1999**, *71*, 2558–2563.

[166] RayIII, K. G.; McCreery, R. L. *J. Electroanal. Chem.* **1999**, *469*, 150 – 158.

[167] Delamar, M.; Hitmi, R.; Pinson, J.; Saveant, J. M. *J. Am. Chem. Soc.* **1992**, *114*, 5883–5884.

[168] Allongue, P.; Delamar, M.; Desbat, B.; Fagebaume, O.; Hitmi, R.; Pinson, J.; Savéant, J.-M. *J. Am. Chem. Soc.* **1997**, *119*, 201–207.

[169] Santos, L.; Ghilane, J.; Martin, P.; Lacaze, P.-C.; Randriamahazaka, H.; Lacroix, J.-C. *J. Am. Chem. Soc.* **2010**, *132*, 1690–1698.

[170] Tornøe, C. W.; Christensen, C.; Meldal, M. *J.Org. Chem.* **2002**, *67*, 3057–3064.

[171] Gooding, J. J. *Electroanalysis* **2008**, *20*, 573–582.

[172] Pinson, J.; Podvorica, F. *Chem. Soc. Rev.* **2005**, *34*, 429–439.

[173] Brooksby, P. A.; Downard, A. J. *J. Phys. Chem. B* **2005**, *109*, 8791–8798.

[174] Kullapere, M.; Mirkhalaf, F.; Tammeveski, K. *Electrochim. Acta* **2010**, *56*, 166 – 173.

[175] Janin, M.; Ghilane, J.; Randriamahazaka, H.; Lacroix, J.-C. *Electrochem. Commun.* **2009**, *11*, 647 – 650.

[176] Wildgoose, G. G.; Abiman, P.; Compton, R. G. *J. Mater. Chem.* **2009**, *19*, 4875–4886.

[177] Leventis, H. C.; Streeter, I.; Wildgoose, G. G.; Lawrence, N. S.; Jiang, L.; Jones, T. G.; Compton, R. G. *Talanta* **2004**, *63*, 1039 – 1051.

[178] Xiong, L.; Batchelor-McAuley, C.; Compton, R. G. *Sens. Actuators, B* **2011**, *159*, 251 – 255.

[179] Wildgoose, G. G.; Leventis, H. C.; Simm, A. O.; Jones, J. H.; Compton, R. G. *Chem. Commun.* **2005**, 3694–3696.

[180] Sljukić, B.; Wildgoose, G. G.; Crossley, A.; Jones, J. H.; Jiang, L.; Jones, T. G. J.; Compton, R. G. *J. Mater. Chem.* **2006**, *16*, 970–976.

[181] Sljukić, B.; Banks, C. E.; Compton, R. G. *Electroanalysis* **2005**, *17*, 1025–1034.

[182] Mirkhalaf, F.; Tammeveski, K.; Schiffrin, D. J. *Phys. Chem. Chem. Phys.* **2009**, *11*, 3463–3471.

[183] Alexeyeva, N.; Shulga, E.; Kisand, V.; Kink, I.; Tammeveski, K. *J. Electroanal. Chem.* **2010**, *648*, 169 – 175.

[184] Sarapuu, A.; Helstein, K.; Vaik, K.; Schiffrin, D. J.; Tammeveski, K. *Electrochim. Acta* **2010**, *55*, 6376 – 6382.

[185] Bianco, A.; Kostarelos, K.; Partidos, C. D.; Prato, M. *Chem. Commun.* **2005**, *0*, 571–577.

[186] Mahouche-Chergui, S.; Gam-Derouich, S.; Mangeney, C.; Chehimi, M. M. *Chem. Soc. Rev.* **2011**, *40*, 4143–4166.

[187] Laviron, E. *J. Electroanal. Chem.* **1979**, *105*, 25 – 34.

[188] Honeychurch, M. J.; Rechnitz, G. A. *Electroanalysis* **1998**, *10*, 285–293.

[189] Kozub, B. R.; Henstridge, M. C.; Batchelor-McAuley, C.; Compton, R. G. *ChemPhysChem* **2011**, *12*, 2806–2815.

[190] Ru, J.; Szeto, B.; Bonifas, A.; McCreery, R. L. *ACS Applied Materials & Interfaces* **2010**, *2*, 3693–3701.

[191] Combellas, C.; Kanoufi, F.; Pinson, J.; Podvorica, F. I. *J. Am. Chem. Soc.* **2008**, *130*, 8576–8577, PMID: 18553968.

[192] Combellas, C.; Jiang, D.-e.; Kanoufi, F.; Pinson, J.; Podvorica, F. I. *Langmuir* **2009**, *25*, 286–293.

[193] Nielsen, L. T.; Vase, K. H.; Dong, M.; Besenbacher, F.; Pedersen, S. U.; Daasbjerg, K. *J. Am. Chem. Soc.* **2007**, *129*, 1888–1889.

[194] Malmos, K.; Dong, M.; Pillai, S.; Kingshott, P.; Besenbacher, F.; Pedersen, S. U.; Daasbjerg, K. *J. Am. Chem. Soc.* **2009**, *131*, 4928–4936.

[195] Ghilane, J.; Martin, P.; Fontaine, O.; Lacroix, J.-C.; Randriamahazaka, H. *Electrochem. Commun.* **2008**, *10*, 1060 – 1063.

[196] Fave, C.; Noel, V.; Ghilane, J.; Trippé-Allard, G.; Randriamahazaka, H.; Lacroix, J. C. *J. Phys. Chem. C* **2008**, *112*, 18638–18643.

[197] Stockhausen, V.; Ghilane, J.; Martin, P.; Trippe-Allard, G.; Randriamahazaka, H.; Lacroix, J.-C. *J. Am. Chem. Soc.* **2009**, *131*, 14920–14927.

[198] Santos, L. M.; Ghilane, J.; Fave, C.; Lacaze, P.-C.; Randriamahazaka, H.; Abrantes, L. M.; Lacroix, J.-C. *J. Phys. Chem. C* **2008**, *112*, 16103–16109.

[199] Ghilane, J.; Martin, P.; Randriamahazaka, H.; Lacroix, J.-C. *Electrochem. Commun.* **2010**, *12*, 246 – 249.

[200] Fontaine, O.; Ghilane, J.; Martin, P.; Lacroix, J.-C.; Randriamahazaka, H. *Langmuir* **2010**, *26*, 18542–18549.

[201] Liu, Y.-C.; McCreery, R. L. *J. Am. Chem. Soc.* **1995**, *117*, 11254–11259.

[202] Kuo, T.-C.; McCreery, R. L.; Swain, G. M. *Electrochem. Solid-State Lett.* **1999**, *2*, 288–290.

[203] Lehr, J.; Williamson, B. E.; Downard, A. J. *J. Phys. Chem. C* **2011**, *115*, 6629–6634.

[204] Gui, A. L.; Liu, G.; Chockalingam, M.; Le Saux, G.; Luais, E.; Harper, J. B.; Gooding, J. J. *Electroanalysis* **2010**, *22*, 1824–1830.

[205] Cohen, T.; Lipowitz, J. *Tetrahedron Lett.* **1964**, *5*, 3721 – 3725.

[206] Andrieux, C. P.; Pinson, J. *J. Am. Chem. Soc.* **2003**, *125*, 14801–14806.

[207] Reilson, R.; Kullapere, M.; Tammeveski, K. *Electroanalysis* **2010**, *22*, 513–518.

[208] Ray, K.; McCreery, R. L. *Anal. Chem.* **1997**, *69*, 4680–4687.

[209] Komura, T.; Isogai, S.; Yamaguchi, T.; Takahashi, K. *J. Electroanal. Chem.* **2000**, *490*, 70 – 78.

[210] Kariuki, J. K.; McDermott, M. T. *Langmuir* **2001**, *17*, 5947–5951.

[211] Prakash, A. *Acta Crystallographica* **1967**, *22*, 439–440.

[212] *Electroanalytical Chemistry a Series of Advances*; Calculated using Advanced Chemistry Development (ACD/Labs) Software V11.02 (1994-2011 ACD/Labs).

[213] Ji, X.; Banks, C. E.; Crossley, A.; Compton, R. G. *ChemPhysChem* **2006**, *7*, 1337–1344.

[214] Li, Q.; Batchelor-McAuley, C.; Compton, R. G. *J. Phys. Chem. B* **2010**, *114*, 9713–9719.

[215] Ceccato, M.; Nielsen, L. T.; Iruthayaraj, J.; Hinge, M.; Pedersen, S. U.; Daasbjerg, K. *Langmuir* **2010**, *26*, 10812–10821.

[216] Kariuki, J. K.; McDermott, M. T. *Langmuir* **1999**, *15*, 6534–6540.

[217] Noël, M.; Chandrasekaran, S.; Basha, C. *J. Electroanal. Chem.* **1987**, *225*, 93 – 109.

[218] McDermott, M. T.; McCreery, R. L. *Langmuir* **1994**, *10*, 4307–4314.

[219] Chang, H.; Bard, A. J. *Langmuir* **1991**, *7*, 1143–1153.

[220] Jose, S. *Global Hydrogen Peroxide Market*; 2012 March 09.

[221] Kinoshita, K. *Electrochemical Oxygen Technology*; pp. 369,8, John Wiley & Sons, Inc., 1992.

[222] Oloman, C. *Electrochemical Processing for the Pulp and Paper Industry*; p. 143, The Electrochemical Consultancy, Romsey, 1996.

[223] Yamanaka, I.; Murayama, T. *Angew. Chem. Int. Ed.* **2008**, *47*, 1900–1902.

[224] Brillas, E.; Sirés, I.; Oturan, M. A. *Chem. Rev.* **2009**, *109*, 6570–6631, PMID: 19839579.

[225] Gyenge, E. L.; Drillet, J.-F. *J. Electroanal. Chem. Soc.* **2011**, *159*, F23–F34.

[226] Scialdone, O.; Galia, A.; Sabatino, S. *Electrochem. Commun.* **2013**, *26*, 45 – 47.

[227] Li, Q.; Henstridge, M. C.; Batchelor-McAuley, C.; Lawrence, N. S.; Hartshorne, R. S.; Compton, R. G. *Phys. Chem. Chem. Phys.* **2013**, *15*, 7854–7865.

[228] Klatt, L. N.; Blaedel, W. J. *Anal. Chem.* **1967**, *39*, 1065–1072.

[229] Dickinson, E. J. F.; Limon-Petersen, J. G.; Rees, N. V.; Compton, R. G. *J. Phys. Chem. C* **2009**, *113*, 11157–11171.

[230] Alden, J. A.; Compton, R. G. *J. Electroanal. Chem.* **1996**, *404*, 27–35.

[231] Britz, D. *Digital Simulation in Electrochemistry*, 3rd ed.; Springer, 2005.

[232] Compton, R. G.; Pilkington, M. B. G.; Stearn, G. M. *J. Chem. Soc. Faraday Trans.* **1988**, *84*, 2155–2171.

[233] Suwatchara, D.; Henstridge, M. C.; Rees, N. V.; Compton, R. G. *J. Phys. Chem. C* **2011**, *115*, 14876–14882.

[234] Amatore, C.; Da Mota, N.; Sella, C.; Thouin, L. *Anal. Chem.* **2007**, *79*, 8502–8510.

[235] Amatore, C.; Da Mota, N.; Lemmer, C.; Pebay, C.; Sella, C.; Thouin, L. *Anal. Chem.* **2008**, *80*, 9483–9490.

[236] Amatore, C.; Da Mota, N.; Sella, C.; Thouin, L. *Anal. Chem.* **2010**, *82*, 2434–2440.

[237] Chen, L.; Colyer, C. L.; Kamau, M. G.; Myland, J. C.; Oldham, K. B.; Symons, P. G. *Can. J. Chem.* **1994**, *72*, 836–849.

[238] Banks, C. E.; Compton, R. G.; Fisher, A. C.; Henley, I. E. *Phys. Chem. Chem. Phys.* **2004**, *6*, 3147–3152.

[239] Welch, C. M.; Banks, C. E.; Simm, A. O.; Compton, R. G. *Anal. Bioanal. Chem.* **2005**, *382*, 12–21.

[240] Hartnig, C.; Koper, M. T. M. *J. Electroanal. Chem.* **2002**, *532*, 165–170.

[241] Li, Q.; Batchelor-McAuley, C.; Lawrence, N. S.; Hartshorne, R. S.; Compton, R. G. *New J. Chem.* **2011**, *35*, 2462–2470.

[242] Wang, J. *Electrochim. Acta* **1981**, *26*, 1721 – 1726.

[243] Friedrich, J.; de León, C. P.; Reade, G.; Walsh, F. *J. Electroanal. Chem.* **2004**, *561*, 203 – 217.

[244] Davison, J. B.; Kacsir, J. M.; Peerce-Landers, P. J.; Jasinski, R. *J. Electroanal. Chem.* **1983**, *130*, 1497–1501.

[245] León, C.; Pletcher, D. *J. Appl. Electrochem.* **1995**, *25*, 307–314.

[246] Alvarez-Gallegos, A.; Pletcher, D. *Electrochim. Acta* **1998**, *44*, 853 – 861.

[247] Gyenge, E. L.; Oloman, C. W. *J. Electroanal. Chem. Soc.* **2005**, *152*, D42–D53.

[248] Saleh, M. M.; Awad, M. I.; Ohsaka, T. *ECS Transactions* **2007**, *3*, 67–78.

[249] Awad, M.; Saleh, M.; Ohsaka, T. *J. Solid State Electrochem.* **2008**, *12*, 251–258.

[250] Wilson, T.; Zhang, J.; Oloman, C. C.; Wayner, D. D. M. *Int. J. Electrochem. Sci.* **2006**, *1*, 99–109.

[251] Fick, A. *Poggendorffs Annel. Physik* **1855**, *94*, 59.

[252] Fick, A. *Phil. Mag.* **1855**, *10*, 30.